Deposit characterization based on pulsed neutron induced borehole n-/γ-spectroscopy

Doctoral Thesis

(Dissertation)

to be awarded the degree

Doctor rerum naturalium

- Dr. rer. nat. -

submitted by

Micha Janosch Zauner

from Buchen (im Odenwald)

approved by

the Faculty of Energy and Economic Sciences,

Clausthal University of Technology

Date of oral examination

30.06.2021

Dean
Prof. Dr. mont. Leonhard Ganzer

Chairperson of the Board of Examiners
Prof. Dr. rer. nat. Hans-Jürgen Gursky

Supervising tutor
Prof. Dr. rer. nat. Andreas Weller

Reviewer
Prof. Dr. rer. nat. Bernd Lehmann

Abstract

Pulsed neutron borehole logging is an established method in the hydrocarbon industry for reservoir characterization. The conservative mining industry historically has been reluctant in implementing it for deposit characterization due to a lack of slim sized logging tools and appropriate results. The need for petrophysical and geochemical deposit characterization based on pulsed neutron induced borehole n-/γ-spectroscopy was addressed in this thesis with a newly developed logging tool (d = 76 mm; l = 3 m; m = 33 kg) called OreLog suitable for elemental logging of ore deposits.

Extensive laboratory test work was realized to determine the appropriate n- and γ-detectors, their operational conditions and physical location within the tool to meet this goal. The development was supported by Monte Carlo N-Particle transport code (MCNP) simulations to determine the behavior of the detectors and deduce elemental logging algorithms by surrounding the tool with different materials. Once the basic tool settings have been determined, field tests in two well explored Australian deposits were carried out: Channel iron deposits in the Pilbara exposing mainly sedimentary and metamorphic rocks and the operating Beverley mine with nearby deposits exposing sedimentary, metamorphic, and igneous rocks. Both geochemical and petrophysical assays from drill core samples and cuttings were collected besides hydrogeological data derived from pump tests at the Beverley deposits. Detailed core logs were compiled including laboratory assays where available. OreLog algorithms were calibrated based on MCNP simulations of common deposit scenarios and well characterized boreholes. Dozens of dry and waterfilled boreholes were logged and the output data was compared to laboratory data. The acquired n-distributions and γ-spectra were processed by template matching for elemental logging and estimation of petrophysical parameters.

The results of the investigated deposits show a neutron penetration diameter up to 1 m around the borehole compared to punctual core data, a strong correlation with Fe, Si, Al, Ca, Cl, and low detection limits. Ti, K, Mn, C, H, Mg are detectable (semi-)quantitatively. Petrophysical quantities like density and porosity are estimated adequately, whereas permeability estimations in variable lithologies are not correlated, neither on core nor regional scale. Real-time elemental logging in HQ (≥ 96 mm) boreholes has been validated. Limitations apply to petrophysical quantities which are more realistically determined by NMR borehole tools. Some further technical improvements and enhancement of calibration parameters alongside a variable neutron pulsing regime could further increase the accuracy and suite of detectable elements.

Zusammenfassung

Die gepulste Neutronenbohrlochmessung ist in der Kohlenwasserstoffindustrie eine etablierte Methode zur Reservoircharakterisierung. Die konservative Bergbauindustrie hat in der Vergangenheit gezögert, diese für die Lagerstättencharakterisierung einzusetzen, da es an schlanken Bohrlochsonden und verwertbaren Ergebnissen mangelte. Die petrophysikalische und geochemische Lagerstättencharakterisierung, mittels der gepulsten neutroneninduzierten n-/γ-Spektroskopie Bohrlochmessung mit einer neu entwickelten Bohrlochsonde (d = 76 mm; l = 3 m; m = 33 kg) namens OreLog, zur Bestimmung der Elementzusammensetzung von Erzlagerstätten, ist Ziel dieser Dissertation.

Es wurden umfangreiche Labortests durchgeführt, um geeignete n- und γ-Detektoren, deren ideale Betriebsbedingungen und geometrische Anordnung innerhalb der Sonde, zu definieren. Die Entwicklung wurde durch Monte-Carlo-Simulationen des N-Teilchen-Transportcodes (MCNP) unterstützt, um die Detektoreigenschaften zu bestimmen und Algorithmen für die Elementanalytik abzuleiten, indem die Sonde von verschiedenen Materialien umgeben wurde. Nachdem die grundlegenden Sondeneinstellungen definiert waren, wurden Feldtests in zwei gut erkundeten australischen Lagerstätten durchgeführt: Kanal- und Bändereisenerzlagerstätten im Pilbara, die hauptsächlich sedimentäre und metamorphe Lithologien vorweisen, und die aktive Beverley-Mine mit umliegenden Lagerstätten, die sedimentäre, metamorphe und magmatische Lithologien beinhalten. Es wurden sowohl geochemische als auch petrophysikalische Analysen an Bohrkernen und -klein zusammengestellt, sowie von Pumpversuchen abgeleitete hydrogeologische Daten der Beverley Lagerstätten. Detaillierte Bohrkerndokumentationen einschließlich vereinzelter dedizierter Laboruntersuchungen wurden durchgeführt. Die OreLog-Algorithmen wurden anhand von MCNP-Simulationen gängiger Lagerstättenzusammensetzungen und gut charakterisierter Bohrlöcher kalibriert. Dutzende von trockenen und wassergefüllten Bohrlöchern wurden geloggt und die Ergebnisse mit Laboranalysen verglichen. Die gewonnenen Neutronenverteilungen und γ-Spektren wurden durch Template-Matching für die Elementzusammensetzung und die Ableitung petrophysikalischer Parameter entfaltet.

Die Ergebnisse der untersuchten Lagerstätten zeigen eine Neutronenpenetrationstiefe von bis zu 1 m Durchmesser um das Bohrloch im Vergleich zu punktuellen Bohrkerndaten, eine starke Elementkorrelation von Fe, Si, Al, Ca, Cl, und niedrige Nachweisgrenzen. Ti, K, Mn, C, H, Mg sind (semi-)quantitativ nachweisbar.

Petrophysikalische Größen wie Dichte und Porosität werden von der Bohrlochsonde adäquat geschätzt, wohingegen Permeabilitätsschätzungen weder auf Bohrkernskala noch auf regionaler Skala korreliert sind. Die Echtzeit-Elementmessung in HQ-Bohrungen (≥ 96 mm) wurde validiert. Einschränkungen gelten für petrophysikalische Größen, die durch NMR Bohrlochsonden realistischer bestimmt werden. Geringfügige technische Verbesserungen und die Erweiterung der Kalibriergrößen zusammen mit einem variablen Neutronenpuls-Regime könnten die Genauigkeit und die Anzahl der messbaren Elemente weiter erhöhen.

Acknowledgements

While completing this PhD thesis, I was supported by many people, who I want to thank at this point.

First, I want to thank the company Umwelt- und Ingenieurtechnik GmbH Dresden (UIT) for offering me this very interesting topic and for funding the project. Therefore, I am very thankful to Dr. Horst Märten, who convinced me to write this PhD thesis and accompanied me throughout this journey by sharing his vast physical knowledge and technical experience besides his extraordinary personal guidance.

Only thanks to the open and very collaborative scientific spirit of my doctoral supervisor Prof. Andreas Weller this highly ambitious and cooperative project between UIT and TU Clausthal was possible. An intensive and regular scientific cooperation between the geophysical institute and several graduate students supervised by UIT who stimulated the scientific exchange was established and formed the ground for new ideas and several publications. I am obliged to Prof. Weller's and Dr. Märten's very expedient way of leading and establishing this fruitful cooperation between academia and industry, which allowed me to deliver this work thanks to their continuous guidance and technical advice. I thank Prof. Bernd Lehmann for taking up the position as second reviewer and for his geological input and constant availability.

A special thanks goes to Dr. Jens Schubert, Dr. Harald Kalka and Dr. Alexander Domula who were always available for technical discussions and supported me on a daily basis. The same accounts for my fellow students and tutors at the IKTP of TU Dresden during my studies of nuclear physics and discussions related to my thesis.

I appreciate the ability of carrying out field tests at two mine and exploration sites in Australia and the provision of relevant data by the responsible mining companies Heathgate Resources and API.

Above all, I want to thank my wife Wanda and my family and friends for relinquishing countless weekends and evenings of my free time to write this thesis and their steady support and motivation. Without them I would never been able to achieve what I have now and I definitely will miss this very intense time of scientific research and exchange with TU Clausthal and colleagues.

Content

List of Figures

List of Tables

List of Abbreviations

a.u.	Arbitrary Units
ADC	Analog to Digital Converter
APFN^{+}	Advanced Prompt Fission Neutron (borehole logging tool)
API	Australian Premium Iron (company)
BGL	Below Ground Level
BGO	Bismuth Germanate crystal $Bi_4Ge_3O_{12}$
BID	Banded Iron Deposit
BIF	Banded Iron Formation
c.u.	Capture Units (1 c.u. = 10^{-3} cm^{-1})
CID	Channel Iron Deposit
cpp	Counts per Primary Particle
cps	Counts per Second (unit of rates)
CPU	Central Processing Unit
CVD	Chemical Vapor Deposition process
DAQ	Data Acquisition
DD	Diamond Drill
DE(P)	Double Escape (Peak)
DLL	Dynamic Link Library (for MS Windows)
DNAPL	Dense Non-Aqueous Phase Liquid
DSC	Depth and Source Strength Correction
DT	Deuterium-Tritium
ECS	Elemental Capture Spectroscopy (tool)
ELAN	Elemental Analysis
EOH	End of Hole
FIFO	Fly-in Fly-out
FLT	Field Leach Trial
FMD	Four Mile Diamictite
FWHM	Full Width Half Maximum
GLT	Geochemical Logging Tool
GPS	Global Positioning System
GUI	Graphical User Interface
HDPE	High-Density Polyethylene
HGR	Heathgate Ressources Pty Ltd (company)
HI	Hydrogen Index

HV	High-Voltage
HVPS	High-Voltage Power Supply
i.a.	Inter Altere (among others)
ISR	In-situ Recovery
IT	Information Technology
JANIS	Java-based Nuclear Data Information System
LAS	Log ASCII Standard (files for geophysical wireline well logs)
LED	Light Emitting Diode
LNAPL	Light Non-Aqueous Phase Liquid
LOD	Limit Of Detection
LOI	Loss on Ignition
LR	Linear Regularisation
MCA	Multi Channel Analyzer
MCNP	Monte Carlo N-Particle (transport code)
MCS	Multi-Channel Scaling
MEM	Maximum Entropy Method
ML-EM	Maximum-Likelihood Expectation Maximization
n	Neutron
NEA	Nuclear Energy Agency
NG	Neutron Generator
NMR	Nuclear Magnetic Resonance
OD	Outer Diameter
ODP	OreLog Data Processing
OECD	Organization for Economic Co-operation and Development
OreLog	Trademark of Ore Logging Borehole Tool
PC	Personal Computer
PE	Polyethylene
PEEK	Polyether Ether Ketone
PFN	Prompt Fission Neutron (borehole logging)
PFTNA	Pulsed Fast and Thermal Neutron Analysis
PHA	Pulse Height Analyzer
PMT	Photo Multiplier Tube
PNG	Pulsed Neutron Generator
POM	Polyoxymethylene
PP	Photo Peak

ppm	Parts Per Million
Preamp	Preamplifier
PUR	Pile-up Rejection
PVC	Polyvinyl Chloride
PZ	Pole Zero
QA/QC	Quality Assessment/Quality Control
R&D	Research and Development
RC	Reverse Circulation (drilling method)
REE	Rare Earth Element
RL	Relative Level
RSICC	Radiation Safety Information Computational Center
SE(P)	Single Escape (Peak)
SGT	Spectral Gamma Templates
SP	Spontaneous Potential
SSD	Source Strength Detector
STDV	Standard Deviation
TM	Trademark
TTL	Transistor-Transistor Logic
UIT	Umwelt- und Ingenieurtechnik GmbH Dresden (company)
USA	United States of America
UTM	Universal Transverse Mercator
WL	Water Level
WPIOP	West Pilbara Iron Ore Project
XRF	X-Ray Fluorescence
YAP	Yttrium Aluminum Perovskit ($YAlO_3$)

1 Introduction

Borehole geophysical logging for exploration and characterization of mineral deposits is playing an increasingly significant role in the mineral resources industry. Most near surface deposits have already been discovered and exploited. Hence the supply of raw materials is progressively being secured by mining deeper as well as unconventional deposits. Exploration becomes more challenging and expensive with increasing depth. The future of mining will focus on deeply situated mineral occurrences which need to be explored by new technologies (Kausch et al., 2013). Besides standard downhole geophysical tools such as caliper, resistivity, γ, induction, and density logs, elemental logging by γ-spectroscopy bears the potential to replace expensive coring and subsequent time-intensive and costly laboratory core analysis. Ore deposits of increasing depth can be characterized in a reliable, fast and cost-effective way.

It has long been recognized that accurately determining elemental concentrations through borehole logging provides important data for evaluating mineral reserves and for obtaining better insight into geological processes. The petroleum industry was the initial and main driver of the development of sophisticated borehole logging tools starting as early as the 1920ies. Until recently, the problem of relating γ-ray intensities to elemental concentrations has been extremely difficult and generally successful for only a few types of restricted environments (Ellis and Singer, 2007). This is due to the fact that most tools currently used in the downhole logging industry are only equipped with γ-spectrometers. A recent improvement has been the development of an analysis procedure combining γ-ray intensities obtained from natural activity, prompt thermal neutron capture reactions, and delayed activity. In conjunction with detected neutron intensities elemental concentrations for 16 elements (Al, Ba, C, Ca, Cl, Cu, Fe, Gd, K, Mg, Mn, Na, Ni, S, Si, Ti) can be obtained, which are significant for describing geological strata and determining ore grades. These new findings have been incorporated, tested, and partially validated within a new borehole logging tool called OreLog. This tool is based on the general technical design and operational software of the existing PFN tool APFN$^+$ (Advanced Prompt Fission Neutron) being a predecessor as explained in chapter 3.1, whereas APFN$^+$ development for other applications ceased in 2015 and the following tasks are the starting point of this thesis.

To achieve this challenging goal and validate these findings, a new and holistic approach to the combined interpretation of neutron- and γ-detector data is required. A geophysical borehole tool needs to be designed and manufactured to provide this

information in real-time for deduction of petrophysical formation parameters and evaluation of the ore characteristics. Since those elemental logging approaches exist already in the oil & gas industry for several decades by using tools with large diameters (>100 mm or 4 in) in dedicated hydrocarbon-specific environments, this work focuses on small tool diameters and exploration of diverse formations (ore genesis and association) with multi-elemental logging. The following tasks are required and addressed in this work:

- Realization of slim tool dimensions (≤76 mm or 3 in),
- Selection of adequate neutron- and γ-detectors,
- Positioning of detectors,
- Reliable and accurate measurement and recording of petrophysical raw data,
- MCNP modeling for expected detector response and elemental template generation,
- Application of a novel hybrid approach between template matching and field/calibration pit data,
- Spectral deconvolution,
- Estimation of elemental abundance besides petrophysical formation parameters like porosity,
- Verification of tool design and performance in laboratory tests and field tests at representative formations (samples) for the intended application by correlation of OreLog output with available laboratory assays (e.g. chemical analysis, density, porosity).

The validation of the model results (MCNP) in laboratory experiments and UIT (Umwelt- und Ingenieurtechnik GmbH Dresden) test borehole measurements is considered as an iterative process increasing accuracy and applicability as much as possible before any extensive field testing. Therefore, it is expected to focus on the detector features and response modeling with respective data processing algorithm development in first place. Field logging campaigns and data comparison with dedicatedly characterized (geochemical assay, petrology, petrophysics) boreholes are an indispensable requirement and the results are considered as the ultimate proof if the elemental logging approaches chosen in this work are beneficial. It is assumed that without any site-specific calibration at reference holes or calibration pits, reliable ore characterization cannot be performed. Therefore, it is envisaged to characterize mineral formations by the developed method for the first time and take elemental borehole logging for ore characterization to new frontiers.

2 Fundamentals of Borehole Logging

2.1 Borehole Logging Techniques

Rust (1938) reports that apparently in 1913 the first borehole resistance log was made in Germany by Richard Ambronn marking the beginning of downhole logging by placing one electrode at the surface and lowering the other through the drilling fluid down a borehole. Nevertheless, it took several decades until the Schlumberger brothers among others established it commercially as industry standard in the hydrocarbon industry (Spies, 1996). In the mineral resources' application, the purpose of geophysical borehole logging (also called well logging, downhole logging, or wireline logging) is to provide parameters, which can be related to the lithology (ore) or the fluids present in case of porous formations. Measurement techniques provide electrical, electromagnetic, radiological (nuclear), and acoustic (seismic) parameters. Usually, a measurement is sensitive either to the properties of the rock (ore) or to the pore-filling fluid often as a substitute for core or fluid sampling. Generally, four categories of logging probes are differentiated: (i) electric logs including electrical resistivity, spontaneous potential (SP) and induction logs, (ii) nuclear logs including γ and neutron logs, (iii) sonic logs including borehole tele-viewer, (iv) miscellaneous logs including caliper, deviation, temperature, gravity, Nuclear Magnetic Resonance (NMR) and other logs (Ellis and Singer, 2007). A sound introduction to borehole logging and the corresponding measurement techniques can be found in Ellis and Singer (2007).

A wireline geophysical borehole logging system is essentially comprised of the following equipment as shown in Figure 2.1:

(1) A downhole tool (or sonde/probe) containing the appropriate sensing systems,
(2) An armored multi-conductor electric cable (the wireline) to which the tool is attached and provides communication and data transmission,
(3) A winch and mast/tripod for lowering and raising the tool in the borehole,
(4) A calibrated sheave on the mast/tripod for measuring the cable length,
(5) A surface power unit,
(6) An electronic recording system for signals/data received from the tool. The resulting data is recorded as a function of depth and constitute the geophysical borehole log (Ellis and Singer, 2007).

For mineral logging applications it is usually mounted on a small logging truck or a pickup with a tripod allowing a quick and versatile setup for data acquisition in the field.

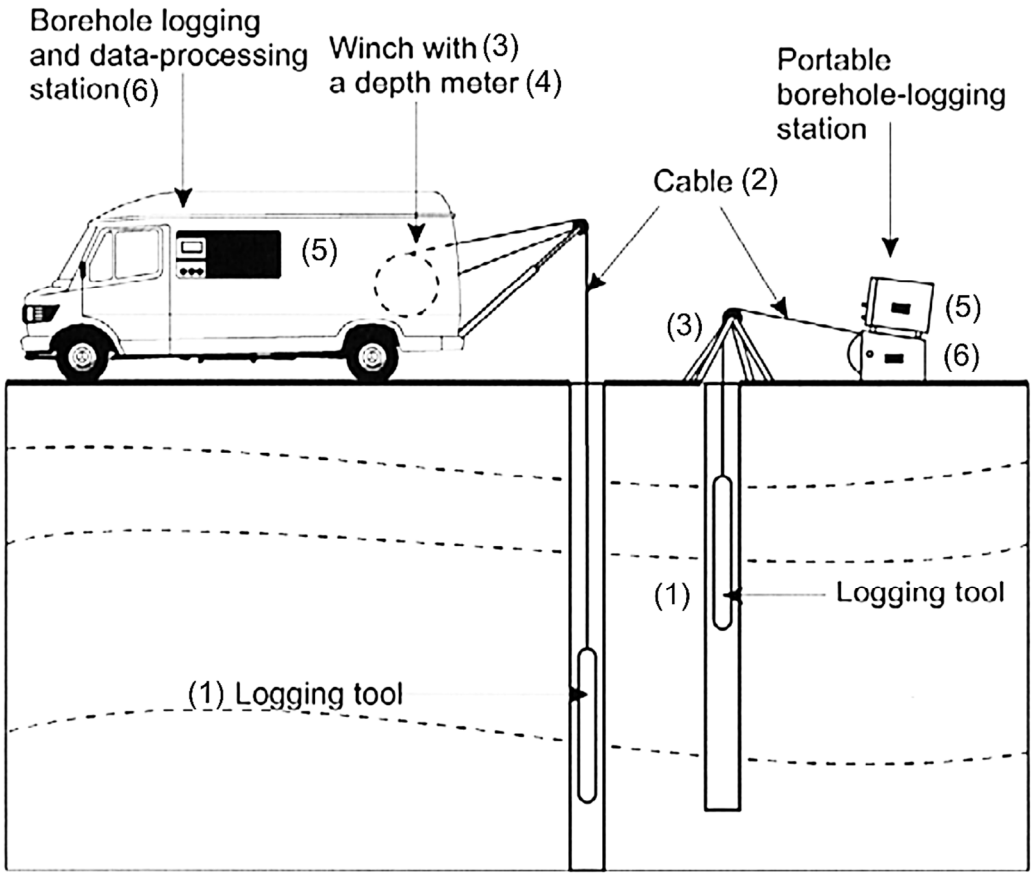

Figure 2.1: Setup and main components of borehole logging equipment. Modified after Wonik and Olea (2007).

The depth of investigation of the individual borehole logging techniques varies significantly ranging from few centimeters up to several meters behind the borehole wall (Fricke and Schön, 1999; Prensky, 2002; Day-Lewis et al., 2017). Depending on the measured parameters and application already minor differences in vertical resolution and penetration depth have a great impact on logging and deposit economics. I.e., the more volume is analyzed with higher resolution the less is the logging cost per analyzed volume and the less is the grade uncertainty and subsequent economic evaluation of the deposit. Figure 2.2 shows an overview of common downhole logging techniques and their corresponding investigation depth and vertical resolution under ideal conditions. The penetration depth depends on the formation properties (density, elemental composition, borehole fluid, etc.) and logging speed and is therefore deposit sensitive (Hertzog, 1988; Ellis and Singer, 2007; Day-Lewis et al., 2017). Conventional neutron logging investigates a radius of maximum one meter and a vertical resolution of about 40 cm.

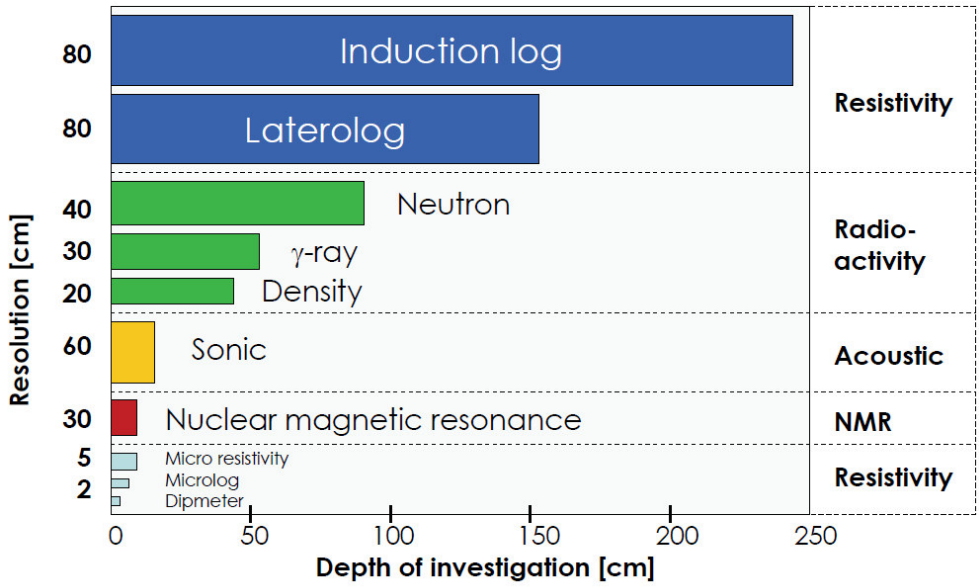

Figure 2.2: Overview on borehole logging techniques summarizing depth of investigation, resolution and physical background. Compiled based on data of Hertzog, 1988; Kenyon, 1997; Ellis and Singer, 2007; Dentith and Mudge, 2014; Day-Lewis et al., 2017.

2.2 State of the Art

2.2.1 Pulsed Neutron Logging

Nuclear (radiological) technology was first applied in borehole logging after the detection of natural radioactivity emitted by soils and rocks. It has found vast applications in the characterization of sedimentary deposits, especially coal and uranium. Whilst this passive logging method (γ-log) is still widely used today, the industry quickly moved to more sophisticated logging techniques that activate rocks with γ-radiation and neutrons and measure the induced radiation to infer characteristics of the material surrounding the borehole (Eisler, 1982; Doveton and Prensky, 1992).

Neutrons are electrically neutral elementary particles that scarcely interact with electrons or coulomb fields. They are unstable as free particles. The mass of a neutron is slightly greater than the mass of a proton. Therefore, the elastic scattering neutrons on hydrogen nuclei is greatest (momentum transfer). Neutrons can be generated from (α,n)-reactions by combining α-emitters like ^{241}Am with ^{9}Be. For this mechanism Am(Be) sources are commonly used: ^{241}Am emits α particles initiating the nuclear reaction ^{9}Be(α,n)^{12}C. Moreover, neutrons can result from spontaneous fission of unstable isotopes like ^{252}Cf (Ellis and Singer, 2007).

First neutron logging devices were tested shortly after World War II (Ellis and Singer, 2007) and contained isotopic neutron sources that primarily responded to the amount of hydrogen in the formation (Fricke and Schön, 1999). The hydrocarbon industry adopted these parameters to identify zones of porosity to assess the reservoir quality (Keys, 1996). Conventional isotopic sources such as ^{241}Am(Be) or ^{252}Cf (cf. chemical source in Figure 2.3) were used to measure the response from the interaction of neutrons with the surrounding formation (neutron scattering and absorption). Such sources imply a significant environmental risk in case of a tool loss in the underground. Besides the existing environmental challenges several technical limitations of continuously 'on' isotopic sources (permanent emitters) like lacking time resolution, steady source depletion, handling issues because of the large shielding volumes necessary for safe transportation and storage amongst others, lead to the development of artificial neutron sources, i.e. neutron generators (Ellis and Singer, 2007).

Specific pulsed neutron generators (PNG) for borehole logging are miniaturized, switchable, sealed-accelerator-tube neutron generators (cf. Figure 2.4). Common accelerator tubes operate by generating ions of deuterium (D) and accelerating them with about 100 kV into a target that contains tritium (T), thus producing a nuclear fusion reaction, resulting in mono-energetic neutrons of about 14 MeV (Smith et al., 1988). These fast neutrons interact with (mostly light) atomic nuclei of the surrounding formation by elastic scattering, thus, reducing their average kinetic energy over orders of magnitude down to 'thermal', typically within microseconds. Figure 2.3 classifies neutrons according to their kinetic energy into three categories: fast ($E > 10$ eV), epithermal (0.2 eV $< E < 10$ eV) and thermal (E < 0.2 eV) (Ellis and Singer, 2007). The relation of energy E (in eV) and velocity v (in cm/µs) is described as follows:

$$v = 0.22\sqrt{\frac{E}{0.025}}. \tag{2.1}$$

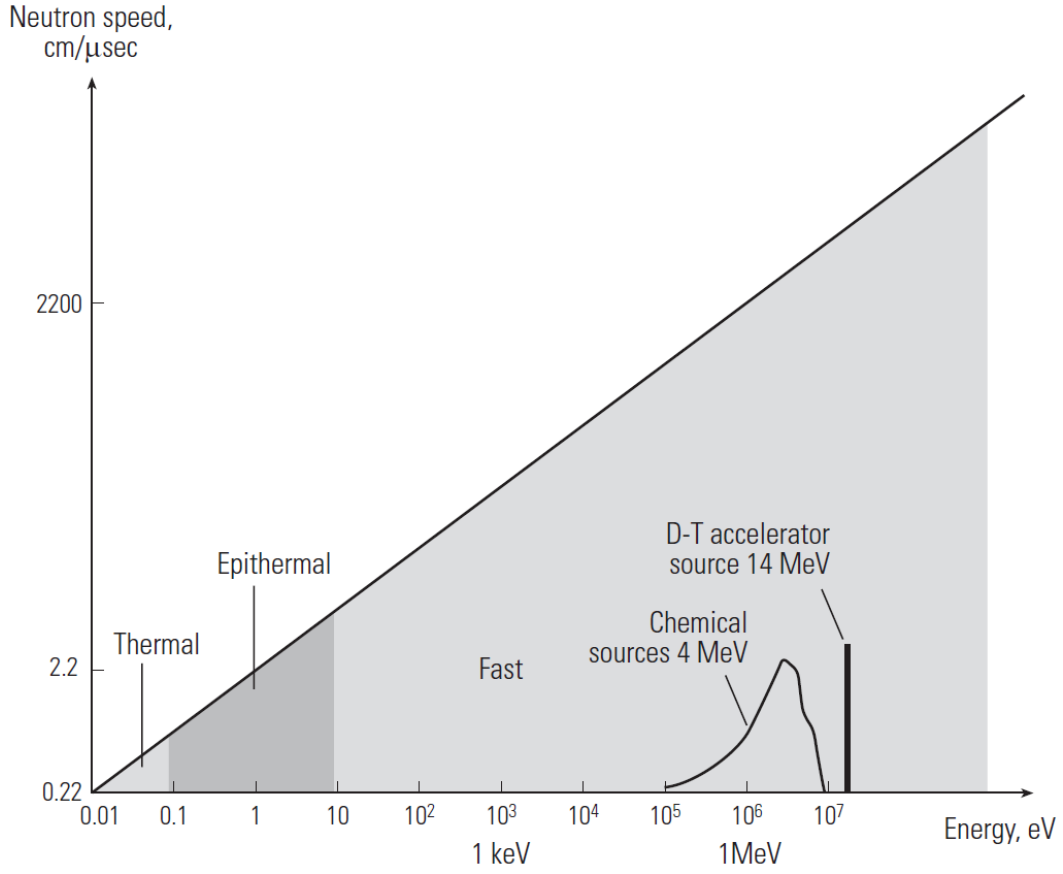

Figure 2.3: The classification of neutrons according to broad energy ranges and their corresponding velocities. Comparison of PNG sources with isotopic (so-called 'chemical') sources and their corresponding energy. Adapted from Ellis (1987).

This means that common pulsed neutron generators contain an artificial neutron source that can be switched on and off. It is equipped with specific power electronics to generate a pulsed high voltage with -40 to -90 kV magnitude (standard operation at about -80 kV) and a nominal operational frequency of 1 kHz at a duty time of about 50 - 100 µs (approximate pulse width or 'burst length'). This pulsed high voltage is used to operate an accelerating column (tube) as shown in Figure 2.4 to generate neutron bursts at a repetition rate of 1 kHz and a neutron burst length of maximum 100 µs. The tube is a miniature accelerator for deuterons to hit a tritium target (tritium bound as metal hydride in Zr on a Zr or Ti target). During the high-voltage pulse, high-energetic neutrons with an energy of about 14 MeV are generated isotropically by the deuterium-tritium (DT) fusion reaction $^{3}H(d,n)^{4}He$ and are emitted nearly spherically.

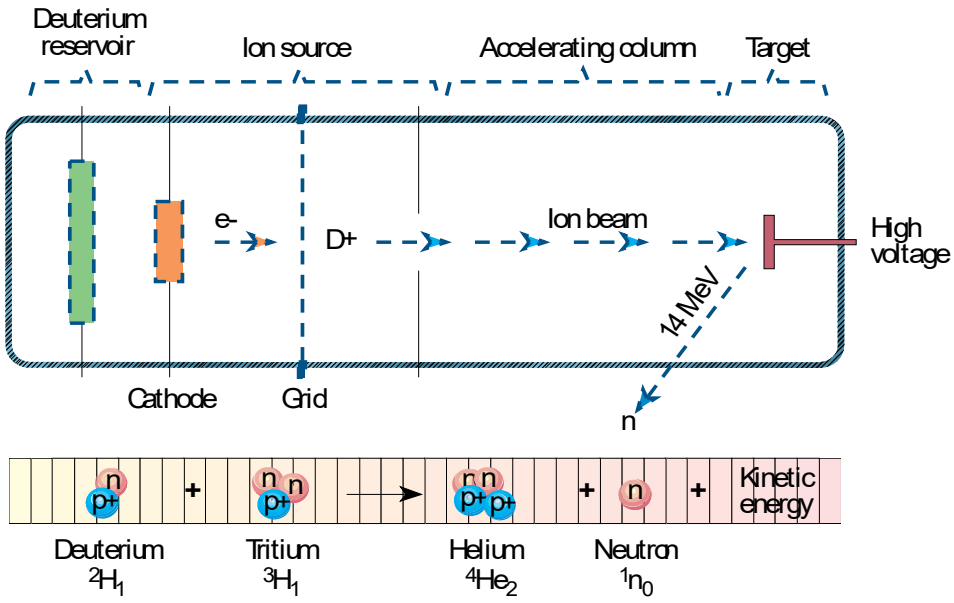

Figure 2.4: Schematic illustration of the operation principle of a pulsed DT-neutron generator. After Philip et al. (2019).

Compared with radionuclide neutron sources like ^{252}Cf (fission neutron spectrum) and AmBe (fast neutron spectrum) a DT-neutron generator (14 MeV neutrons) in pulsed mode (1 kHz, 10 % duty time) has the following advantages:

- High and controllable neutron source strength ($> 10^8$ primary neutrons per second),
- Flexible measuring modes:
    - Effect (generator on) versus background (generator off) measurement,
    - Multi-scaling (time windows between the neutron bursts).

The detailed functionality of the PNG implemented in OreLog is described in chapter 3.3. Hertzog (1988) summarizes the applications of pulsed neutron logging in the petroleum industry since its beginning and Humphreys et al. (1983) in the specific case of uranium exploration, whereas only in the last two decades serious approaches have been undertaken to adapt this state-of-the-art technology to the entire mining industry despite its highly promising potential (McMonnies et al., 2007).

Typical applications of a PNG result in neutrons penetrating the borehole surrounding matter and getting progressively slowed down mostly by successive elastic collisions. This slowing down is called thermalization where each collision causes the transfer of a percentage of neutron kinetic energy from the incident to the target nucleus as exemplified in Figure 2.5 until the neutrons reach thermal equilibrium. Besides the described elastic collision mechanisms neutrons initiate three fundamental types of

interactions (cf. Figure 2.5) that result in the production of secondary particles forming the 'backbone' of this work (Rinard, 1991):

- **Inelastic Scattering (n,n'γ):** Interaction of a fast neutron with a nucleus forming a very short lived instable isotope in an excited state, whereas the secondary neutron energy is reduced. The excited intermediate nucleus returns quite quickly to its ground state by emitting a γ-ray or more. To initiate this reaction the energy of the incident neutron has to be above an element-specific threshold.
- **Capture (n,γ):** Once a neutron is slowed down to thermal energy it can be absorbed by a nucleus resulting in an excited state. It decays nearly instantaneously to the ground state by emitting one or more γ-rays. The created isotope is either stable or itself radioactive.
- **Activation (n,...):** Absorption of a neutron by a nucleus or any other neutron induced reaction resulting in the activation of the residual nucleus and the subsequent delayed isotope-specific de-excitation process (γ-emission mainly).

A fourth reaction type which is not further considered here is nuclear fission (n,f) induced by thermal neutrons that conventional PFN tools use to accurately determine the uranium grade (^{235}U) within a rock formation as exemplary illustrated on the right side in Figure 2.5 (Humphreys et al., 1983). Such tools have already been implemented as part of the routine logging suite in uranium exploration and mining for decades (Märten et al., 2015).

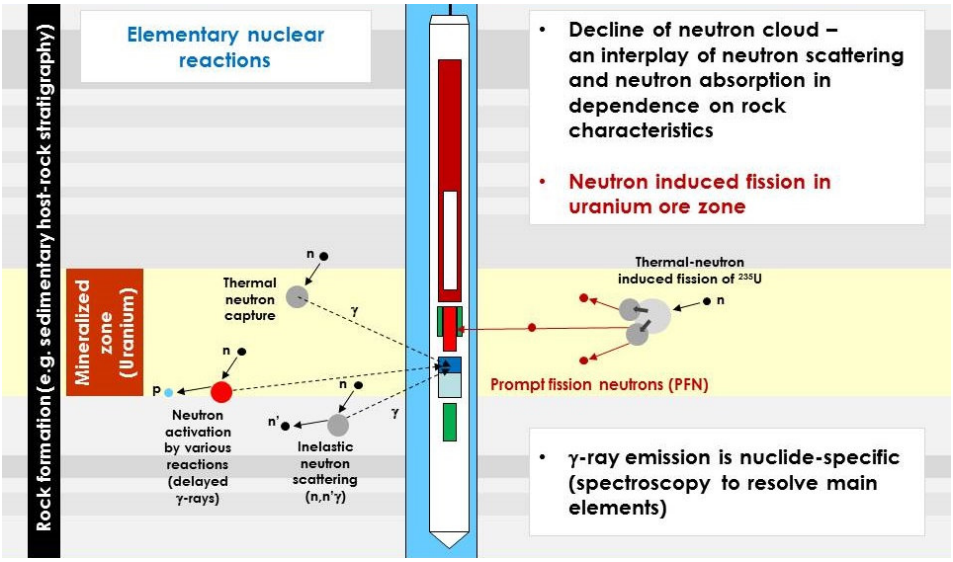

Figure 2.5: Schematic of elementary nuclear reactions induced by a PFN tool (e.g. APFN^{+}) exemplified by the application to a uranium deposit. Illustration of four reactions (scattering, capture, activation, fission) typically appearing by fast and thermal neutrons. Modified after Ellis and Singer (2007).

The probability of the above-described events is determined by the isotope-specific neutron cross-section. The cross-section is the apparent surface which a target nucleus exposes to an arriving particle (Koelzer, 2001). Its complexity is shown in Figure 2.6 by exemplifying the contributions of potential neutron interactions to the total cross-section (Rinard, 1991).

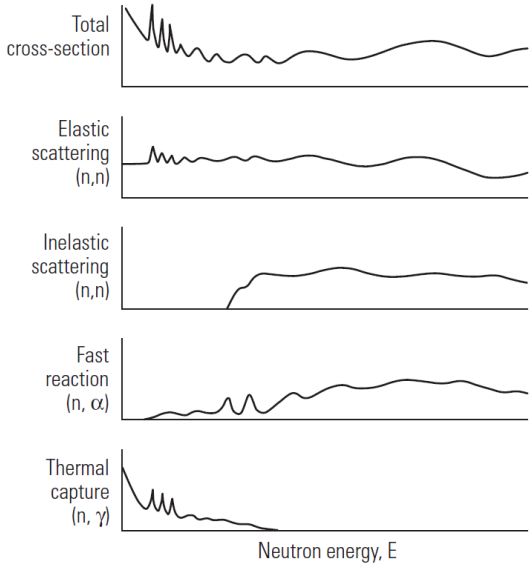

Figure 2.6: A schematic illustration of the energy variation of the total neutron cross-section and its components. Adapted from Ellis and Singer (2007).

Hence, this is a very important parameter for pulsed neutron logging. For practical purposes (generalization) and the application in logging some gross properties for neutron interactions with materials are derived despite the actual complexity of the individual microscopic cross-sections shown above. For the understanding of these fundamental interaction processes, measurements are performed with thick samples containing a mixture of elements representing approximately naturally occurring compositions (e.g. ore minerals, formation lithology). These gross properties described by using the macroscopic cross-sections are appropriate for the investigated bulk materials. The macroscopic cross-section (important rock parameter) in m^{-1} is defined as the product of the cross-section (σ_i) in question of atoms of type i times the number N of atoms per volume (m^3):

$$\sum i = N\sigma_i = \frac{N_{Av}\rho_b}{A}\,\sigma_i \qquad (2.2)$$

where N_{Av} is Avogadro's number, ρ_b is the rock (bulk) density and A is the atomic weight. The cross-sections for most neutron reactions are determined experimentally since they depend on the incoming radiation (energy and angle), type of interaction

and the specific material (Ellis and Singer, 2007). Eisler (1982) describes three main applications of those rock parameters in pulsed neutron logging. These are:

(a) the measurement of rock porosity,
(b) the determination of lithology and
(c) the measurement of the chemical concentrations of selected constituents.

The following chapter will explain option c in detail because it presents the fundamental application this work is based on.

2.2.2 Geochemical Logging

Traditionally, geochemical data are gathered by analyzing core samples. This method provides the most detailed, accurate and reliable information, but it also implies three major disadvantages: (i) it is based on expensive coring, (ii) it provides data only very lately after laboratory-based analyses and (iii) the sample volume is very small and therefore not fully representative. The in-situ and real-time measurement of elemental composition of mineral formations is therefore an attractive alternative for exploration and mining purposes. The application of γ-ray spectroscopy techniques for the evaluation of elemental concentrations has been mainly developed in the oil and gas industry (Hertzog, 1988; Hertzog et al., 1989).

The main characteristics of the γ-rays (cf. Figure 2.5) produced by a DT-neutron generator in a borehole environment include (Evans et al., 1981; Hertzog et al., 1989; Ellis and Singer, 2007):

- Capture γ-rays:
  - Emitted after capture of thermal neutrons between the bursts (according to the decline of thermal-neutron intensity due to absorption),
  - Energy spectrum from 0 to about 10 MeV.
- γ-rays from inelastic fast-neutron scattering (n,n'γ)
  - Produced by high-energy neutrons during the burst,
  - Energy spectrum from 0 to about 4.5 MeV (Carbon γ-rays), much less beyond.
- Prompt fission γ-rays
  - Emitted after thermal neutron induced fission between the bursts mainly,
  - Continuous energy spectrum from 0 to about 10 MeV mainly.
- γ-rays from neutron activation

  - Activation by neutrons at various energies,
  - Time distribution determined by half-life (less than 1 s up to thousands of years), i.e. small contribution practically not varying in the time window between the bursts.
- Natural γ-rays from the formation
  - No time dependence,
  - γ-rays from ^{40}K and the decay chains of ^{235}U, ^{238}U and ^{232}Th mainly,
  - Constant background in the active-mode (NG on) measurement.

In order to determine the elemental concentrations within a formation pulsed fast and thermal neutron analysis (PFTNA) is the preferred method as already introduced in the previous section. The advantage of the PFTNA systems is an ability to separate the γ-ray spectrum of inelastic scattering reactions (n,n'γ) from thermal neutron capture (n,γ) and activation reactions γ-ray spectra. The data acquisition system collects data during the neutron pulse at one memory address (specific memory location in soft- and hardware) and then switches to another memory address to acquire data between pulses. The data collected during the pulse is primarily from (n,n'γ)-reactions and the data collected between pulses is primarily from (n,γ)-reactions. Often systems are designed to be shut off for a few minutes to collect short-lived activation products such as ^{16}O(n,p) ($t_{1/2} \approx 16$ s). It is a common misconception that the frequency and duration of the neutron pulses is chosen to maximize the data from the (n,n'γ)-reactions. In fact, these parameters are chosen to maximize the (n,γ)-reactions or more precisely the thermal neutron flux. The neutron pulse frequency determines whether the thermal neutron flux is kept nearly constant or if it is allowed to diffuse (Vourvopoulos and Womble, 2001).

The most common minerals and corresponding elements of sedimentary formations, which are measured by state-of-the-art tools mainly from the oil and gas industry, are summarized in Table 2.1.

Table 2.1: Most common minerals and corresponding elements in sedimentary formations.

Mineral/Fluid	Elements
Quartz	O, Si
Calcite	O, Ca, C
Dolomite	O, Ca, Mg, C
Kaolinite	O, Si, Al, H
Illite	O, Si, Al, H, K, Mg, Fe
Chlorite	O, Si, Al, H, Mg, Fe
Smectite	O, Si, Al, H, Na, Mg, Fe
Feldspars	O, Si, Al, K, Na, Ca
Micas	O, Si, Al, H, K, Mg, Fe and others
Pyrite	S, Fe
Siderite	O, Fe, C
Ore minerals	Fe, Cu, U, C, Ti, Gd, Mg, Ba, Mn, P, N, Sr, Pb, Zn, Sn
Groundwater	O, H, Cl, Na, i.a.
Drilling fluid	O, H, Cl, Na, Br, Ba, Fe, i.a.

Hardly any information regarding geochemical logging of metamorphic and igneous deposits is found in literature. Most elements occurring in sedimentary deposits are also incorporated in other deposit types and therefore allow transferring the existing knowledge while considering the potential impact of genesis-related matrix properties (McMonnies et al., 2007). Nuclide-specific (element) information from γ-ray spectroscopy can be gathered from various nuclear processes comprising:

- Natural radioactive decay,
- Activation (neutron absorption forming long-living radioactive nuclides that decay in time),
- Inelastic fast-neutron scattering (n,n'γ) combined with the prompt emission of γ-rays,
- Thermal neutron capture resulting in the emission of γ-rays.

The detectability and preferred reaction mechanism (nuclear interaction) of each element varies, whereas some can be detected by multiple mechanisms. Senftle et al. (1972) and Schweitzer et al. (1987) reviewed the discussed reaction mechanisms and corresponding detectability preferences in detail. The major task in geochemical logging is to translate elemental concentrations, measured by the use of nuclear physical effects (cf. Table 2.2), into mineral abundances as listed in Table 2.1. Table 2.2 summarizes the main elements detectable by nuclear spectroscopic logging.

Table 2.2: Nuclear process modes along with typically detectable elements according to Hertzog (1988).

Reaction mechanism	Detectable elements
Natural radioactivity (incl. decay chains)	K (^{40}K), U, Th (decay chains)
Neutron activation	Al, Na, Mg, Cl, Ca, Ti, V, Mn
Inelastic fast-neutron scattering	C, O, Si, Ca, Fe
Thermal-neutron capture	H, B, Mg, Si, S, Cl, Ca, Ti, Fe, Gd, Ba

Over the decades the methods have improved considerably as summarized in Barson et al. (2005), whereas the main historical steps include:

1. Manual step-by-step analysis based on few parameters (1940's to 1950's),
2. Overlays, correlations within simple models with few parameters (1960's),
3. Sequential or deterministic methods, iterative, incl. few to many parameters (1970's),
4. Simultaneous or statistical methods, i.e. constrained inversion through minimization of uncertainties, many parameters (1980's to 1990's),
5. Neural network, implicit models, minimal number of parameters (1990's to 2000's),
6. DecisionXpress System, automated processing, implicit model with a minimum number of parameters (2000's).

From the major neutron interactions caused by a DT-neutron generator, capture γ-ray spectroscopy is the most attractive one due to the vast range of detectable elements, but needs supplementary methods to complete the determination of most important elements in geological formations. The elemental integrity is only achieved with respect to reasonable deductions of mineral abundances, either by additional nuclear logging methods or by assumptions regarding missing elements. Certain formation type databases for the individual (isotope-specific) γ-rays are available, e.g. for those originating from thermal-neutron capture (International Atomic Energy Agency, 2007). The detection of γ-rays is a two-step process based on the interaction of the γ-rays with the detector material. It first results in the partial or full conversion of their energy in ionizing radiation which is secondly converted to a measurable electrical signal. The first phase is characterized by one or more of the γ-ray matter interactions as described in Figure 2.5 whereas the second phase relies on various principles. There are three general types of γ-ray detectors in current use: Gas ionization counters, scintillation detectors and solid-state detectors. Gamma scintillation detectors are the most common

detector types that are also used in this work and therefore are described in more detail. In this case the incoming γ-rays impart their energy to a cascade of secondary electrons which are finally trapped by impurity atoms within the crystal lattice of the usually thallium-activated sodium iodide crystal. The trapped electrons emit visible or near-visible light which is then detected by a photomultiplier tube optically coupled to the crystal. The light flashes are transformed into an electrical pulse as illustrated in Figure 2.7 and allow the correlation of the output pulse height with the total energy deposited in the crystal by the initial energetic electron. By doing so, the great advantage of scintillation detectors is the ability of realizing γ-ray spectroscopy by deducing the actual energy of the incident γ-ray, hence enabling elemental logging (Ellis and Singer, 2007).

The γ-ray detection efficiency of the various scintillator crystals and geometries is discussed hereinafter and in further detail in chapter 3.4.1.

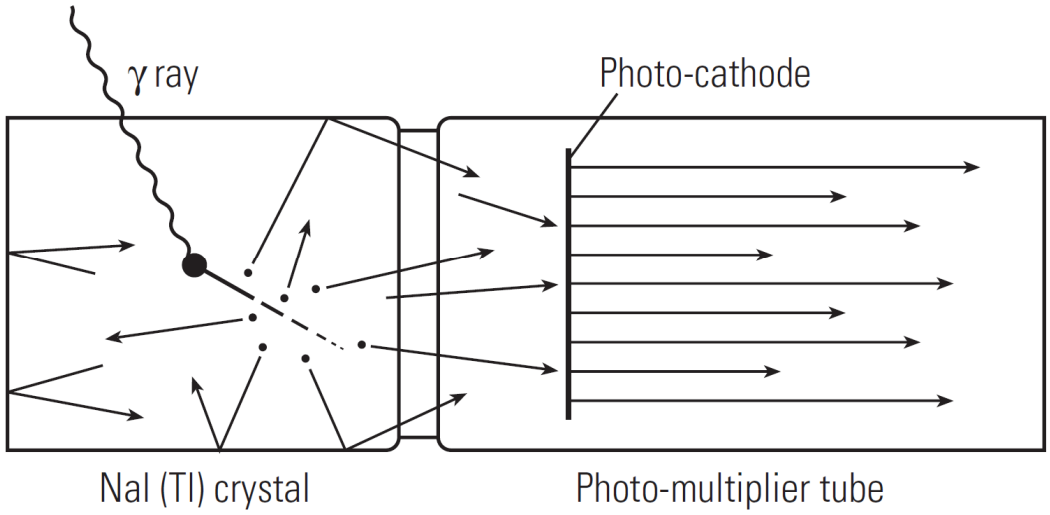

Figure 2.7: Schematic illustration of a scintillation detector with its associated photo-multiplier tube (PMT). The photocathode responds to a flash of light in the crystal by releasing electrons. The release of electrons is amplified by the PMT into a detectable electrical pulse. After Ellis and Singer (2007).

The selection of the γ-ray detector is a compromise of resolution, detection efficiency, stability, and specific detection characteristics (scintillation pulse length, scintillation dead-time, pulse pile-up effects) as proven in various studies of Eisler (1982), Hertzog et al. (1989), Borsaru (1993), Borsaru and Charbucinski (1997), Borsaru et al. (2001), Borsaru et al. (2006), Barzilov et al. (2012), and Zhang et al. (2017). In order to enable excellent spectroscopy performance, the output signals of the γ-ray detector have to be processed as shown in Figure 2.8. Specialized high-performance electronics is required to appropriately handle the signal volume which is often in excess of counting rates

beyond 2.5 x 10^6 cps. The sophisticated data processing finally results in a pulse-height spectrum which is then used for post-processing and quantification of elements at surface (cf. Figure 2.9 and Figure 2.10).

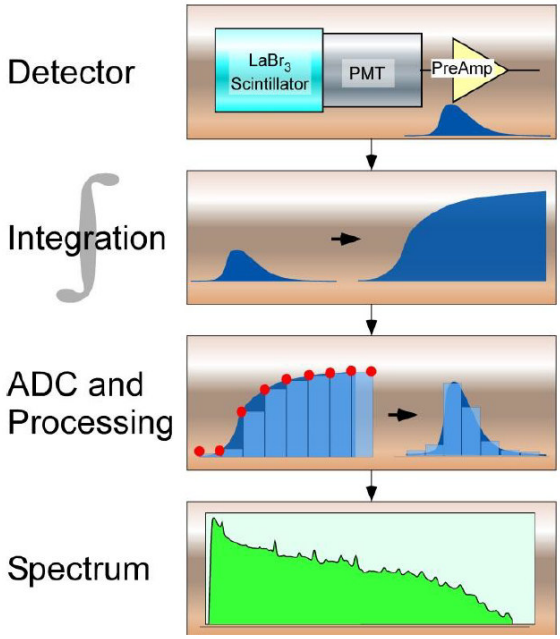

Figure 2.8: Schematic of the spectroscopy acquisition system from γ-ray detection to final spectra output. Signals from the detector pass through an integrator and analogue-to-digital converter (ADC) and are then processed to form the pulse-height spectrum. After Radtke et al. (2012).

Modern and sophisticated geochemical logging tools mainly originating from the hydrocarbon industry provide high resolution spectra for both inelastic scattering and neutron capture as shown in Figure 2.9.

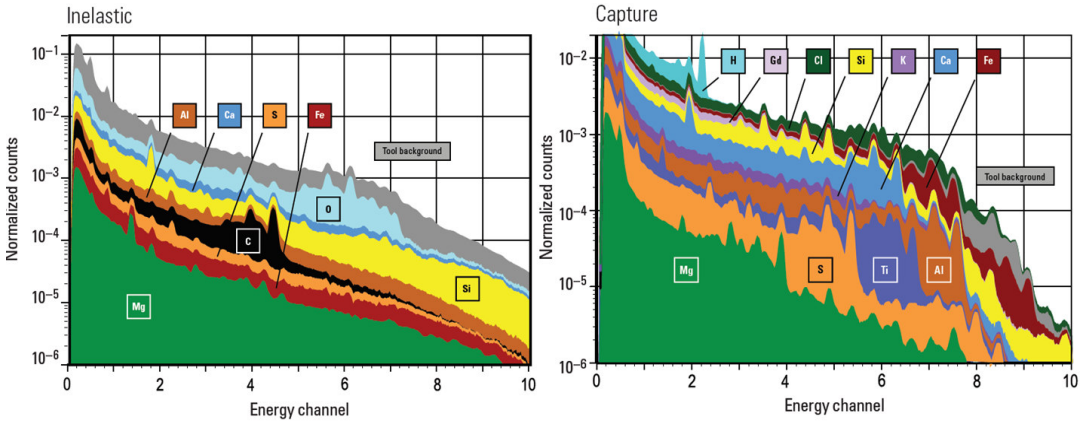

Figure 2.9: A measured inelastic scattering (left) and capture γ-ray spectrum (right) from the Litho Scanner tool brochure (Schlumberger, 2017). The spectra show the main components contributing to the spectroscopic response function.

The fast and reliable decomposition of the complex response functions is most important for data processing. Photo-peak-based approaches as developed for high-

resolution (but low-efficiency) Ge detectors are not applicable to highly-efficient γ-ray detectors with moderate resolution like BGO (Bismuth Germanate crystal $Bi_4Ge_3O_{12}$) or NaI (Rahman et al., 2009; Zhang et al., 2017). Template matching is the most advanced method for the spectral decomposition and determination of (relative) elemental fractions and also used as preferred approach in this work (Herbach et al., 2009). Templates are the detector response functions resulting from individual reactions. Usually they are simulated by Monte-Carlo techniques applied to measurement conditions in a tool, i.e. considering the measuring environment and all secondary effects, which are presented in detail in chapter 4.2 (Werner, 2017). The detector energy resolution effects certainly belong to the most important parts in the simulation of realistic spectra. The source model (cf. chapter 4.2.1), representing all potential γ-ray emitters, is related to the templates – thus, statistical methods can be employed to determine the fractions of individual γ-ray spectra (measure of elemental concentrations) as shown in chapter 4.

Spectral stripping based on calibrated element-specific spectral signatures is realized to obtain elemental weight fractions for a suite of elements which are application and deposit related. State of the art tools as presented in chapter 2.2.3 usually cover the following suite of elements (capture and inelastic γ-ray spectroscopy): Al, Ba, C, Ca, Cl, Cu, Fe, Gd, H, K, Mg, Mn, Na, Ni, O, S, Si, and Ti. Figure 2.10 illustrates an example of a geochemical log with quantitative elemental concentrations from a pulsed neutron logging tool compared to core analysis. In this case, the elemental standards and sensitivities were derived from experimental laboratory measurements of standardized geochemical formations supported by MCNP simulations as described in Radtke et al. (2012). These standards provide relative elemental yields as a function of the volumetric proportion of an element in the measurement region (borehole environment) and specific tool sensitivity. The state of the art conversion of relative spectral yields from neutron capture into absolute elemental concentrations is conventionally achieved through an iterative inversion technique such as elemental log analysis (Quirein et al., 1986) or via a modified geochemical oxides closure model (Grau and Schweitzer, 1989; Grau et al., 1989):

$$W_i = F\left(\frac{Y_i}{S_i}\right), \tag{2.3}$$

whereas the weight fraction W_i of element i at given depth is a function of a closure normalization factor F, the measured relative yield Y_i of element i at that depth and the tool's sensitivity S_i to element i for capture reactions. The normalization factor F

is determined at each depth by solving the simple closure relation with A_i accounting for all the unmeasured elements that are associated with element i:

$$F \sum \left(\frac{A_i Y_i}{S_i}\right) = 1. \tag{2.4}$$

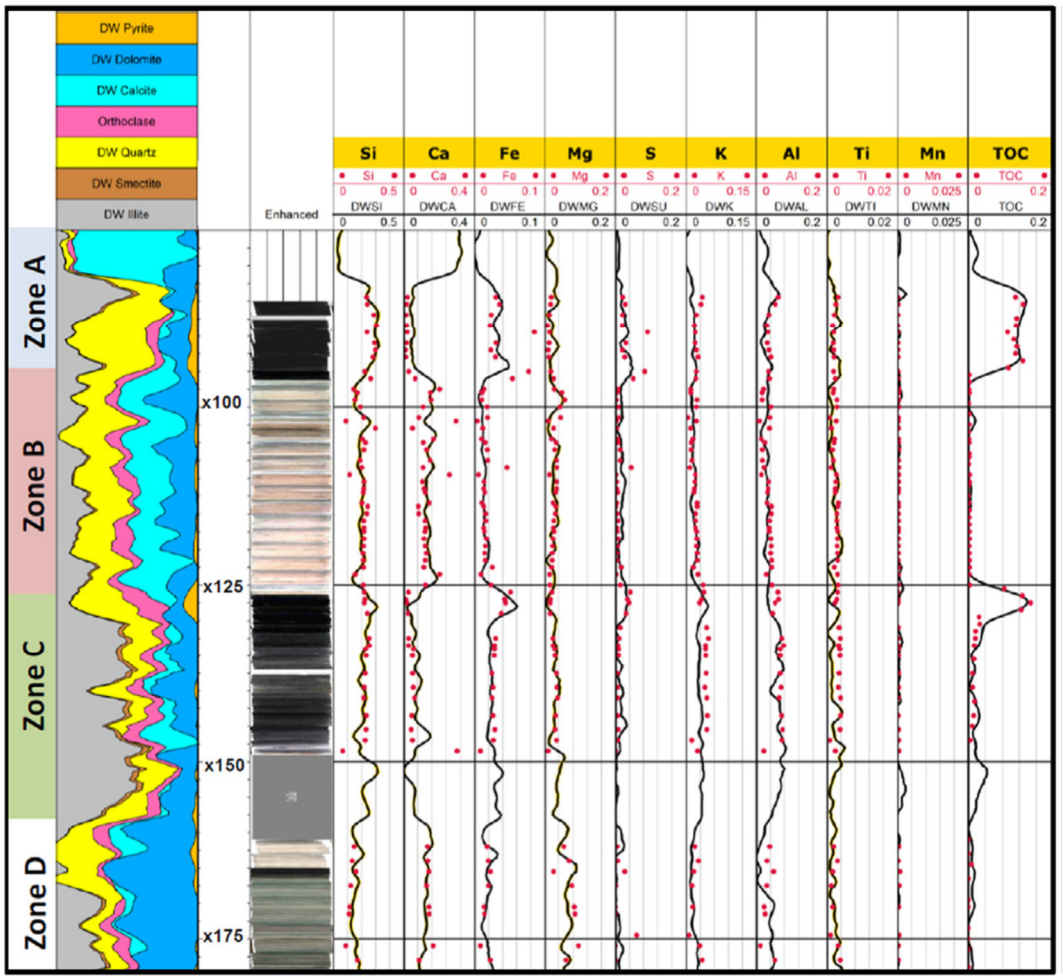

Figure 2.10: Exemplary geochemical log from a borehole of the hydrocarbon bearing Bakken Formation in North Dakota. Black curves compare elemental weight fractions measured by Litho Scanner with those derived by laboratory core analysis (red points). After Radtke et al. (2012).

Nuclear techniques are more widely used in the oil industry than in the mineral industry since they provide vital information for the oil industry which cannot be obtained by any other means. However, new applications were developed for the mining industry in the last decades and more applications are expected when new type of detectors becomes available. Nuclear geophysics is a mature field of research and therefore incremental development rather than spectacular findings is expected in the near future. Recent examples of attempts to apply the presented technology for ore grade estimation in nickel, copper, iron or coal deposits are presented in the works of Borsaru

and Charbucinski (1997), McDowell et al. (1998), Borsaru et al. (2001), Charbucinski et al. (2003), Charbucinski et al. (2004), Borsaru et al. (2004), Borsaru et al. (2006), Smith et al. (2013) and Tian et al. (2017).

2.2.3 Review of Similar PNG Logging Tools

The recent attempts of geochemical logging in the mining industry require a review of available industrial PNG logging tools. Modern neutron-induced γ-ray spectroscopy or elemental spectroscopy logging tools yield concentration logs of important rock-forming elements. For example, Litho Scanner reports concentrations of the major elements Si, Ca, Fe, Mg, S, K, Al, Na, and C as well as some minor or trace elements, such as Mn, Ti, and Gd (Radtke et al., 2012; Aboud et al., 2014).

As a reference, three of the apparently most advanced geochemical logging tools developed by Schlumberger in the hydrocarbon industry should be emphasized (Barson et al., 2005):

- GLT Geochemical Logging Tool (1986):
  - ^{252}Cf neutron source for activation measurements,
  - DT-neutron generator for capture γ-ray spectroscopy,
  - NaI detector within a Boron sleeve for γ-ray spectroscopy,
  - Combined with several other detection systems (e.g. multiple thermal/epithermal neutron detectors for porosity measurements, natural γ-ray tool, Al activation tool),
  - 21.3 m long, 2 runs for complete logging,
  - $<$ 3 m/min logging speed.

- ECS Elemental Capture Spectroscopy Tool (1996):
  - AmBe neutron source,
  - Large BGO detector for γ-ray spectroscopy (with Boron sleeve),
  - 4.57 m long, 12.7 cm outer diameter (OD), min. borehole size 16.51 cm,
  - 9 m/min logging speed.

- Litho Scanner Tool (2015):
  - DT-neutron generator,
  - $LaBr_3$ detectors and YAP detector,
  - 2.74 m long, 11.4 cm OD, min. borehole size 13.97 cm,
  - max. 18 m/min logging speed.

Table 2.3 provides an overview of all currently available neutron logging tools with potential applicability of geochemical logging. The information was compiled based on technical specification sheets and brochures provided by the manufacturer or

commercial service companies of the tools and does not claim to be complete. Important technical and operational parameters are compared to the OreLog tool (last row in Table 2.3) and tools with similar characteristics are highlighted in blue. Some of them have already been discussed previously. The only tools available for mining applications are FastGrade 100 and 170 from Sodern at the time of writing.

Table 2.3: Comparison of state-of-the-art neutron logging tools.

Tool	Manufacturer	Length [mm]	Diameter [mm]	Weight [kg]	T [°C]	Pressure [Mpa]	Source	Neutron flux	Neutron detectors	Gamma ray detectors	E range [MeV]	Measurement mode
ECS	Schlumberger	3090	127	132	177	138	AmBe	na	none	1 x BGO	0.6 - 8	Capture spectroscopy
Litho Scanner	Schlumberger	2740	114	132	177	138	PNG	3×10^8	none	1x $LaBr_3$	1 - 10	Inelastic-capture spectroscopy
RSTPro	Schlumberger	7040	43	45	150	103	PNG	na	none	2 x GSO	na	Sigma, CO
Pulsar	Schlumberger	5580	43	40	177	103	PNG	na	none	2x $LaBr_3$, 1x	na	Sigma, gas, CO, inelastic-
GEM	Halliburton	3140	127	167	177	138	AmBe	na	none	1x BGO	0.6 - 9.5	Capture spectroscopy
RMT-3D	Halliburton	4660	54	39	163	103	PNG	na	none	3x BGO	na	Sigma, gas, CO, inelastic-capture spectroscopy
FLEX	Baker Hughes	4800	124	na	177	138	PNG	na	none	1x BGO	na	Inelastic-capture spectroscopy
RPM	Baker Hughes	5700	43	34	177	138	PNG	na	none	3x NaI	na	Sigma, gas, CO
Raptor 2.0	Weatherford	6340	43	43	na	138	PNG	na	none	4x $LaBr_3$	na	Sigma, gas, CO
GSI	Weatherford	3510	83	na	177	na	PNG	na	none	1x $LaBr_3$	na	Inelastic-capture spectroscopy
RAS Sigma Tool	Probe	3573	43	20	160	103	PNG	na	none	3x $LaCl_3$	na	Sigma, CO
PDN	Antares	5742	43	39	150	100	PNG	1×10^8	none	2x NaI	na	Sigma
AINK-73C-2	VNIIA	2507	73	na	120	60	PNG	2×10^8	none	2x $LaBr_3$	na	Sigma, CO, inelastic-capture spectroscopy
AINK-89C-2	VNIIA	2730	96	na	120	60	PNG	2×10^8	none	2x $LaBr_3$	na	Sigma, CO, inelastic-capture spectroscopy
FastGrade 100	Sodern	3400	102	72	35	4	PNG	5×10^7	none	1x $LaBr_3$	0.5 - 10	Inelastic-capture spectroscopy
FastGrade 170	Sodern	2000	170	100	35	0.5	PNG	na	none	1x $LaBr_3$	0.3 - 10	Inelastic-capture spectroscopy
OreLog	UIT	3000	76	33	80	10	PNG	1×10^8	$5 \times {}^3He$ 1 x CVD	1x CeBr3	0.5 - 10	Inelastic-capture-activation spectroscopy and neutron multi-scaling with template matching

3 The OreLog Tool

3.1 Tool History

The development and application of the OreLog tool is based on the predecessor tool APFN$^+$ (Märten et al., 2015), which was developed and engineered by UIT since 2008. The reason for UIT's in-house borehole logging tool development was that an affiliated mining company was not satisfied with conventional PFN tools available on the market concerning accuracy and reliability. Therefore, a proprietary UIT tool was engineered from scratch to meet the customer's demand. Several prototypes were assembled from 2008 onwards and the first tools were sold in 2012. The APFN$^+$ tool was exclusively developed for and applied to uranium exploration. Hence the main objective of the initial tool development was the highly reliable and accurate quantification of uranium with a LOD (limit of detection) of several tens of ppm in ore deposits based on the PFN principle by detection of fission neutrons as described in chapter 2.2.1. Currently several APFN$^+$ tools of UIT are in operation on a regular basis in uranium exploration and mining since 2013.

The APFN$^+$ hardware and software is intellectual property of UIT and its shareholders, that decided not to patent the tool for various reasons. The existing APFN$^+$ tool fleet is maintained and upgraded by UIT whenever necessary. Based on the satisfying experience during several years of field operation the substantial hardware components and the operational software (firmware and Graphical User Interface (GUI)) were considered as mature. The idea of developing a spin off tool (OreLog) for the general ore exploration and deposit characterization in the mining industry arose based on a market evaluation as presented in chapter 1. Therefore, the APFN$^+$ development status of 2015 was used as a starting point of the OreLog tool regarding basic components, tool dimensions and operational system (firmware and GUI). An existing platform was essential to enable a new tool in such a short time. New hardware components (e.g. detectors) and software algorithms for the application field of OreLog were required to meet the intentions of this work.

3.2 Design and Operation

The OreLog tool was developed and designed for downhole geophysical exploration of mineral deposits as shown in Figure 3.2. It consists of a pulsed neutron generator, five ^{3}He neutron detectors, one γ-ray spectrometer with a large, high-performance $CeBr_3$

scintillation crystal, an inclinometer, telemetry and power supply. The equipment is contained in a reactor-grade zircon housing with a diameter of 76 mm and a length of 3 m and a total tool weight of 33 kg (Figure 3.1). The tool is connected to the winch and the control unit via a 4-pin cable of 1000 m length. It is operational up to 70 °C internal tool temperature and maximum pressure of 10 MPa, which corresponds to a maximum borehole temperature of 50-60 °C and a water column of max. 1000 m.

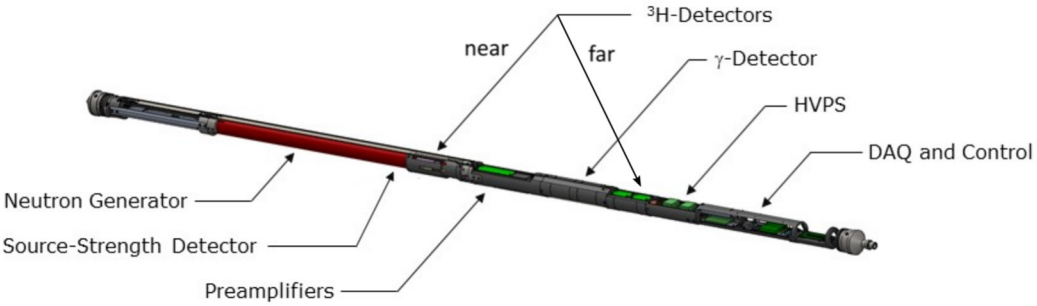

Figure 3.1: Technical draft of OreLog design and major components. HVPS = High-Voltage Power Supply; DAQ = Data Acquisition.

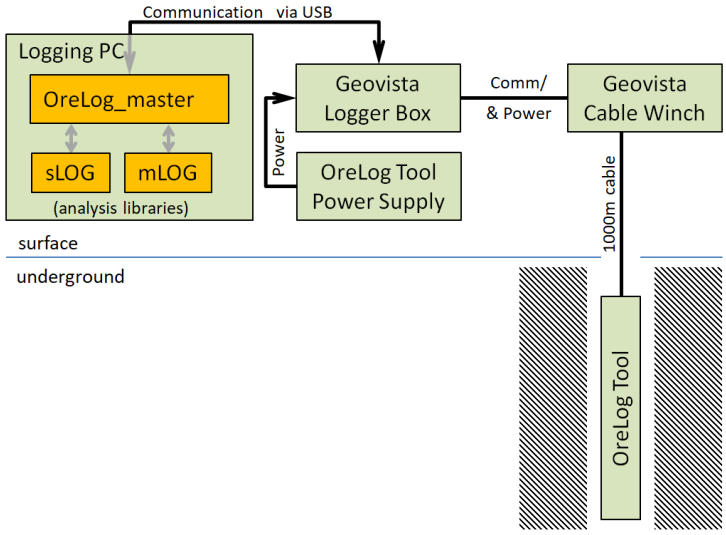

Figure 3.2: Sketch showing all components of the logging process , starting from the OreLog tool to the analysis libraries mLOG and sLOG operated by the OreLog control software OreLog_master.

The details and justifications of detector selection and positioning within the tool are expatiated in chapter 3.4. The logging PC runs the up-hole control-software OreLog_master and records the acquired data. The software provides all functionalities to operate the OreLog tool. Essentially the OreLog_master requests the analysis libraries mLOG and sLOG to interpret the raw data recorded by the logging tool. It

hands over Multi Channel Scaling (MCS) data to mLOG and spectral data to sLOG. The libraries return interpretations of the raw data, e.g.

- porosity, permeability, etc. from mLOG, and
- borehole radius, correction factors, elemental composition, etc. from sLOG.

The multichannel analyzer (MCA) is an important tool component which can measure distributions of input signals consisting of pulses. It operates in two different modes: pulse height analyzer (PHA) mode, and MCS mode. In PHA mode, the input pulses are sorted into bins (channels) according to their amplitude, while in MCS mode they are sorted according to the time when they are detected (with reference to neutron burst). The mLOG dataset is a data analysis package for MCS data. No spectral data is analyzed by mLOG. The dataset provides estimates on porosity, density, thermal-neutron absorption cross-section, and more.

The sLOG dataset is a data analysis package for spectral data and MCS data. The major goal is the analysis of spectral data, i.e. the analysis of the burst-spectrum and the capture spectrum. However, the sLOG-interface has the option to submit MCS data in addition to the spectral data. This makes it easier to calculate corrections for geophysical parameters whose non-corrected values are (traditionally) calculated by mLOG.

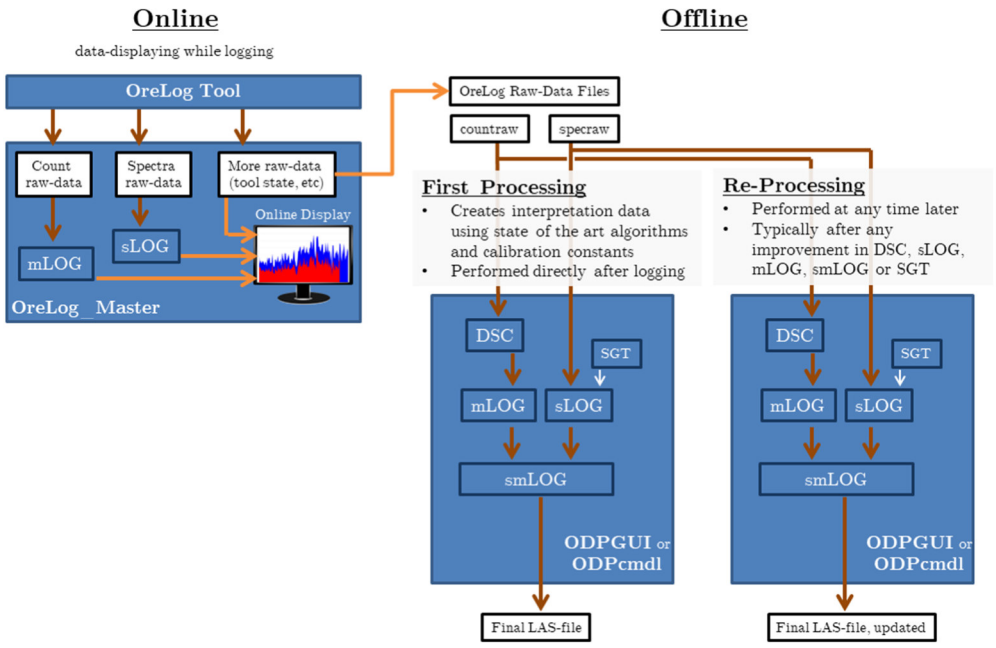

Figure 3.3: Flow of OreLog data all the way from logging to the final LAS-file (an international, open, binary standard ASCII format for point data for import to WellCAD or other standard log composite/visualization software; cf. Crangle, R.D., Jr. (2007)). Colored boxes indicate a software (SW) module, white boxes indicate data. The arrows pointing to/from a SW module indicate that the data are processed by algorithms in this SW module.

Figure 3.3 provides an overview of the overall OreLog data flow and the most important software modules including the relation between both. The following chapters 3.2.1 to 3.2.7 present the details of that scheme.

3.2.1 OreLog_Master

OreLog_Master is an executable program written in LabVIEW code with a GUI as shown in Figure 3.4. This software runs on the logging PC in the field and it is directly used by the OreLog operator. The software has the following features and tasks:

- Control of the OreLog tool
  - Switch neutron-generator on and off,
  - Switch detectors for neutrons and γ-rays on and off,
  - Other actions such as setting of n-generator HV (high-voltage), setting of communication parameters etc.
- Recording of any OreLog raw data, i.e. write OreLog raw data files
  - Including neutron-detector counts, γ-ray detector counts, γ-ray energy-spectra, n-generator monitoring data, orientation sensor data, winch data.
- Data display
  - In online mode (i.e. displaying while logging),
  - In offline mode (i.e. replay of logging, relies on raw OreLog data files).

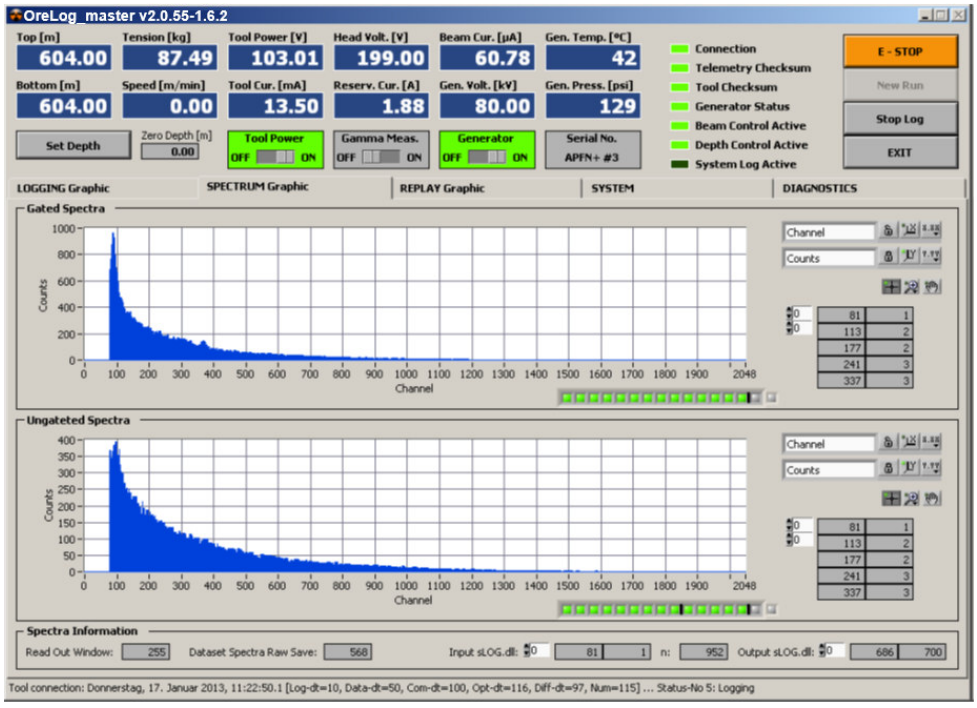

Figure 3.4: GUI of OreLog_Master software showing major operational parameters and functionality.

3.2.2 Depth and Source Strength Correction

Depth and Source Strength Correction (DSC) is a dataset that transforms series of raw counts of detectors into count rates which are already:

(i) corrected for a periodic variation of source strength of neutron-generator, and

(ii) corrected for the fact that detector counts registered by different OreLog detectors at one common time t are assigned to different depths d_{Det} (detectors are located at different positions within the OreLog tool) instead of being assigned to one common depth d.

Concerning neutron-detector counts it is required to quantify the neutron-production source-strength P_n (i.e. number of 14 MeV-neutrons produced per second) in various timescales. A timescale of 1 s is selected to determine the accurate number of neutrons emitted to the borehole and its surrounding formation in time. There are short-term-variations of P_n changing the actual neutron-production by $\pm$ 8 % within times of 10 to 60 s. On a timescale of ten hours to several hundred hours there is a continuous decrease of P_n due to source depletion (consumption of D and T). From an operational point of view, it is important to know P_n because of maintenance reasons (NG tube replacement) and QA/QC (Quality Assessment/Quality Control). The absolute value enables to compare or benchmark the individual tools which is then a QA/QC parameter for tool uniformity and the relative value is considered as tool internal QA/QC indicator.

The first task of the DSC dataset is to correct any measured detector count rate $R_{\mathrm{Det,meas}}(t)$ for this (unwanted) source strength variation caused by the NG. This results in a strength corrected (SCor) count rate $R_{\mathrm{Det,SCor}}(t)$. Since there is exactly one nominal tool depth $d_{\mathrm{nom}}(t)$ at each time t resulting in a corrected count rate $R_{\mathrm{Det,SCor}}(d_{\mathrm{nom}}(t))$ as a function of nominal depth d_{nom}. The nominal depth d_{nom} is the distance from top of borehole to top of tool.

The second task of the DSC dataset is to get the detector-specific count rate of detector *Det* as a function of real depth d. Therefore one needs to assign each strength corrected count rate $R_{\mathrm{Det,SCor}}(d_{\mathrm{nom}})$ to a real depth $d = d_{\mathrm{nom}} + \Delta d_{\mathrm{Det}}$. This is called depth correction (DCor) and it results in a depth and strength corrected count rate $R_{\mathrm{Det,SCor\&DCor}}(d)$:

$$R_{\mathrm{Det,SCor\&DCor}}(d) = R_{\mathrm{Det,SCor}}(d_{\mathrm{nom}} + \Delta d_{\mathrm{Det}}). \tag{3.1}$$

Having $R_{\mathrm{Det,SCor\&DCor}}(d)$ allows to compare detector counts from different OreLog detectors recorded at the same depth d. These $R_{\mathrm{Det,SCor\&DCor}}(d)$ values are required by the mLOG dataset.

A further feature of the DSC-dataset enables the algorithm to accept data recorded with varying OreLog tool speed.

3.2.3 mLOG

The mLOG dataset consists of 32 count rates measured by four detectors (SSD, near-, far-, and γ-detector) in eight time windows (4x8) with different window sizes ranging from width=50µs to width=200µs (cf. Table 3.1). The number N_{ij}^{D} of counts from detector D (D=SSD, far, near, γ) in detection window i (i = 1, ..., 8) for generator cycle j (j=1, 2, ...) is accumulated over 300 generator periods. The resulting set of the 4 x 8 = 32 numbers N_i^D is simply

$$N_i^D = \sum_{j=1}^{300} N_{ij}^D \tag{3.2}$$

The 32 input count rates are calculated by the DSC dataset, i.e. they are the rates $R_{\mathrm{Det,SCor\&DCor}}(d)$ mentioned in chapter 3.2.2. They should be considered as one set of detector-responses referring to the formation material within a certain depth interval d ± Δd. The output of the mLOG dataset consists of geological interpretation variables like density, hydrogen index, neutron absorption strength, etc. Any of these interpretation-variables is estimated from the 32 count rates mentioned above. One set of 32 input count rates refers to a certain depth interval and is used to calculate geological interpretation variables referring to this depth interval.

3.2.4 sLOG

The input of the sLOG dataset is spectral data from the γ-ray detector. It is distinguished between two modes expecting different input:

- Active-generator mode. Input consists of three γ-ray energy-spectra, namely burst-, capture-, and activation-spectrum,
- Passive-generator mode: Input is one single γ-ray energy-spectrum, the so-called natural γ-spectrum.

The output of the sLOG dataset consists of any interpretation data exploited from the spectral data. Typically, these are interpretation data obtained by deconvolution of measured spectra or by single-peak fits. Possible interpretation data includes:

- Passive-generator mode: uranium, thorium and potassium mass fractions,
- Active-generator mode: Size and shape of hydrogen-peak relevant for borehole diameter, and elemental mass fractions (elemental logging).

3.2.5 Spectral Gamma Templates

Spectral Gamma Templates (SGT) is a database of γ-ray energy spectra. This module just provides a collection of γ-ray energy spectra, i.e. the templates. The templates can be either used for active-generator mode or for passive-generator mode. They can be created by computer simulation (MCNP) or they can be obtained from real measurements. The SGT database is a collection of templates with an SGT version number. Version-number helps in bookkeeping since there are many templates and they are subject of change while in development during this work.

3.2.6 smLOG (ODP)

smLOG is a software package interfacing and/or performing any OreLog Data Processing (ODP) all the way from OreLog raw data files to final LAS output files. Its most important task is the merging of the two asynchrony data streams from counter board (the 32 count rates) and MCA (any γ-ray energy spectrum). Once they have been synchronized a joint interpretation of counter board data and γ-ray spectra data can be realized.

3.2.7 ODP GUI and ODPcmdl

There are two executable programs performing the ODP all the way from OreLog raw data files to final LAS files:

(1) ODP GUI
(2) ODPcmdl

Both of them basically exploit the dataset smLOG, i.e. both of them are just interfaces to smLOG. The main tasks of ODP GUI and ODPcmdl are user selection of input data and output folders, and selection of further options.

ODP GUI: ODP GUI is a user-friendly SW tool relying on a graphical user interface (GUI) to manipulate recorded data.

ODPcmdl: The corresponding ODP command line tool is intended for *development* work and processing of multiple OreLog raw data files. It has more flexibility than ODP GUI but it is more complicated to be operated.

3.3 Neutron Generator

A miniaturized and customized neutron generator (Figure 3.5) is incorporated in the OreLog tool. Its accelerator is a vacuum tube, which is hermetically sealed and assembled within a tight metallic pressure cylinder. The neutron generator itself is a pressure canister, which is hermetically sealed as well. Before operation, the neutron generator canister needs to be filled with the high-voltage protection gas SF_6 at a nominal pressure of 0.85 MPa.

The following radioactive characteristics result from the tritium within the accelerator tube, which is illustrated in Figure 3.5:

Radioactive isotope: ^{3}H (T),

Maximum activity: 111 GBq (3 Ci or 0.31 mg),

Chemical form: Metal hydride within Zr lattice.

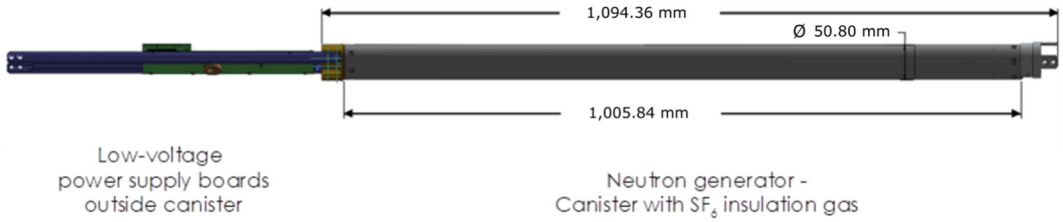

Figure 3.5: Sketch of neutron generator as implemented in OreLog.

In particular, the multi-scaling illustrated in Figure 3.6 enables the discrimination between γ-rays from inelastic scattering, thermal-neutron capture and neutron activation according to the time windows in Table 3.1. The γ-rays from inelastic scattering are recorded during the burst, γ-rays from thermal-neutron capture correspond to the capture window and γ-rays from neutron activation (short half-life) occur in the last window of the cycle. OreLog could also be run in stationary mode (fixed tool position) to measure the γ-rays from neutron activation of Al with a 2.2 min half-life of the produced radioactive isotope ^{28}Al. The measuring cycle includes an activation phase (NG on) followed by the measuring phase (NG off).

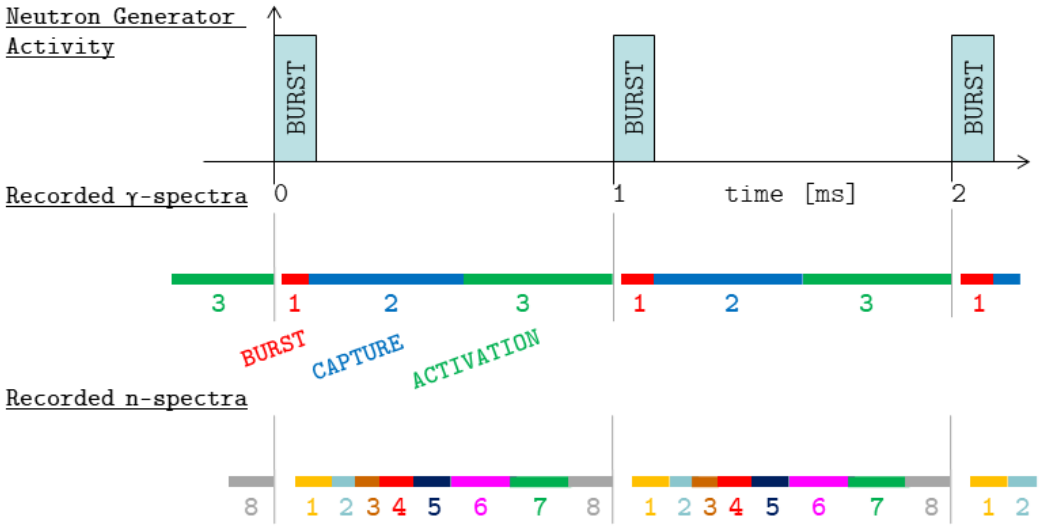

Figure 3.6: Pulsed NG operational scheme and γ- and neutron-detector recording scheme. For exact time windows see Table 3.1.

Table 3.1: Time windows of PNG operation and detector recording scheme.

Setting	Spec/Type	Start [µs]	End [µs]	Width [µs]
Neutron-trigger ON	-	0.0	100.0	100.0
Actual neutron production	-	10.0	90.0	80.0
Gamma detector time windows	Burst	10.0	40.0	30.0
	Capture	125.0	567.5	442.5
	Activation	567.5	1010.0	442.5
Neutron detectors time windows	1	50	150	100
	2	150	200	50
	3	200	250	50
	4	250	350	100
	5	350	450	100
	6	450	650	200
	7	650	850	200
	8	850	1000	150

The reasons for the definition of the time windows as compiled in Table 3.1 are manifold:

- OreLog data processing (firmware and software) allows the simultaneous recording of three spectra only: burst, capture, activation.

- The burst spectrum should not be spoiled by γ-ray from thermal-neutron interactions. The γ-rays from inelastic neutron-scattering (as typical in the burst-range with fast neutrons) should be as pure as possible. However, the more the focus is on the very first time-range in the primary-neutron production window, the purer becomes the spectrum, but statistics decrease.
- The capture spectrum should not start before the trigger-pulse ceases (n-production is OFF). It should start even later to make sure that there are no fast-neutron interactions anymore.
- The activation-window should be as long as possible to record enough counts (statistics). For practical reasons, the time window of the activation spectrum should have the same length as the time window of the capture spectrum enabling easy subtraction of the activation spectrum part from the capture spectrum part.

3.4 Detectors

The OreLog tool is equipped with a variety of different detectors for neutron- and γ-spectroscopy as schematically illustrated in Figure 3.1. The detailed installation and design of the individual detectors within the tool is confidential and can be disclosed on request. A total of six neutron- and one gamma-detector are mounted. Their technical details and contribution to elemental logging will be explained in the following paragraphs.

3.4.1 Gamma-ray Detector

An overview to all components of the γ-detector is depicted in Figure 3.7. The actual γ-detection unit consists of a scintillator crystal coupled to a PMT. The preamplifier board converts the charge signal coming from the PMT into a voltage step signal (sharp fast-rising edge, exponentially slowly falling tail). The MCA obtains these step-signals, measures their height (corresponds to energy), and accumulates the pulse-heights of the step-signals in a histogram to obtain a pulse height distribution. During active pulsed-neutron-generator mode the MCA accumulates three γ-spectra simultaneously (Figure 3.6).

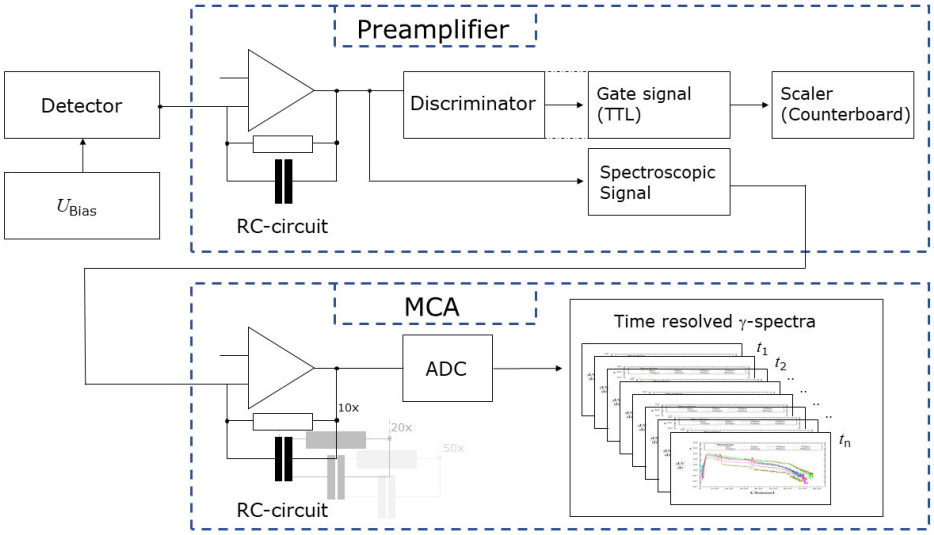

Figure 3.7: Schematic overview of components of γ-ray spectroscopy module. The processor on the preamplifier board converts the charge signal in a spectroscopic signal. If the spectroscopic signal is high enough, i.e. above a defined trigger threshold, then a counter-signal pulse is created by the processor, a counter signal which is sent to the counterboard. Abbreviations are transistor-transistor logic (TTL), multichannel analyzer (MCA), analog-digital-converter (ADC).

The scintillator crystal is the core part of the γ-ray detector concerning the physical γ-detection principle. In the beginning of the detection process a photon transfers all (or part) of its energy to an electron in the crystal. This fast electron interacts with the crystal resulting in many low energy photons in the visible wavelength range, the so-called scintillation photons. Three commonly used and state-of-the-art crystals were tested: NaI(Tl), $LaCl_3$, and $CeBr_3$. Unfortunately, the highly promising Saint Gobain $LaBr_3$(Ce) scintillator crystals (Saint-Gobain, 2018) were not available for the OreLog tool and the present work. Therefore, only a comparison of the three previously mentioned crystals is given in Table 3.2. Clear advantages of one crystal over the other are marked with (+), disadvantages with (−). It had to be decided which crystal to implement in the γ-ray module. This means the advantage of many decades experience of NaI(Tl) had to be weighed against fast pulses and better energy resolution ($CeBr_3$ crystal).

Table 3.2: Comparison of the most important parameters of NaI(Tl), $LaCl_3$, and $CeBr_3$ scintillator crystals.

Properties of tested crystals	NaI(Tl)	$LaCl_3$	$CeBr_3$
Diameter [mm]	44.5	44.5	44.5
Length [mm]	92.7	76.0	76.0
Crystal-internal background [counts/s]	not relevant (<10)	600 (−)	negligible (<0.01) (+)
Manufacturer	REXON	SCIONIX	SCIONIX
Hygroscopic	yes	yes	yes
Linearity	good	very good	very good
Scintillation decline time [µs]	0.23 (−)	0.028	0.026 (+)
Brightness [photons/MeV]	38,000 (−)	46,000	50,000 (+)
Density [g/cm³]	3.7	3.8	5.1
Energy resolution @ 661 keV [%]	7 (−)	4 (+)	4 (+)
Energy resolution @ 2.6 MeV [%]	4 (−)	2.5	2 (+)

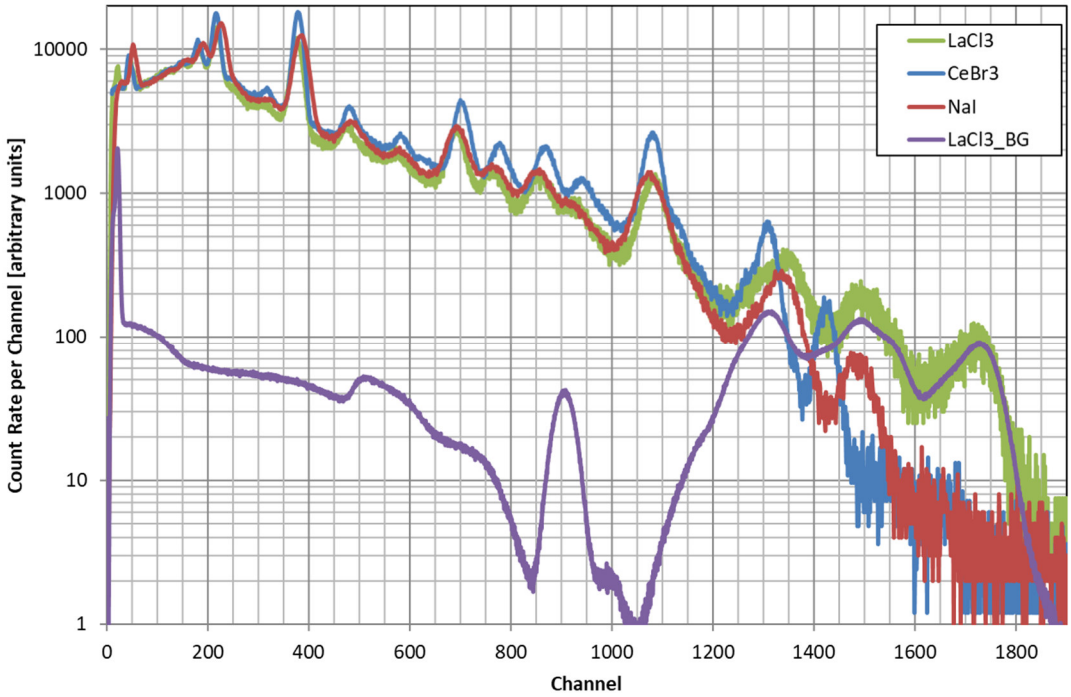

Figure 3.8: γ-ray spectra of uranium recorded by different scintillator crystals. The green ($LaCl_3$), blue ($CeBr_3$), and red line (NaI) indicate the scintillator crystal type. The purple line ($LaCl_3$_BG) is a crystal-internal background of $LaCl_3$ measured with detector inside some lead shield. The hydrogen peak at 2.2 MeV corresponds to channel 1300.

Figure 3.8 shows a comparison of uranium-ore spectra recorded by the scintillator crystals NaI(Tl), $LaCl_3$ and $CeBr_3$ with the characteristics presented in Table 3.2.

Crystal-internal background ($LaCl_3$_BG) of the $LaCl_3$ crystal is also shown. The detailed analysis of the total-spectrum composition shows an interesting dependence on the scintillator crystal material: In the energy-range above the 2.2 MeV-(channel 1300 in Figure 3.8) hydrogen-peak about 50 % of all signals contributing to the total spectrum are due to neutron-interactions with the scintillator-crystal material.
To better understand the contribution of the detector material to resolution and background, the neutron induced cross-sections were plotted by using the JANIS 4.1 (JAva-based Nuclear Data Information System) software, which is developed by the OECD Nuclear Energy Agency (NEA) Data Bank to facilitate the visualization and manipulation of nuclear data (Soppera et al., 2014). The neutron induced cross-sections were estimated from these plots and the results are shown in four energy ranges in Table 3.3.

Table 3.3: Neutron induced cross-sections in millibarn. Note: Natural abundances of Cerium: Ce-140 (88.48 %) and Ce-142 (11.08 %). Ce-136 (0.19 %) and Ce-138 (0.25 %) are neglected. Natural abundances of Bromine: Br-79 (50.7 %) and Br-81 (49.3 %).

		Alpha Production				**Proton Production**			
		Energy Range [MeV]				Energy Range [MeV]			
	Max	14	10	5	1	14	10	5	1
	Min	10	5	1	0.1	10	5	1	0.1
NaI Detector									
Na-23	max	100	100	1	-	80	80	2	-
	average	100	20	-	-	80	40	<0.1	-
I-127	max	10	-	-	-	10	1	-	-
	average	5	-	-	-	10	1	-	-
$CeBr_3$ Detector									
Ce-140	max	10	1	-	-	10	1	-	-
	average	2	0.1	-	-	4	-	-	-
Ce-142	max	10	-	-	-	10	0.1	-	-
	average	3	-	-	-	1.5	-	-	-
Br-79	max	12	5	0.1	-	50	20	10	-
	average	8	1	-	-	50	20	7	-
Br-81	max	8	0.5	-	-	50	10	1	-
	average	4	0.1	-	-	50	4	0.2	-

The alpha production is lower in $CeBr_3$ compared to NaI. The proton production cross-sections of NaI and $CeBr_3$ are similar. Na-23 dominates the proton production in NaI, Br dominates the proton-production in $CeBr_3$. The rough estimate, $0.5 \cdot 80$ mb + $0.5 \cdot 10$ mb result in 45 mb for NaI, and $0.25 \cdot 10$ mb + $0.75 \cdot 50$ mb = 40 mb for $CeBr_3$. These are the two numbers for proton production. The two materials (NaI, $CeBr_3$) have comparable proton production cross-sections. The γ-production cross-sections are dominated by iodine (in case of NaI) and bromine (in case of $CeBr_3$), and the γ-production cross-sections of NaI-detector and $CeBr_3$-detector are similar.

Both energy resolution performance and crystal internal background are decision criteria. The major contributing processes are the result of neutron activation processes, which result from:

- β-decay + γ-ray from ^{23}Ne, production by ^{23}Na(n,p)^{23}Ne $T_{1/2}$ = 37.2 s,
- β-decay + γ-ray from ^{20}F, production by ^{23}Na(n,α)^{20}F $T_{1/2}$ = 11.0 s,
- β-decay + γ-ray from ^{16}N, production by ^{23}Na(n,2α)^{16}N $T_{1/2}$ = 7.13 s,
- β-decay ^{24}Na^{m}, production by ^{23}Na(n,)^{24}Na^{m} $T_{1/2}$ = 20.2 ms.

Compared to a NaI scintillation crystal, a $CeBr_3$ scintillation crystal almost completely avoids background built-up by crystal-internal processes because no short-living isotopes are produced within the crystal. The 'Chart of Nuclides' (Pfennig et al., 1995) does not indicate any disturbing (unfavorable) activation process for $CeBr_3$. Table 3.4 lists all isotopes appearing in a $CeBr_3$ crystal with an evaluation of the risk of generating crystal-internal background.

Table 3.4: Potential background contribution of isotopes incorporated in $CeBr_3$ crystal

Isotope with natural abundance in % in ()	Background contribution	Description
^{136}Ce (0.19),^{138}Ce (0.25),	Uncritical	-
^{140}Ce (88.48)	Uncritical	Only production of ^{137}Ba^{m} is slightly critical because of $T_{1/2}(^{137}Ba^{m})$ = 2.55 m, but resulting γ-ray with energy of 662 keV is uncritical.
^{142}Ce (11.08):	Uncritical	Very little background from ^{142}La produced by ^{142}Ce(n,p)^{142}La but T1/2(^{142}La) = 92.5 m, (n,α) reaction is unlikely but would only result in ^{139}Ba with T1/2(^{139}Ba) = 83 m.

^{79}Br (50.69)	Uncritical	^{80}Br production by (n,) reaction but T1/2(^{80}Br) = 17.6 m is uncritical, ^{80}Br^{m} production by (n,) reaction but only rare or tiny decay signals.
^{81}Br (49.31)	Acceptable	^{82}Br production by (n,) reaction but T1/2(^{80}Br) = 35 h is uncritical, ^{82}Br^{m} production by (n,) reaction, β-decay with branching fraction of 2.4 % to ^{82}Kr with Q = 3.1 MeV is acceptable and much better than NaI behavior.

Beside the removal of crystal-internal background the $CeBr_3$ also has the following advantages:

- faster scintillation-signal,
- higher density resulting in higher detection efficiency in the range of γ-energy E_γ = 2 to 10 MeV,
- higher energy resolution and higher photon yield.

It is important to suppress γ-rays created by neutron-tool interactions as good as possible. One large background are the γ-rays created by n-capture of cadmium foil conventionally wrapped around the detectors providing shielding of an extremely large contribution due to γ-ray created in thermal-neutron capture of scintillator material. Therefore, the γ-detector is wrapped with boron carbide (B_4C) instead, that still provides protection against thermal neutrons appearing in the scintillator, but the capture of boron does not produce γ-rays and, consequently, shielding against thermal-neutron would not generate extra contributions in the measured spectrum.

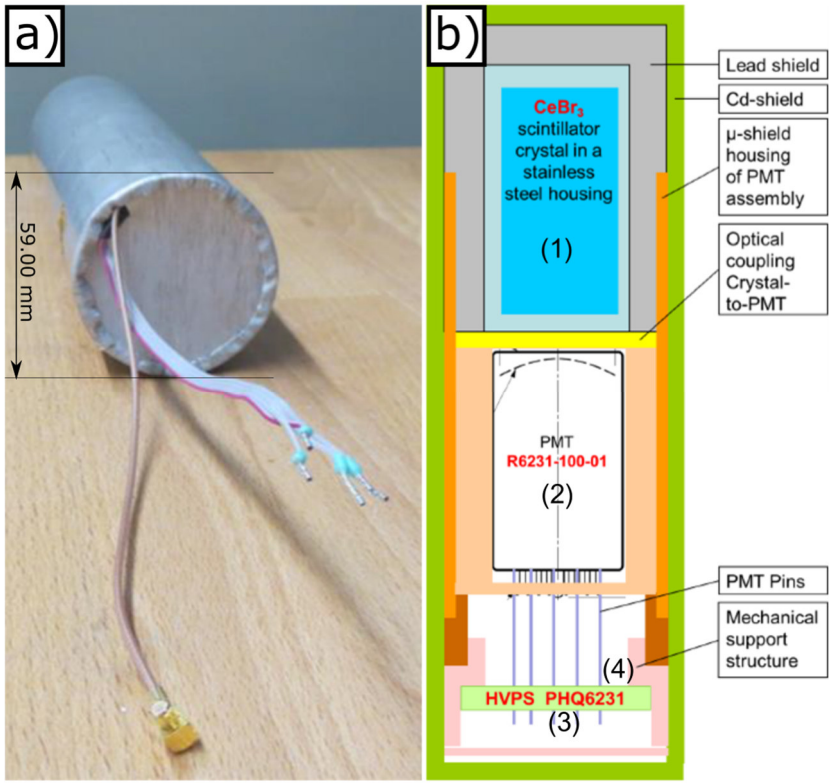

Figure 3.9: γ-ray spectrometer: a) Picture of assembled γ-detector unit. b) Schematic drawing of γ-detector unit.

Based on the previous reasoning and several years of extensive testing, the following γ–ray spectrometer unit has been implemented in the OreLog tool:

(1) $CeBr_3$ scintillator crystal,

(2) Photomultiplier tube (PMT),

(3) High Voltage Power Supply (HVPS)

(4) Mechanical-support structure for HVPS at PMT rear-side.

The installed HVPS has been developed especially for operation in the γ-spectrometer module of the OreLog tool. It does not only supply high-voltage to the cathode of the PMT, but it also supplies all dynodes of the PMT with the 'correct' (i.e. highly stabilized) high-voltage. Therefore, the HVPS is mounted directly at the rear side of the PMT contacting all the 11 PMT pins. The motivation for this HVPS installation was the idea to improve/stabilize the electrical potential of the PMT dynodes because unstable dynode potential results in degraded energy resolution. In the current design of the HVPS to the cathode and the dynodes, i.e. in the actual HVPS design, there is a separation between the definition of the potential and the stabilization supply-currents to the dynodes. The energy resolution in OreLog active mode (n-generator on) is worse than in OreLog passive mode (n-generator off). Reason is the quick change

(1 ms) of dynode de-load current due to the quick changes in γ-ray rate from 10^5 cps in the n-pulse to about 10^3 cps about 700 μs after the neutron pulse.
A support structure for HVPS at the PMT has been constructed and manufactured. It gives mechanical support to the HVPS at the rear side of the PMT. It consists of a ring and a lid. Within the assembled γ -detector unit the HVPS is screwed onto the ring and the ring is screwed onto the rear-side of the PMT. The lid closes the overall backside of the unit. A schematic drawing of the complete γ-detector unit is shown in Figure 3.9b. It provides a view to the HVPS at the rear side of the PMT assembly as well as a view onto the fully assembled γ-detector unit (Figure 3.9a).

3.4.2 Neutron Detectors

As stated in the chapter fundamentals of borehole logging (cf. chapter 2.2.2), elemental logging relies on both γ- and n-spectroscopy that has to be designed such that both detectors are integrated in one single tool. The design of the ^{3}He counter tubes belongs to the most important components of the OreLog tool design. This chapter documents the issues and MCNP (for details refer to chapter 4.2) calculations defining the design of the ^{3}He counter tubes.

Source Strength Detector

The source strength detector (SSD) or fast neutron detector is a CVD (chemical vapor deposition process) neutron-detector with ideal dimensions and properties for its installation. It measures the current neutron-production-rate of the pulsed neutron generator. The main advantage of a CVD neutron detector is that it can measure the exclusive neutron flux with neutron-energy $E_n > 5.8$ MeV due to the exploitation of the reaction $^{12}C(n,\alpha)^9Be$ as shown in Figure 3.10. In addition to this fast neutron flux measurement, it also measures thermal neutron-flux simultaneously and with efficient background elimination as described in Kavrigin et al. (2016) and Weiss et al. (2016).

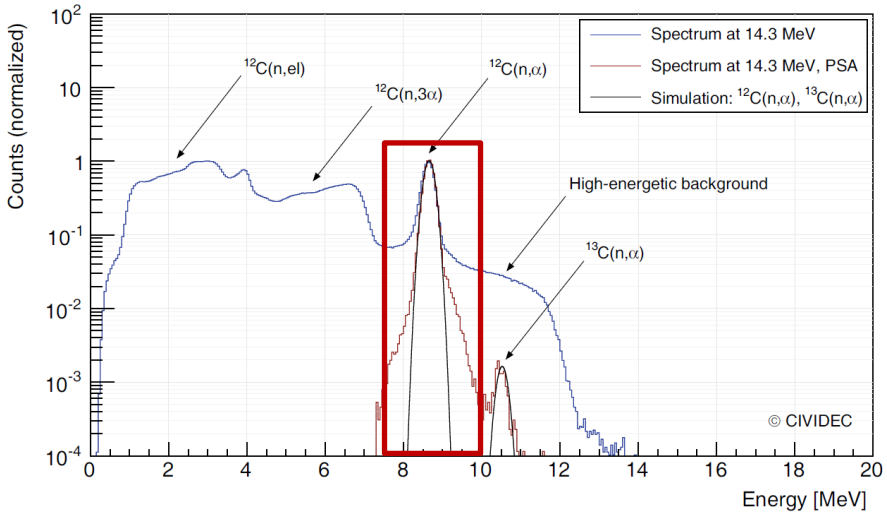

Figure 3.10: Energy spectra at 14.3 MeV neutron energy : total spectrum, spectrum with the applied pulse-shape analysis conditions, and spectra of $^{12}C(n,\alpha)^{9}Be$ and $^{13}C(n,\alpha)^{10}Be$ simulated with Geant4. Modified after Kavrigin et al. (2016).

In Figure 3.10 the measured and simulated deposited energy spectrum in diamond with 14.3 MeV neutrons from the detector manufacturer (Kavrigin et al., 2016) is shown. In the simulation the electronic noise is not considered. In the measurements the electronic noise broadens the peaks in the deposited energy spectrum. Neutron elastic scattering is dominating the spectrum at lower energies. A contribution of the $^{12}C(n,3\alpha)$ reaction is seen between 4 MeV and 7 MeV. The peak of the $^{12}C(n,\alpha)^{9}Be$ reaction is at 8.3 MeV. The peak of the $^{13}C(n,\alpha)^{10}Be$ reaction is at 10.2 MeV. The source strength detector is installed directly at the radial outer surface of the neutron generator at the location where the neutrons are emitted.

Near Thermal Neutron Detector

The near thermal-neutron detector consists of four proportional ^{3}He counter tubes which are connected in parallel. To improve the charge collection at the anode wire of the small diameter tube a denser gas (argon) was added to the filling gas, resulting in a total tube pressure of 0.61 MPa. It is intended to measure the thermal neutrons from the surrounding formation nearby the source. All tubes are fully wrapped in Kapton-foil to isolate the high voltage.

Far Thermal Neutron Detector

The far thermal-neutron detector is a proportional ^{3}He counter tube. It is important to put an electromagnetic shield around the detector; the shield must be grounded. It is intended to measure the thermal neutrons from the surrounding formation far from the source. The tubes are fully wrapped in Kapton-foil to isolate the high voltage.

4 Data Processing

The understanding of the composition of the spectra acquired by OreLog and the impact of its constrained inversion in the interplay with dedicated error evaluation is one of the key aspects in this work. Under certain conditions (detector, electronic components and measuring environment), data from the same spectra obtained by different unfolding algorithms have different results. The accuracy of qualitative and quantitative analysis of ore formations is determined by γ- and neutron-spectra unfolding techniques. This chapter provides a short overview on spectral analysis and application of the most convenient spectral deconvolution algorithms and technologies in denoising, background subtraction and overlapping peak separation.

Spectral deconvolution is of outmost importance to generate reliable elemental logs based on γ-spectra. The detector is irradiated with γ-rays having many different primary energies. All the γ-rays can be classified by their source. In case of natural γ-ray spectra there are only three sources:

1. Uranium decay chain (^{238}U),
2. Thorium decay chain (^{232}Th),
3. Potassium decays (^{40}K).

Each of these three sources has its own energy distribution of primary γ-rays. Hence, there are only three templates, i.e. one template corresponding to each one of these three sources. Each natural γ-spectrum recorded by OreLog must be a linear combination of the three templates. In case of active-generator spectra the situation is similar. However, there are more degrees of freedom, i.e. there are many more sources independent from each other. Basically, the primary neutrons from the generator interact with an element X of the formation surrounding the OreLog tool (and the OreLog tool itself). A γ-ray may be produced from this interaction X(n,γ + anything)Y. Assuming that the element mass fractions f_X in the formation can vary independently from each other, there are basically as many sources (independent contributions to the spectrum) as isotopes. Or in other words: each element X has its own (independent) template. The total spectrum is just a linear combination of all these templates.

Spectral decomposition is the determination of each template's contribution to the total spectrum. A given set of templates is defined as follows: which linear combination of templates provides the most likely modeling of the measured spectrum. The answer is provided by the coefficients of the linear combination. Obviously, there are many second-order effects and their correction terms to be considered, but they are not

mentioned at this point. The raw picture is that we are looking for the coefficients of the linear combination. The program Minuit developed by James and Roos (1975) and various fitting techniques relying on Minuit help to find the most likely linear combination. Minuit is a numerical minimization computer program which searches for a minimum in a user-defined function with respect to one or more parameters using several different methods as specified by the user. In addition to that it can compute confidence intervals for the parameters by scanning the function around the minimum (James and Roos, 1975). Relevant spectral deconvolution algorithms are introduced in the following paragraphs and their role for elemental logging is evaluated.

4.1 Spectral Deconvolution Algorithms

Meng and Ramsden (2000) discuss three common spectral deconvolution algorithms in their work based on an industry-standard 3 x 3 in NaI detector: Maximum Likelihood, Maximum Entropy and Linear Regularization. Other methods for the unconstrained deconvolution of γ-ray spectra are: Singular-value Decomposition, Linear Regularization, Maximum-Likelihood Fitting by Expectation Maximization and Maximum Entropy Method.

For the Maximum Likelihood Estimation using Expectation Maximization (ML-EM) the underlying function is discretized into a series of elements $f_i,\ i = 1,2,\dots N$, each an independent variable with Poisson distribution. This algorithm generates a sequence of estimated spectra (f_j^{new}) and each new estimate increases the likelihood function defined in Shepp and Vardi (1982) until a global maximum likelihood estimator is reached:

$$f_j^{new} = f_j^{old} \sum_{i=1}^{M} \frac{f_i^* R_{ij}}{\sum_{j=1}^{N} f_j^{old} R_{ij}}, \tag{4.1}$$

where f_i^* is the measured spectrum and R_{ij} is the probability that an incident γ-ray with energy corresponding to bin i is detected in bin j.

Another promising deconvolution method to deal with ill-posed problems by both remarkably enhancing the resolution and reducing noise in spectral analysis at the same time is the maximum entropy method (MEM). It is a probabilistic method that maximizes the equation for the system's entropy according to Jaynes (1957):

$$L(f,\lambda) = \lambda S(f,m) - \frac{1}{2}\chi^2, \tag{4.2}$$

where the λ term is the smoothing or regularizing parameter. The entropy term $S(f,m)$ ensures the information, which is contained in the distribution f (the solution) with respect to an a priori model m. The expression for entropy reaches its maximum when

both distributions are identical ($f = m$), whereas the solution f must be positive and additive corresponding to the entropy definition of Jaynes (1988):

$$S(f,m) = \sum_{j=1}^{N} f_j - m_j - f_j \log\left(\frac{f_j}{m_j}\right), \tag{4.3}$$

Meng and Ramsden (2000) also suggest the Linear Regularisation (LR) method, which is a method of inversion with constraints. The sum of the squares of the second derivatives are minimized to avoid an oscillating solution:

$$C \propto \int [f'(E)]^2 \, dE \propto \sum_{j=1}^{M-1} [f_j - f_{j+1}]^2, \tag{4.4}$$

where the underlying function $f(E)$ is the incident γ-ray spectrum. The solution $f(E)$ must also be consistent with the observed data. Therefore χ^2 and C are simultaneously minimized to find the final solution:

$$L(f,\lambda) = \chi^2 + \lambda C, \tag{4.5}$$

where λ is the Lagrange multiplier. Although simple to implement, this method is not suitable for the intended spectral analysis due to several drawbacks: it bans sharp features and the solution derived is not positively constrained. Hence, it leads to difficulty in defining relevant peak areas.

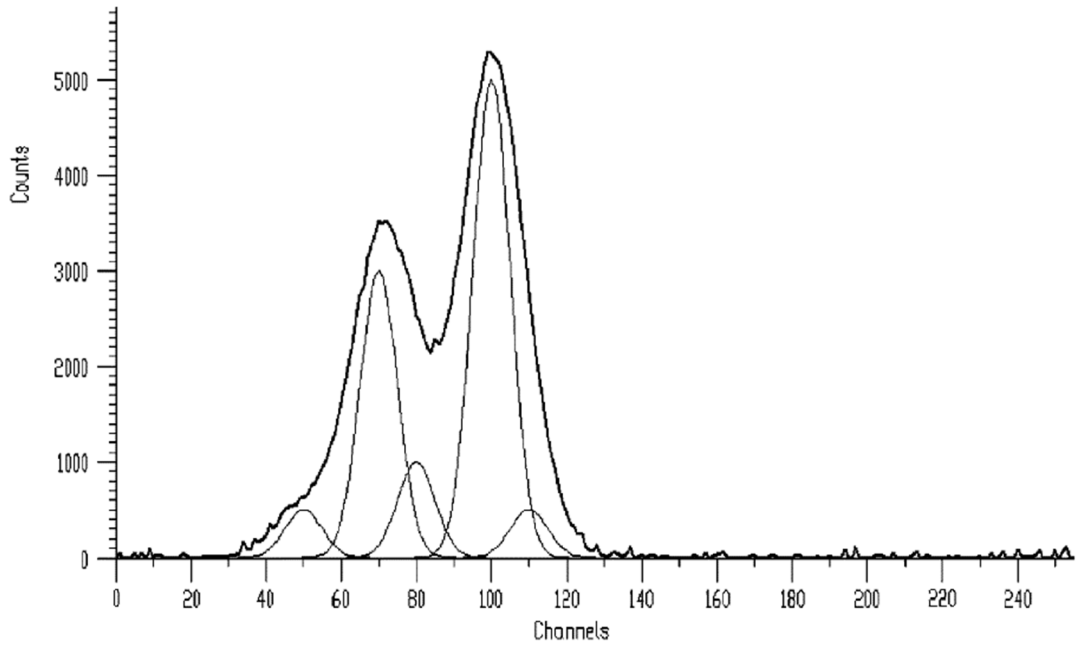

Figure 4.1: Testing example for spectral deconvolution with acquired spectra with added noise in bold and five underlying Gaussian peaks after Morháč (2006).

The best peak-resolving power was achieved by the ML-EM algorithm, as well as best peak-to-valley ratio and narrowest peak widths. The LR method is linear and it is easier to understand the relation between incident and output spectrum. However, due to limitations in the algorithm, the deconvolved spectral quality is poor compared to the other two methods. ML-EM and MEM return better deconvolved spectra and can work with a low number of counts per channel and they are intrinsically positively constrained. Conversely, many iterations are required to reach convergence. The ML-EM algorithm is very effective, also with low signal-to-noise ratio data. Poisson statistics can be modeled in each detection element and resolution is good (Meng and Ramsden, 2000).

Another promising candidate is the Gold deconvolution algorithm (Gold, 1964), which is analyzed and modified by Morháč (2006) and exemplarily visualized in Figure 4.1. For a discrete system, the relationship between a measured value $x(i)$ and a raw result of measurement $y(i)$ is expressed as

$$y(i) = \sum_{k=0}^{i} x(k)h(i-k), \quad i = 0,1,\dots,N-1, \tag{4.6}$$

with $h(i)$ being an impulse response. This system can be written in matrix form:

$$\mathbf{y} = \mathrm{H}\mathbf{x} + \mathbf{n}, \tag{4.7}$$

where the matrix H has dimension $N \times M$, the vectors $\boldsymbol{y}$, $\mathbf{n}$ have length N and the vector $\mathbf{x}$ has length M, while $N \geq M$ (overdetermined system). Since this work exclusively investigates spectroscopic data (histograms) it is assumed that the elements of the vector $\mathbf{y}$ as well as the matrix H are positive integers (Morháč, 2006).

By choosing a local variable relaxation factor and substituting it into the Van Cittert algorithm (van Cittert, 1931), the following equation results:

$$x^{(n+1)}(i) = \frac{y(i)}{\sum_{m=0}^{M-1} A_{im} x^{(n)}(m)} x^{(n)}(i), \tag{4.8}$$

which is the Gold deconvolution algorithm (Gold, 1964) where $A = H^T H$, $y' = H^T y$ and $n = 0,1,2,\dots$ is the iteration step.

The Richardson–Lucy deconvolution algorithm (Richardson, 1972; Lucy, 1974) is based on the Bayes formula and has the following form for discrete data:

$$x^{(n)}(i) = x^{(n-1)}(i) \sum_{j=0}^{N-1} h(j,i) \frac{y(j)}{\sum_{k=0}^{M-1} h(j,k) x^{(n-1)}(k)}. \tag{4.9}$$

It converges to the maximum likelihood solution for Poisson statistics in the data.

The positive definite deconvolutions based on iterative solution of the system of linear equations (Gold, Richardson-Lucy) converge to the stable states. It is necessary to

change the particular solution and repeat the iterations with a non-linear boosting function. The proposed algorithm for boosted (Gold) deconvolution is:

1. Set initial solutions: $x^{(0)} = [1,1,\dots,1]^T$,
2. Set required numbers of repetitions R and iterations L,
3. Set the number of repetitions $r = 1$,
4. According to Gold deconvolution algorithm for $k = 0,1,\dots,L-1$ find solution $x^{(L)}$,
5. If $r = R$ stop calculation, else
    a. Apply boosting operation, set $x^{(0)}(i) = [x^{(L)}(i)]^p$; $i = 0,1,\dots N-1$ and p is boosting coef. >0,
    b. $r = r + 1$,
    c. Continue in step 4.

In previous studies Morháč et al. (1997) describe a non-oscillating Gold deconvolution method generalized for multidimensional spectra. Van Cittert and Gold methods are successful for the decomposition of γ-ray multiplets[1]. In particular, the Gold method provides good results and its property that the solution is always positive, is an important constraint for further spectra processing. However, computationally it is a demanding process:

$$ {}^{k+1}x_n^{(n)}(i) = \frac{y(i)}{\sum_{m=0}^{M-1} A_{im} x^{(n)}(m)} \; {}^{k}x_n^{(n)}(i), \tag{4.10} $$

where k is the number of iterations.

A mathematical method of optimization is explained for 1- and 2-dimensional Gold deconvolution. The optimization makes the calculation of the Gold algorithm much less time- and memory-consuming.

The same spectrum (cf. Figure 4.1) was deconvolved with different procedures: by solving the linear equation system, Van Cittert deconvolution, Fourier deconvolution and Gold deconvolution. Solving the linear equations system does not give any practical solution. The Van Cittert algorithm decomposes multiplets in the spectrum, oscillations are smaller than in the previous case, but the result contains several negative values, which are unrealistic. Fourier algorithm is also not the best method: it still has negative values, although multiplets can be decomposed to some extent and oscillations are smaller than with the Van Cittert method. Figure 4.2 shows the result of the Gold deconvolution which has proven to be the best of the investigated methods: the method

[1] Group of related spectral lines

unfolds multiplets, does not oscillate, it does not contain negative values and preserves peak positions and peak areas.

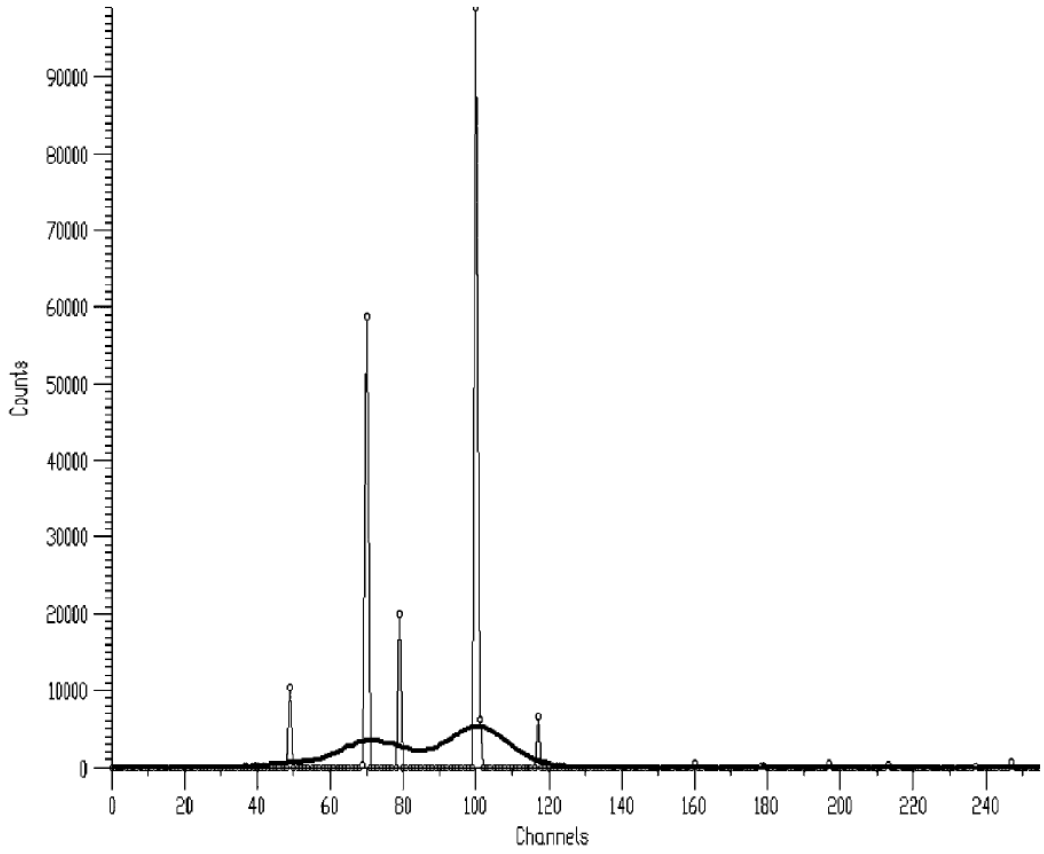

Figure 4.2: Result of deconvolution of the testing spectrum (cf. Figure 4.1) by using the boosted Gold deconvolution.

The proposed optimization algorithm benefits from the fact that the detector response function has only limited, relatively small number of channels with non-zero counts. The processing of multiparameter spectra consists of background elimination (separation of useless information), improvement of the resolution in the spectrum by deconvolution, determination of peaks' positions in the spectrum and fitting of peaks. After eliminating the background in the spectra, resolution can be improved by applying the Gold deconvolution method. The analysis of peaks in spectra consists in determining peaks' positions and corresponding fitting techniques. The positions of peaks can be found by peak searching algorithm (Morháč et al., 2000), where the algorithm is generalized for multidimensional spectra. The analysis of multiparameter spectra consists in determination of peaks' positions and subsequent fitting. The positions can be determined by employing peak searching algorithm or by finding local maxima of separated peaks after deconvolution. Peaks' positions are fed as initial values into fitting algorithm, and it allows fitting large blocks of data and large number of

parameters simultaneously. Deconvolution techniques are used to determine the areas of individual overlapping peaks in γ-ray spectroscopy, and these methods are a very important consideration for spectra-analyzing software (Navarro et al., 2015). The method of least squares has been successful in the analysis of spectra containing doublets and random Gaussian noise (Liu et al., 2017).

It is shown that all methods are based on the compromise between the maximum resolution enhancement and the minimum intensity of the side lobes. It must be emphasized that there is no general solution for all deconvolution problems and the optimal deconvolution algorithm should be chosen with regard to the particular analytical problem under study and optimized for this purpose. A single algorithm cannot meet the complex spectrum unfolding requirement. Therefore, the general approach to select the quasi optimal algorithm as suggested by Dubrovkin (2014) is pursued.

4.2 Monte Carlo N-Particle Transport Code Simulations

MCNP is a general-purpose Monte Carlo N–Particle code used for neutron, photon, electron, or coupled neutron/photon/electron transport, including the capability to calculate eigenvalues for critical systems. It is the standard software package for the simulation of nuclear processes (fission and particle interaction), which was developed by Los Alamos National Laboratory in the US and is currently being distributed by Radiation Safety Information Computational Center (RSICC) based in the National Laboratory of Oak Ridge in the US, and by the NEA in Paris. The code treats an arbitrary three-dimensional configuration of materials in geometric cells (cf. Figure 4.3) bounded by first- and second-degree surfaces and fourth-degree elliptical tori. Important standard features that make MCNP very versatile and user-friendly include a powerful general source, criticality source, and surface source. Additionally, both geometry and output tally plotters, a rich collection of variance reduction techniques, a flexible tally structure, and an extensive collection of cross-section data are available. In the present study, MCNP version 6.2 following the manual of Werner (2017) is used to model the detector response of the OreLog tool to a given environment. It tracks neutrons generated inside the tool, secondary neutrons (e.g. from fission), and photons through the material of the tool and the tool's immediate environment (Briesmeister, 2000).

The MCNP simulations were realized simultaneously on several computers (multi-core) by taking advantage of parallel computing to allow for statistically significant

model outputs in relatively short processing times (few hours). The PTRAC option of MCNP was used to provide tracking information of the resulting particle tree of each primary-source particle. Therefore, the Ptrac-analyzer, a program written by UIT, serves for the simulation of neutron-induced γ-ray spectra and their decomposition. It is the basis for the generation of templates. Ptrac provides access to simulation-data on a very detailed level. Especially the ability to completely decompose a total γ-ray spectrum into contributions from different isotopes makes a very useful tool out of Ptrac-Analyzer but also the decomposition into burst- and capture-spectrum would not be possible that effectively without Ptrac-analyzer.

4.2.1 MCNP Input Model

In order to run any MCNP simulations, it is required to set up a representative model of both the OreLog tool and the surrounding formation of interest. The OreLog MCNP input model is only configured once including all relevant material properties and geometries, whereas the formation parameters are changed according to the required simulation purpose. Formation parameters are for instance elemental composition, density, water saturation, formation porosity, borehole diameter among others and the impact of their variation is further elaborated in chapter 4.4 and 6.3.2. The standard case is defined as 150 mm borehole diameter, pure quartz formation (SiO_2) at a density of 2.65 g/cm^3, and a water-filled porosity of 30 %.

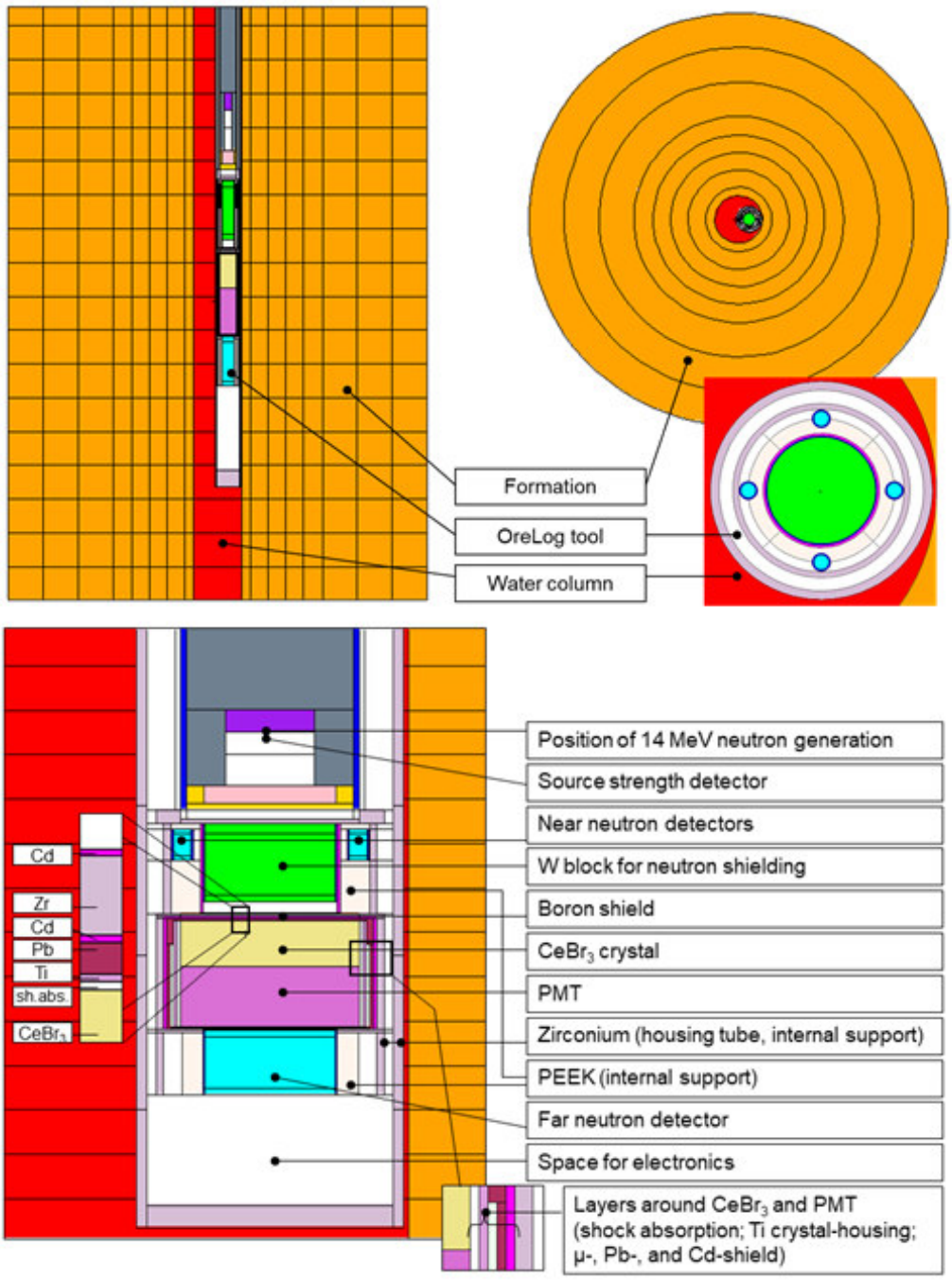

Figure 4.3: Illustrations of the MCNP input model of the OreLog tool. Cross-section (top left) and plane view nearby the neutron detectors (top right) and model details with captions in the zoomed cross-section (bottom) are shown. Note: Polyether ether ketone (PEEK) is used as internal support material and strutting.

4.2.2 Template Generation

A multitude of formation scenarios have been simulated. The results of these simulations are distributions of energy depositions with respect to time, γ-ray generation reaction, and other nuclear physical criteria. However, field data obtained

from the OreLog tool are frequency distributions in MCA-channels. In order to have expectations or simulations of these MCA-channel distributions it is required to take into account:

(i) Smearing of the deposited energies
(ii) Translation of smeared deposited energies to channels

A first approach is a linear dependence between MCA channel C and smeared deposited energy E,

$$C = m(E - e_0) \tag{4.11}$$

as a function of parameters m and e_0. The two parameters have approximately the values

$$m = \frac{2048\text{chn}}{3.0\text{MeV}} \approx 683.7\frac{\text{chn}}{\text{MeV}} \qquad \text{(natural gammas)} \tag{4.12}$$

$$m = \frac{2048\text{chn}}{10\text{MeV}} \approx 204.8\frac{\text{chn}}{\text{MeV}} \qquad \text{(n induced gammas)} \tag{4.13}$$

$$e_0 = -45 \ldots + 45\text{keV}. \tag{4.14}$$

Non-linearities are negligible for $CeBr_3$ crystals.

In addition, energy smearing has to be considered since MCNP only simulates the amount of deposited energy but in truth the amount of deposited energy causes a light signal in the crystal and the height of this light signal is statistically smeared with respect to E_{dep}. The amount of light is called the measured value E_{meas}. In the simulation process, one possibility is to translate each deposited energy E_{dep} to a measured value E_{meas} by

$$E_{\text{meas}} = E_{\text{dep}} + r \cdot \sigma\left(E_{\text{dep}}\right), \tag{4.15}$$

where r is a random number following a standard normal distribution ($\mu=0$, $\sigma=1$) and $\sigma(E_{\text{dep}})$ is given by

$$\sigma\left(E_{\text{dep}}\right) = \frac{1}{2.3548} \cdot R_{661} \cdot \sqrt{0.661\text{MeV} \cdot E_{\text{dep}}}, \tag{4.16}$$

with R_{661} being the energy resolution at 661 keV, $\sigma(E_{\text{dep}})$ is quasi the width of a peak at energy E_{dep} expressed in multiples of Gauss-sigmas.

However, this solution is not good at low statistics (i.e. low count rates at the high-energy end of a spectrum) because unnecessary statistical fluctuations are incorporated. A better approach is to perform a mathematical convolution of the E_{dep} distribution ($\mathrm{d}N/\mathrm{d}E_{\text{dep}}$) resulting in an E_{meas} distribution ($\mathrm{d}N/\mathrm{d}E_{\text{meas}}$). This is the preferred solution for implementing energy-smearing in this case, i.e.

$$\frac{\mathrm{d}N}{\mathrm{d}E_{\mathrm{meas}}} = \int_{E_{\mathrm{dep}}=-\infty}^{E_{\mathrm{dep}}=+\infty} f\left(E'_{\mathrm{dep}}, E_{\mathrm{meas}}\right) \frac{\mathrm{d}N}{\mathrm{d}E'_{\mathrm{dep}}} \mathrm{d}E'_{\mathrm{dep}}, \tag{4.17}$$

where f is the energy resolution function, i.e. a Gauss function with width $\sigma = \sigma(E_{\mathrm{dep}})$ as defined in Equation 4.16 mean value $\mu = E_{\mathrm{dep}}$.

4.3 Template Matching

This chapter briefly reviews how the energy templates are combined in the analysis of a single spectrum of a dataset and compared to real data according to the well-established workflow shown in Figure 4.4.

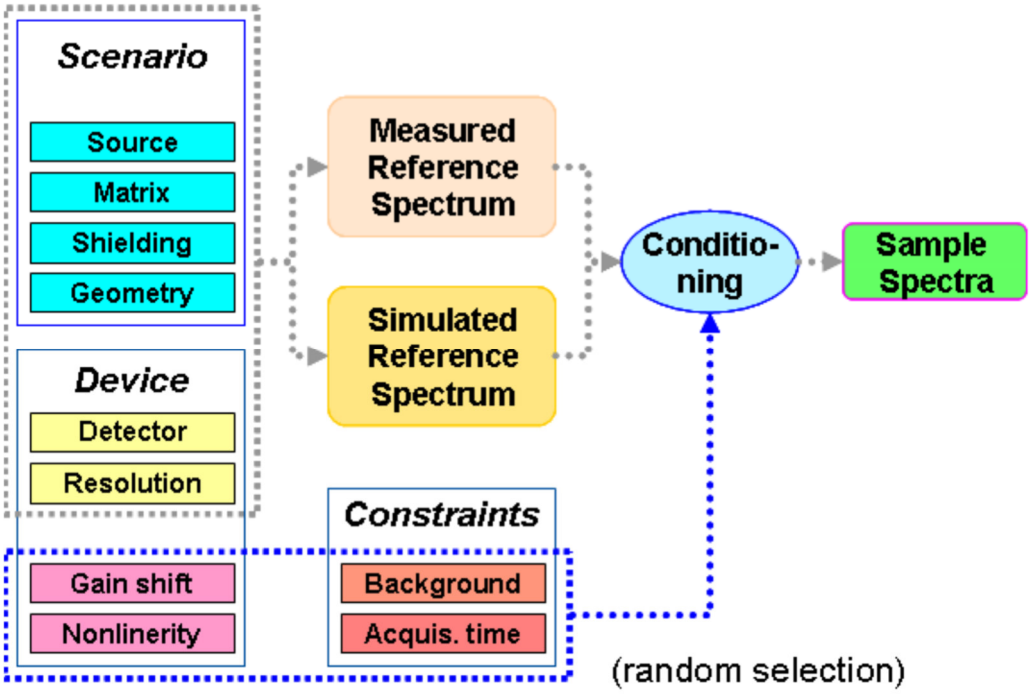

Figure 4.4: Simulation scheme applied to generate ensembles of 'real' sample spectra corresponding to the conditions of typical in-field applications, after Herbach et al. (2009).

The basis of template adaption is a χ^2 sum:

$$\chi^2 = \sum_{i=1}^{N} \left(\frac{E_i - D_i}{U_i}\right)^2, \tag{4.18}$$

with

- i being the bin number of the spectrum in OreLog bin format (an OreLog bin is a merge of neighboring MCA-bins),
- D_i being the number of counts in the i-th OreLog bin of the spectrum to be analyzed,
- E_i being the expectation from the model-function describing the spectrum, and
- U_i being the statistical uncertainty on D_i.

The terms D_i and U_i are given by the data itself.

The term E_i is the total number of expected counts in the region of the i-th OreLog bin:

$$E_i = D_i^{\mathrm{Exp}} = \int_{E_{\mathrm{dep},i\,\mathrm{lower}}}^{E_{\mathrm{dep},i\,\mathrm{upper}}} c^{\mathrm{Exp}}\left(E_{\mathrm{dep}}\right)\ \mathrm{d}E_{\mathrm{dep}}. \tag{4.19}$$

Here $D_i^{\mathrm{Exp}}$is a symbol for the expectation on data value D_i. The term $c^{\mathrm{Exp}}\left(E_{\mathrm{dep}}\right)$ is the number of expected counts ΔC^{Exp} per energy bin width ΔE_{dep}, all as a function of deposited energy E_{dep}:

$$\frac{\Delta C^{\mathrm{Exp}}}{\Delta E_{\mathrm{dep}}}\left(E_{\mathrm{dep}}\right) \approx c^{\mathrm{Exp}}\left(E_{\mathrm{dep}}\right) = \frac{\mathrm{d}C^{\mathrm{Exp}}}{\mathrm{d}E_{\mathrm{dep}}}\left(E_{\mathrm{dep}}\right). \tag{4.20}$$

Lower-case c denotes the derivative $\mathrm{d}C^{\mathrm{Exp}}/\,\mathrm{d}E_{\mathrm{dep}}$. The 'count-density' $c^{\mathrm{Exp}}\left(E_{\mathrm{dep}}\right)$ is integrated over the energy E_{dep} from the low-energy side of OreLog bin i (E_{dep}, i lower) to the high-energy side of OreLog bin i (E_{dep}, i upper).

The integrand in Equation 4.23 is a linear combination of contributing processes, i.e.:

$$c^{\mathrm{Exp}}\left(E_{\mathrm{dep}}\right) = \sum_j b_j \cdot c^{\mathrm{Exp},j}\left(E_{\mathrm{dep}}\right). \tag{4.21}$$

The terms $c^{\mathrm{Exp},j}\left(E_{\mathrm{dep}}\right)$ represent the required energy templates for template matching. The software MCNP allows to simulate these energy templates, i.e. MCNP simulations can give reasonable expressions for $\tilde{c}^{\mathrm{Exp},j}\left(E_{\mathrm{dep}}\right)$ as presented in chapter 6.3.3.

4.3.1 Forward and Backward Modeling

The general approach to real-data spectrum analysis has two parts: forward modeling and backward modeling.

Forward Modeling

In this part a reasonable set of input scenarios is used to produce a sufficient set of simulated data:

- One input scenario is assembled by multiple input conditions like: borehole radius r_{BH}, formation's bulk density ρ_B, formation porosity ϕ, mineralogical composition of formation, energy resolution R_{661} of OreLog tool, etc.
- Reasonable set means that the range of the input conditions should cover the complete range one is interested in, i.e. r_{BH} = 5 to 15 cm, ρ_B = 1.5 to 5 g/cm³, ϕ = 0 to 50 %, R_{661} = 4.0 to 12.0 %, etc.
- Simulated data are spectral data and MCS data. They are specific to the values of the input scenario, i.e. one input scenario results in one simulated spectrum-pair and one simulated MCS dataset.

The major step in the forward modeling is performed by MCNP. MCNP simulations provide a first version for expectation on measured spectral and MCS data. However, MCNP results cannot be used directly as expectation as will be discussed later.

Backward Modeling

The backward modeling has to recover input conditions from spectral and MCS data. One example: The spectrum analysis dataset sLOG (cf. 3.2.4) determines the area A_H of the hydrogen peak in the capture spectrum and subsequently it uses the r_{BH}-to-A_H relation (very strong and clear correlation) to estimate the true borehole radius.

A good backward modeling recovers input conditions with high robustness and high accuracy. The backward modeling implemented in the spectrum analysis dataset sLOG uses techniques like e.g. function adaption to spectral data via χ^2 terms.

4.4 Petrophysical Parameters

As introduced and presented in detail in chapter 3.1, the neutron and γ detectors measure a set of quantities, which are recorded and available for processing. The conceptual model of data processing to obtain petrophysical quantities from measured base quantities is shown in Figure 4.5.

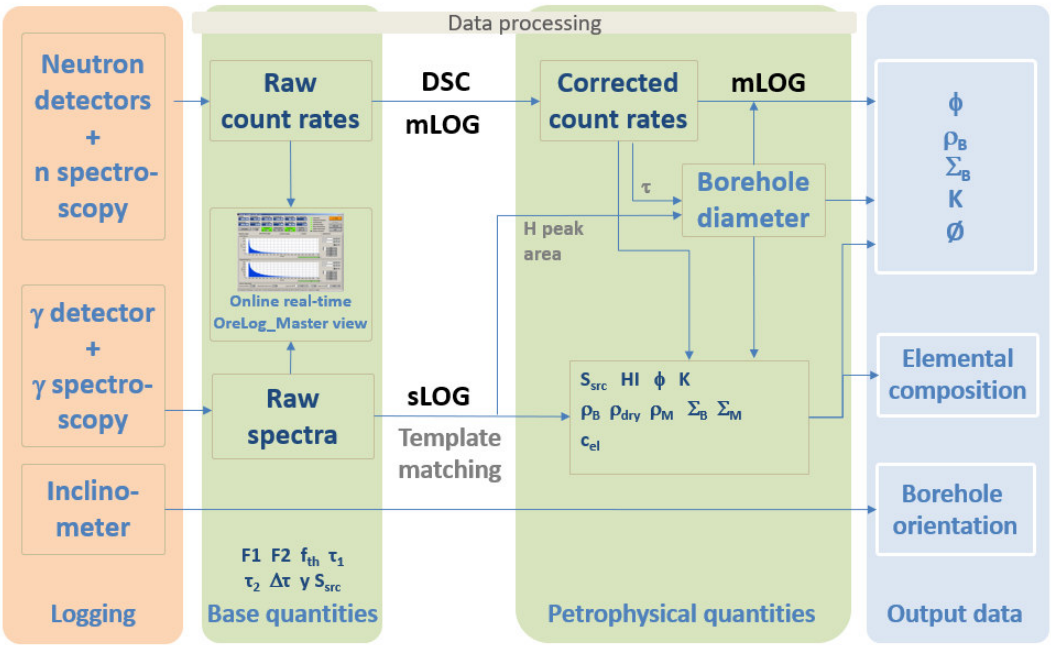

Figure 4.5: Data processing from measured base quantities to petrophysical formation parameters and final output data for WellCAD.

4.4.1 Base Quantities

The following base quantities are calculated from the raw data of the SSD, near, far and γ-detector time windows (1-8) without any corrections (4 x 8 count rates R) nor additional parameters:

- S_src: S_{src} = count rates from the SSD;
- fTH_burst: $f_{th} = \frac{R_{TH1}^{(burst)}}{R_{TH2}^{(burst)}}$; unitless; time window 1;
- tau_TH1: τ_1 = neutron decline in µs from near detector; time window 4 to 8;
- tau_TH2: τ_2 = neutron decline in µs from far detector; time window 4 to 8;
- tauB_TH1: $\tau_1^{(burst)} = \frac{\Delta t_{32}}{\ln R_{TH1}^{(2)} - \ln R_{TH1}^{(3)}}$; in µs; time window 2 to 3;
- tauB_TH2: $\tau_2^{(burst)} = \frac{\Delta t_{32}}{\ln R_{TH2}^{(2)} - \ln R_{TH2}^{(3)}}$; in µs; time window 2 to 3;

  with time interval $\Delta t_{32} = t_3 - t_2 = 200\,\mu s - 150\,\mu s = 50\,\mu s$ (see Table 3.1);
- DTAU: $\Delta\tau_{norm} = \frac{\tau_2 - \tau_1}{\frac{1}{2}(\tau_2 + \tau_1)}$; unitless;
- TH1_R: $ratio = \frac{\tau_1^{(burst)}}{\tau_1}$; unitless.

4.4.2 Petrophysical Quantities

Based on the MCNP output (cf. chapter 4.2) and the base quantities, several petrophysical quantities can be calculated. These present a first important step from raw logging data to geological formation interpretation. To achieve this, additional tool-specific parameters are required and presented hereinafter. These values were obtained from OreLog model calibration on both real logging data from the predecessor tool APFN$^+$ (cf. chapter 3.1) and MCNP simulations. For calculation of the petrophysical quantities the parameter values (e.g. Table 4.1) are stored in the mLOG dataset as explained in chapter 3.2.3.

HI – Hydrogen Index

The calculation of the hydrogen index HI (unitless) is calculated from the base quantity f_{th} (ratio of the burst rates in far and near neutron-detectors) plus five additional parameters (m, f_{th0}, o, p, and m_{max}) as defined in Table 4.1. The final parameterization for the HI estimator is:

$$HI = \begin{cases} 0 & \text{for: } f_{\text{th}} \le f_{\text{th0}} \\ m \cdot (f_{\text{th}} - f_{\text{th0}}) + o \cdot e^{p \cdot f_{\text{th}}} & \text{for: } f_{\text{th0}} < f_{\text{th}} \le f_{\text{th1}}, \\ m_{\max} \cdot (f_{\text{th}} - f_{\text{th1}}) + n_2 & \text{for: } f_{\text{th1}} < f_{\text{th}} \end{cases} \tag{4.22}$$

with n_2 and f_{th1} being chosen such that the total function is a continuously differentiable function at the transition from case 2 to case 3 in Equation 4.22, i.e.:

$$\frac{d}{d\,f_{\mathrm{th}}}\,HI(f_{\mathrm{th}}=f_{\mathrm{th1}})=m_{\max}=\frac{d}{d\,f_{\mathrm{th}}}\Big|_{f_{\mathrm{th1}}}\left(\;m\,(f_{\mathrm{th}}-f_{\mathrm{th0}})+\;o\cdot e^{p\cdot f_{\mathrm{th}}}\right)$$
$$\Longrightarrow f_{\mathrm{th1}}=\frac{1}{p}\,\ln\left(\frac{m_{\max}-m}{op}\right) \tag{4.23}$$

and

$$n_2=HI(f_{\mathrm{th}}=f_{\mathrm{th1}})=m\cdot(f_{\mathrm{th1}}-f_{\mathrm{th0}})+\;o\cdot e^{p\cdot f_{\mathrm{th1}}}. \tag{4.24}$$

Table 4.1: List of parameters for the calculation of HI.

Symbol	Name	Value	Unit
m	PAR_HI_M	0.05	-
f_{th0}	PAR_HI_FTH0	1.7	-
o	PAR_HI_O	3.0E-04	-
p	PAR_HI_P	1.5	-
m_{max}	PAR_HI_MMAX	0.15	-

Effective Porosity

The porosity of a rock is the fraction of the volume of space between the solid particles of the rock to the total rock volume. The space includes all pores, cracks, vugs, inter- and intra-crystalline spaces. The porosity is conventionally given the symbol ϕ, and is expressed either as a fraction varying between 0 and 1, or a percentage varying between 0 % and 100 %:

$$\phi=\frac{V_{pore}}{V_{bulk}}=\frac{V_{bulk}-\,V_{matrix}}{V_{bulk}}=\frac{V_{bulk}-\left(\frac{m_{dry}}{\rho_{matrix}}\right)}{V_{bulk}}, \tag{4.25}$$

with V_{pore} = pore volume, V_{bulk} = bulk rock volume, V_{matrix} = volume of solid particles composing the rock matrix, m_{dry} = total dry weight of the rock, ρ_{matrix} = mean density of the matrix minerals. The effective porosity is the ratio of the connected pore volume to the total volume. The ineffective (closed or dead-end) porosity is the remaining porosity.

Hydrogen index and porosity are only identical if all hydrogen is attributed to free water in the pores. As soon as the formation contains other sources of hydrogen, e.g. clays with significant bound water (hydrated), the two terms become different. Once HI is known, the total porosity ϕ (in m^3/m^3) is calculated based on four parameters (k_C, $\Delta\tau_0$, f_{cmax}, and HI_{max}):

$$\phi(\mathrm{HI},\Delta\tau)=\left(1-\frac{\mathrm{f}_{Cmax}}{1+e^{k_C\cdot(\Delta\tau-\Delta\tau_0)}}\right)\cdot\min(\mathrm{HI}_{max},\mathrm{HI}). \tag{4.26}$$

It estimates the effective porosity.

In the expression above the variables HI and $\Delta\tau$ are the results from two estimators previously defined, i.e.:

HI = estimator of Hydrogen Index as defined in Equation 4.22,

$\Delta\tau$ = τ_{far} - τ_{near} = difference between measured neutron decline times, and the remaining variables are four mLOG parameters as compiled in Table 4.2.

Table 4.2: List of parameters needed to estimate porosity ϕ.

Symbol	Name	Value	Unit
k_C	PAR_CLAYFRAC_KC	0.06	1/µs
$\Delta\tau_0$	PAR_CLAYFRAC_DTAU0	25	µs
$f_{C\ max}$	PAR_CLAYFRAC_FCMAX	0.7	-
HI_{max}	PAR_POR_HIMAX	0.45	-

The quotient containing the exponential function in Equation 4.26 can be considered as a 'soft switch' assigning the fraction f_{Cmax} of the hydrogen index HI to clay and the complementary fraction (1- f_{Cmax}) to mobile water in pores. Since only a certain fraction of HI can be considered to origin from mobile water in pores the minimum between HI and HI_{max} (instead of HI) is used.

Bulk Density

The bulk density estimator ρ_B is defined by:

$$\rho_B = a \cdot [c \cdot (y - y_0)]^b, \tag{4.27}$$

with the parameter y defined by:

$$y = \frac{TH2\_1}{10^8 \cdot S_{src}}\ , \tag{4.28}$$

and the base quantities:

TH2_1 = count rate of far detector in time window 1,

S_{src} = source strength as defined in 4.4.1,

and the mLOG parameters defined in Table 4.3.

Table 4.3: List of parameters needed to determine the bulk density ρ_B.

Symbol	Name	Value	Unit
y_0	PAR_BULK_0	2.19111E-05	-
a	PAR_BULK_A	5.800	g/cm³
b	PAR_BULK_B	0.101	-
c	PAR_BULK_C	1.588235	-

Dry and Matrix Density

The values of the two deduced densities ρ_{dry} (dry density) and ρ_M (matrix density) are given by:

$$\rho_{dry} = \rho_B - \phi \cdot \rho_{fl,} \tag{4.29}$$

and

$$\rho_M = \frac{\rho_{dry}}{1-\phi}, \tag{4.30}$$

with the estimators:

ϕ = estimator of porosity as defined in Equation 4.26,

ρ_B = estimator of bulk density as defined in Equation 4.27,

and the mLOG parameters:

ρ_{fl} = const. = fluid density = 1 g/cm³ (in investigated formations).

Here the term matrix refers to the grain or mineral density ($\rho_M > \rho_B$).

Hydraulic conductivity and permeability

DARCY's law for one-dimensional steady state flow in saturated porous media (in z direction) is given by:

$$v_f = -K \frac{\partial h}{\partial z}, \tag{4.31}$$

where v_f is the discharge velocity (filter velocity), K is the saturated hydraulic conductivity and $\partial h/\partial z$ is the hydraulic head gradient. The minus sign indicates that the flow always proceeds in the direction of decreasing hydraulic head (which remains valid even for the unsaturated case).

$\partial h/\partial z$ is the change in total hydraulic head in flow direction. The hydraulic head:

$$h = \Psi + z, \tag{4.32}$$

is the sum of elevation head and pressure head Ψ:

$$\Psi = \frac{P}{\rho_{fl} g}, \tag{4.33}$$

where P is the pressure, ρ_{fl} is the fluid density and $g = 9.81$ m/s^2 the gravity acceleration constant. 10 kPa represents a pressure head of 100 cm H_2O.

The saturated hydraulic conductivity K is a quantitative measure of the ability of a saturated porous media to transmit water when subjected to a hydraulic gradient. K depends on the permeability of the porous media k, the fluid viscosity μ_{fl} and fluid density ρ_{fl}:

$$K = k \cdot \frac{\rho_{fl}\, g}{\mu_{fl}}, \tag{4.34}$$

where g is the gravity acceleration constant. Note that k is a property of the porous media alone (independent of any fluid characteristics). The viscosity of water is:

$$\mu_{fl} = 0.91 \text{ mPa·s} \qquad \text{(at 25 °C)}.$$

The hydraulic conductivity and permeability have different physical units:

- hydraulic conductivity K in m/s or m/d,
- permeability k in m^2 or Darcy.

The unit Darcy is a non-SI unit. A medium with a permeability of 1 Darcy permits a flow of 1 cm^3/s of a fluid with viscosity 1 mPa·s under a pressure gradient of 1 atm/cm acting across an area of 1 cm^2. The conversion formula from Darcy to SI units is:

$$1 \text{ Darcy} \approx 0.9869 \cdot 10^{-12} \text{ m}^2.$$

Typical values of permeability range from 100,000 Darcy for gravel, to less than 0.01 µDarcy for granite. Sand has a permeability of about 1 Darcy. The conversion factor between conductivity and permeability for pure water ($\mu_{fl} = 0.91$ mPa·s, $\rho_{fl} = 1.0$ g/cm^3, T = 25 °C) is given by:

$$\frac{\rho_{fl}\, g}{\mu_{fl}} = \frac{1.078 \cdot 10^7}{m \cdot s}, \tag{4.35}$$

which yields:

conductivity $K\left[\frac{m}{s}\right] = 1.078 \cdot 10^7 \cdot k\,[m^2] = 1.064 \cdot 10^{-5} \cdot k\,[Darcy]$,

conductivity $K\left[\frac{m}{d}\right] = 0.931 \cdot 10^{12} \cdot k\,[m^2] = 0.919 \cdot k\,[Darcy]$,

permeability $k\,[Darcy] = 0.940 \cdot 10^5 \cdot K\left[\frac{m}{s}\right] = 1.088 \cdot K\left[\frac{m}{d}\right]$.

The permeability k (in Darcy) is based on the porosity ϕ defined in Equation 4.26 and the matrix neutron cross-section Σ_M defined in Equation 4.44. For the calculation three additional parameters are required (C_1, C_2 and ϕ_0) as compiled in Table 4.4.

$$k = C_1 \frac{\phi_{eff}^3}{(1-\phi_{eff})^2} \cdot e^{-C_2 \Sigma_M}, \tag{4.36}$$

where $\phi_{eff} = \phi - \phi_0$.

Table 4.4: List of parameters required for the permeability k.

Symbol	Name	Value	Unit
C_1	PAR_PERM_C1	75	Darcy
C_2	PAR_PERM_C2	0.001	1/c.u.
ϕ_0	PAR_PHI0	0	-

The latter parameter ϕ_0 may be considered as a kind of immobile/stagnant water representing closed or dead-end porosity. The estimator ϕ is tuned such that it represents the effective porosity (mobile water).

Neutron Absorption Bulk Cross-Section

The relation between the neutron decline time τ and the thermal-neutron absorption cross-section Σ of the formation traversed by the thermal neutrons is deduced. The number of neutrons after traveling a path-length x through a medium is given by:

$$N(x) = N_0 \cdot e^{-\frac{x}{L}} = N_0 \cdot e^{-x \cdot \Sigma}. \tag{4.37}$$

The relation between the path-length x travelled by the thermal neutron and the time t needed for travelling is given by:

$$x = t \cdot v, \tag{4.38}$$

with the velocity of the thermal neutrons, v. Inserting this relation into the previous equation results in:

$$N(x) = N_0 \cdot e^{-t \cdot v \cdot \Sigma} = N_0 \cdot e^{-\frac{t}{\tau}}, \tag{4.39}$$

where the thermal neutron decline time τ was defined in the second step of the equation, i.e.:

$$\tau = \frac{1}{v \cdot \Sigma}. \tag{4.40}$$

The average velocity of the thermal neutrons, v, is given by the temperature T, the Boltzmann constant k, and the neutron mass m,

$$\frac{1}{2} m v^2 = kT \qquad \Longrightarrow \qquad v = \sqrt{\frac{2kT}{m}} = 2\,199\ m \cdot s^{-1}, \tag{4.41}$$

where:

$$\begin{aligned} k &= 1.380\,648\,8 \cdot 10^{-23}\ J \cdot K^{-1}, \\ m &= 1.674\,927 \cdot 10^{-27}\ kg, \\ T &= 20°C = 293.15\ K. \end{aligned} \tag{4.42}$$

This is used to transform Equation 4.40 into the relation defining the estimator for the bulk cross-section Σ_B:

$$\Sigma_B = \frac{k}{\tau_2} - \Sigma_0, \tag{4.43}$$

where Σ_B is given in capture units c.u. (with 1 c.u. = 10^{-3} cm^{-1}), the base quantity τ is given in µs and provided by the far detector (see chapter 4.4.1), k and Σ_0 are defined in Table 4.5.

Neutron Absorption Matrix Cross-Section

The value of the deduced matrix cross-section Σ_M is given in c.u. by:

$$\Sigma_M = \frac{\Sigma_B - (\phi + \phi_0) \cdot \Sigma_{fl}}{1 - (\phi + \phi_0)}, \tag{4.44}$$

with the quantities

ϕ = estimator of porosity as defined in Equation 4.26,

Σ_B = estimator of bulk cross-section as defined in Equation 4.43,

and the mLOG parameters defined in Table 4.4 and Table 4.5.

Table 4.5: List of parameters required for the neutron absorption cross-sections Σ_B and Σ_M.

Symbol	Name	Value	Unit
k	PAR_SIGMAB_K	4550	c.u./µs
Σ_B	PAR_SIGMAB_OFFSET	5.0	c.u.
Σ_{fl}	PAR_SIGMA_F	22.2	c.u.

4.5 Elemental Logging

As stated in chapter 4.4, the formation matrix has a large influence on the accuracy and detection limits of elemental logging. For instance, doubling the abundance of element X in the formation does neither result in doubling the size of the element-X-specific γ-ray spectrum nor the partial γ-ray spectrum from element X. Due to this matrix dependency the measured signal of the γ spectrometer changes as a function of:

- n_i – atom-number density of element X_i in the formation (in units of $1/cm^3$), and
- Σ_B – macroscopic neutron-absorption cross-section (in c.u.)

The element-X-specific, spectroscopic signal measured by OreLog is always a signal resulting from the entire formation-matrix. Obtaining the measured spectroscopic signal-yield of element X alone does not imply the translation of this measured spectroscopic signal-yield of element X into an element-abundance of X in formation. The macroscopic neutron-absorption cross-section Σ_B is needed for the translation of

measured spectroscopic signal-yield of element X into an element-abundance of X in formation.

4.5.1 Derivation of Elemental Abundance Estimator

The number $N_{\mathrm{Cap}\,i}$ of neutron-capture reactions by element X_i is given by:

$$N_{\mathrm{Cap}\,i} = \varphi^{\mathrm{n}} \sigma_i N_i, \tag{4.45}$$

or, emphasizing the local nature of the equation, by:

$$\frac{N_{\mathrm{Cap}\,i}}{\Delta V} = \varphi^{\mathrm{n}} \sigma_i \frac{N_i}{\Delta V}, \tag{4.46}$$

$$n_{\mathrm{Cap}\,i} = \varphi^{\mathrm{n}} \sigma_i \; n_i, \tag{4.47}$$

with φ^{n} being the neutron flux (in units of neutrons per cm^2), σ_i being the microscopic neutron capture cross-section (in units cm^2), N_i being the number nuclei of element X_i in volume-element ΔV. Taking the sum over all elements in the formation results in:

$$\sum_j n_{\mathrm{Cap}\,j} = \sum_j \varphi^{\mathrm{n}} \sigma_j \; n_j. \tag{4.48}$$

Division of Equation 4.47 by Equation 4.48 results in:

$$\frac{n_{\mathrm{Cap}\,i}}{\sum_j n_{\mathrm{Cap}\,j}} = \frac{\sigma_i \; n_i}{\sum_j \sigma_j \; n_j}. \tag{4.49}$$

Here, the denominator of left-hand-side is approximately a constant number. It is the number of all neutron-captures in the formation. Under ideal conditions (i.e. zero-tool-diameter and zero-borehole-diameter) this would be equal to the number of all neutrons emitted by the NG within a certain time window, for instance 10^8 neutrons/s. Practically, this is the number of all neutrons emitted by the neutron generator into the formation solid-angle (non-water-column- and non-tool solid-angle). At the right-hand-side of Equation 4.49 the denominator is nothing else but the macroscopic neutron-absorption cross-section Σ_{B}, i.e.:

$$\sum B = \sum j \, \sigma_j n_i. \tag{4.50}$$

With these interpretations of denominators in Equation 4.49 it can be converted as follows:

$$n_{\mathrm{Cap}\,i} \quad \propto \quad \sigma_i \; n_i \; \frac{1}{\Sigma_{\mathrm{B}}}. \tag{4.51}$$

This means the number of neutron captures of element X_i in formation is proportional to the product of the microscopic absorption cross-section of element X_i, the number density of element X_i, and the reciprocal of the neutron-absorption bulk-cross-section

Σ_B. High accuracy in the Σ_B measurement is required and needs to be monitored carefully. The current quality of the Σ_B estimation is presented in chapter 4.4.2. Making the reasonable assumption that $N_{\gamma i}$, the number of capture γ-rays from element X_i, is proportional to $n_{\mathrm{Cap}\ i}$ the following equation is obtained:

$$N_{\gamma i} \;=\; C_0 \;\sigma_i \, n_i \;\frac{1}{\Sigma_B}, \tag{4.52}$$

with C_0 being some constant proportionality-factor. Just by rearranging this equation, a preliminary estimator for the abundance of element X_i in the formation is obtained:

$$n_i \;=\; \frac{1}{C_0} N_{\gamma i} \;\; \Sigma_B \;\; \frac{1}{\sigma_i}. \tag{4.53}$$

The periodic changes and source depletion (operational hours > 100 h) of the neutron generator source-strength is monitored by the source strength detector as described in chapter 3.4.2. Thus, the mere task of the source strength detector is to accurately measure the source strength signal $S_{src14MeV}$ by measuring the pure production rate of neutrons with an energy of 14 MeV. This indispensable correction turns Equation 4.54 in the following elemental abundance estimator:

$$n_i \;=\; \frac{1}{C_0} \frac{S^{(\mathrm{nom})}_{\mathrm{src14MeV}}}{S_{\mathrm{src14MeV}}} N_{\gamma i} \;\; \Sigma_B \;\; \frac{1}{\sigma_i}, \tag{4.54}$$

with superscript (nom) indicating some nominal source-strength (i.e. 10^8 neutrons/s). Equation 4.54 nicely illustrates the matrix-dependency as follows. At constant atom-number-density n_i: The higher Σ_B the lower is $N_{\gamma i}$. Measuring extremely rare number $N_{\gamma i}$ does not necessarily mean that there is a very small number of X_i-type nuclei – if Σ_B is very large there can still be a high number of X_i-type nuclei.

The term $N_{\gamma i}$ in Equation 4.54 denotes the number of capture γ-rays from element X_i as totally produced, i.e. not detected. But only a fraction of it is measured by the γ-ray detector of OreLog. Assuming that $N_{\gamma i}^{(\mathrm{meas})}$ is the number of element-X_i-specific γ-rays determined from OreLog γ-ray spectrum (determined by spectrum deconvolution). This turns Equation 4.54 into:

$$n_i \;=\; \frac{1}{C_1} \frac{S^{(\mathrm{nom})}_{\mathrm{src14MeV}}}{S_{\mathrm{src14MeV}}} N^{(\mathrm{meas})}_{\gamma i} \;\; \Sigma_B \;\; \frac{1}{\sigma_i}, \tag{4.55}$$

with C_1 being some alternative proportional factor to C_0. The approximate value of C_1 would be:

$$C_1 \;=\; C_0 \;\; \frac{N^{(\mathrm{meas})}_{\gamma i}}{N_{\gamma i}}. \tag{4.56}$$

Equation 4.55 can be transferred from an atom-number-density expression ($n_i = \rho_i^{(a)}$) to a mass-density expression (ρ_i) by multiplication with the molar mass M_i of element i:

$$\rho_i \;=\; \rho_i^{(a)}\, M_i \;=\; M_i\, \frac{1}{C_1} N_{\gamma i}^{(meas)} \;\; \Sigma_B \;\; \frac{1}{\sigma_i}. \tag{4.57}$$

The outstanding achievement of this elemental abundance estimator as expressed in Equation 4.55 is the direct combination of observables from neutron-channels and from γ-ray spectral data in one single formula. Hence, both γ- and neutron-spectroscopy are considered to characterize the formation.

4.5.2 Elemental Logging Principle

This section briefly describes the processing of γ-ray pulse-height-distributions finally resulting in element mass fractions of logged borehole sections.

Energy Calibration

The first step is the energy calibration. Pulse-heights of γ-ray signals are assigned to γ-ray energies. As a result, pulse height distributions are transferred into energy-distributions. This is achieved by aligning the 2048-channel energy spectra with respect to energy by measuring the locations of known and prominent energy peaks (cf. Figure 6.16).

Capture Spectrum and Depth-Binning

A total capture-spectrum is created from Spec1 and Spec2 of raw data. Depending on desired depth bin-widths, all capture-spectra of one depth-bin are summed up to one total capture-spectrum of the depth-bin.

Model Function describing Capture Spectrum

The capture-spectrum of each depth-bin is then analyzed depth-bin by depth-bin. Therefore the measured capture-spectrum is described by a model-function $f_{\mathrm{Model,tot}} = f_{\mathrm{Model,tot}}(E_\gamma|\vec{s})$ where E_γ is the γ-ray energy and $\vec{s}$ is a vector of element-specific weighting-factors, i.e. $\vec{s} = (s_{\mathrm{H}}, s_{\mathrm{Fe}}, s_{\mathrm{Al}}, s_{\mathrm{Si}}, s_{\mathrm{Tool}}, s_{\mathrm{Ca}}, s_{\mathrm{K}}, s_{\mathrm{Mg}}, s_{\mathrm{Mn}}, s_{\mathrm{Ti}}, s_{\mathrm{Cl}})$. Generally, the model function is a linear combination of element-specific energy-distributions $f_{\mathrm{Model},X}(E_\gamma)$ with X being some element, i.e.:

$$f_{\mathrm{Model,tot}}(E_\gamma|\vec{s}) = \sum_{X=H,Fe,Al,\ldots} s_X \cdot f_{\mathrm{Model},X}(E_\gamma). \tag{4.58}$$

The corresponding functions $f_{\mathrm{Model},X}$ have been created mainly from MCNP simulations. They are commonly called element-specific templates or elemental standards.

Chi-square Fit

The actual analysis of the capture-spectrum by the model-function is performed by minimization of a χ^2 function describing the distance between capture-spectrum and model-function. As a result, optimized values of the weighting-factors called $\vec{s}^{\,\mathrm{opt}} = (s_{\mathrm{H}}^{\mathrm{opt}}, s_{\mathrm{Fe}}^{\mathrm{opt}}, s_{\mathrm{Si}}^{\mathrm{opt}}, \cdots)$ are obtained.

Combination of Neutron Data with Gamma Data

In a next step, weighting-factors $\vec{s}^{\,\mathrm{opt}}$ are combined with data from neutron-channels (see chapter 4.4.2) and subsequently multiplied by some element-specific calibration factor C_X specific to element X (with $X =$ Fe, Si, ...) resulting in element-specific mass fraction k_X measured by OreLog.

Energy Range of Fit

This is the energy range used in model-to-measurement comparisons during adaption of $f_{\mathrm{Model,tot}}$ parameters. In case of fully realistic modelling of element-specific energy distributions there would just be one fit-range, more precisely the full energy range from 0 to about 10 MeV. However, some of the fit-results reach a significantly better agreement to laboratory data if the fit-range is adapted, more precisely spoken, if the energy fit-range is adapted to the range with the most significant patterns. For instance, calcium exhibits the most significant patterns of $f_{\mathrm{Model},Ca}$ in the energy-range of about 1.5 to 3.0 MeV. Therefore, the preliminary processing algorithm relies on the following fit-ranges for extraction of element-specific template-scalers $\vec{s}$:

- Fit-range FR1: 0.5 to 9.0 MeV for elements: Fe, Al, K, H,
- Fit-range FR2: 1.6 to 9.0 MeV for elements: Mn, Mg, Ti, Cl,
- Fit-range FR3: 1.6 to 3.0 MeV for element: Ca,
- Fit-range FR4: 2.4 to 5.5 MeV for element: Si.

5 Data Acquisition

The OreLog tool was developed, engineered, manufactured and tested at UIT in Dresden. Therefore, basic functionality testing and initial data acquisition was realized in-house. A so called 'Strahlenschutzgenehmigung' (operation license for radioactive tools) from the local radiation protection authority (in Saxony: Landesamt für Umwelt, Landwirtschaft und Geologie) is required to use the tool. The operation of the neutron generator and hence borehole logging is currently only licensed for the premises of UIT (borehole and neutron laboratory), pre-approved boreholes within the State of Saxony and boreholes within Australia. For the purpose of this work the licensed regions guarantee enough variability for data acquisition and tool testing. This chapter presents the locations and the site-specific conditions, as far as relevant, where and how OreLog was tested and what data was acquired.

5.1 UIT Neutron Laboratory and Borehole

The first location for tool testing is obviously where it was assembled: in UIT's neutron laboratory as shown in Figure 5.1. Data was acquired within the water tank to demonstrate general tool functionality and to record spectra for detector evaluation. Detectors were also tested with deactivated NG by placing various sources next to the tool. This allows the exact quantification of element specific peaks and hence a detailed evaluation of the overall detector performance.

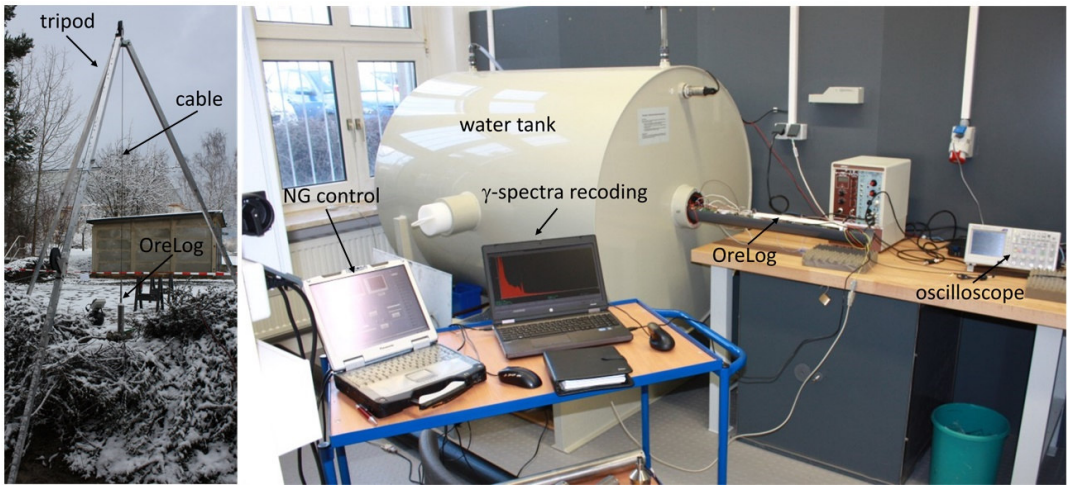

Figure 5.1: UIT borehole for testing purposes on the left and the neutron laboratory for tool development and safe NG operation within the water tank on the right.

5.1.1 Detector Performance

For ideal detector operation parameters such as HV, trigger threshold, and others have to be adjusted accordingly to the expected OreLog output. Therefore, the following sources (cf. Figure 5.3 and Figure 5.4) were used for calibration and evaluation of detector performance:

- ^{60}Co with 3 peaks,
- ^{137}Cs with 1 peak (662 keV as shown in Figure 5.2),
- ^{22}Na with 2 peaks,
- ^{214}Bi and ^{214}Pb (uranium ore hand specimen) with 9 peaks,
- NG.

The isotopic sources and the NG were placed at different locations and distances during detector performance tests in various experimental set-ups (Figure 5.4). Once the ideal position of the detectors within the OreLog tool was defined the following laboratory tests and tasks were performed: detector calibration (by comparing with expected spectra and resolution as exemplarily shown in Figure 5.2), optimization of resolution, repeatability of detector response, environmental influences, and γ-detector linearity checks.

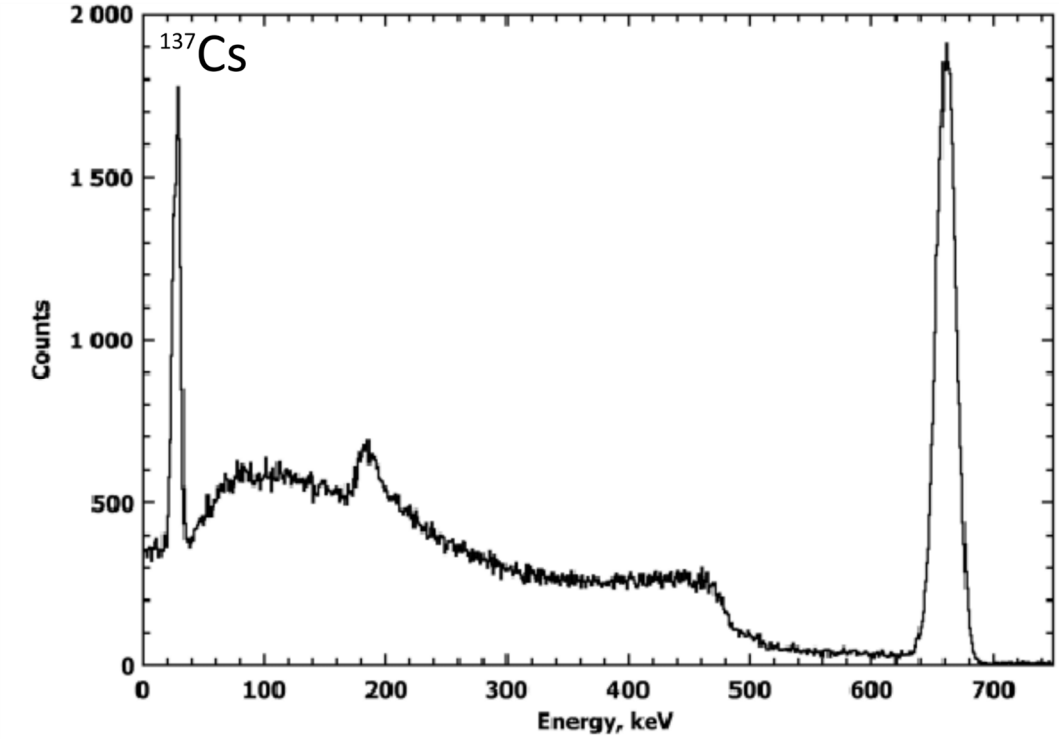

Figure 5.2: γ-ray spectrum of isotopic source ^{137}Cs for calibration purposes as recorded by a $LaBr_3(Ce)$ scintillator crystal (Smirnova et al., 2016).

5.1.2 Temperature Dependency

Besides the linearity of the γ-detector, the temperature stability of the scintillator crystal of the γ-detector unit is of utmost importance for reliable measurements exposed to high-temperature geological environments. Neutron detector temperature impact is considered being neglectable and therefore an experimental setup was realized as illustrated in Figure 5.3 to record γ-ray spectra at different temperatures. Most of the γ-detector unit (PMT, scintillator crystal, lead shield, HVPS) was wrapped by a water-filled hose. The partial γ-detector unit was put into an insulation vessel (thermobox) guaranteeing stable temperature conditions while water was circulated through the hose at variable temperature. An online temperature-sensor was attached directly between hose and γ-detector. In addition, everything needed to record γ-ray spectra has been put into the setup (preamplifier, MCA, control PC, power-supply). A γ-source (Cs-137, Co-60, U-ore) was put directly next to the γ-detector. The temperature was increased stepwise from ambient temperature to 60 °C and energy spectra were recorded with one minute record-time each spectrum.

For evaluation of long-term temperature stability, the high temperature (60 °C) setup was conducted continuously overnight for approximately 18 hours under constant conditions.

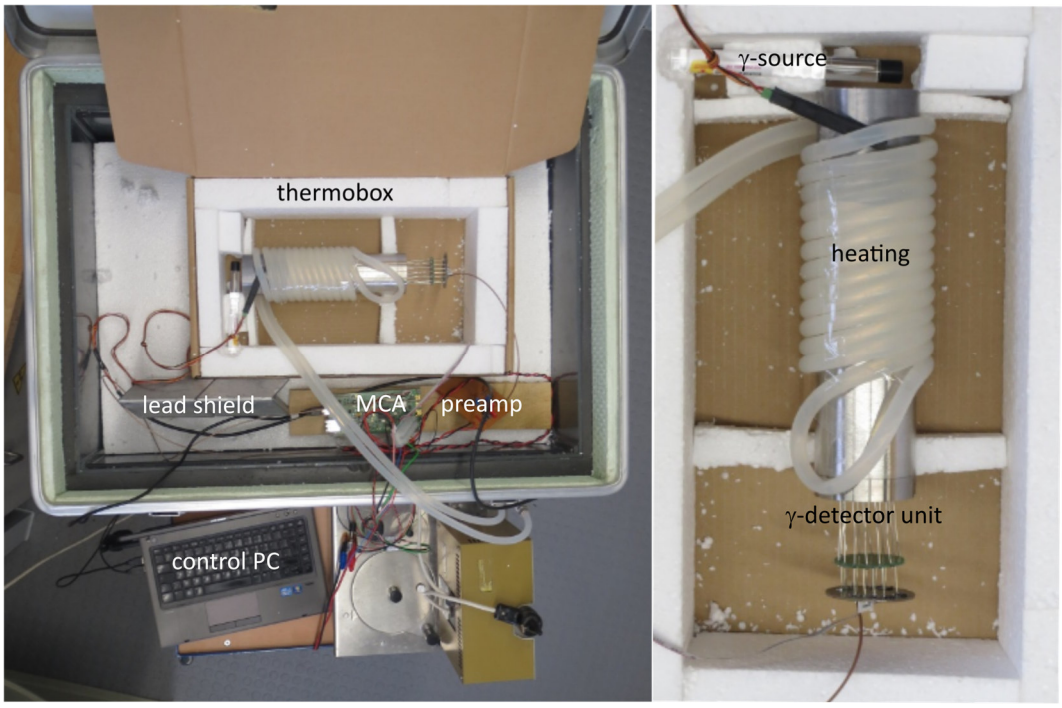

Figure 5.3: Experimental setup for recording γ-spectra at different temperatures.

5.1.3 Elemental Logging

Elemental logging capability with active NG was initially laboratory-tested by inserting various elements besides the tool into the water tank opening. An identical experimental setup was prepared for testing of each element as exemplarily shown for MgO in Figure 5.4. In all setups the test material surrounding the OreLog tool was inserted in a concentric cylindrical manner. By doing so the entire space between the tool and the water tank was filled with the corresponding material. This results in the following structure in radial direction from tool center to periphery (cf. Figure 5.4): $r \leq 35$ mm: OreLog tool without pressure housing, $35 < r \leq 55$ mm: layer of test material, $r > 55$ mm: cylindrical water tank filled with water. Element-specific spectra were recorded for the following elements by inserting the respective material:

- Fe by a stainless-steel tube,
- C by a polyethylene (PE) tube,
- Cl by a polyvinyl chloride (PVC) tube,
- Ca by gypsum powder ($CaSO_4$),
- Mg by magnesium oxide powder (MgO),
- Si by quartz sand (SiO_2).

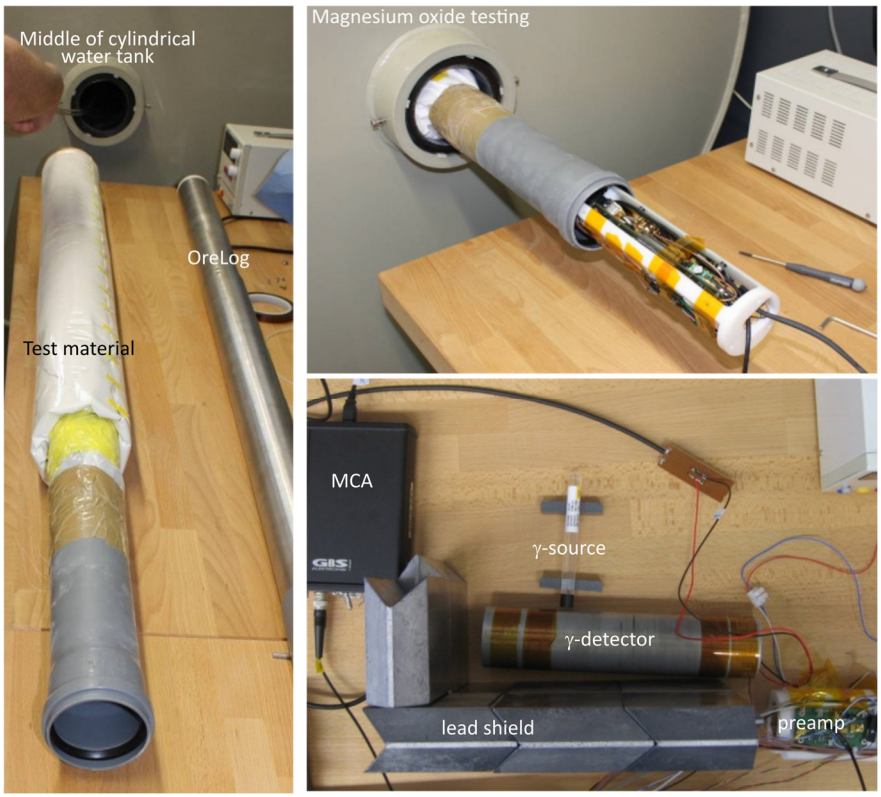

Figure 5.4: Experimental setup for both detector performance testing/calibration and generation of element-specific active-generator spectra by fully surrounding the tool with test material in the water tank.

5.2 Four Mile Deposits nearby the Beverley Mine in South Australia

Various boreholes of several Four Mile prospects surrounding the active ISR uranium mine Beverley were logged in 2019. Heathgate Resources Pty Ltd operates the Beverley Uranium Mine on a Fly-in Fly-out (FIFO) basis due to its remote location 550 km north of Adelaide, South Australia, on the plains between the northern Flinders Ranges and Lake Frome. It has operated since 2000 under close environmental scrutiny (Jeuken et al., 2007). Since the discovery and mining of the original Beverley uranium resources (Curtis et al., 1990), additional uranium deposits have been found in the area and mining is extending over a larger area. Uranium deposits are discovered in the Tertiary Namba Formation (Curtis et al., 1990), the Tertiary Eyre Formation, and Cretaceous sediments (Stoian, 2010). Objective of the logging program was the validation of the elemental logging algorithm and deposit characterization in typical sedimentary uranium deposits as well as demonstration of tool performance. The mere determination of the uranium grade by fission neutrons was not part of the scope since this is already a well-established method by conventional PFN tools since the 70ies and is conducted routinely by uranium mining companies.

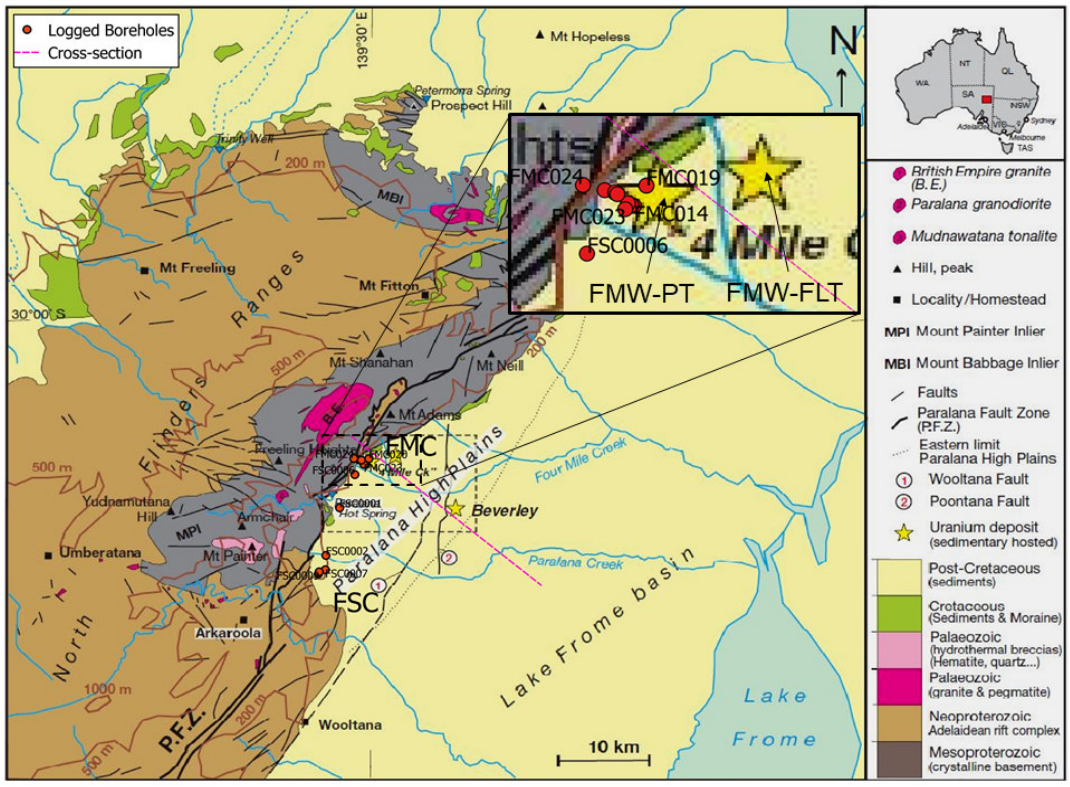

Figure 5.5: Regional setting of the Beverley mine and surrounding Four Mile deposits (FMC and FSC). The logged boreholes are indicated in red as listed in Table 5.3. The cross-section is shown in Figure 5.6. The yellow stars in the zoom-in represent the pump test area as indicated in Table 6.2. After Wülser et al. (2011).

5.2.1 Geology of Sedimentary-hosted Uranium Deposits

Approximate ages for the mineralization events in the Frome Basin can be obtained from *U-Pb* dating of *U*-minerals, such as: coffinite and carnotite, which yield 6.7 to 3.4 Ma for the time of *U*-mineralization in the Beverley deposits (Wülser et al., 2011). The *U*-source is inferred to be the Northern Flinders Ranges Proterozoic basement (MPD; >100 ppm *U* in metasomatic halos), related Miocene formations and alluvial fans of the Willaworina Fm. (Wülser et al., 2011; Penney, 2012). Three periods of regional uplift with associated weathering events and three possible episodes of *U*-mineralization since Late Mesozoic are considered as the driving mechanisms of the *U*-mineralization in this zone (Skirrow, 2009). These deposits are hosted in shallow (< 500 m depth) variably consolidated sediments. Among the many types of *U*-deposits, sandstone-hosted deposits are the most widespread worldwide (Abzalov, 2012). They are characterized by low to medium ore-grades and small to medium sizes. They can occur in numerous clusters generally along the same horizons achieving large cumulative tonnages. Most of the deposits found in the Lake Frome region belong to roll-front and tabular categories, including further sub-divisions based on morphology. Some of these deposits show recycling and/or hybrid features (Skirrow, 2009). Their classification and ore-forming models are explained in detail in Dahlkamp (2010), Lehmann (2008), Robb (2020), Skirrow (2009), and references therein.

Tabular Type Deposits

Tabular deposits are epigenetic and consist of uranium matrix impregnations that form irregularly shaped lenticular masses controlled by lithology within selectively reduced sediments. The mineralized zones are largely oriented parallel to the depositional trend (cf. Figure 5.6), but on a small scale they crosscut sedimentary features of the host fluvial sandstone. These deposits are best developed in cross stratified, medium- to coarse-grained (arkosic) sandstones. The depositional environment of the host rock are mainly fluviatile comprising stream channels, flood plains, fluvial coalesced alluvial fans or deltaic/lagoonal environments (Dahlkamp, 2010). The tabular deposit type is characterized by its significant pyrite content and is further subdivided into classes based on uranium fixing agents occurring in fluvial systems. These are either amorphous organic material of extrinsic origin (e.g. humate) or detrital plant debris of intrinsic origin or metallic associations (e.g. vanadium), which can be determined and correlated by petrophysical core analysis (Zauner et al., 2020). The dominant ore minerals occurring in the reduced zone are pitchblende and coffinite, to some extent

associated with vanadium oxide minerals. Within the oxidized zone the important U-minerals are carnotite, tyuyamunite or francevillite, all of which are uranyl vanadates. Accessory elements are Mo, Se, Cu and others. This type of uranium deposit is found mainly in the Tertiary, Jurassic, Triassic, and Carboniferous periods. The main ore districts are the Grants Mineral Belt (USA), the Agades Region in Niger, the sub-Andean zone of Argentina and the Lake Frome embayment in South Australia. In plan the ore bodies show amoeba-shaped to lenticular oblong contours. The lateral extension is several tens to several thousand meters. Thicknesses vary between 1 and 5 m and can be up to a maximum of 15 m. Individual deposits can contain up to 150,000 t of U at average grades ranging from 0.05 to 0.5 %, occasionally up to 1 % (Dahlkamp, 2010).

Roll-front Type Deposits

The lithology and provenance of the host rock for roll-front type deposits is very similar to those of tabular deposits. The ore bodies are epigenetic U matrix impregnations and are controlled by lithology and chemohydrology. It is called 'roll-type' or 'roll-front', because of its specific arch like shape (roll) which crosscuts the sedimentary bedding (Figure 5.6). U-mineralization follows the contact between oxidized and reduced sandstone. This boundary is regarded as the furthest downdip or outer penetration front of oxidizing groundwater (Dahlkamp, 2010). According to Skirrow (2009) ore deposits and associated altered rock probably were formed by the action of ore-bearing solutions that contained oxygen and U and percolated through the permeable layers of the host rocks, while reacting with the pyrite and organic carbon compounds. The minerals of such a C-shaped ore zone were continually oxidized and dissolved along the edge of the deposit and redeposited a short distance downstream. The oxidation front and the entire deposit must migrate much more slowly than the ore-bearing solution (Skirrow, 2009). A further characteristic is the interbedding of this mineralized permeable layer in semi- or impermeable horizons (clay-, siltstones etc.). The dip of the strata is generally less than 5° unless post-ore tectonics occurred. The ore bodies transect the stratification of the host rock and are thus discordant with the strata. In cross-section, the form of the ore bodies resembles a crescent (Figure 5.6). The plan view of the deposits is like that of an irregularly laid pipe. Main ore minerals are uraninite and coffinite. In addition, selenium as ferroselite (as native Se in the protore) is enriched on the convex side of the roll-front. Molybdenum (jordisite) and calcite are enriched on the concave side of the roll-front. Moreover, arsenic, phosphorus and copper seem to occur in minor amounts coincidentally with U. Stratigraphically, roll-front type deposits occur primarily in the Tertiary strata, but they also occur in strata of the

Jurassic period. The main districts of these deposits are the intracratonic sedimentary basins of Wyoming, the Texas Gulf Coast, Kazakhstan, and South Australia. The dimensions of the ore fronts in the apex zones are up to 15m (average: few tens of cm to 10 m); the widths between a few centimeters and several hundred meters, while the strike lengths extend up to several kilometers. Resources can range from a few hundred tons to several thousands of tons of U, at grades averaging 0.05 to 0.25 % (Dahlkamp, 2010).

5.2.2 Field Work

HGR holds various exploration and mining leases surrounding the Beverley mine and Four Mile deposit (Figure 5.6). A total of 19 holes were logged during various campaigns in 2019 as indicated in Figure 5.5. Staff was accommodated at the Beverley mine camp and infrastructure and logistics were provided by the mine operator HGR. Since the focus was not on uranium detection, the field work was oriented towards the investigation of holes with sufficient reference data (drill core assays) and intersecting various sedimentary lithologies (cf. Table 5.1) as well as preferably granitic basement. The logged boreholes lie within the western part of the geological Lake Frome Embayment, which in turn is part of the Callabonna Sub-basin of the Eyre Basin (Callen, 1977). The local geology (Table 5.1) is dominated by diamictite and other sedimentary rocks grading from clay- to sandstone with occasional silcrete layers. Only the Proterozoic crystalline basement consists of igneous/metamorphic rocks such as granitoids with occasional quartz veins or quartzite. For detailed lithology and core characterization see appendix A.1.2.

Table 5.1: Overview of regional lithostratigraphy of main formations at the Beverley Mine and adjacent areas in the Frome Basin. Age limits (dashed lines) were drawn approximately. Modified after Wülser et al. (2011).

Epoch	Formation	Depositional environment	Characteristics
Pleistocene	Willawortina	Lacustrine-fluviatile, debris flows	Sandy mud; framework and matrix-supported gravels
Pliocene			
Miocene	Namba	Lacustrine-fluviatile (brackish to fresh water lakes)	Immature, fine to medium-grained poorly sorted sands; clay interbeds (Callaboona Sub-basin)
Oligocene			
Eocene			
Paleocene	Eyre	Fluvial (braided river systems)	Quartz-rich, poorly sorted sands (silt-pebble), locally silcrete-overprinted (silica cemented); kaolinitic interbeds; lignite seams (Lake Eyre Basin)
Upper Cretaceous			
Lower Cretaceous	Bulldog Shale	Shallow marine shelf, cold climate conditions	Dark grey mudstone with fine-grained silt-/sandstone intervals; carbonatic (Eromanga Basin)
	Cadna-Owie	Non-marine - marine; glacial	Feldspathic sand-/siltstones and polymict breccias (Eromanga Basin)

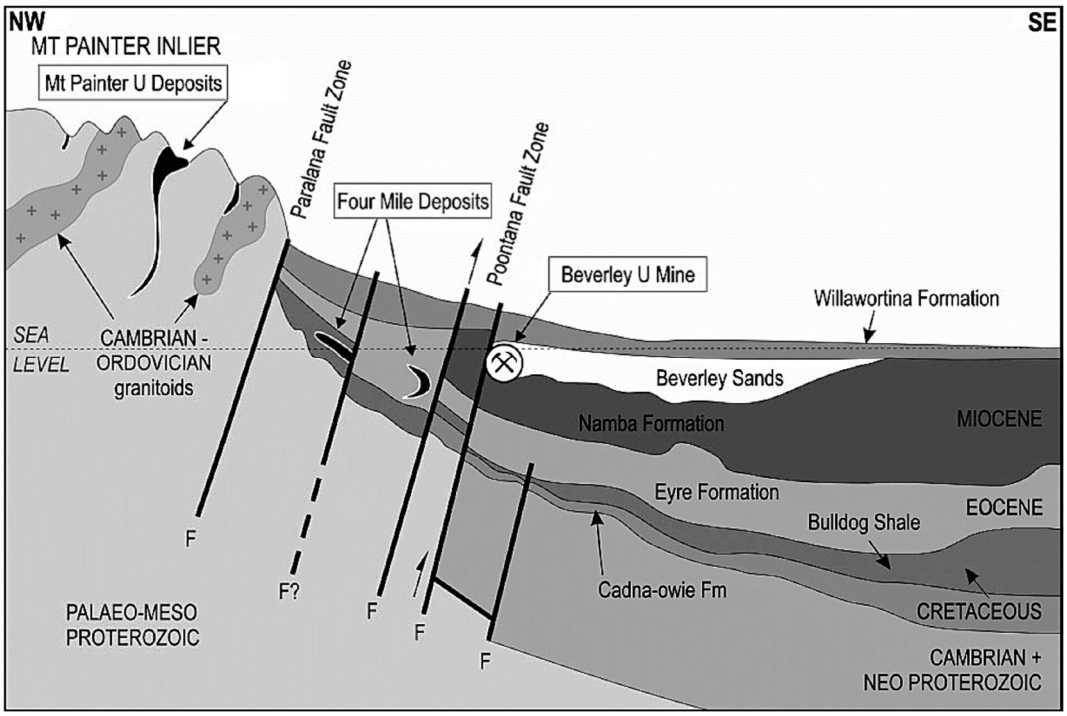

Figure 5.6: Schematic cross-section (purple line in Figure 5.5) of the Northern Flinders Range and Lake Frome Basin through the Four Mile deposits and Beverley uranium mine showing main formations, faults (F) and basin architecture; not to scale. Modified after Penney (2012).

The investigated boreholes at the Four Mile deposits are genetically assigned to the first and second basement uplift period as indicated in Figure 5.7. The age of the various lithologies forming the host rock of the prospective uranium mineralizations varies between 110 and 43 Ma. The Beverley deposit is only included as reference but was not investigated in this work. Both classical roll-fronts and tabular type mineralization occur. Since uranium is not part of the elemental scope of OreLog and can already be quantified accurately by commercial borehole tools like APFN^{+} (Märten et al., 2015), the focus was on the characterization of the uranium host rock and the surrounding formations.

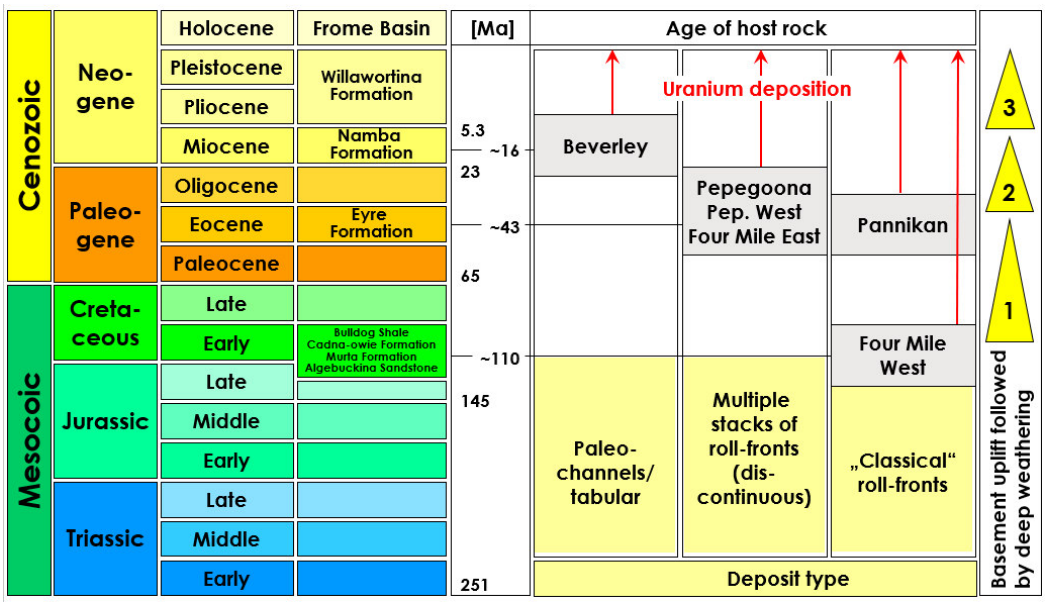

Figure 5.7: Local deposit genesis and dating (compiled after internal documents).

Figure 5.8: Picture of 4 core trays showing dry drill cores of borehole FMC014 from 148.81 to 154.69 m (left) and 157.95 to 165.00 m (right).

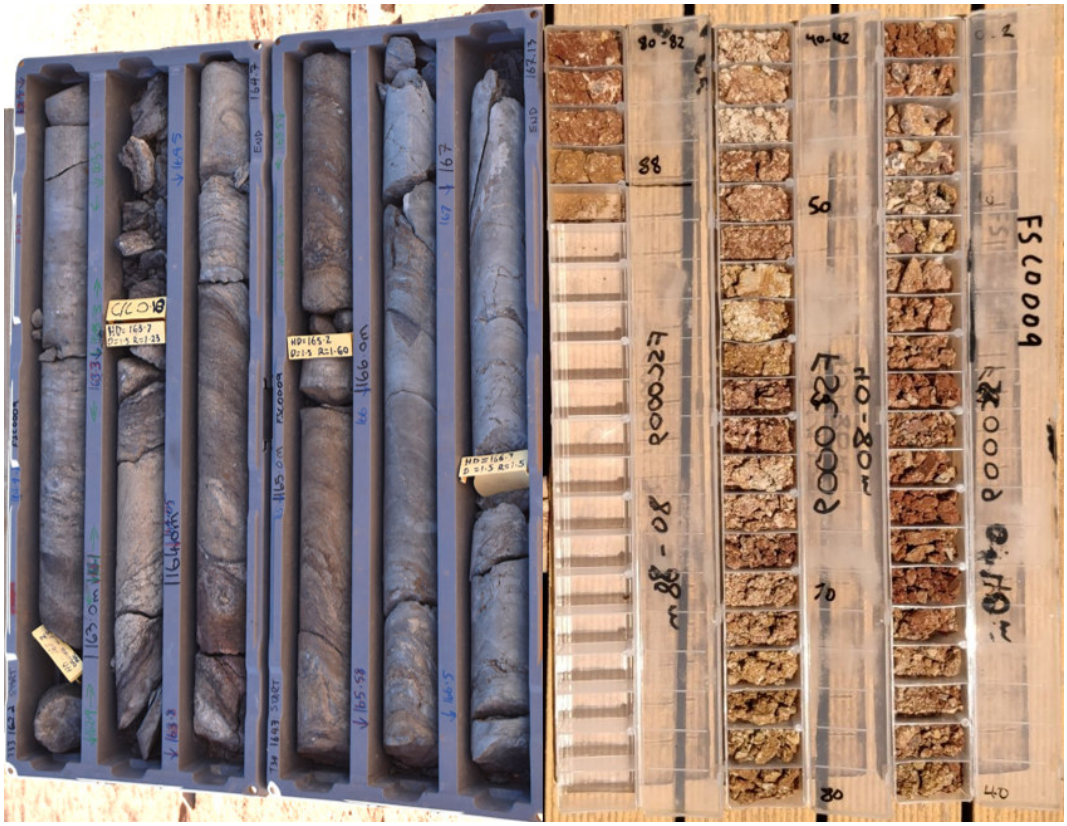

Figure 5.9: FSC0009 full drill core from 162.2 - 167.13 m in core boxes (left) and RC chip samples from 0 – 88 m at 2 m sample intervals in chip trays (right).

For the RC drilled part a sample pile was created for 2 m intervals analogue to sampling procedure in Pilbara as shown in Figure 5.13, which were representatively subsampled and sent in for geochemical assays resulting in a single bulk measurement for the entire interval. Borehole cuttings are also archived in chip trays (Figure 5.9), whereas duplicates and blind samples were submitted for QA/QC purposes. On the other hand, the cored sections were usually sampled at 0.5 m intervals whereas ¼ core[2] was submitted for whole rock geochemical assay. If visual core logging on site (cf. Figure 5.9) revealed interesting petrological features, ½ core of this interval was submitted for detailed petrology. Therefore, a more detailed data base is available for the cored sections. Borehole FMC005 represents an exceptional case since it has been cased as shown in Figure 5.10 and defined as reference hole by HGR for calibration purposes of various geophysical logging tools. The borehole completion was realized with various materials (cf. sketch in Figure 5.10) typical of local well field construction for ISR purposes. Hence, FMC005 is the most dedicatedly investigated borehole with the most complete reference database (samples, geochemical-petrophysical-

[2] ¼ or ½ core refers to core cutting along the longitudinal drilling axis.

mineralogical assays, other geophysical logs). As shown in Figure 5.10 left, the OreLog tool was lowered in FMC005 at regular intervals to monitor for any potential tool parameter drift over time. The characteristics of FMC005 were ideal for this purpose and played a major role in the success of the Four Mile field campaign.

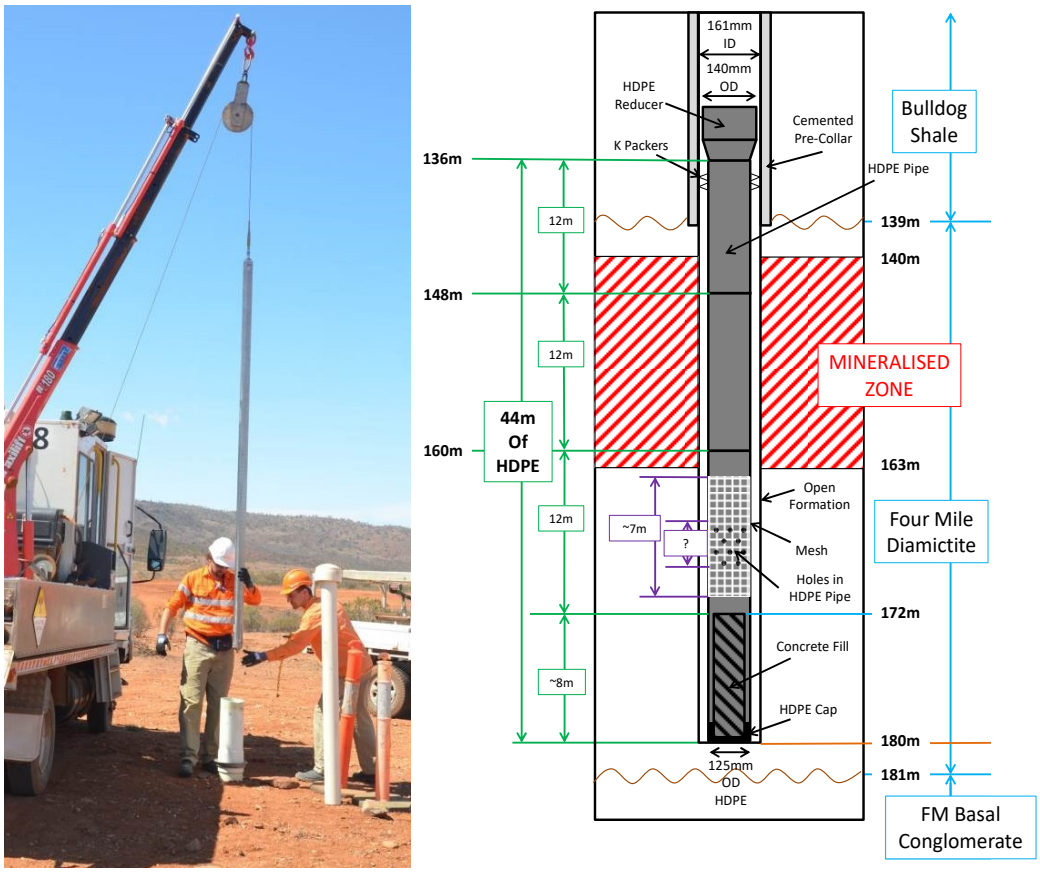

Figure 5.10: Logging at reference borehole FMC005 (left) and schematic draft of the borehole completion including its relevant components. The casing of the borehole's upper part consists of PVC (inner diameter = 161 mm, wall thickness = 8 mm).

Besides the extensive investigation of FMC005, core hole FMC004 was selected for detailed quantification of hydrological parameters. Therefore, the core interval at a depth of 135 to 225 m was investigated in detail with core plugs as compiled in Table 5.2 being sent to external laboratories. In total seven core plugs were analyzed for density, porosity, and permeability.

Table 5.2: Specifications of core samples (FMD = Four Mile Diamictite)

No.	From (m)	To (m)	Formation	Lithology
1	138.8	139.1	Eyre	Sand
2	153.65	153.9	Bulldog	Silt
3	167.95	168.23	FMD	Silty sand
4	177.5	177.8	FMD	Silty sand
5	184.14	184.5	FMD	Silty sand
6	186.1	186.4	FMD	Silty sand
7	193.77	194.06	FMD	Silty gravel

In addition, pump tests were performed at two different sites (FMW-FLT and FMW-PT) by HGR hydrologist in 2009 and 2012 to determine the hydraulic conductivity (Heathgate Resources Pty Ltd, 2013). The results were provided for this work and therefore borehole FMC004 in the direct vicinity of the pump test boreholes WC04, FW0007, 4MT001, 4MT002r, 4MT001 served to evaluate the performance of the hydraulic parameter quantification as introduced in chapter 4.4.2.

5.2.3 Logging Program

The hole diameter averaged 140 mm and the location of the logged holes within the mining lease ML6402 is shown in Figure 5.15. Table 5.4 compiles the relevant information of all logged holes. Except for FMC005 all holes were logged uncased (open hole) directly after drilling. The upper part was usually RC[3] (Reverse Circulation) drilled with chip samples available for assays whereas the interesting intervals were DD[4] (Diamond Drilled) core holes (cf. Figure 5.9).

The minimum quality criteria to include both the OreLog output data and the laboratory assay in the results chapter are defined as follows:

- OreLog: data completeness, consistency, continuous run (no interruption by e.g. tool failure or borehole blockage),
- Laboratory assay: standard deviation, completeness, plausibility.

[3] Reverse circulation drilling is a form of percussion drilling that uses compressed air to flush material cuttings out of the drill hole in a safe and efficient manner.

[4] Exploration diamond drilling (DD) is used in the mining industry to probe the contents of known ore deposits and potential sites by withdrawing a small diameter drill core.

Table 5.3: Coordinates and characteristics of logged holes.

No.	Hole-ID	Drilled Depth [m]	UTM Coordinates (GDA94)	
			Easting	Northing
1	FMC004	224.0	355458.0	6663547.0
2	FMC005	180.0	354711.4	6663618.8
3	FMC011	180.0	355490.8	6663662.1
4	FMD0399	279.0	359841.7	6666961.8
5	FWD0201	180.0	354810.0	6663254.0
6	FMC014	162.3	355159.5	6663305.8
7	FMC015	162.3	355039.6	6663357.6
8	FMC016	164.0	355084.0	6663331.0
9	FMC017	198.5	354666.0	6663660.0
10	FMC018	164.0	354994.5	6663383.7
11	FMC019	180.3	355476.4	6663844.1
12	FMC020	181.2	355491.4	6663844.0
13	FMC021	155.1	354395.2	6663724.0
14	FMC022	159.5	354666.0	6663660.0
15	FMC023	159.0	354935.0	6663228.0
16	FMC024	160.1	353824.1	6663876.6
17	FMC025	193.6	354664.0	6663681.0
18	FSC0001	115.0	352228.0	6658288.0
19	FSC0002	119.0	350696.0	6652904.0
20	FSC0006	160.7	353929.6	6662050.4
21	FSC0007	225.3	350628.0	6651283.0
22	FSC0008	300.4	349855.0	6650817.0
23	FSC0009	240.0	349945.0	6651049.0
24	FWD0001	216.0	355475.0	6663645.0
25	FWD0002	242.0	355419.0	6663590.0
26	FWD0003	202.0	355504.0	6663575.0
27	FWD0004	236.0	355384.0	6663557.0
28	FWD0005	218.0	355415.0	6663498.0

5.3 Pilbara Region in Western Australia

The OreLog tool was tested during a three-week logging program at iron ore deposits located in the Upper Wyloo Group (Figure 5.11) in the Western Pilbara region (Western Australia) from May 8th until May 27th, 2018. Australian Premium Iron (API) provided all necessary infrastructure and logistics. Staff was accommodated at the Cardo exploration camp (Figure 5.15) in the Western Pilbara. Cardo camp is located on Mt Stuart Access Road about 27.5 km north of Nanutarra Road. The camp is accessible by car from Karratha airport in about three hours.

Objective of the logging program was the validation of the elemental logging algorithm and deposit characterization in typical iron ore deposits as well as demonstration of tool performance.

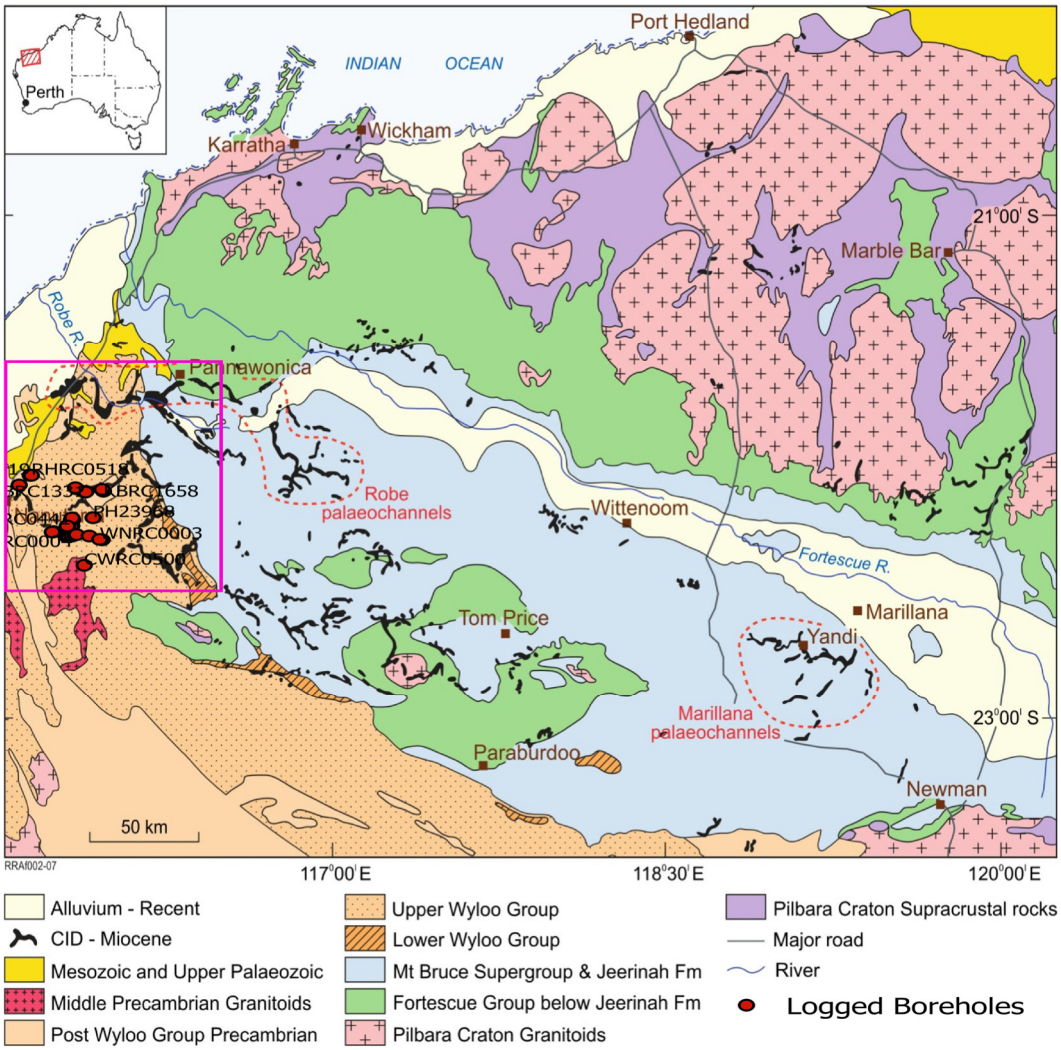

Figure 5.11: Geological map of the Pilbara Craton and its margins showing the distribution of channel iron deposits. The purple rectangle indicates the area of investigation (details in Figure 5.15). Modified after Ramanaidou and Morris (2010).

5.3.1 Geology of Iron Ore Deposits

The West Pilbara Iron Ore Project (WPIOP) mineral resource is predominately comprised of hematitic and goethitic Channel Iron Deposit (CID) mineralization. Deposits occur as partly buried palaeochannels, originating from ancient river systems draining away from the Hamersley Ranges. These ancient river systems were filled with iron rich material which cemented together to form an iron-rich deposit resistant to erosion. Most of the WPIOP deposits are mesaform CID's (Type I; Figure 5.12) shaped due to the weathering and erosion of the surrounding basement rocks therefore exposing the palaeochannel deposits over time. Two of the CID deposits, Buckland Hills and Red Hill Creek, occur in the upper parts of the palaeochannel systems they occupy and are valley constrained deposits (Type II; Figure 5.12). Distance from source, iron material type, ancient river setting and current conditions, including exposure to water, determine the grade of the CID (Morris and Ramanaidou, 2007; Ramanaidou and Morris, 2010).

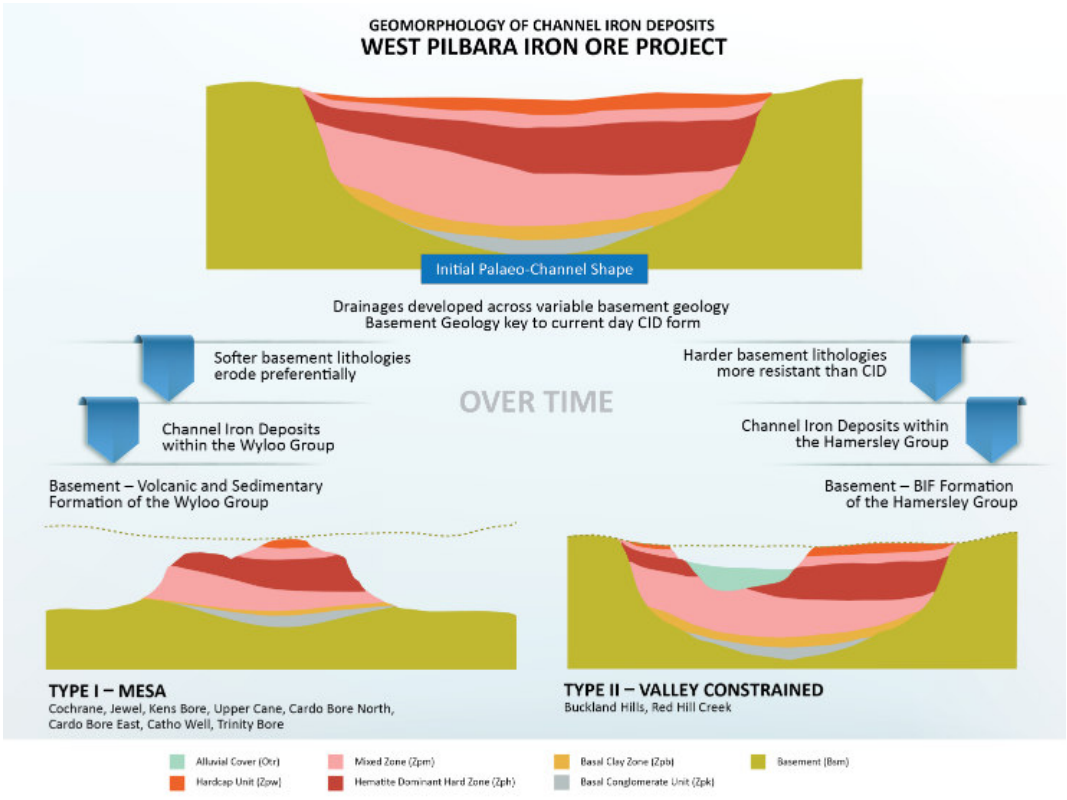

Figure 5.12: Channel Iron Deposit morphology and genesis. Modified after Morris and Ramanaidou (2007).

The Hardey Bedded Iron Deposit (BID) is hosted by the Hamersley Group, which is comprised of banded iron formations (BIF) and sediments. Within the Hamersley Group stratigraphy, the Marra Mamba and Brockman Iron Formations are the two

major units hosting iron ore deposits. Both these formations are comprised of alternating sedimentary layers of BIF, shale and chert. The highest-grade BID has been upgraded by chemical and weathering processes which remove much of the shale and chert. Iron mineralization occurs as a result of multiple phases of supergene enrichment and burial metamorphism (Ramanaidou and Morris, 2010).

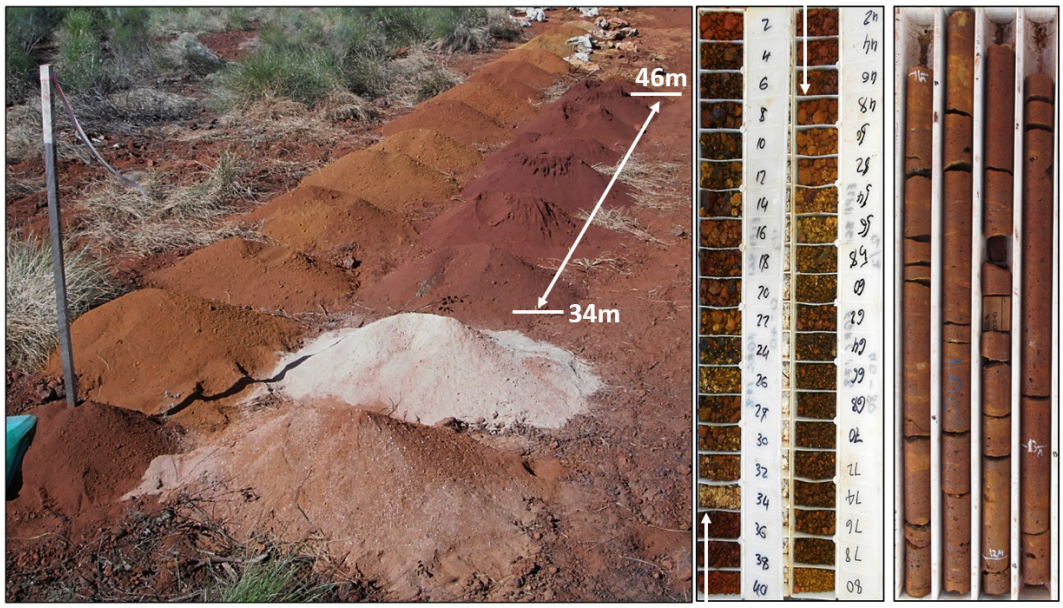

Figure 5.13: Image of typical RC chip sample piles at 2 m intervals (left) with the corresponding archived samples (middle) from a hematite rich zone of hole FQRC0178 and an exemplary drill core from a DD hole (FQDD004) from a goethite rich zone (right).

The CID's are mainly composed of hematite and goethite with Fe grades over 56 wt%. Minor lithologies are chert, clay, shale, dolomite and volcanic rocks. Figure 5.13 presents an overview of RC chip samples and drill cores of CID of the WPIOP. The following mineralization stratigraphy was logged: hardcap, hematite dominant zone, goethite dominant zone, mixed, basal clay zone, clay, lithic, and basal conglomerate. A cross-section of a mesa type CID is shown in Figure 5.14.

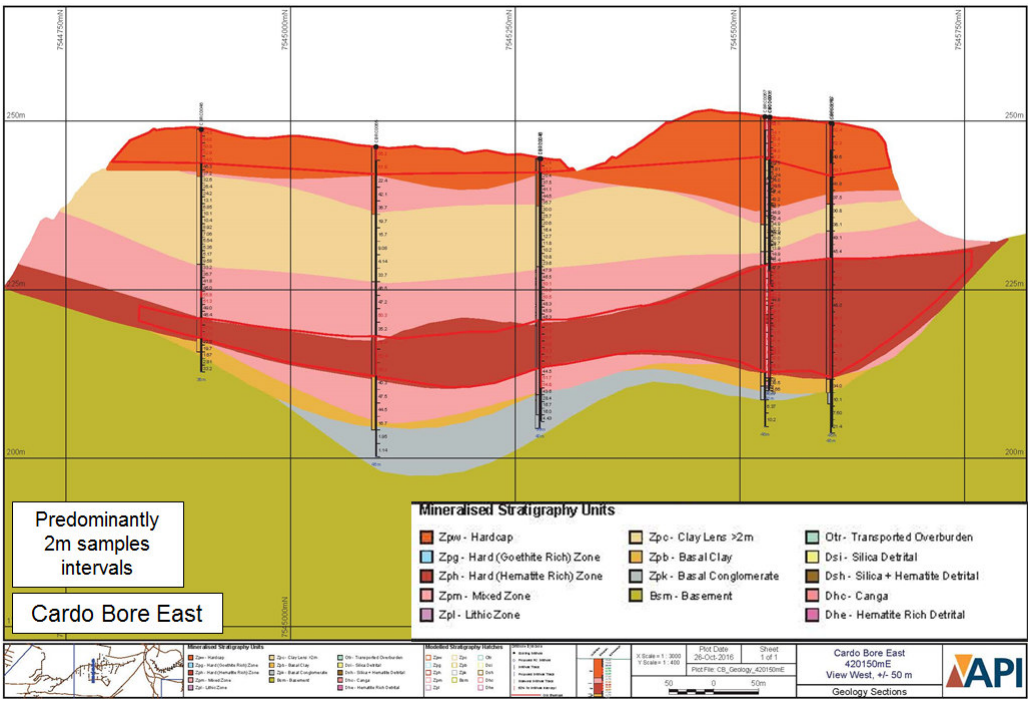

Figure 5.14: Cross-section of drill holes at Cardo Bore East indicating a typical sequence of clay and iron rich layers after API (2016).

5.3.2 Field Work

API holds various exploration leases (cf. Figure 5.15) covering an area of about 8,000 km² in the Western Pilbara. During the field work a 16-day logging program of various channel iron deposits was successfully completed. A total of 46 uncased holes have been logged by OreLog. Both RC and DD holes were logged. The majority of the holes were recently RC drilled and remained open and uncased. Only few historical DD holes have been accessible. The reachable hole depth was usually between 20 and 40 m with a maximum depth of 50 m.

The logged drill holes are mainly in the surroundings of Cardo camp and as demonstrated in Figure 5.15 several locally constrained CID occurrences of a few kilometers' extensions were investigated.

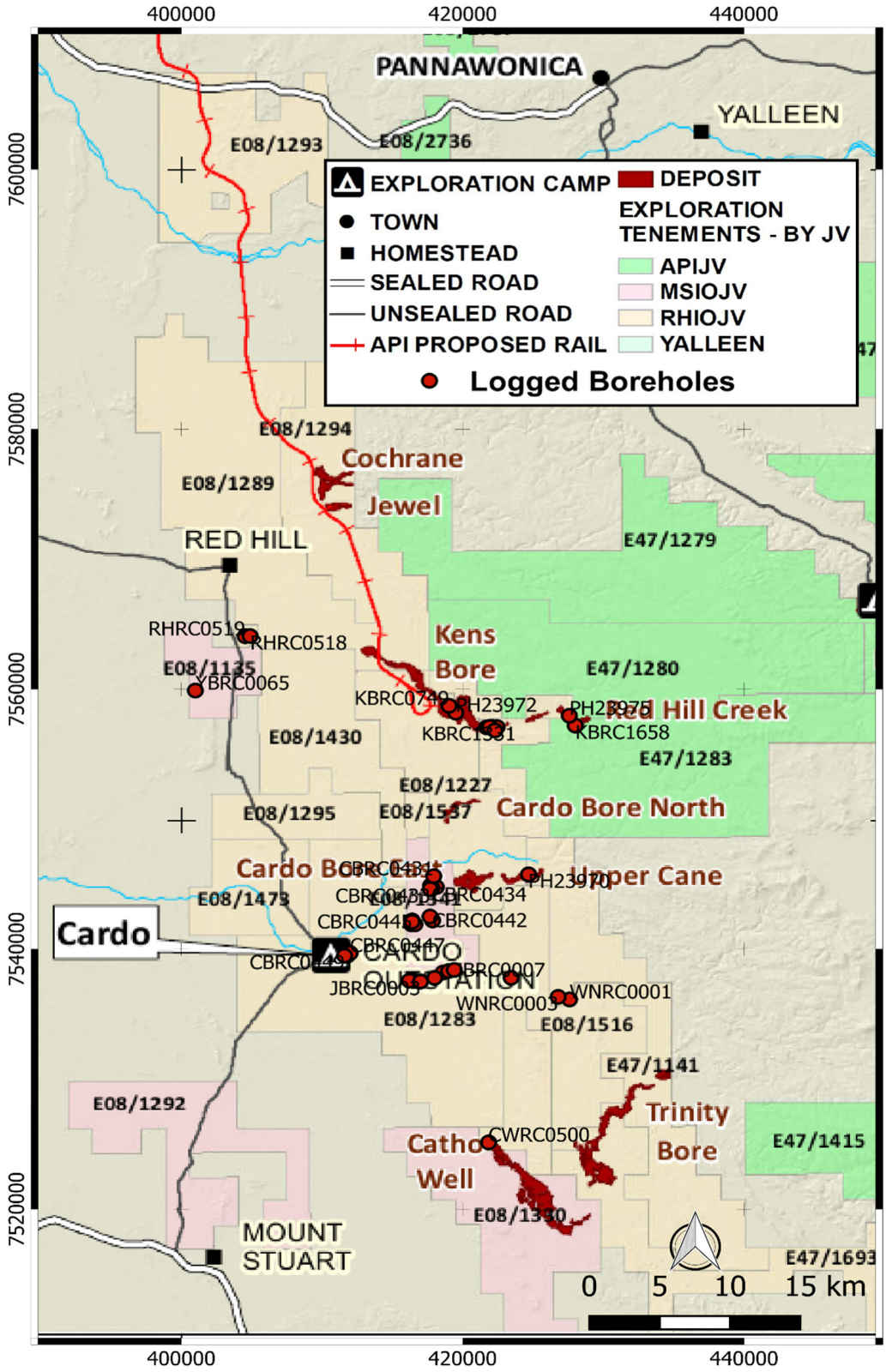

Figure 5.15: Map of investigated tenements, deposits, and infrastructure during the Pilbara logging campaign. See Figure 5.11 for location. Compiled from Golder Associates Pty Ltd (2016) report and personal field notes.

5.3.3 Logging Program

The hole diameter averaged 140 mm and the location of the logged holes is shown in Figure 5.15. Table 5.4 compiles data of all logged holes. More details about the logging program can be found in the appendix.

Table 5.4: Coordinates and characteristics of logged holes. Drilled depth and collar elevation was not provided for all holes.

No.	Hole-ID	Drilled Depth [m]	Collar Elevation [m]	UTM Coordinates (GDA94)	
				Easting	Northing
1	CBRC0448	40.0		411804	7539502
2	CBRC0447	40.0		411994	7539703
3	PH23968			424679	7545728
4	PH23970			424679	7545736
5	KBRC1344			422306	7557080
6	KBRC1331			422116	7557094
7	KBDD0025			422192	7557003
8	KBRC1337			422191	7557003
9	KBRC1310			421707	7557064
10	KBRC1352			422447	7557089
11	CBRC0444	58	243	416405	7542200
12	CBRC0446	58	231	416358	7541899
13	CBRC0443	58	236	416600	7541902
14	CBRC0442	58	241	417856	7542200
15	CBRC0441	40	236	417676	7542500
16	CBRC0449	28.0		411598	7539499
17	CBRC0436	46.0	229	417718	7544878
18	CBRC0435	52	252	418122	7544763
19	CBRC0434	52	247	417802	7544703
20	CBRC0433	46	250	417691	7544609
21	CBRC0431	52	231	417943	7545598
22	KBRC1658	58		428004	7557207
23	KBDD0023			428004	7557207
24	PH23976			427582	7557962
25	PH23975			427582	7557966
26	KBRC1320	58		421914	7557100

27	JBRC0002	40	416600	7537545
28	JBRC0001	40	416200	7537580
29	JBRC0003	40	417000	7537510
30	JBRC0005	40	418600	7538200
31	JBRC0004	40	418000	7537790
32	JBRC0006	40	419000	7538320
33	JBRC0007	40	419400	7538400
34	PH23972		419501	7558198
35	KBRC1347		422295	7556830
36	KBRC0749		419026	7558724
37	PH23969		424679	7545732
38	RHRC0517	40	404097	1564263
39	RHRC0519	40	404533	7564067
40	RHRC0518	40	404889	7564078
41	YBRC0065	40	400997	7559895
42	WNRC0001	40	427596	7536138
43	WPRC17040	48	423441	7537802
44	WNRC0003	40	426787	7536334
45	CBRC0445	58	416409	7542102
46	CWRC0500		421842	7525116

6 Results

6.1 Performance of Neutron Detectors

The performance of the neutron detectors as laboratory-tested and finally tested for full-functionality in the UIT borehole is presented in the following paragraphs since their accurate, reliable, and repeatable operation under changing conditions is an indispensable requirement at first for elemental logging. The relevant signal chain and data processing of both neutron and γ-detectors is shown in Figure 3.7 providing a good introduction and overview of the structure of the following detector results.

6.1.1 Source Strength Detector

The source strength detector as described in chapter 3.4.2 was tested directly at the target plane of the operating neutron generator. There was no cable between the detector and the preamplifier during the tests to minimize potential interference sources. The neutron generator was operated in active pulsed mode at 1 kHz and producing 14 MeV neutrons as specified under chapter 3.3. The neutron bursts are about 100 µs wide and occur every millisecond (1 kHz) as demonstrated by the histogram in Figure 6.1. Hence, also the neutron generator performance and pulsing regime as indicated in Figure 3.6 and Table 3.1 were confirmed. The energy spectrum of the same pulses is shown in Figure 6.2. A qualifier[5] is set to 7 MeV to account exclusively for fast neutrons (energy of interest for source strength) and the energy channels are shown up to 12.5 MeV with a logarithmic arbitrary count scale. The spectrum is shown in red whereas the part above the qualifier (Q) is marked in green. The blue selection in the spectrum shows the typical peak of the $^{12}C(n,\alpha)^{9}Be$ reaction at 8.3 MeV and indicates the expected distribution as explained under chapter 3.4.2 and illustrated in Figure 3.10. During the measurement, also the $^{12}C(n,3\alpha)$ and the $^{12}C(n,n')^{12}C$ reactions were identified at the energy channels predicted by the Kavrigin et al. (2016) 14.3 MeV simulations and the datasheets provided by the manufacturer.

[5] user-defined value to determine the radiation type and fill the respective histogram.

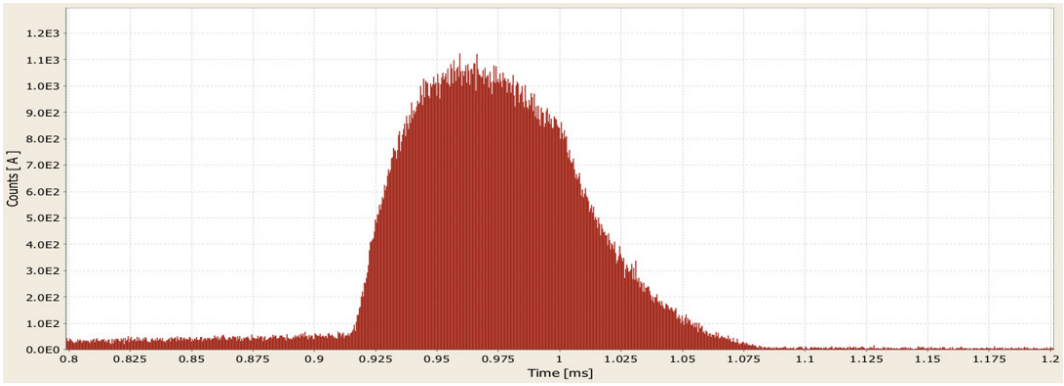

Figure 6.1: Histogram from the source strength detector of one pulse at the pulse rate of 1 kHz.

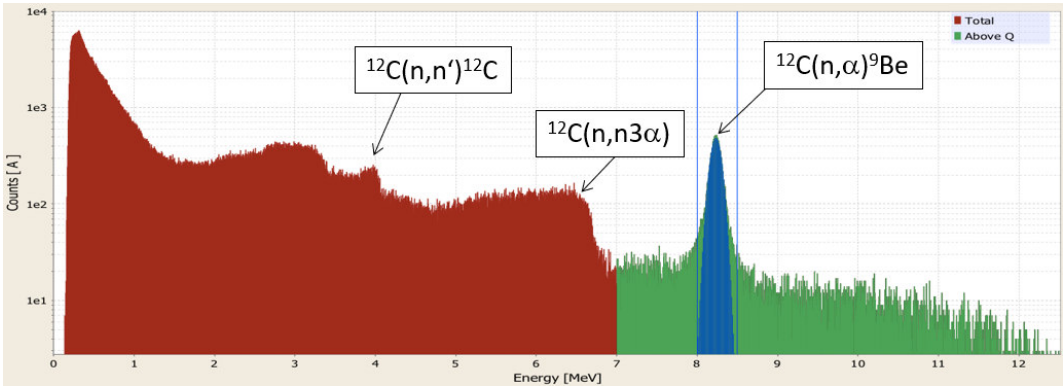

Figure 6.2: Logarithmic energy spectrum measured while producing 14 MeV neutrons with NG in operation according to the setting explained in the text.

6.1.2 Near and Far Detectors

The time evaluation of the neutron cloud in a specific formation is essential for the correct interpretation of the γ-spectra to determine elemental abundances. Since the reconstruction of the time evaluation is based on the count rates measured in the near- and far-detector the dynamic behavior of those detectors was investigated. The pulsed NG provided the neutrons for testing the individual detectors at their permanent position in the OreLog tool.

As shown in Figure 3.7, the signal of a ^{3}He counter tube is also amplified by a preamp-board. A threshold discriminator creates gate-signals (TTL standard), which are counted by a multichannel scaler on the counterboard. Therefore, the voltage of the preamplifier has to be set correctly to avoid signal pile-up.

The dead time of the system has been investigated by measuring the single count rates of the four tubes of the near detector unit respectively compared to the rates of the full ensemble. Since the source strength for the different runs (tube 1 to 4 and all tubes)

varies, the count rates were corrected by using the source strength detector as shown in Figure 6.3. Accordingly, the system has a dead time of 0.96 ± 0.09 µs per event.

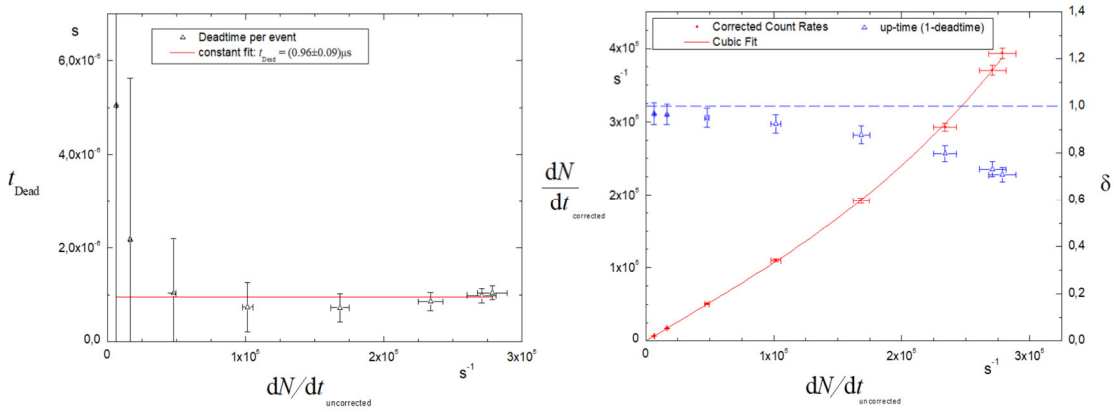

Figure 6.3: Dead time per event investigated for the near ^{3}He-tubes with a Sallen-Key-Filter in the preamplifier (left). The corrected count rates in dependency of the measured ones from the scaler are approximated by a cubic fit (right).

The corrected count rate $\mathrm{d}N/\mathrm{d}t|_{\mathrm{corrected}} = n_{\mathrm{cor}}$ shows good agreement (χ^2/DoF = 0.51116, $R^2 = 0.99984$) with the cubic approximation

$$n_{\mathrm{cor}} = \mathrm{a} \cdot n_{\mathrm{uc}} + \mathrm{b} \cdot (n_{\mathrm{uc}})^2 + \mathrm{c} \cdot (n_{\mathrm{uc}})^3 \qquad (6.1)$$

as a function of the uncorrected, counted rate $\mathrm{d}N/\mathrm{d}t|_{\mathrm{uncorrected}} = n_{\mathrm{uc}}$ with a = 1.04703 ± 0.01791, b = (-3.7472 ± 3.4545)·10^{-7} and c = (5.7534 ± 1.1788)·10^{-12}. The approximation can only be applied for signal-height independent gate-signals: A standard discriminator starts and ends the rectangle-shaped gate-signal based on a specific voltage-value which is exceeded or underrun, respectively. Since the falling edge of a standard differentiated signal rises much faster than it decays, the length of the corresponding gate-signal depends on the signal-height: the higher the signal the longer the gate-pulse (cf. Figure 6.4 left). Whereas this standard system is perfect for applications with low count rates where the dead time is negligible such as the far detector, the near detector needs a more sophisticated system, which allows fast counting at a well-known dead time. Both requirements were met by integration of a Sallen-Key-Filter into the gate-generator signal-chain. The filter ensures a fast-falling edge with an almost fixed time-relation to the rising edge (cf. Figure 6.4 right).

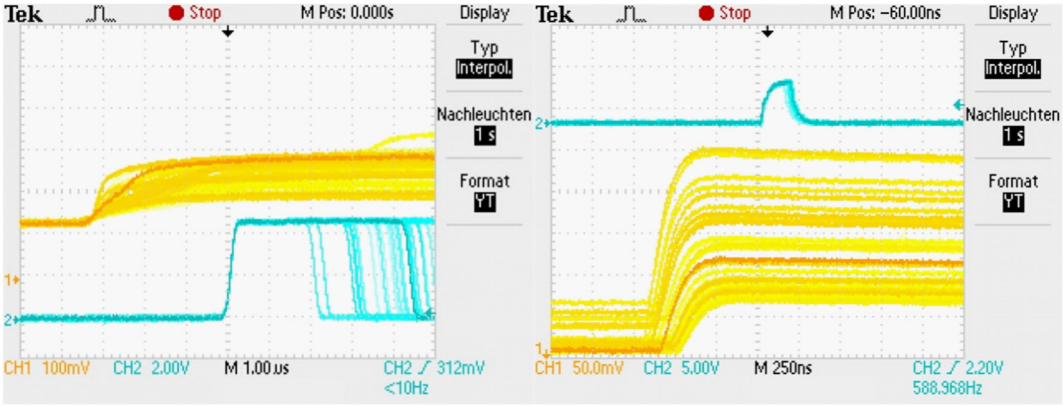

Figure 6.4: Gate signals of the slow far-detector (left) and the near-detector (right).

For reliable gamma vs. neutron discrimination, the reasonable adjustment of the trigger threshold of neutron counter pulses is indispensable and requires a properly adjusted HV supply. Figure 6.5 exemplarily shows how this was achieved for the far-detector and correlates with the expected neutron spectrum from literature (Ellis and Singer, 2007). The low-energy peak (Figure 6.5 left) originates from γ-photons and does not contribute to the neutron spectrum.

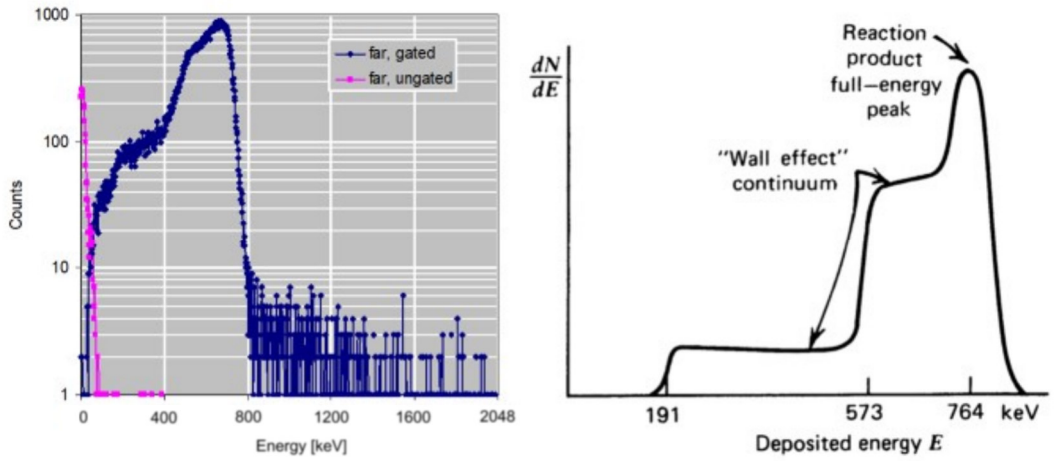

Figure 6.5: Neutron spectrum of far-detector (left) compared to a sketch of a typical expectation for a neutron spectrum recorded by a ^{3}He tube according to Ellis and Singer (2007) (right). The blue line shows the spectrum resulting from counts above the trigger threshold whereas the purple line shows the spectrum resulting from counts below the trigger threshold.

6.2 Performance of Gamma-Detector

The γ-detector is an essential component of OreLog for elemental logging for deposit characterization and therefore its accurate, reliable and repeatable operation under changing conditions is investigated and fine-tuned in detail. To benchmark the characteristics for different conditions and parameter changes the 661 keV γ-peak from a ^{137}Cs-source (282 kBq) was considered (Figure 6.8 left). The crucial values from the peak fit are the peak center and x_c (FWHM as shown in Figure 6.8 left) and finally their dependency on parameter changes. The following subsections discuss the influence of the most relevant parameters in the signal chain and data processing as illustrated in Figure 3.7.

6.2.1 Bias Voltage of the PMT

First key characteristics include amplification and bias voltage dependent peak resolution: With increasing bias voltage the peak width becomes increasingly narrow. Due to statistical processes in the PMT, the width converges to a certain value, so another increase of bias voltage would not show any improvement. Even if the γ-detector unit has an active stabilization for the last dynodes (see Chapter 3.4.1) an optimum bias voltage needs to be as high as necessary to gain best resolution (cf. Figure 6.6) and not higher than reasonable to prevent high currents on the last dynodes. This optimum enables a dynamic range for stable operation and constantly high resolution at higher currents due to the maximum counting throughput during the neutron burst. An investigation of the long-term stability of the detector system showed that the most significant instability occurs after powering (ramping) up the PMT (Figure 6.7). According to the performed measurements the residual peak walk is lower than 1 % at a time of 159 ± 9 s after powering up. Therefore, a minimum of three minutes γ detector initialization phase should be considered before any measurements.

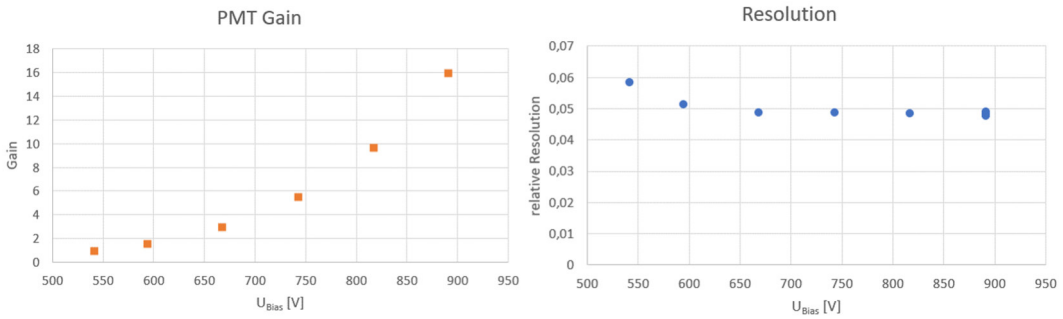

Figure 6.6: Evaluation of γ-detector unit for its bias voltage dependent amplification in arbitrary units (left) and the relative peak resolution (right).

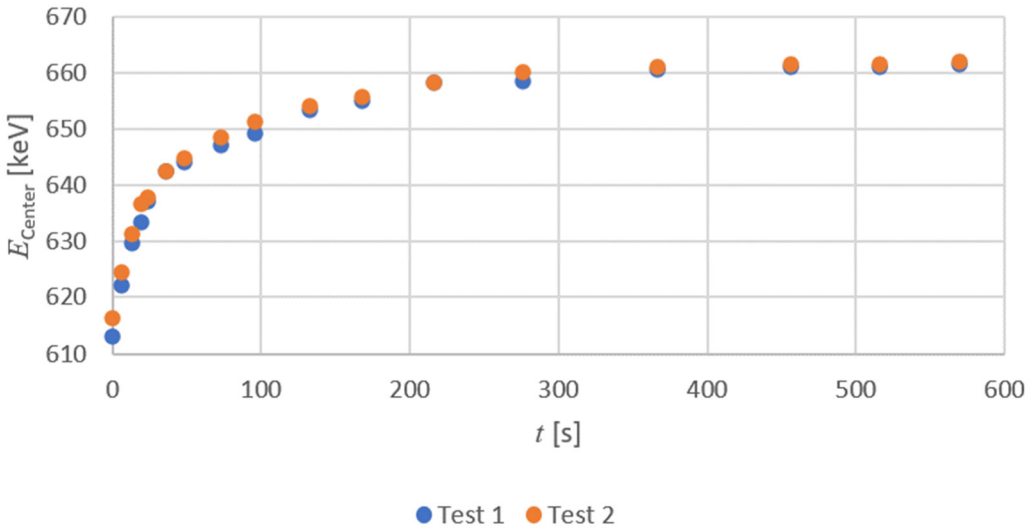

Figure 6.7: γ-detector unit PMT energy stability : After powering up the detector needs some time to reach stable conditions regarding the peak position.

6.2.2 Shaping Parameters

Once the γ-detector operates with ideal parameters its signals with their energy-proportional pulse height need to be recorded by the DAQ system (cf. Chapter 3.1). The DAQ of OreLog consists of a low-noise preamplifier which amplifies and shapes the signal and a sampling ADC as MCA. The custom-made preamplifier shapes the signal to a fall-time of 50 µs, which is optimized for the MCA. The MCA digitizes the pulses by sampling, application of mathematical filters and finally by determining the digital value for every signal, which is proportional to the initial photon energy. As main result the MCA provides pulse-height spectra for specific time intervals after the neutron burst (Figure 6.8).

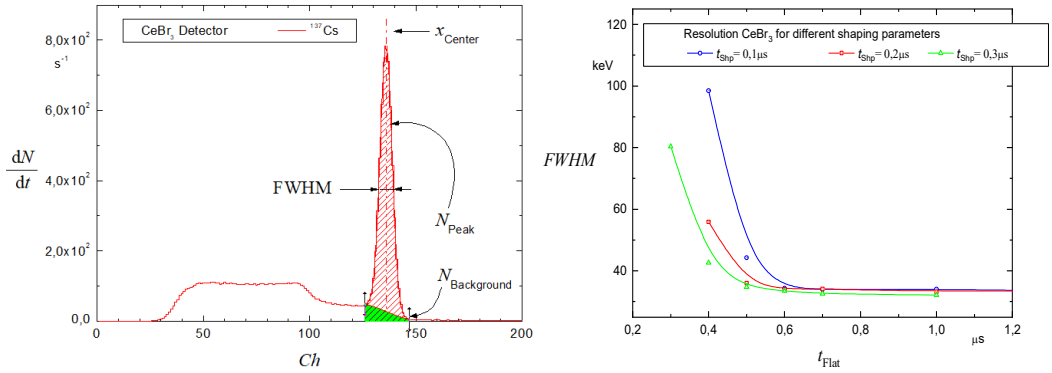

Figure 6.8: Influence of shaping parameters : γ-radiation causes a full-energy-peak at the energy proportional position x_{Center} with the width FWHM and the area N_{Peak} (left). The influence of shaping-parameters t_{Shp} and t_{Flat} to the resolution was investigated (right).

An essential step in the digitization process is the application of filters as described above. Basically, the filter is described by two parameters: the 'shaping time' t_{Shp} and the 'flat-top-time' t_{Flat} (shaping parameters). The shaping time defines the length of the spectroscopically filter, or how many values before and after the voltage step are averaged to evaluate the pulse height. It is half the rise or integration time. Flat-top-time is a parameter introduced with digital MCA's and is adjusted to the rise time of the preamplifier.

The noise decreases with increasing flat-top and shaping times, thus, resulting in a better resolution (Figure 6.8). The processing time per event increases proportional to t_{Flat} and to t_{shp}. The associated increase in dead time becomes critical at high count rates as evident during the neutron burst (Figure 6.9). To establish best system performance, the ideal parameters were chosen for a maximum detector resolution even at high count rates.

The highly disproportional increase of dead time with increasing shaping time leads to the lowest possible value of $t_{shp} = 0.1$ µs. Since the same resolution level is reached with an increasing flat-top time this loss to resolution was compensated by setting up a higher flat-top-time of $t_{Flat} = 0.7$ µs.

6.2.3 Dead Time

Based on those shaping parameters the dead time of the system was investigated. Since elemental logging is based on the measured γ-spectra, the understanding of occurrence, control and correction of dead time are key features for a reliable analysis.

Dead time tests were performed with a ^{137}Cs source as done in the previous chapter. The count rate of the source, which was laterally fixed next to the $CeBr_3$-crystal, was about 5000 s^{-1}, which causes a negligible dead time to the system. Assuming that the related count rate n_0^{661} in the 661 keV-peak is constant, the count rate decreases to $n^{661}(n_{\text{throughput}})$ at higher counting-throughputs of the entire γ-detector-system $n_{\text{throughput}}$ due to dead time losses. The ratio of the peak-count-rates:

$$\delta(n_{\text{throughput}}) = \frac{n^{661}(n_{\text{throughput}})}{n_0^{661}} = 1 - p_{\text{dead}}, \tag{6.2}$$

relatively quantifies the time interval that the detection system was able to detect a signal. Alternatively, one can use a notation with the relative dead time p_{dead}. Accordingly, a dead time affected count rate $n_{\text{uncorrected}}^{E_\gamma}$ in a peak with the energy E_γ is corrected by applying:

$$n_{\text{corrected}}^{E_\gamma} = n_{\text{uncorrected}}^{E_\gamma} \cdot \delta(n_{\text{throughput}})^{-1}, \tag{6.3}$$

with the use of the up-time δ (Figure 6.9) which depends on the counting throughput of the MCA based on the entire spectrum.

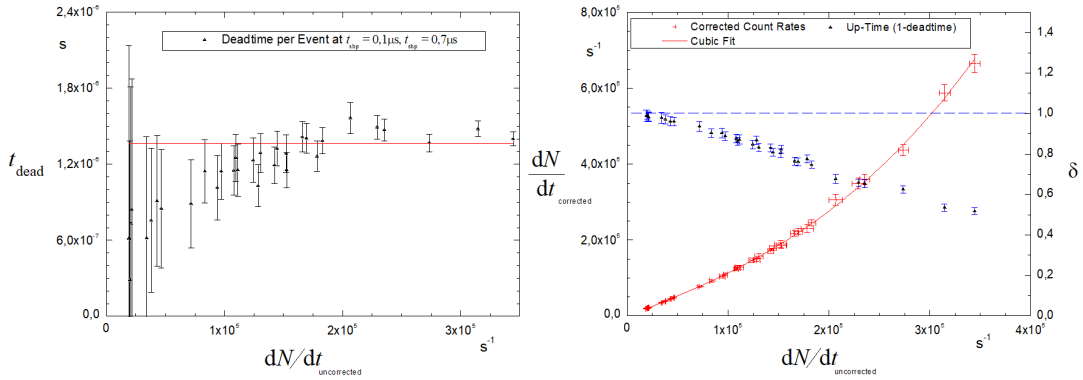

Figure 6.9: Dead time investigation by the use of a ^{137}Cs source to be constant in the uncertainty-range (left). A clear relation between corrected and uncorrected count-rate was deduced (right).

The investigation showed that the system has a fixed dead time per event of t_{dead} = 1.35 µs, independently of the deposited energy. This results from the varying composition of the spectra with regard to intensities in different energy regions for different count rates (Figure 6.10). A cubic fit according to Equation 6.1 with a = $1.01568 \cdot 10^{-7}$, b = $3.3138 \cdot 10^{-7}$ and c = $3.4834 \cdot 10^{-12}$ describes the relation between corrected $dN/dt|_{corrected} = n_{cor}$ and uncorrected $dN/dt|_{uncorrected} = n_{uc}$ count rate satisfactorily. The parameters show that non-linearities become effective from a throughput of several thousand events per second. This confirms the initial assumption for the ^{137}Cs source to cause a very short and therefore neglectable dead time.

6.2.4 Pole-Zero Compensation

The deposited energy in the γ-detector of an incoming particle causes a fast signal built-up at the integrator of the preamplifier (integration-capacitor) and a subsequently long decay of this signal. Since the MCA is carefully tuned for the decay time, the digital pulse processing can process a signal properly, which rises on the falling edge of a previous signal. Its origin shows that this Pole-Zero-Compensation becomes increasingly important at high count rates. A wrong or non-ideal tuning of this parameter results in a count rate dependent peak shift (cf. Figure 6.10).

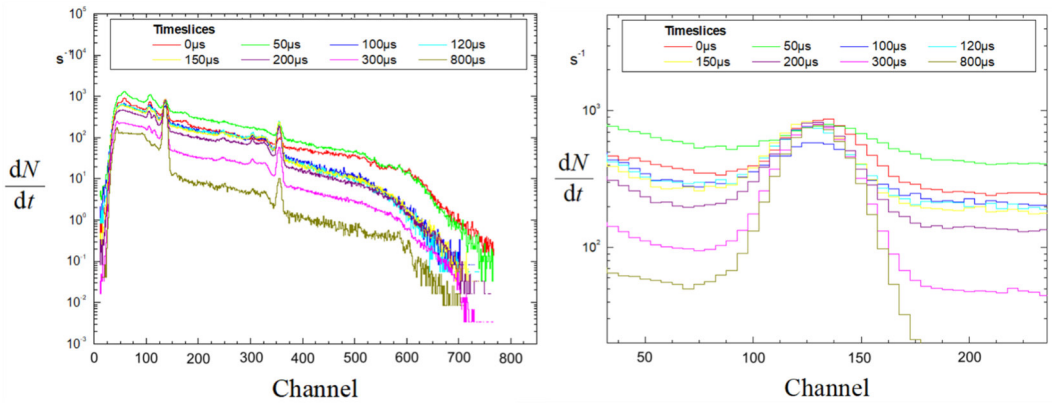

Figure 6.10: Investigation of the γ-detector unit performance at varying count rates by acquiring γ-spectra in several time windows after a neutron burst (left). The stability of the system was investigated based on the 661 keV peak of a ^{137}Cs source (right).

In analogy to the above the peak shift was investigated with the use of a ^{137}Cs source. For each time window the peak was fitted with a Gaussian and a constant term, a linear term, and a step-function as background model.

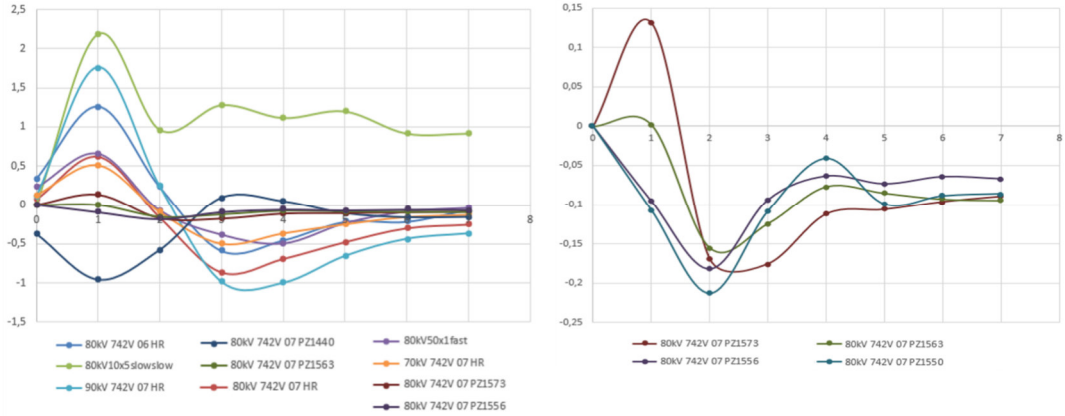

Figure 6.11: Relative peak walk of all time windows (window 1 to 8 corresponding to x-axis numbers 0 to 7) for (1) different neutron throughputs (NG accelerator-voltage 70, 80, 90 kV), (2) different trigger filters (slow-slow='-1,0,1' fast='1,-2,1', HR='1,0,-2,0,1') (3) different shaping parameters (t_{Flat}=0.6-0.7 µs) and (4) different PZ-values (left). The minimal peak walk was achieved with a PZ of 1556 (right). For individual time window length see Figure 6.10.

Then the peak position was plotted relative to the initial value for the different time windows (Figure 6.11). According to the manufacturer the Pole-Zero (PZ)[6] value was quantified as being 1773 based on the measured fall-time of 50 µs. Due to the high peak walk for this PZ-value an empirical investigation was performed. The corresponding plot illustrates the investigation: Whereas the initial value of PZ = 1773 causes a

[6] The unitless pole zero correction is applied to make sure that a voltage step starting from the MCA line is evaluated with the same amplitude as the signal sitting on the falling slope of a proceeding step. Without correction the slope is causing an error.

positive peak drift at increasing count rate, a negative drift was observed at a value of 1440. Coming from a peak walk in the range of 2 % for PZ = 1770, most stable conditions were found for a PZ-value of 1556 with a peak walk of 0.17 %.

6.2.5 Trigger Filter

Further investigations were focused on the variation of the trigger filter type (Figure 6.11). This algorithm preprocesses the signal in a fast and simple way to distinguish noise from a detector signal (cf. chapter 4.1). Once the signal is identified by the trigger filter to be a physical detector signal it becomes digitally processed but if rejected as noise, no dead time is caused. The quality of differentiation strongly depends on the complexity of the filter: the more complex the filter, the higher the discrimination quality but the more processing time is needed per event.

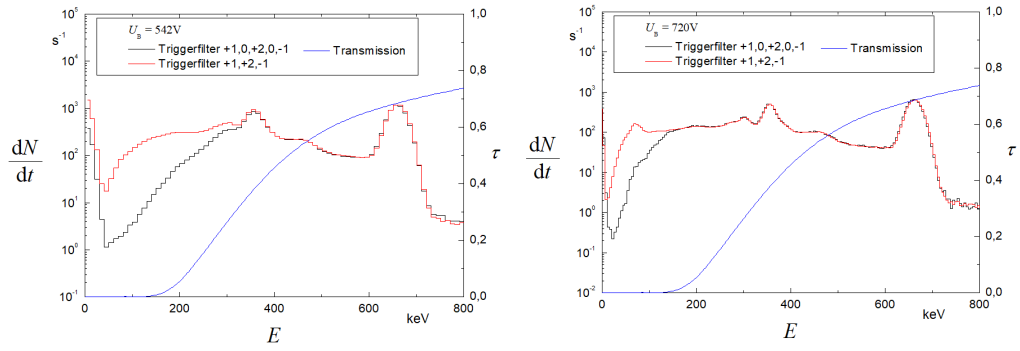

Figure 6.12: Investigations of the influence of the trigger filter for two different tube-amplifications to reduce dead time. A faster trigger filter (black) affects the lower energy cutoff compared to the default filter (red). In both cases the energy cutoff was lower than the cutoff due to the photon absorption in the lead chassis of the scintillator crystal, which is shown by the transmission τ (blue).

Thus, the trigger filter influences the dead time. It turned out that the trigger filter has no significant effect on the dead time reduction but leads to a lower energy cutoff. At lower bias voltage and therewith lower PMT amplification the signals of low energetic events have a smaller size. Whereas the slower filter can identify those as signal, the fast filter rejects them as noise (Figure 6.12).

6.2.6 Amplifier Gain

Once a particle interacts in the detector it causes light in the $CeBr_3$ scintillator. The light sensitive PMT produces a tiny current signal which becomes amplified and shaped to an energy proportional voltage pulse by the preamplifier (cf. Chapter 3.4.1 and Figure 3.7). The MCA input voltage range, which is given by the coarse gain, depends on the height of the preamplifier signal (Figure 6.13 left) especially for dynamic

applications with high counting rates. Since the preamplifier signal has a fast rising- (500 ns) and a slow falling-edge (50 µs) a signal could rise on the falling edge of an antecedent one. The probability of this pile-up effect increases at higher count rate, which leads to a signal height which is a multiple of the height of a single signal. In case a pile up signal exceeds the MCA input range, no signal is counted and registered until the signal decays back into the MCA measuring range. This counting loss was revealed during dead time investigations (Figure 6.13 right): at the same signal throughput (corrected rate) a lower rate is registered if the signal was out of the MCA measuring range (red). Due to this dynamic behavior the selection of the MCA input range and amplification required a very careful tuning.

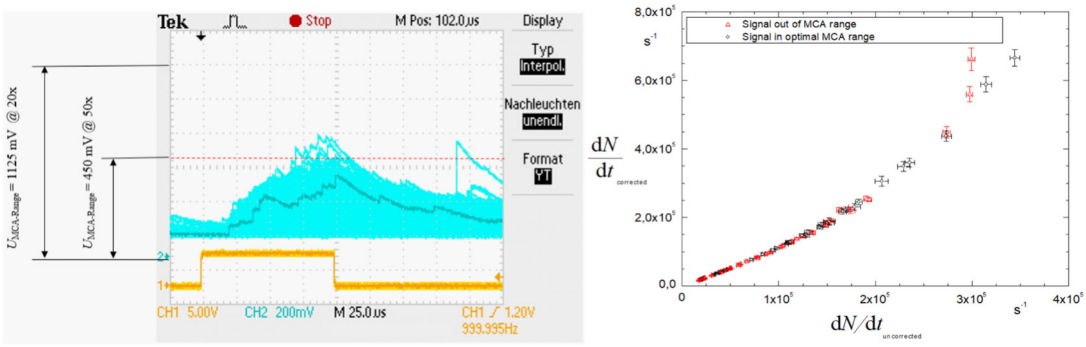

Figure 6.13: Amplifier Gain : Coarse gain constraining a voltage range for the MCA input signal. High counting throughput leads to a signal pile-up which results in an exceeding of the acceptance range if the voltage range is chosen too small (left). In particular the resulting loss of counting events influences the dead time determination: increasing the real counting throughput ($dN/dt_{corrected}$) leads to a kind of saturation effect for the count rate ($dN/dt_{uncorrected}$) suddenly – at the point when the signal exceeds the MCA voltage range (right).

The input range is selected by the coarse gain of the MCA internal amplifier. Since the signal-to-noise ratio depends on the gain of an amplifier, its influence on the resolution was investigated (Figure 6.14). The resolution is better, the higher the coarse gain, but the dependence is more significant at 660 V PMT bias voltage. At 743 V and 817 V the change is comparably small.

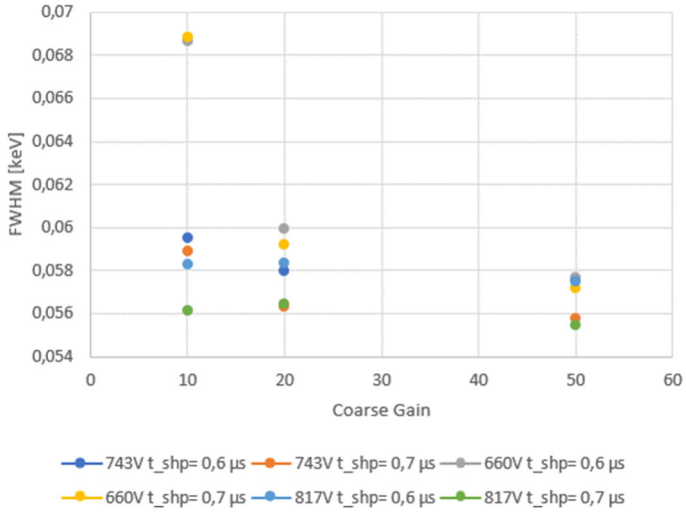

Figure 6.14: FWHM behavior of the 661 keV ^{137}Cs peak in dependency of the MCA coarse gain at different PMT voltages and different flat-top times t_{Flat}.

Assuming the gain with the highest resolution, the MCA input voltage range of -50 mV to 450 mV for the coarse gain 50 was enough for standard γ spectroscopy applications. At high count rates, like during the neutron burst, the signal exceeds the MCA range (Figure 6.13 left). A decrease of the preamplifier amplification (C_{int} = 2.8 to 10 nF) results in a decline of resolution.

Since the resolution only slightly decreases with lower MCA gain at a PMT bias voltage of 743 V the coarse gain of 10 was chosen. To use the full input voltage range, the (+)130 mV signal offset of the preamplifier output was eliminated by changing the output to a capacitive coupling with 47 µF. The window of (-)250 mV to (+)2500 mV provides enough dynamic range for 166 % and 156 % at a NG acceleration voltage of 80 and 90 kV respectively (Figure 6.15). Thus, the choice of the input range accounts for a formation dependent increase of the γ-production rate.

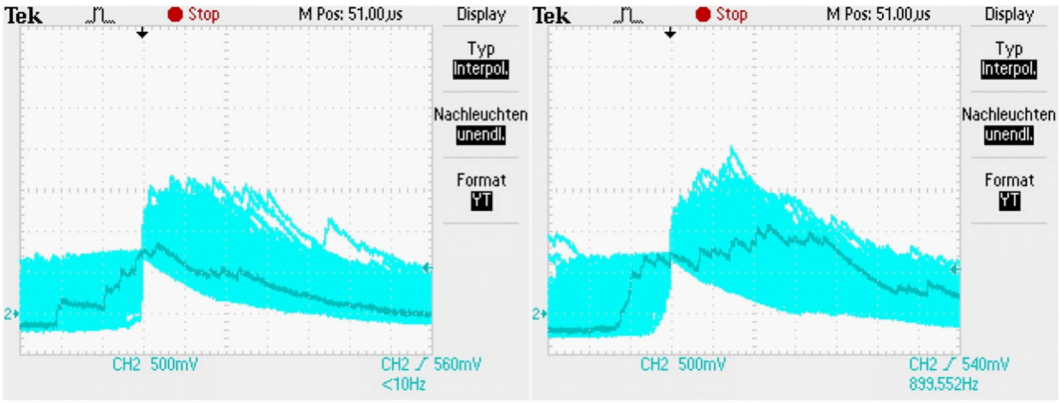

Figure 6.15: γ-preamplifier signal for different signal throughputs at 80 kV (left) and 90 kV (right) NG acceleration voltage was checked with regard to the MCA input voltage range.

6.2.7 Temperature Stability and Linearity

A total of 2570 spectra were recorded during varying temperature setups of the γ-detector presented under chapter 5.1.2. The energy resolution at elevated temperatures (60 °C) is stable over time.

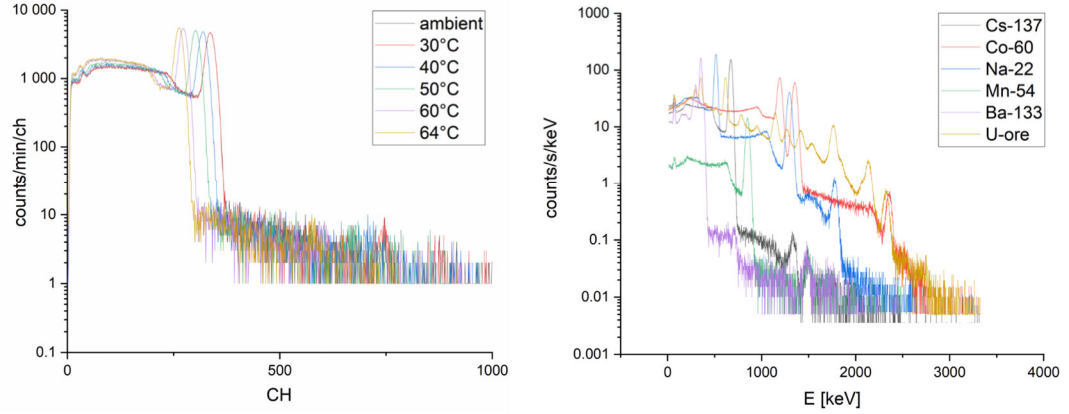

Figure 6.16: Spectra of ^{137}Cs at different temperatures (1 min/spectrum) before channel to energy conversion (left). Energy spectra recorded with the γ-detector unit according to the experimental setup shown in Figure 5.4 (right).

The spectra recorded from the γ sources listed in chapter 5.1.1 by the ideally tuned and calibrated γ-detector unit are shown in Figure 6.16 (logarithmic count-rate axis). The left diagram shows the ^{137}Cs spectra at varying ambient temperatures and a 1024-channel horizontal axis. A peak shift with increasing temperature is observable but the spectrum shape maintains identical. This is of outmost importance because it allows the peak finding algorithm to identify the peak independent of the channel position. Due to confirmed detector linearity at varying temperatures, the peak shift is accounted for during the channel to energy conversion. The spectra demonstrate an excellent energy resolution and linearity. Characteristic radioisotope peaks are shown in the right diagram of Figure 6.16 (^{137}Cs at 662 keV; ^{60}Co at 1173 and 1332 keV; ^{22}Na at 511 and 1275 keV; ^{54}Mn at 835 keV; ^{133}Ba at 356 keV; uranium ore at 609, 1120, 1764, 2447 keV). The laboratory-measured uranium spectra clearly prove the high detection efficiency and good resolution which was expected as already discussed in the scintillator crystal selection in chapter 3.4.1. The curve shape and the FWHM prove the ability of the chosen settings to resolve peaks of interest allowing the algorithm to realize an accurate channel to energy conversion.

6.2.8 Elemental Logging Tests

The resulting γ-spectra (burst and capture) of the laboratory elemental logging experiments with various materials as defined in chapter 5.1.3 are shown in Figure 6.17. The burst spectra do not show any significant patterns except for carbon. Neutron-capture cross-sections of carbon are too small (0.0035 barn) to generate any significant signal-rate from γ-rays produced in neutron capture processes, but there are three significant peaks in the inelastic γ-ray spectrum (burst). At 4.4 MeV the photo peak (PP) is visible and at 3.9 and 3.4 MeV the corresponding single escape (SE) and double escape (DE) peaks produced by inelastic scattering of neutrons at carbon contained in PE via $^{12}C(n,n'\gamma)^{12}C$ reactions. Large background contributions are present in the burst spectrum and have to be considered in field applications.

Therefore, the main potential of elemental discernibility is provided by the capture spectrum. The various materials cause different capture spectra as shown in the lower diagram in Figure 6.17. The most significant pattern is observed for stainless steel (Fe), i.e. iron causes a significant pattern in the energy spectrum with three typical peaks at 7.6 MeV (PP), 7.1 MeV (SE) and 6.6 MeV (DE). This clear pattern demonstrates unambiguously the ability of OreLog to determine iron in an investigated formation.

The second significant pattern is generated by chlorine in PVC. Figure 6.17 shows the elevated pattern with peaks around 6 MeV allowing the differentiation of chlorine form the background at laboratory scale. Magnesium, calcium and silicon do not significantly defer form the background (no tube) curve of the capture γ-ray spectrum. Their elemental microscopic neutron capture cross-section is with 0.063, 0.431, and 0.171 barn respectively relatively small to be detected considering the limited volume of test material surrounding the tool in the experimental setup. Therefore, the detectability of these elements in the field is most likely only possible in case of larger elemental mass fractions.

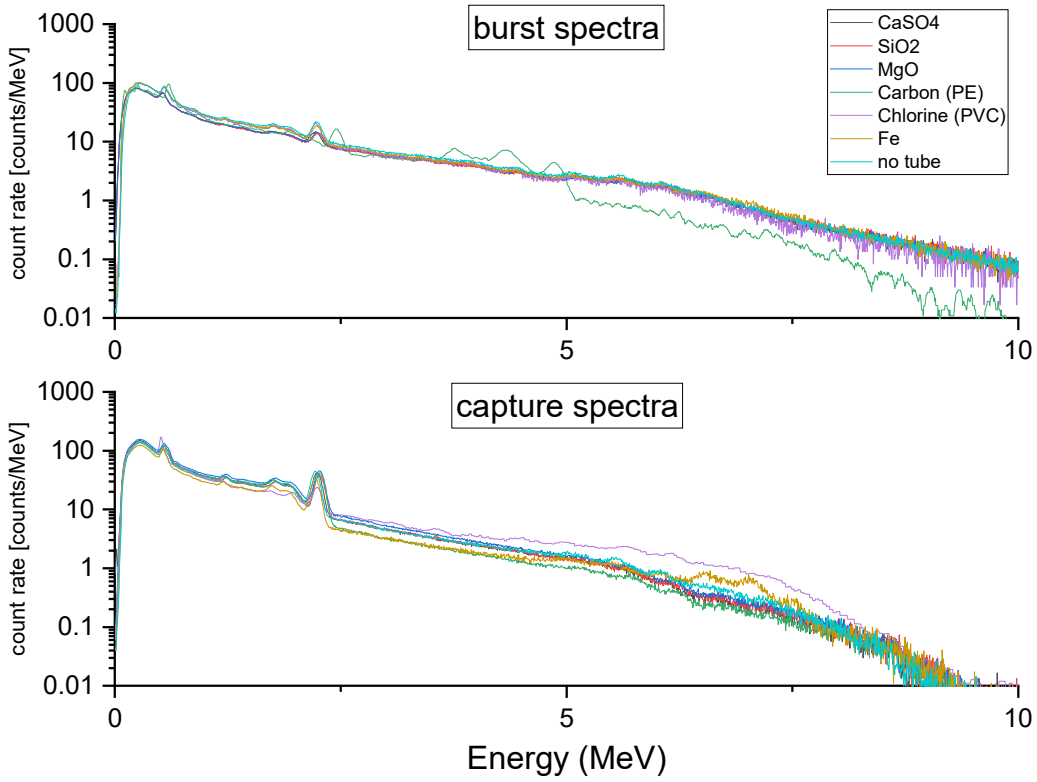

Figure 6.17: Burst (inelastic scattering) and capture energy-spectra recorded as a function of different test materials surrounding the tool or without any material: 'no tube'.

The encouraging results for iron detection from the presented experimental results are confirmed by MCNP simulations of pyrite-bearing sandstone formations considered as a base case and elaborated in detail in chapter 6.3.2. An overlay plot (Figure 6.18) was compiled illustrating the previously presented laboratory data (same data as in Figure 6.17) and simulated data of a capture spectrum corresponding to a formation containing 3 % pyrite (FeS_2). The overlay clearly illustrates that there is not only a significant contribution between 5 and 8 MeV, but the appearance of this significant contribution is also understood – it is a contribution from iron as illustrated by the bright-blue colored part of the simulation in Figure 6.18.

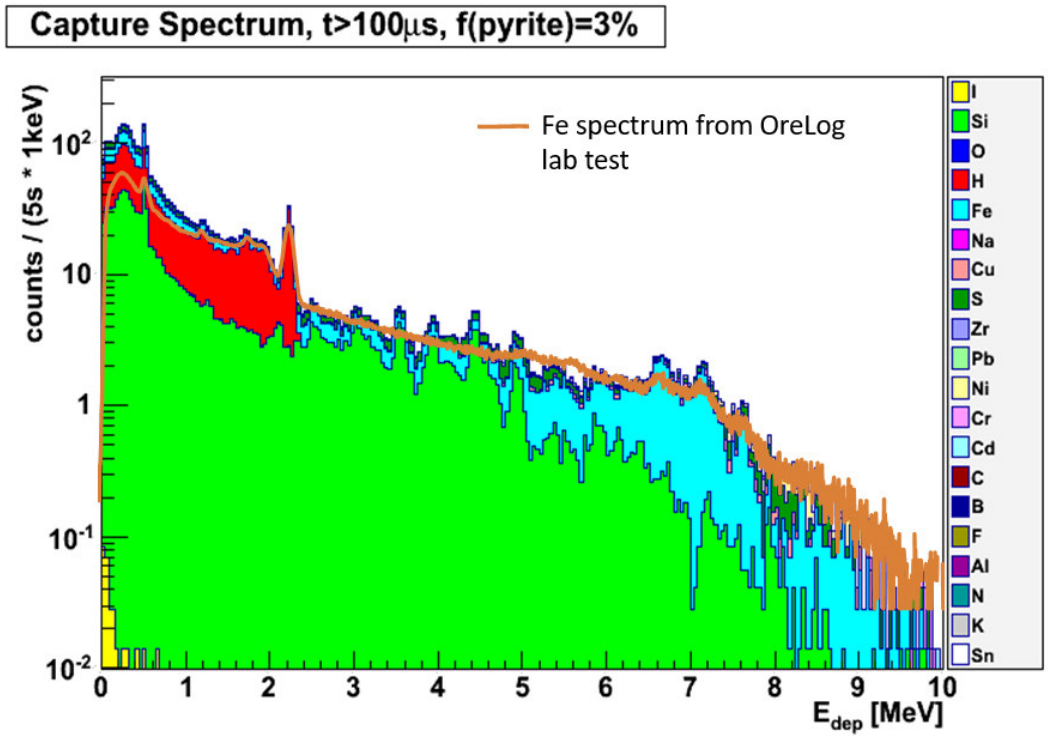

Figure 6.18: Capture spectrum from MCNP simulation (stacked colored histograms) and measured data (brown line). The measurement was performed in a water tank with Fe around the OreLog tool as described under chapter 5.1.3. The simulation relies on a sandstone formation with 30 % porosity and 3 % pyrite. The peaks around 7 MeV appear in data and simulation.

6.3 MCNP Simulations

6.3.1 Neutron Cloud and Distribution

The shape and size of the neutron cloud depends strongly on the hydrogen index (HI), due to the high capability of protons (H) to slow neutrons down. In MCNP, simulations were designed to model a punctual neutron source (NG) surrounded by a standard formation (pure sandstone) with variable gravimetric water content (0, 5, 15, 45 wt% H_2O and corresponding SiO_2 content). At radial distances from the source up to 5 m, equidistant spherical surfaces were assumed every 2 cm in the simulation in order to determine the neutron flux. The plots in Figure 6.19 provide an overview of the neutron distribution over time with a punctual neutron source and a burst width of 100 µs. The position axis (horizontal) and the time axis (vertical) are kept constant whereas the color-coded neutron density is differently adjusted in each plot. Therefore, these plots are considered qualitative, not

quantitative, and they give an idea of how neutrons are distributed in the formation.

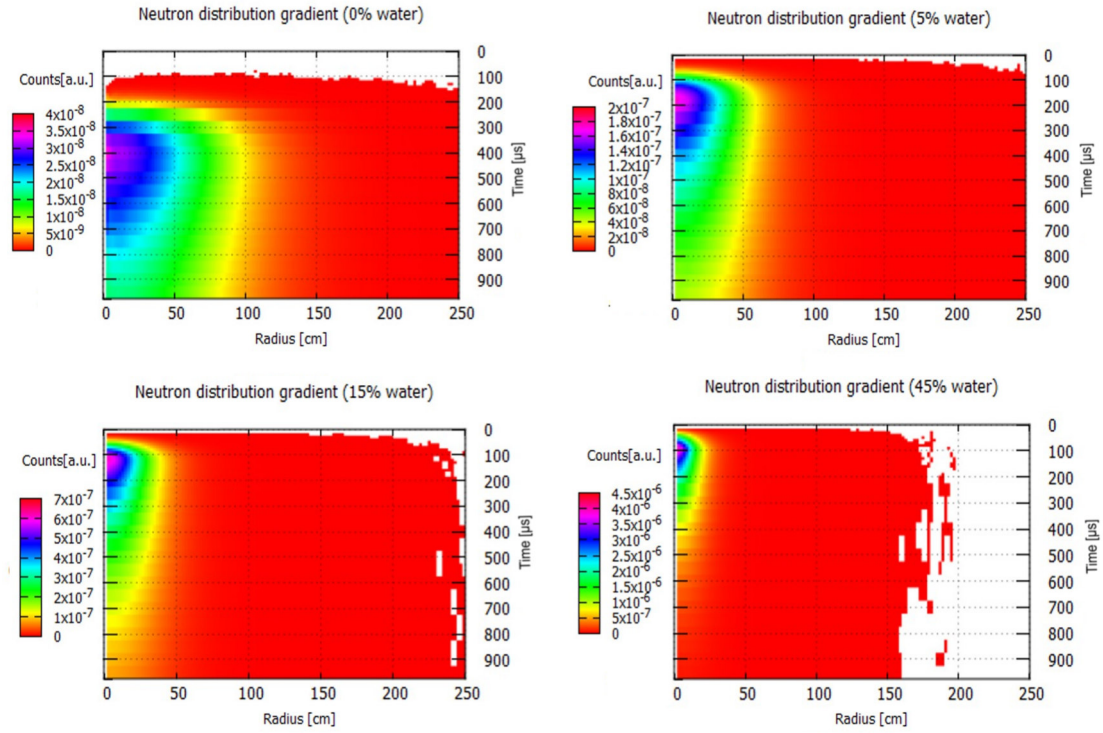

Figure 6.19: Neutron distribution (neutron density in a.u.) for extended source (100 µs) in a standard formation over time with increasing water content (in wt%).

The content of water in the formation has the biggest effect in the neutron cloud's extent. If there is no water, neutrons interact less and will reach 1 m of distance at a neutron density of $5x10^{-9}$ n/cm³ after 400 µs. Only in the 100 % quartz scenario there is no immediate neutron density response at the tool because of the macroscopic cross-section of Si. The more water is present the earlier a neutron density peak is reached; at 45 % water already after 100 µs just at the end of the neutron burst. With 5 % water content, the penetration depth of neutrons is about 60 cm; with 15 % water the neutrons will reach 40 cm and a water content of 45 % results in a maximum reach of only 30 cm.

As it can be observed, while having high water contents, an increase in water percentage will not change much the neutron cloud extent. On the other side, a small change while in low water levels (from 0 to 5 %, for instance) will bring a much bigger change in the neutrons' behavior.

A realistic estimation of the neutron (primary photons) cloud extensions and frequency distributions around the tool is shown in Figure 6.20. The PTRAC option of MCNP is used to provide this highly relevant information of the position coordinates (spatial

distribution) of the neutron-induced photon γ_{prim} directly at the generation of γ_{prim}. (primary photon whose progenies deposit energy in the detectors). The simulation outcome is based on the OreLog input model (cf. chapter 4.2.1) and a representative 'standard scenario' with a water-filled borehole (water column of about 15 cm diameter) surrounded by a simple sandstone formation (quartz-sand; porosity of 35 %, fully H_2O-saturated) representing average open-pit blast hole scenarios, that are considered as primary target applications. The cross-section depicts the very high and spatially very constraint (punctual source) neutron frequency at the NG and similar at the γ-detector but extended longitudinally along the tool axis due to the detector dimensions and scintillator activity. Besides the tool inherent photon frequencies, the matrix-dependent neutron penetration depth into the surrounding formation can be deduced. According to the simulation a maximum penetration depth of 60 cm is reached, whereas matrix-dependent formation properties such as water content (H_2O), density, mineral phases and their corresponding macroscopic neutron cross-section cause a higher neutron absorption and hence a decrease in the depth of penetration.

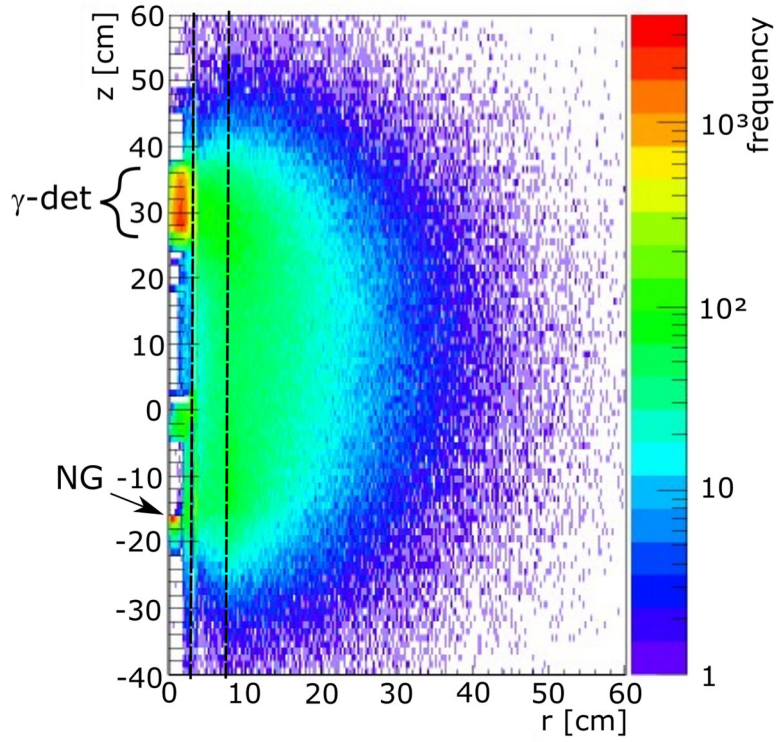

Figure 6.20: Frequency of production vertices of the primary photon γ_{prim} in the z-r-plane. (z = coordinate along longitudinal OreLog logging axis; r = radius, i.e. distance to center-axis of OreLog). The color code states the logarithm of the frequency. From center to periphery: r = 0 to 3.8 cm: OreLog tool (1st dashed line); r = 3.8 to 7.5 cm: water column (2nd dashed line); r > 7.5 cm: quartz sand formation with H_2O-saturated pores. At z = - 16 cm (red) there is the production of the 14 MeV neutrons, i.e. high neutron density. At z = 28 to 35 cm there is the $CeBr_3$ scintillation crystal.

Therefore, in average the properties of a maximum 40 cm distanced atom are considered as accessible corresponding to a reliably analyzed maximum volume of a sphere of approximate 0.8 m diameter (d) as illustrated in Figure 6.21. Considering the logging speed of the tool and the vertical resolution (z) set to 20 cm, the investigated volume is then a cylinder surrounding the tool from collar to end of hole with the corresponding volume for each logging interval of about 0.1 m^3 according to

$$V = \pi\left(\frac{d}{2}\right)^2 z. \tag{6.4}$$

This compares to an analyzed volume of 0.00009 m^3 in conventional geochemical drill core analysis of $\frac{1}{4}$ core of most commonly used 47.6 mm DD diameter NQ[7]. In RC drilling this corresponds to 2 m chip sampling intervals at most commonly used 114 mm diameter, which results in a volume of 0.002 m^3 for a comparable 20 cm interval.

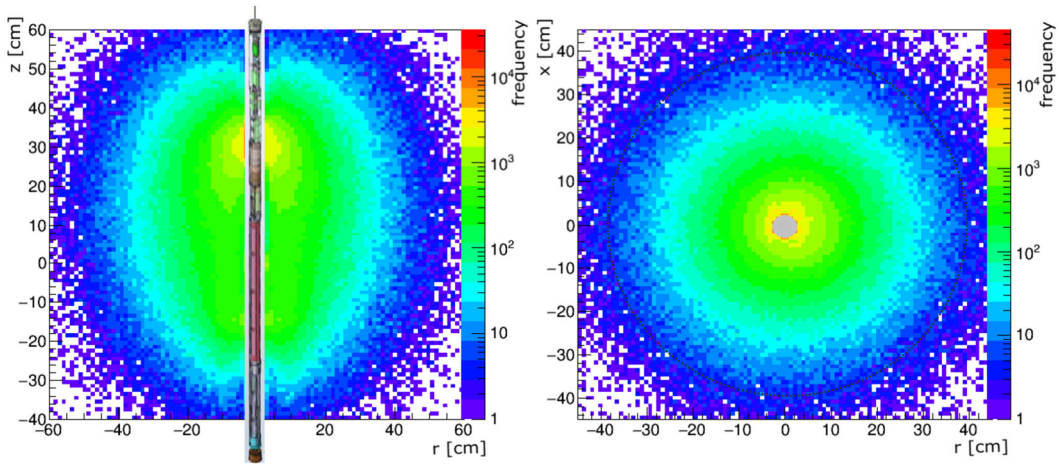

Figure 6.21: Neutron cloud distribution based on data from Figure 6.20 in simplified illustration in cross-section view (left) and top view (right). Black dotted line indicates estimated analyzed volume.

6.3.2 Simulated OreLog Spectra

The customized PTRAC analyzer described in chapter 4.2.2 enables the complete deconvolution of γ-ray spectra into contributions from different isotopes in both the burst and capture time window. The deconvolution of the activation window is also possible but is not considered here since the planned OreLog application and data interpretation do currently not rely on the activation window and it is beyond the scope of this work. Figure 6.22 to Figure 6.25 show the spectrum decomposition of a

[7] Most common DD drill bit sizes and their hole and core (in parenthesis) diameter according to Cumming (1951): AQ = 48 (27) mm; BQ = 60 (36.5) mm; NQ = 75.7 (47.6) mm; HQ = 96 (63.5) mm; PQ = 122.6 (85) mm.

simulation with the OreLog tool in the 'standard scenario' under the conditions as previously described.

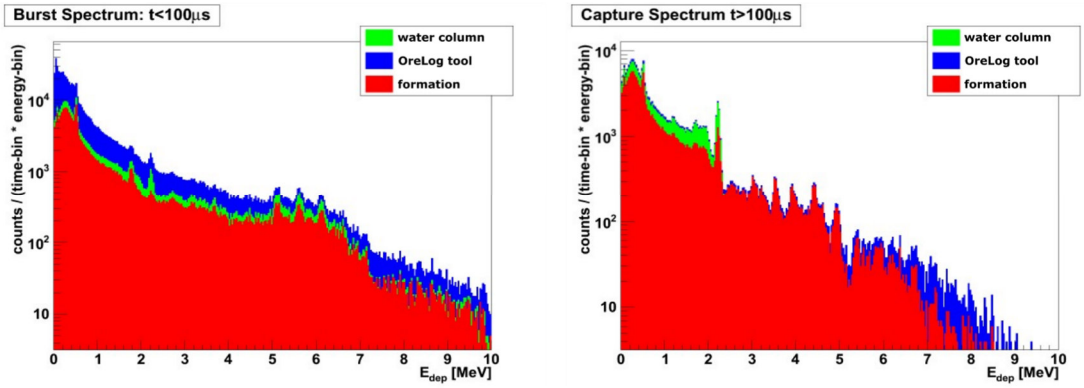

Figure 6.22: Burst spectrum and capture spectrum decomposed into three fractions depending on the spatial range of the production vertex of γ_{prim} (the primary γ; see text). The production originated in (i) the water column, (ii) in the OreLog tool, or (iii) in the surrounding formation. An energy resolution of 7.5 % was assumed in the simulation.

The spectral decomposition into contributions originating from the OreLog tool, water column and formation (actual volume of interest) are illustrated in Figure 6.22 in the time dependent burst (left) and capture (right) spectrum. The burst spectrum is still significantly affected by unwanted tool and water column contributions throughout the entire energy range of the spectrum. The capture spectrum is already formation dominated with minor tool contributions (mainly in the high energy range) and water column contributions only up to 2 MeV.

In a next step the contribution of various chemical elements to the time dependent spectra is investigated. Only Si, H and O are formation relevant elements, whereas all the other elements are tool associated (internal components). Figure 6.23 shows the simulated spectra of the 'standard scenario' and the individual elemental contributions showing that the burst spectrum is dominated by various elements. The capture spectrum in contrast resembles the tool surrounding elements (H, Si) very well. In Figure 6.24 and Figure 6.25 the decomposition into fractions of a selection of different chemical elements X is illustrated, where X refers to the nuclei type in the γ-ray generation process X(n,γ)Y. Those graphs indicate the ability and the likelihood to measure individual elements based on their individual response in the γ detector by the energy deposition spectrum. These simulated spectra were generated for all elements of interest and provide valuable insight and understanding regarding the expected outcome and informational value of the burst and capture time window. These

interpretations were used to compile element-specific templates as elaborated in chapter 6.3.3.

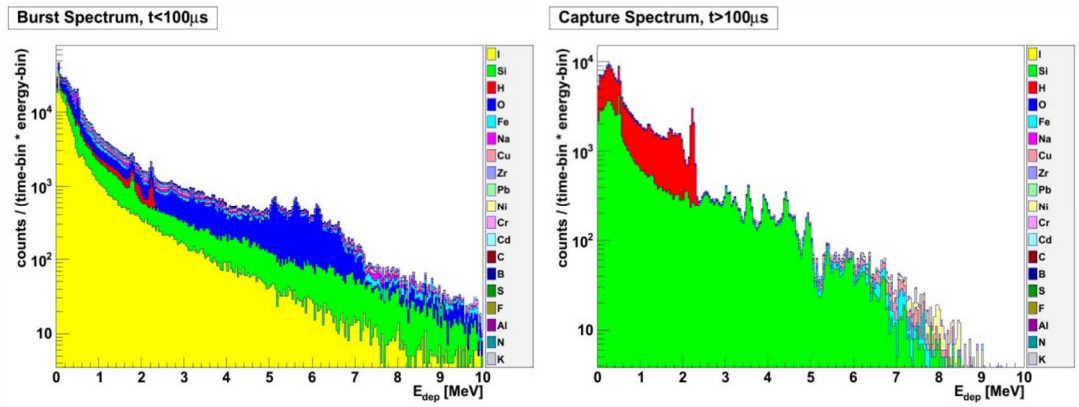

Figure 6.23: Burst spectrum (left) and capture spectrum (right) decomposed into chemical element fractions. Decomposition is with respect to the element used to produce the primary photon γ_{prim} in a neutron-induced reaction. An energy resolution of 7.5 % was assumed in the simulation.

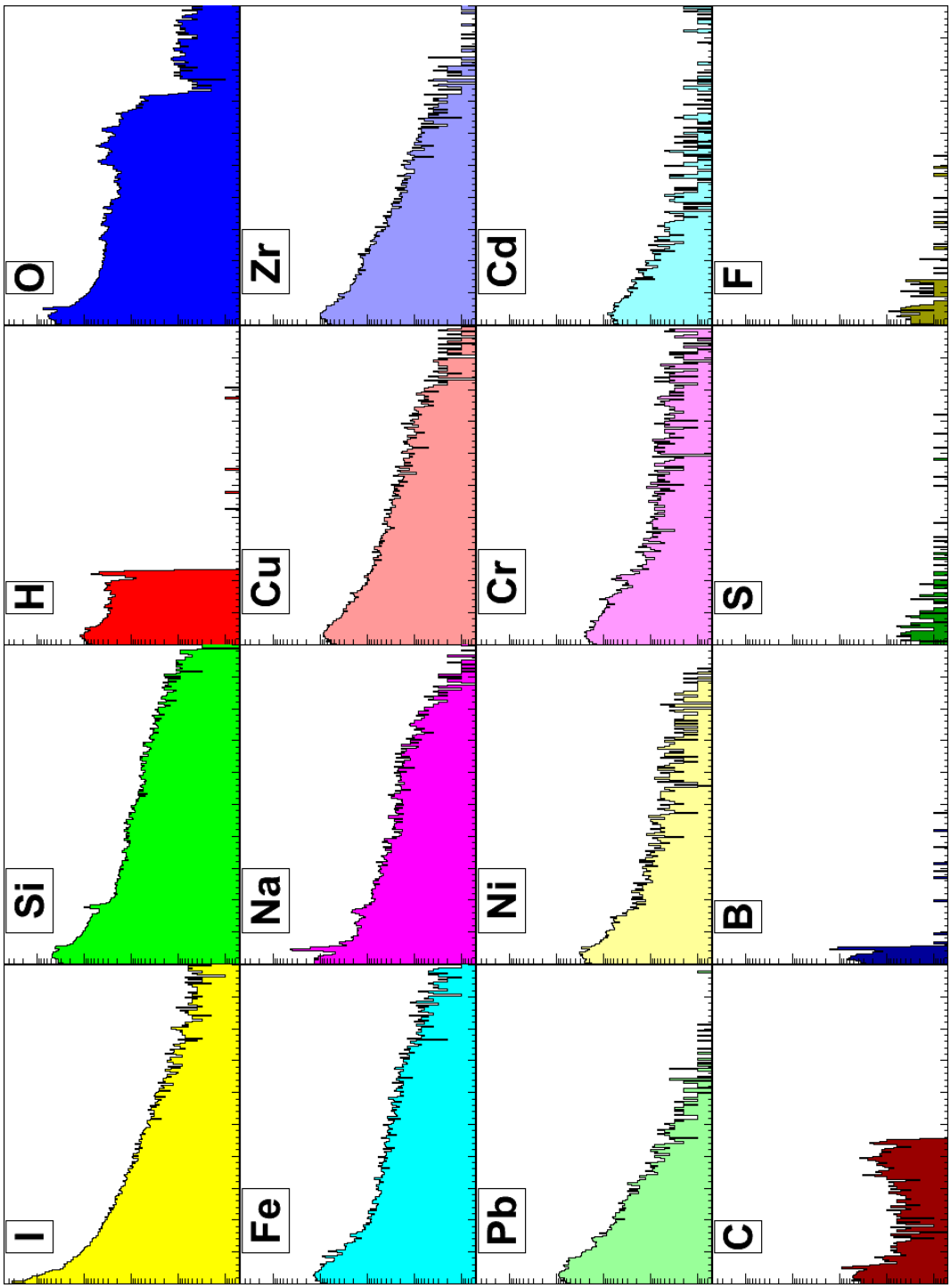

Figure 6.24: Fractions of the burst spectrum due to the element Z in the γ_{prim} generation reaction ${}^{A}_{Z}X$ ${}^{A}_{Z}X$+ n $\rightarrow$ γ_{prim} + anything. (x-axis: Energy from 0 to 10 MeV, y-axis: logarithmic count rate [a.u.]).

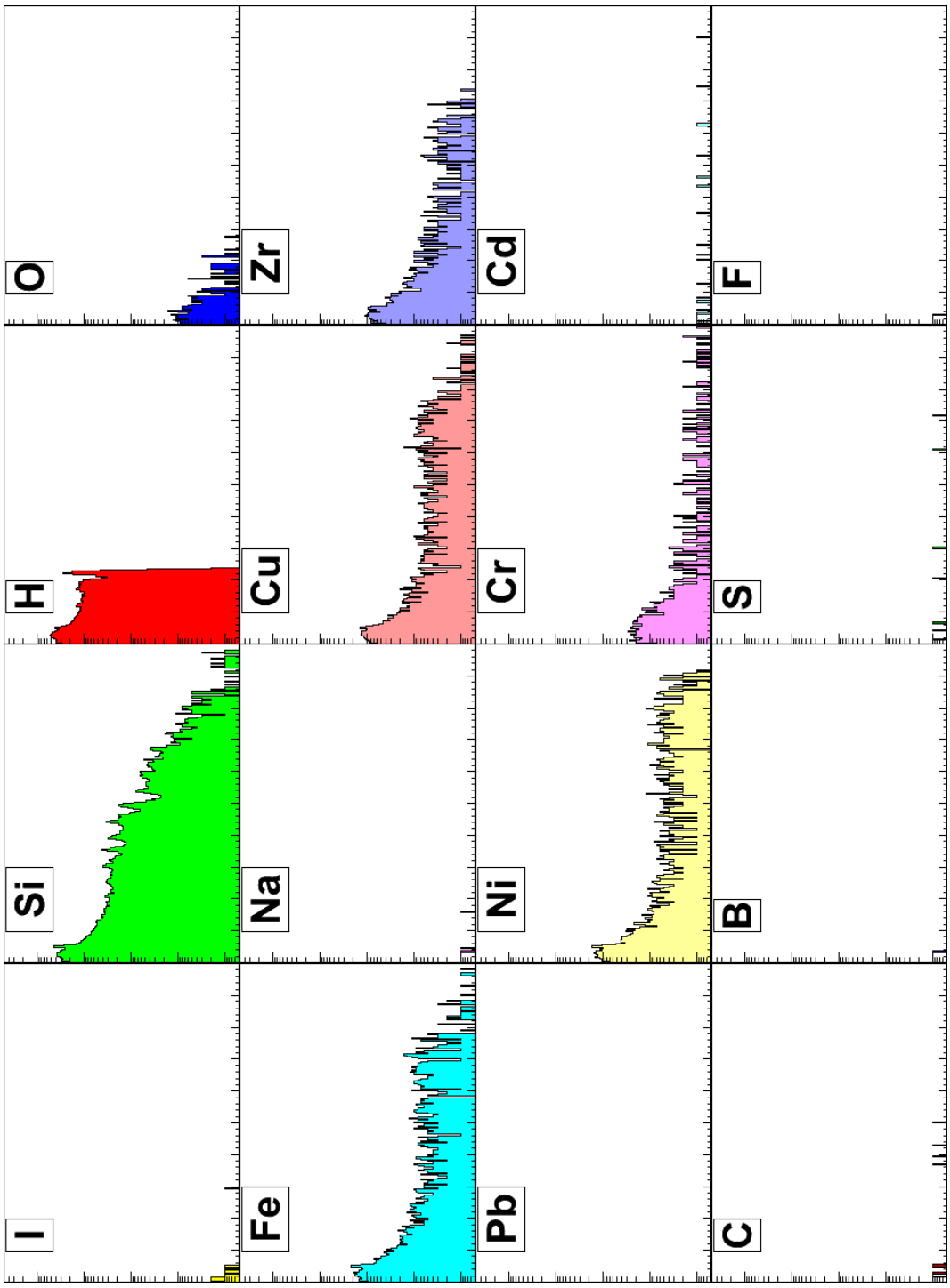

Figure 6.25: Fractions of the capture spectrum due to element Z in the γ_{prim} generation reaction ${}^{A}_{Z}X + n \rightarrow \gamma_{prim} +$ anything. (x-axis: Energy from 0 to 10 MeV, y-axis: logarithmic count rate [a.u.]).

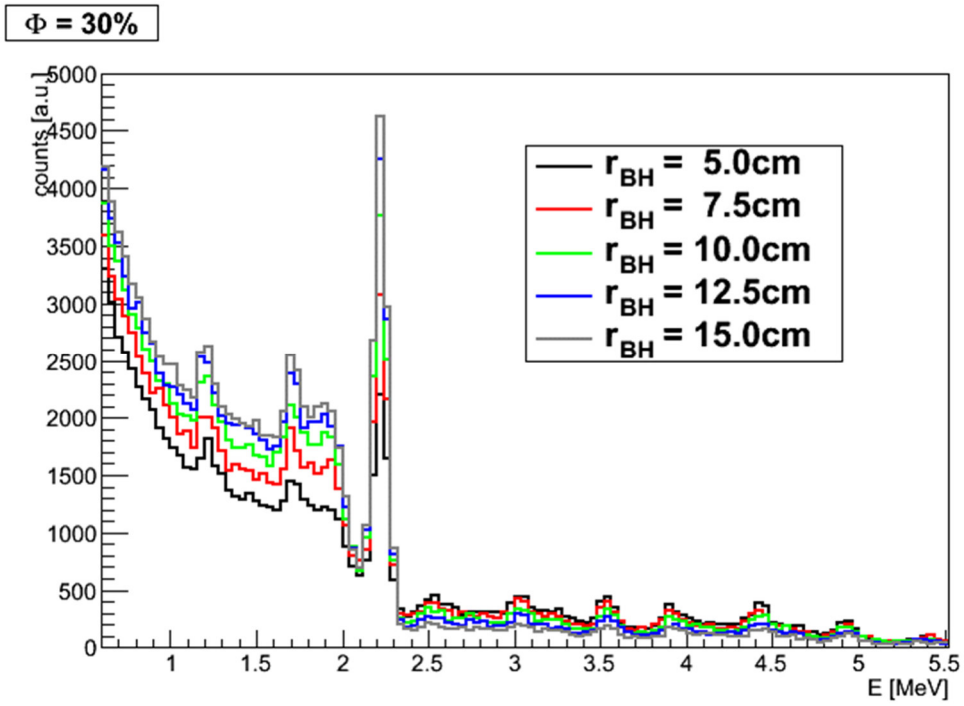

Figure 6.26: Capture spectra of simple sandstone formations with 5 different borehole radii r_{BH}. Shown are spectra with a detector energy-resolution of 7.5 %.

Besides the elemental contribution and the formation porosity impact to the resulting spectra, many other parameters were investigated while only the borehole diameter dependency of the 'standard scenario' is presented here. Figure 6.26 compares simulated capture spectra with $\Phi = 30$ % and different values of r_{BH}. The borehole radius significantly effects the size of the hydrogen peak as well as the corresponding Compton edge at its low-energy side and a decreased borehole radius results in increased Si peaks. The above results are directly translated into a routine to measure the borehole radius. Here, the porosity Φ (measured by OreLog algorithm as introduced in chapter 4.4.2) is a minor correction only. The knowledge of the borehole radius enables a much better correction of all OreLog results for the effect of the water column surrounding the tool. In addition, it is important for the correction of the γ-ray spectra as basis for determining the elemental concentrations in the formation.

6.3.3 Element-specific Templates

In order to decompose real-data spectra the templates or shapes of the components of the investigated spectra need to be understood as described in the previous chapter. The PTRAC output of an MCNP simulation and the subsequent processing of this output by the PTRAC-analyzer directly gives element-specific patterns corresponding to the simulated scenario. As a result of the previously mentioned parameters affecting

elemental logging, a database of MCNP simulation outputs representing sufficient parameter variations and scenarios has been established.

As an example, the element-specific template for each neutron induced γ-spectrum of 10 wt% Fe_2O_3 is shown in Figure 6.27. It clearly shows that iron contributes to the overall spectrum in every time window. Nevertheless, the iron contribution is most significant and unambiguous in the capture spectrum, which is therefore used as the primary element-specific template spectrum.

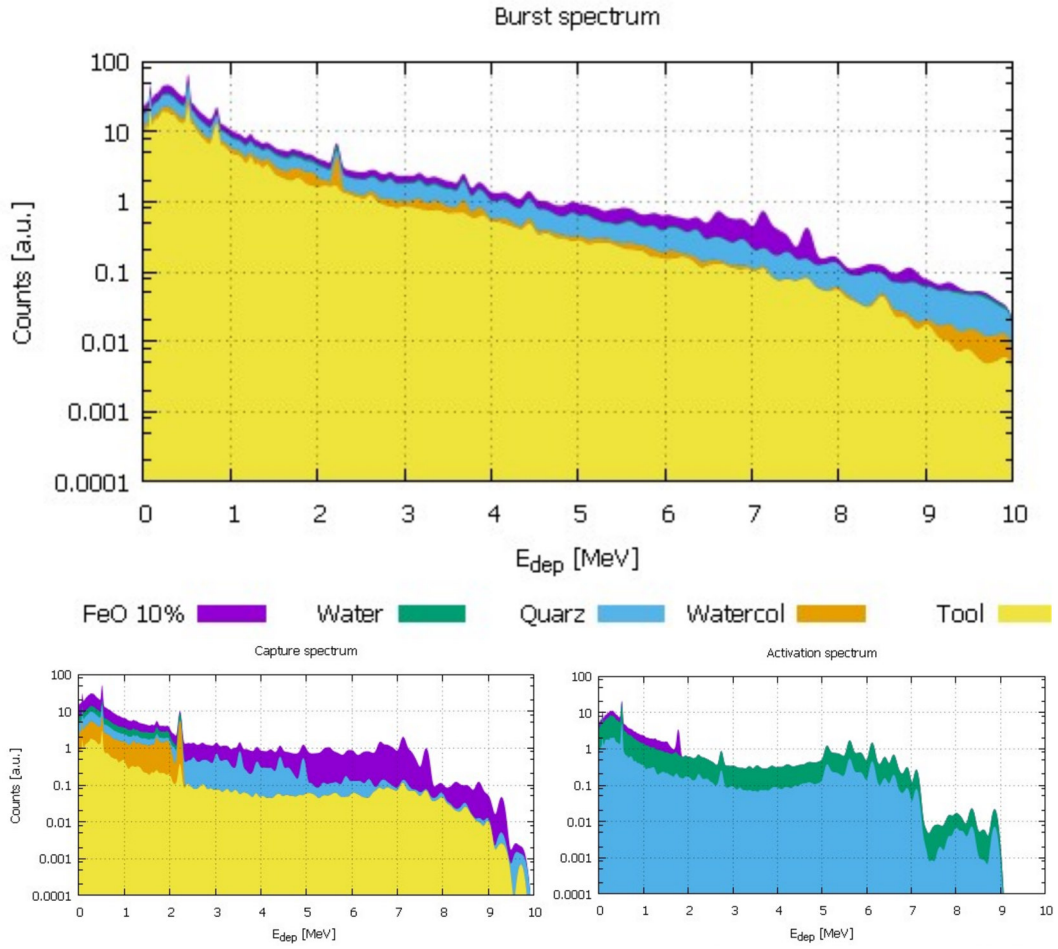

Figure 6.27: Deconvoluted element-specific templates for 10 wt% FeO in respective spectra.

Considering only the iron signal (without deconvolution) in the capture spectrum at various concentrations results in Figure 6.28. The typical iron pattern between 6 and 8 MeV is visible and therefore detectable by the deconvolution algorithm up to 60 % Fe_2O_3. At higher concentrations, the iron pattern changes significantly. It does not show pronounced peaks anymore, making it difficult for identification during spectral deconvolution if using this template. The reason for the disappearance of the pattern is the macroscopic neutron absorption impeding sufficient capture gammas reaching

the γ-detector since they are absorbed by the formation itself. This illustrates the dilemma that element-specific templates need to deliver the individual 'fingerprint' at a wide range of concentrations. Therefore, a generalized approach to compile representative element-specific templates based on several thousand simulations is followed.

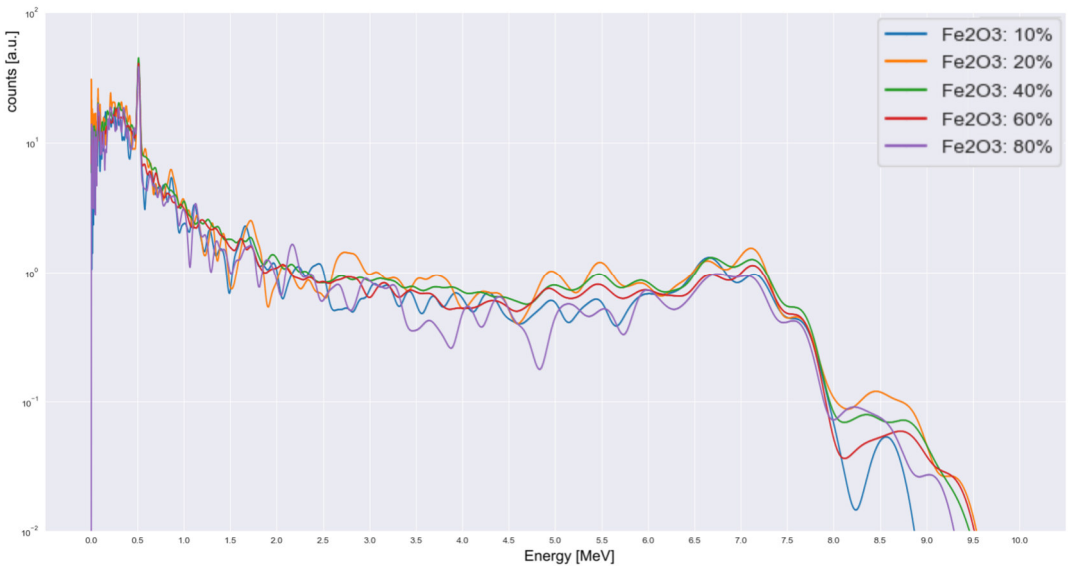

Figure 6.28: Iron template in dependence of Fe concentration. 10 % porosity (H_2O) and remaining quartz.

As a result of the previously mentioned parameters affecting elemental logging, a database of MCNP simulation outputs representing sufficient parameter variations and scenarios has been established. Based on this a representative collection of element-specific templates for the OreLog tool was created as shown in Figure 6.29. The compilation contains only templates relevant for OreLog application fields to be tested in the subsequent chapters. These standard element-specific templates were created to be included as default into the sLOG dataset for elemental logging. The respective element-specific energy template of Figure 6.29 is then inserted in Equation 4.21 as described in chapter 4.3.

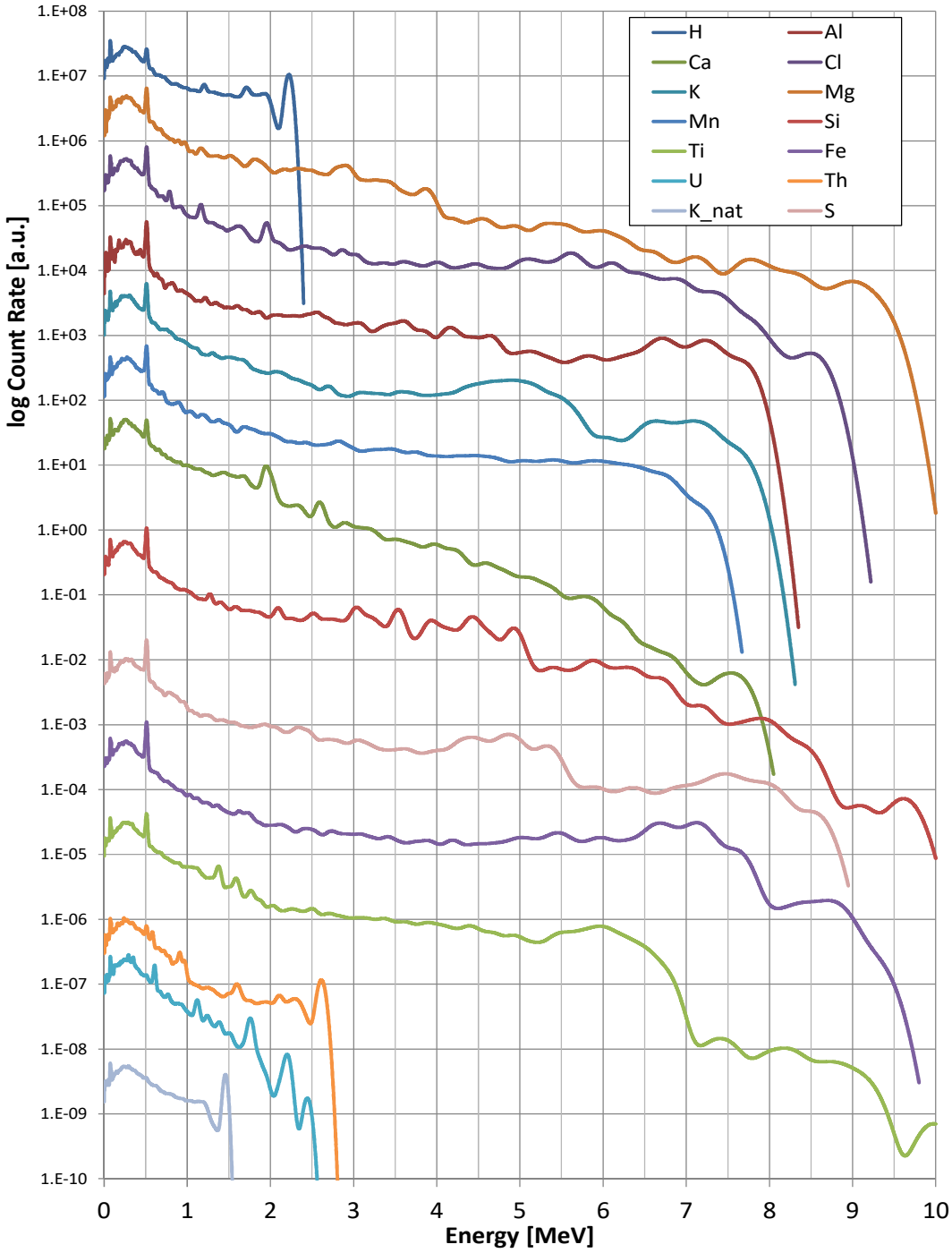

Figure 6.29: Element-specific templates f_(Model,X) as used in the Model-function describing measured pulse-height spectra. All of them have been generated using MCNP. For an optimized presentation each of the f_(Model,X) has been scaled by a constant factor, i.e. individually for each element X.

6.4 Petrophysics

All field tests were successful without any serious tool failures nor external interruptions. The main petrophysical results are compiled in the following sections. An element-by-element comparison is presented in chapter 6.5. Results from petrophysical laboratory core analysis of selected core intervals, which were provided by HGR, are presented in Table 6.1. Permeability (K_{air}) and pore volume measurements were made on the samples at 800 psi confining stress. Klinkenberg permeabilities (K_{inf}) were determined directly from the CMS-300 since it operates by unsteady-state principles. Porosity data was obtained by combining pore volumes from the CMS^{TM}-300 with grain volumes from the Ultrapore^{TM} porosimeter.

Table 6.1: Porosity, permeability, grain density and hydraulic conductivity for core plugs of borehole FMC004 determined by the CMS^{TM}-300 Core Measurement System, Model 300 Stage 4.00 at 800 psi confining stress (source: Core Laboratories Australia PTY LTD). Abbreviations: H – horizontal, V – vertical, K_{inf} – Klinkenberg permeability (equivalent liquid permeability), K_{air} – equivalent air permeability.

ID	Sample Depth	Confining Stress (800 psi)			Hydraulic Conductivity at 20 °C	Dry Bulk Density	Grain Density
		K_{inf}	K_{air}	Porosity			
	m	mD	mD	%	m/d	g/cm^3	g/cm^3
1H	138.82	530	549	37.0	4.40E-01	1.673	2.654
1V	139.00	4.89	9.57	36.3	4.06E-03	1.679	2.637
2V	153.71	0.161	0.415	30.4	1.34E-04	1.838	2.642
2H	153.82	0.276	0.622	31.9	2.29E-04	1.800	2.643
3V	168.06	424	471	37.4	3.52E-01	1.646	2.627
3H	168.12	607	673	37.8	5.04E-01	1.637	2.633
4H	177.64	753	766	39.2	6.25E-01	1.621	2.665
4V	177.76	637	654	39.9	5.29E-01	1.581	2.629
5H	184.20	684	700	37.7	5.68E-01	1.639	2.631
5V	184.41	521	536	38.2	4.33E-01	1.647	2.666
6H	186.14	341	356	37.8	2.83E-01	1.681	2.704
6V	186.32	181	199	37.0	1.50E-01	1.666	2.642
7H	193.82	1040	1080	31.8	8.66E-01	1.836	2.691
7V	194.00	1470	1490	34.1	1.22E+00	1.777	2.698

6.4.1 Density

The dry density ρ_{dry} is derived and estimated according to Equation 4.29 and compared to core analysis as shown in Figure 6.30. For comparison reasons and due to unsatisfying field results based on Equation 4.29 previously derived according to MCNP simulations and laboratory data, another approach for the ρ_{dry} estimation (Equation 6.5) based on HI instead of ϕ as in Equation 4.29 is also plotted.

$$\rho_{dry}(HI) \quad = \quad \rho_B - HI \cdot \rho_{fl} \tag{6.5}$$

Dry density values calculated from HI are in better agreement with core sample data than those calculated from ϕ. Dry densities calculated from quantity HI from OreLog slightly overestimate dry density values for core samples 3 to 6.

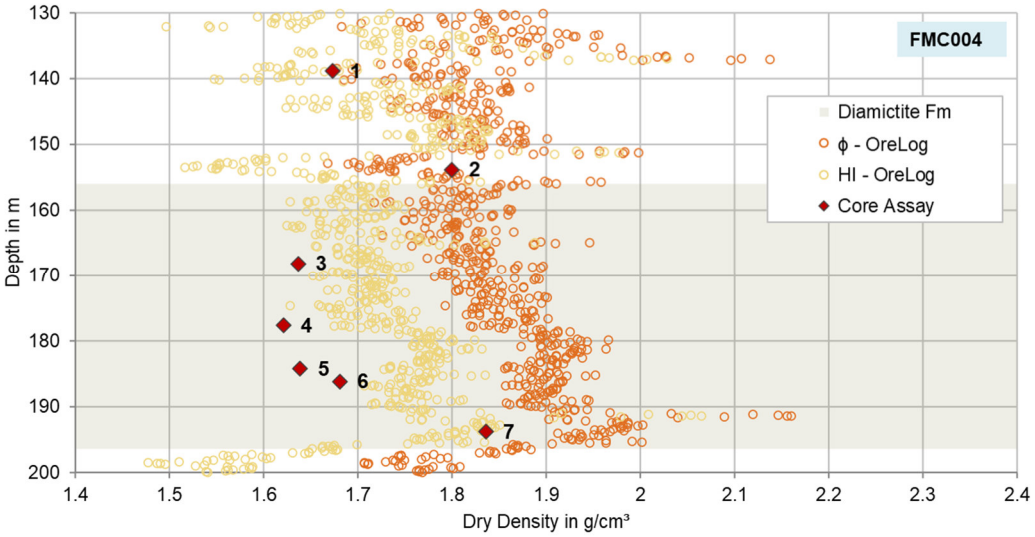

Figure 6.30: Comparison of density (g/cm³) from core analysis and OreLog logging at borehole FMC004. Density calculations are based on Equations 4.29 and 6.5.

Figure 6.31 shows repeatability of results by comparing boxplots for $\rho_{dry}(\phi)$ and $\rho_{dry}(HI)$ based on OreLog data from FMW-FLT area in two subsequent logging runs. Both $\rho_{dry}(\phi)$ *and* $\rho_{dry}(HI)$ are inside the data range of core sample data and show good repeatability.

The following observations are made:

- The general porosity relation, $HI \geq \phi$, suggests $\rho_{dry}(HI) \leq \rho_{dry}(\phi)$. Too small ϕ values will overestimate the dry density of core sample data. Exactly this is observed for FMC004 in Figure 6.30.
- In contrast to FMC004 the data from FMW-FLT area suggest a good agreement for both $\rho_{dry}(HI)$ and $\rho_{dry}(\phi)$.

In any case, reworking the OreLog algorithm to calculate ϕ from HI will improve the density prediction as well.

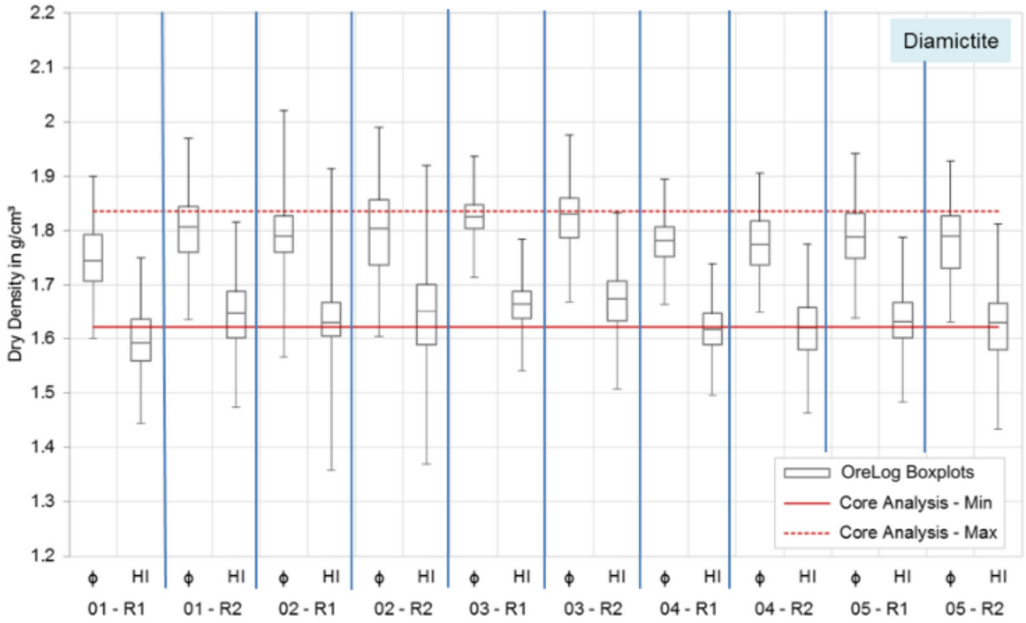

Figure 6.31: Boxplots for dry density calculated from ϕ and HI for 5 delineation holes (01-05) with 2 runs (R1, R2) for each hole at FMW-FLT area.

6.4.2 Porosity

Table 6.1 presents laboratory results for porosity ϕ and hydraulic conductivity K of core plugs in horizontal and vertical direction. Porosity values range from 30 – 40 %. The lowest porosities can be observed for the bulldog shale (sample 2). Hydraulic conductivity ranges from $K = 2{\cdot}10^{-4}$ up to 1 m/d, whereby a very low K is derived for the bulldog shale (sample 2). The remaining samples lie within the same order of magnitude. As expected for a stratified sedimentary deposit, vertical K is smaller than horizontal K, except for sample 7. According to the core analysis data, anisotropy (quotient of horizontal K to vertical K) is for the Eyre Formation (sample 1: anisotropy about 100) much larger than for the FMD (samples 3 to 7: anisotropy 1.3).

The comparison between the two OreLog porosity estimation approaches HI and ϕ and core analysis data for borehole FMC004 are shown in Figure 6.32 and for five boreholes (FWD0001-0005) with pump test data in Figure 6.33 in form of boxplots. HI from OreLog is in good agreement with porosities for core samples 1, 2, and 7, but underestimates the porosities from core samples 3, 4, 5, and 6. Porosity values from OreLog are generally smaller than HI – due to Equation 4.30 (cf. Figure 4.5). Therefore, the OreLog output porosity ϕ underestimates core analysis data almost by factor 2.

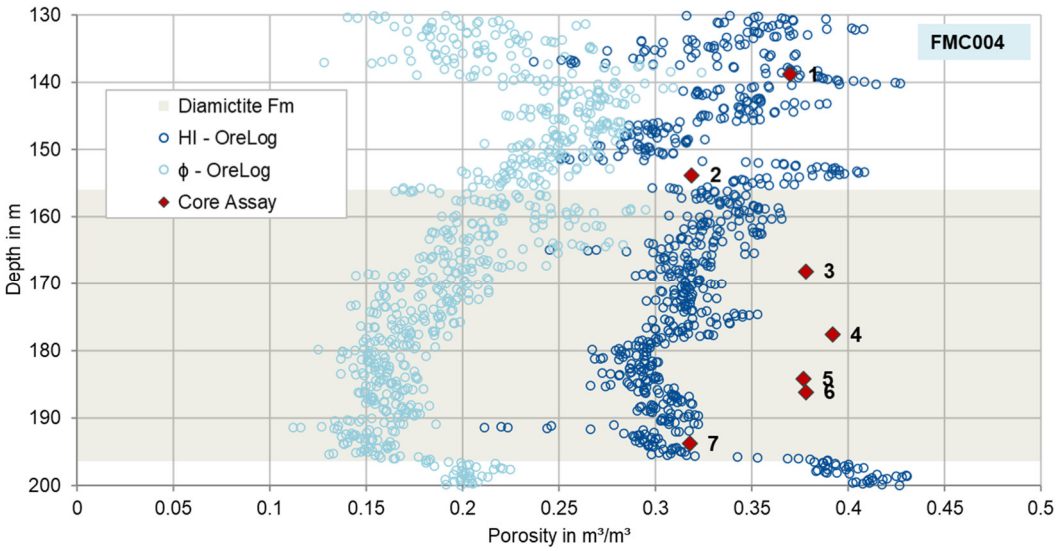

Figure 6.32: Comparison of porosity (m^3/m^3) from core analysis and OreLog logging at borehole FMC004. Porosities from OreLog are shown as Hydrogen Index (HI) and ϕ (Phi).

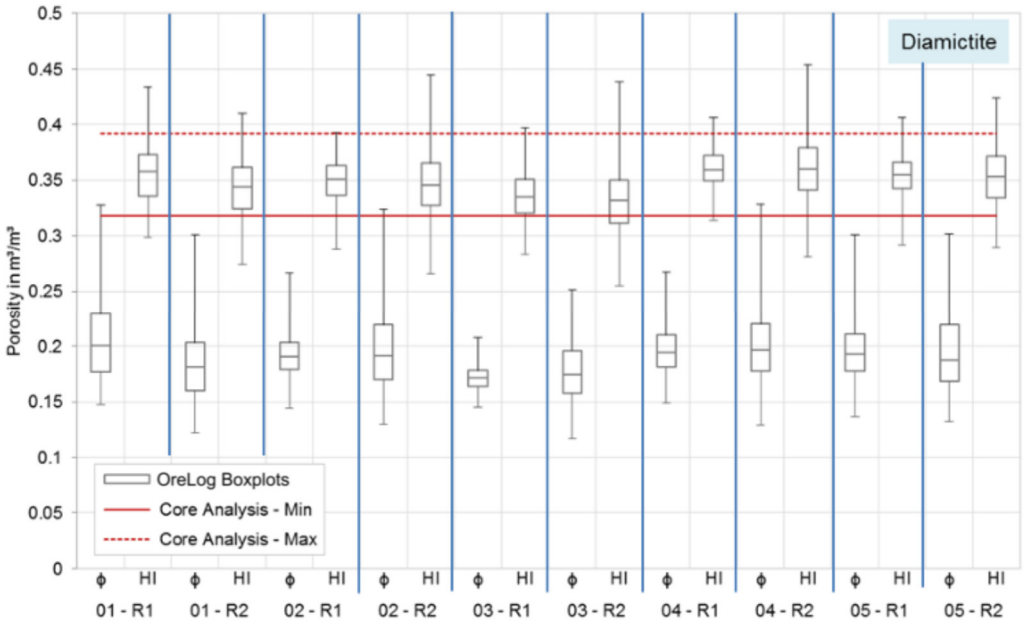

Figure 6.33: Boxplots for porosity ϕ and HI from OreLog for 5 boreholes FWD0001-FWD0005 (01-05) with 2 runs (R1, R2) for each borehole.

The boxplot in Figure 6.33 confirms repeatability of both HI and ϕ. The quantity HI (OreLog) provides a better estimation of core sample porosity than ϕ (OreLog). The

latter underestimates core analysis data. The OreLog algorithm to calculate ϕ from HI should be improved to better fit the core sample data.

6.4.3 Permeability

Figure 6.34 compares permeability data derived from core analysis and OreLog logging at FMC004 as well as from pump tests at FMW-PT and FMW-FLT area (cf. chapter 5.2.2). The comparison reveals that permeability from OreLog is in good agreement with core analysis samples 1, 3, 4, 5, and 6 (in Eyre and Diamictite Formation) and with pump test at FMW-PT area. The permeability is underestimated by OreLog for core analysis sample 7. This sample lies within the transition zone of FMD and fractured rock basement. Large deviations are observed for core sample 2 where OreLog overestimates permeability by several orders of magnitude, which might be caused by a thin clay layer or concretion.

Table 6.2: Conductivities K (m/day) estimated from pumping tests at FMW. For details see internal report of Heathgate Resources Pty Ltd (2013). Data provided as courtesy of HGR (Heathgate Resources Pty Ltd, 2013).

Test Performed		Date	Well	Zone		
				Diamictite		
				Min	Max	Average
Aquifer Test	Step Drawdown Test	5/8/2009	4MT001/ 4MT002r	0.035	0.042	0.04
FMW-PT	Constant Rate Test	5/10/2009	4MT001	0.70	1.30	1.00
	Best estimate	8/2/2009		0.14	1.30	0.72
Aquifer Test	Step Drawdown Test	8/17/2009	WC04	-	-	0.56
FMW-FLT	Step Drawdown Test	11/15/2012	FW0007	-	-	0.54
	Constant Rate Test	11/15/2012	FW0007	0.30	0.48	0.39

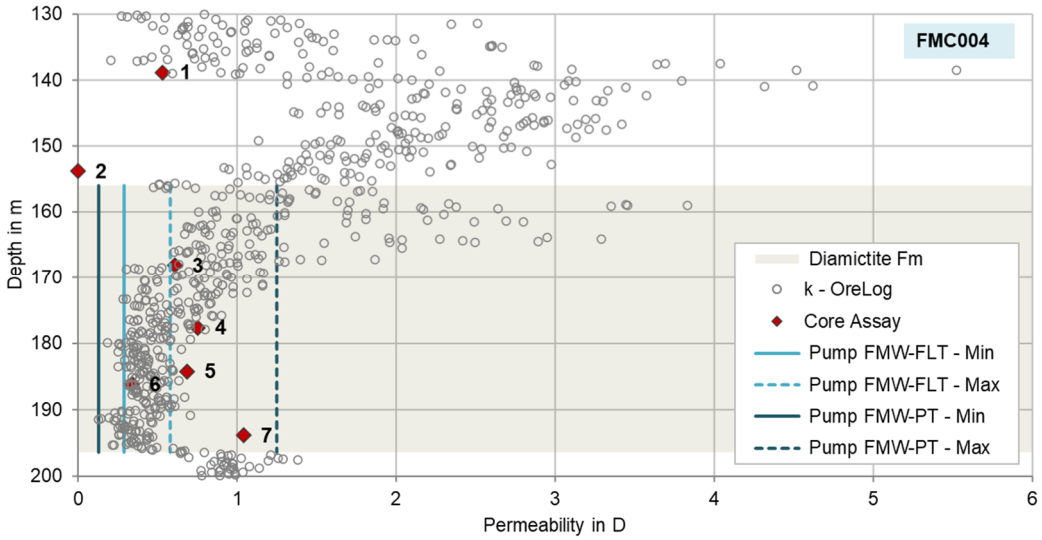

Figure 6.34: Comparison of permeability (Darcy) from core analysis, pump test (FMW-FLT and FMW-PT area) and OreLog logging at borehole FMC004.The distribution of permeability values predicted by OreLog is visualized in form of boxplots in Figure 6.35. Only the depth interval within the Diamictite Formation where the pump test has been realized is considered here. The comparison shows that most of OreLog permeability values lie within the range of core analysis data. For hole 01-R1, 02-R2, 04-R2 and 05-R2 about $\frac{1}{4}$ of the OreLog permeability results overestimate the laboratory measured core permeability. There is a quite good agreement between OreLog permeabilities and values taken from core analysis and pump test at FMW-PT area. Discrepancies are observed for OreLog permeabilities and pump test at FMW-FLT area.

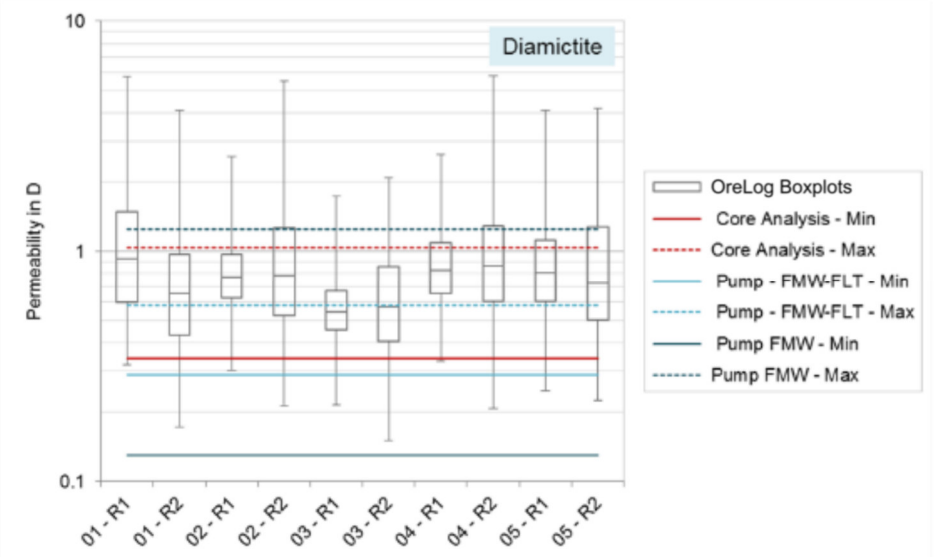

Figure 6.35: Comparison of permeability (Darcy) from core analysis, pump tests (FMW-FLT and FMW-PT area) and OreLog logging for 5 boreholes FWD0001-FWD0005 (01-05) with 2 runs (R1, R2) for each borehole.

6.5 Elemental Logging

This chapter compiles the main results of elemental logging from field data by focusing on single elements and evaluating the respective tool performance. The results are assessed on an element-by-element basis.

6.5.1 Overview

Besides the full suite of geochemical assays, selected holes of interest were also described in detail with regard to lithology and petrophysics as shown in the appendix A.1. During core logging in the field systematic recording and measuring of as much relevant information as required was realized to determine the lithology (major/minor), mineralogy, potential geological history, structure, texture, oxidation, color, and alteration zones. The final and interpreted OreLog output as industry standard WellCAD file in combination with the geologist's lithology log is shown in Figure 6.36.

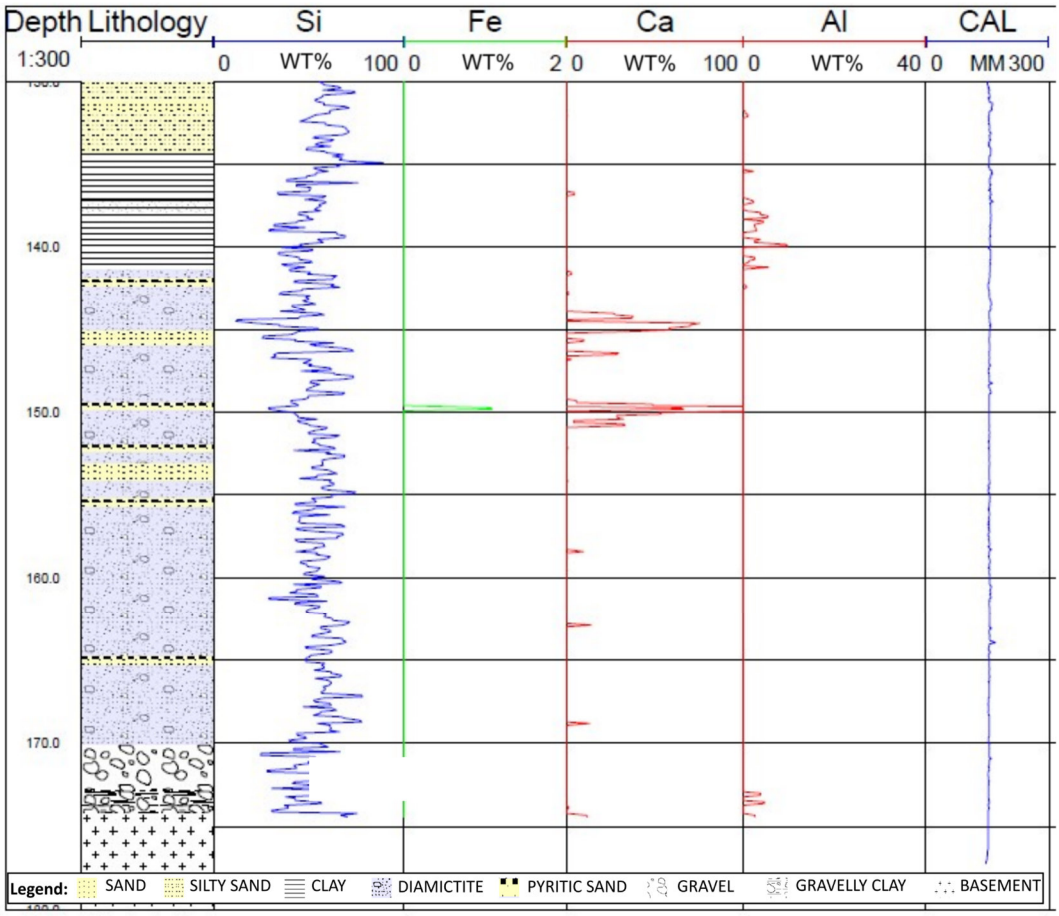

Figure 6.36: WellCAD example of final output file of borehole FWD0201 for elemental logging in comparison to subjective lithology logging by geologists (first column). Pyritic sand layer induces Fe peak. CAL represents caliper log.

Four Mile

Ten boreholes from the central area (FMC005, FMC015 to FMC022; FMC24) and five boreholes from the southern area (FSC0001, FSC0002, FSC0007, FSC0008 and FSC0009) met the quality criteria of both chemical laboratory assays and OreLog output. The highest correlation was reached in hole FSC0009, where the significant iron peak at 165 m (Figure 6.39) recorded both in OreLog and laboratory assay is also visible in the drill core (Figure 5.9). The increase in Mg is also plausible explaining the lithology towards mafic minerals with increased Fe and Mg concentrations that are very well captured by OreLog. In contrast, sedimentary strata around 120 m as demonstrated in Figure 6.37 shows elevated Al and K concentrations which indicate clayey lithologies as confirmed by the core log (Table A.2 in appendix A.1.2). For the interval from 117 – 124 m kaolinitic clay is identified, which corresponds to the silica decrease of both OreLog and laboratory data.

Figure 6.37: Zoom-in of kaolinitic clay interval between 117 - 124 m in FSC0009. For detailed core log see appendix A.1.2.

Pilbara

The main focus of the Pilbara tests was on the identification of iron layers and their characterization in terms of thickness and purity, i.e. quantification of impurities. A total of 35 boreholes logged in the Pilbara (cf. Table 5.4) met the quality criteria of both chemical laboratory assays and OreLog output. Due to its favorable nuclear physical properties and economic importance elemental logging of iron plays a major role in this results chapter. Therefore, details of the Pilbara (iron) logging are presented in the next chapter. Further results of MCNP output from chapter 6.3.2 are compared with logging data from Pilbara and the deconvolution and template matching are illustrated at the example of iron in representation of all other elements.

6.5.2 Iron

Iron is an element very appropriate for being detected by neutron-induced γ-rays. It has a large thermal neutron capture-cross-section (2.56 barn) often dominating the

macroscopic neutron capture cross-section of the formation. Its abundance in the formations logged during Pilbara tests reached from values of 50 wt% or even more down to about 1 wt%. At Four Mile it was only locally peaking to about 20 wt%. The energy spectrum of γ-rays produced by iron-neutron-interaction results in features very beneficial for iron detection as already described in chapter 6.2.8.

This chapter shows OreLog-vs-Laboratory comparisons of iron mass fractions. Comparisons are shown with logarithmic and linear scale on mass fraction, whereas the OreLog data points are usually in 0.1 m intervals and the laboratory data depending on the source (RC chips or core) varies between 0.2 and 2 m intervals.

The distribution of iron mass fraction versus depth is basically always in agreement with laboratory data. Figure 6.38 depicts a selection of Pilbara boreholes showing the very good correlation in high grade goethite zones in iron ore deposits whereas Figure 6.39 also confirms agreement in sedimentary and metamorphic or igneous lithologies from low to high Fe grades. Especially the contact between felsic and mafic schist (cf. Figure 5.9) is resolved well and supported by the increase in other mafic elements (cf. chapter 6.5.9) as well. The iron increase in the diamictite formation of borehole FMC024 initiated at about 115 m is associated with a change from oxidizing to reducing conditions (Figure 6.40) evident in the core log (for details see appendix A.1.1) and cause the related increase in iron-bearing sulfidic minerals (mainly pyrite).

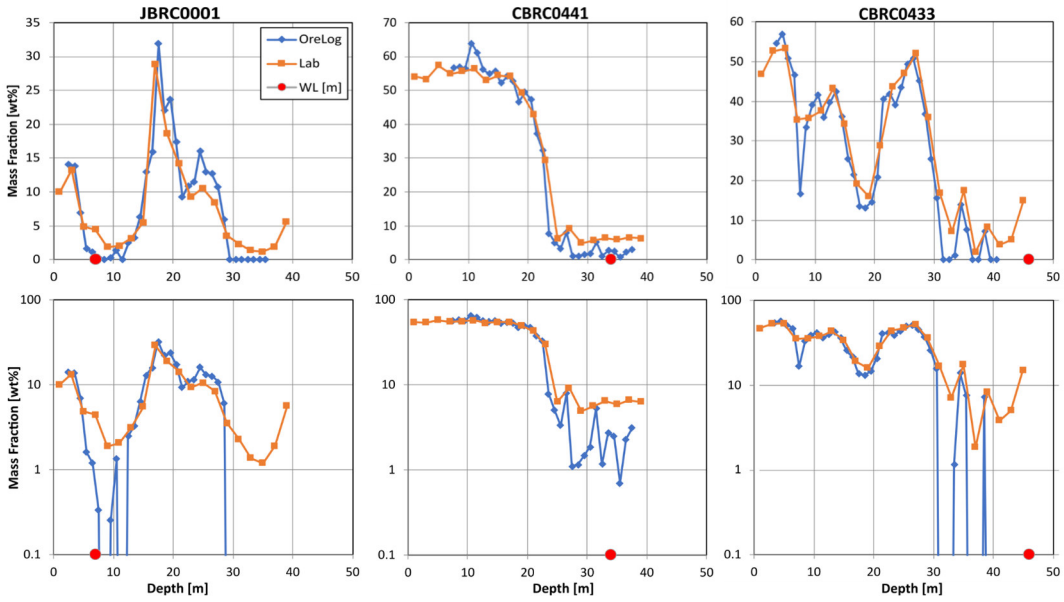

Figure 6.38: Mass fraction of iron (Fe) for three different Pilbara boreholes with linear (top) and logarithmic (bottom) scale for mass fraction. Blue diamonds (♦) indicate OreLog-results, orange squares (■, Lab) indicate RC chip sample or core data derived in laboratory. A red circle symbol (●, WL) indicates the water level in the borehole during OreLog logging. This legend is valid for all subsequent figures.

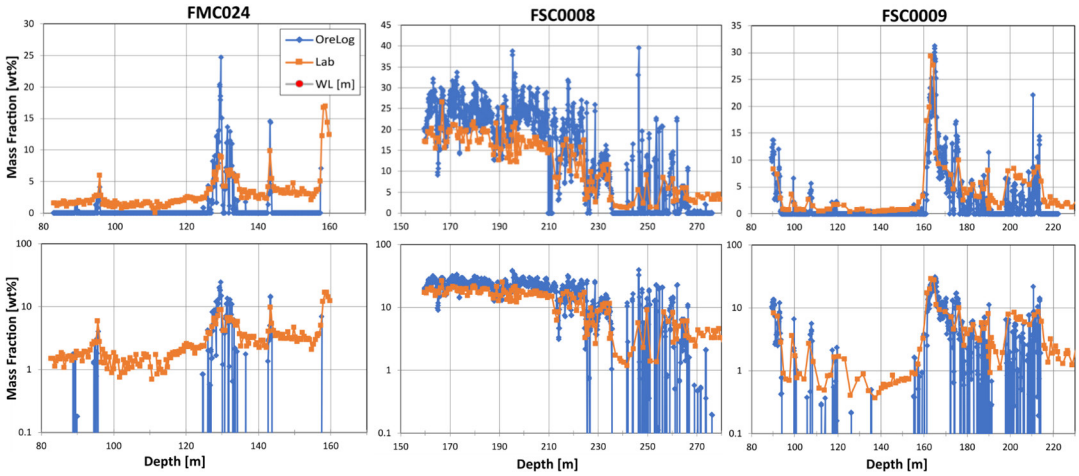

Figure 6.39: Mass fraction of iron (Fe) for three different Four Mile boreholes with linear (top) and logarithmic (bottom) scale for mass fraction. All below water table.

The combination of adapted model function based on chapter 6.3.3 and measured energy spectra is demonstrated at the example of one Pilbara borehole. A collection of typical adaptions of model-function $f_{Model,tot}$ to measured spectra for borehole CBRC0441 (cf. Figure 6.38) are shown in Figure 6.41 and Figure 6.42. The diagrams impressively illustrate how (from top to bottom of hole) iron declines, and aluminum, silicon, and potassium increase. At the very bottom of the hole there is also hydrogen present (due to logging below water table).

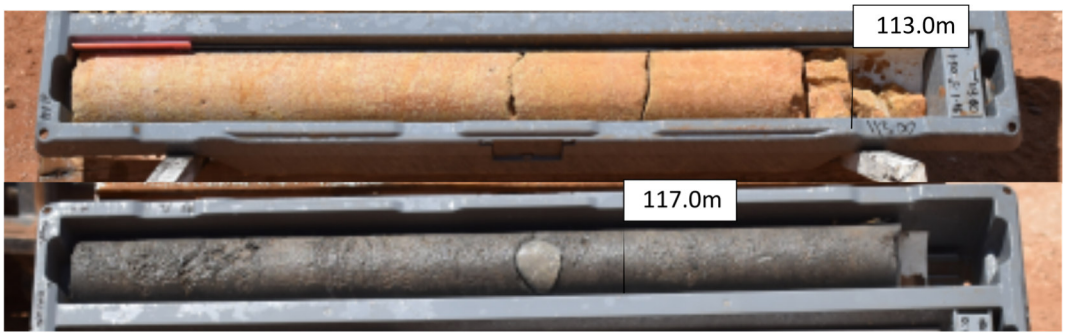

Figure 6.40: Transition from oxidizing to reducing zone in diamictite in borehole FMC024 showing representative drill core from the respective zones. Drill direction from left to right.

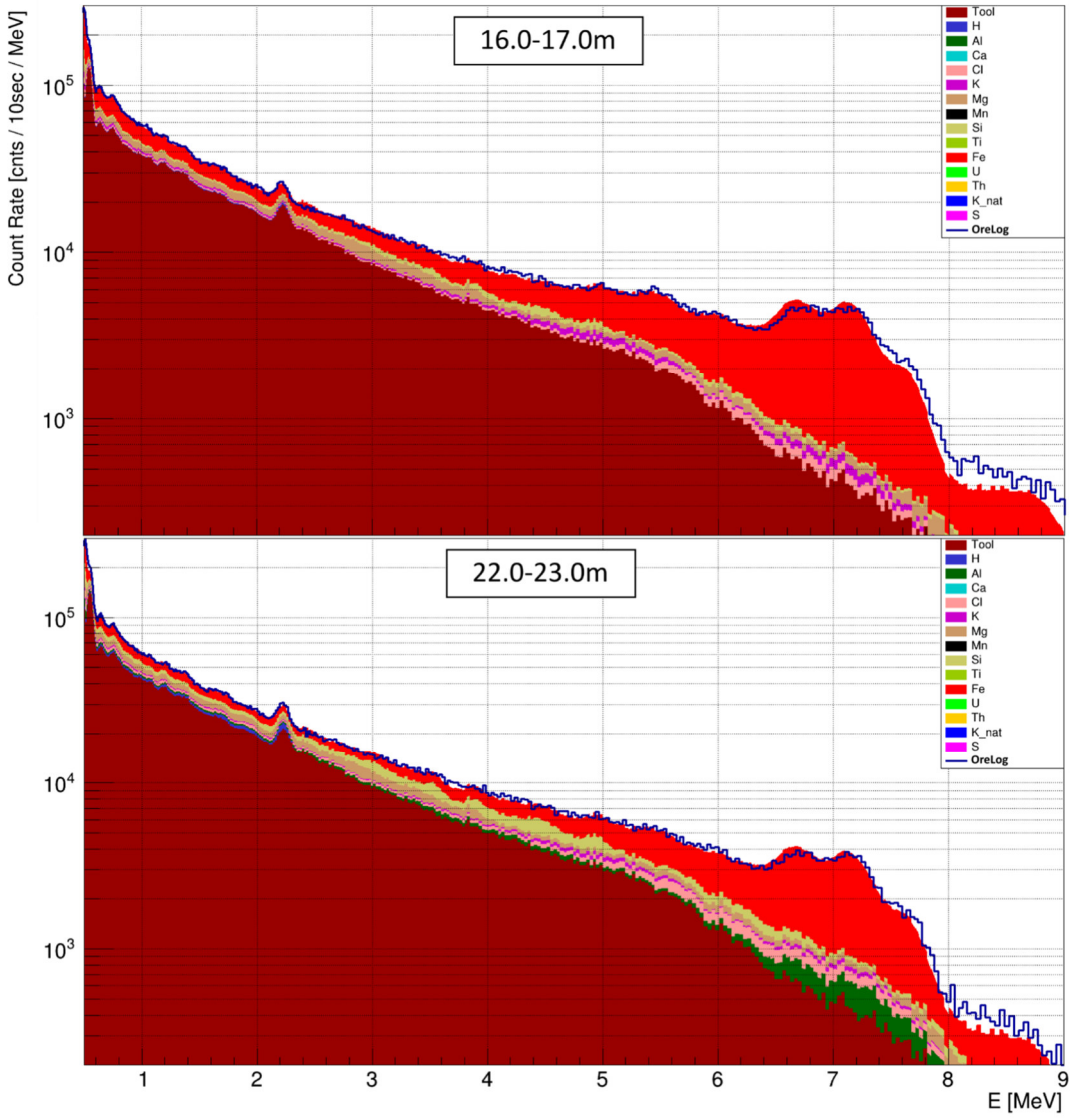

Figure 6.41: Measured energy-spectra (blue line with legend-entry 'OreLog') overlaid with adapted model-function fModel,tot. Element specific contributions to the model-function are displayed by different fill-colors. Top and bottom diagram show different depth intervals of borehole CBRC0441.

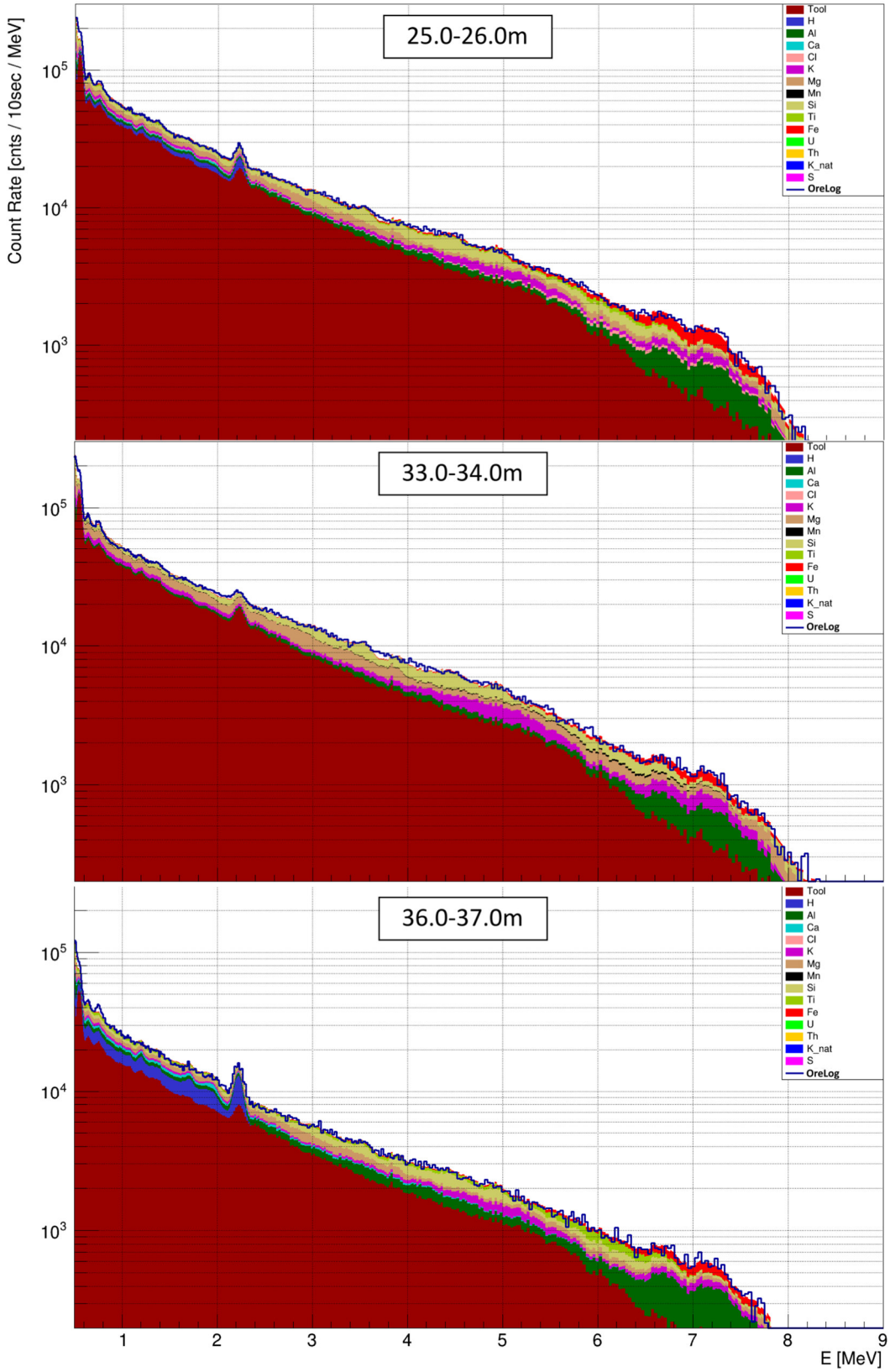

Figure 6.42: Measured energy-spectra (blue line with legend-entry 'OreLog') overlaid with adapted model-function $f_{Model,tot}$. Element specific contributions to the model-function are displayed by different fill-colors. Top, middle and bottom diagram show different depth intervals of borehole CBRC0441.

6.5.3 Aluminum

The thermal neutron capture cross-section of aluminum (0.232 barn) is less than a tenth of the thermal neutron capture cross-section of iron (2.56 barn). The significant part concerning γ-ray detection at 7.7 MeV of the energy-spectrum of aluminum is very similar to the one of iron (cf. Figure 6.29). However, OreLog's energy-resolution (as described in chapter 6.2) during the field tests was sufficient to enable Al-Fe-discrimination. For aluminum only 20 % of all capture γ-rays contribute to the significant Al γ-ray-pattern at 7.7 MeV. But in case of iron more than 50 % of all capture γ-rays contribute to the significant part of γ-ray-pattern at 7.7 MeV. The detailed statistics regarding energy distribution, uncertainties and other significant prompt γ rays of elements of interest are compiled in Lone et al. (1981).

A selection of good aluminum examples is shown in Figure 6.43. For concentrations larger than 5 wt% the results of Al mass fractions show an acceptable agreement between OreLog data and laboratory data. For Al grades below 1 wt% there is only minor agreement between OreLog data and laboratory data. In general, the shape of the Al profile (i.e. Al mass fraction vs depth) can be nicely reproduced showing relative values whereas it is more difficult to determine the absolute values of the Al mass fractions.

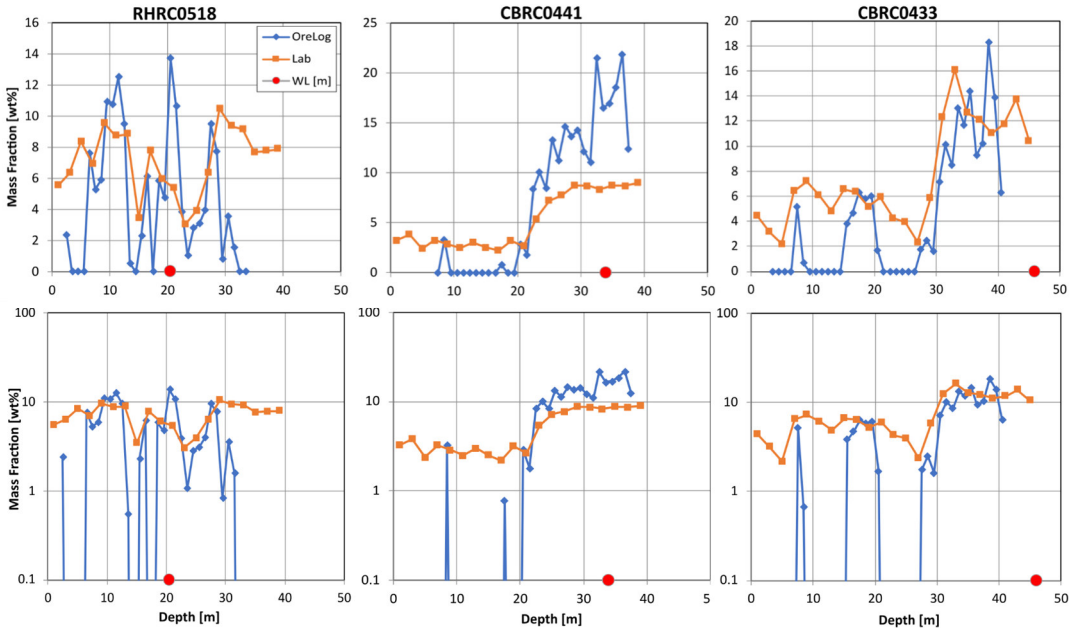

Figure 6.43: Mass fraction of aluminum (Al) for three different Pilbara boreholes with linear (top) and logarithmic (bottom) scale for mass fraction.

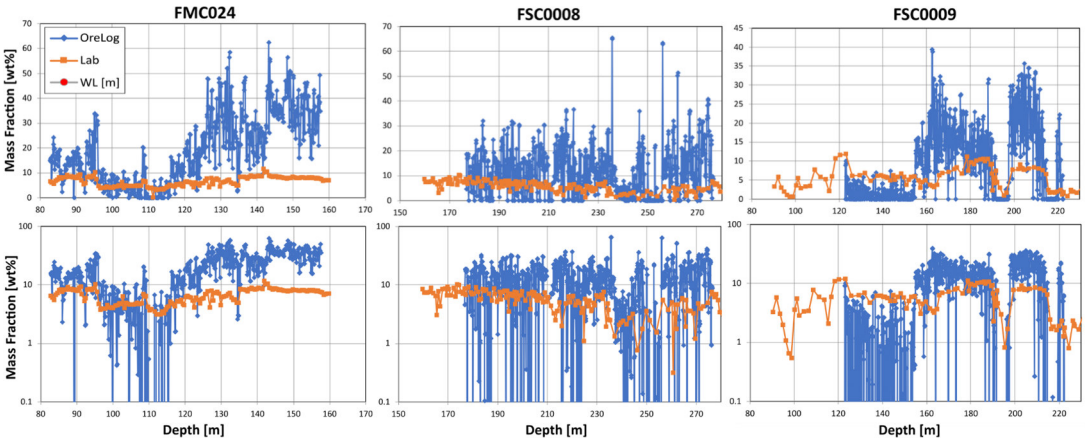

Figure 6.44: Mass fraction of aluminum (Al) for three different Four Mile boreholes with linear (top) and logarithmic (bottom) scale for mass fraction. All below water table.

6.5.4 Silicon

The thermal neutron capture cross-section of silicon (0.172 barn) is even smaller than the one of aluminum (0.232 barn) and far smaller than the one of iron (2.56 barn). However, in contrast to aluminum the γ-ray pattern of silicon is more significant because it has predominant capture-γ rays (at energies of 3.5 and 5.0 MeV).

A selection of good examples is compiled in Figure 6.45. As in case of aluminum, for concentrations larger than 5 wt% the results of Si mass fractions show good agreement between OreLog data and laboratory data. It is generally better for silicon than for aluminum.

In some cases, absolute scaling is slightly off, but the shape of the profile mostly agrees well between OreLog data and laboratory data.

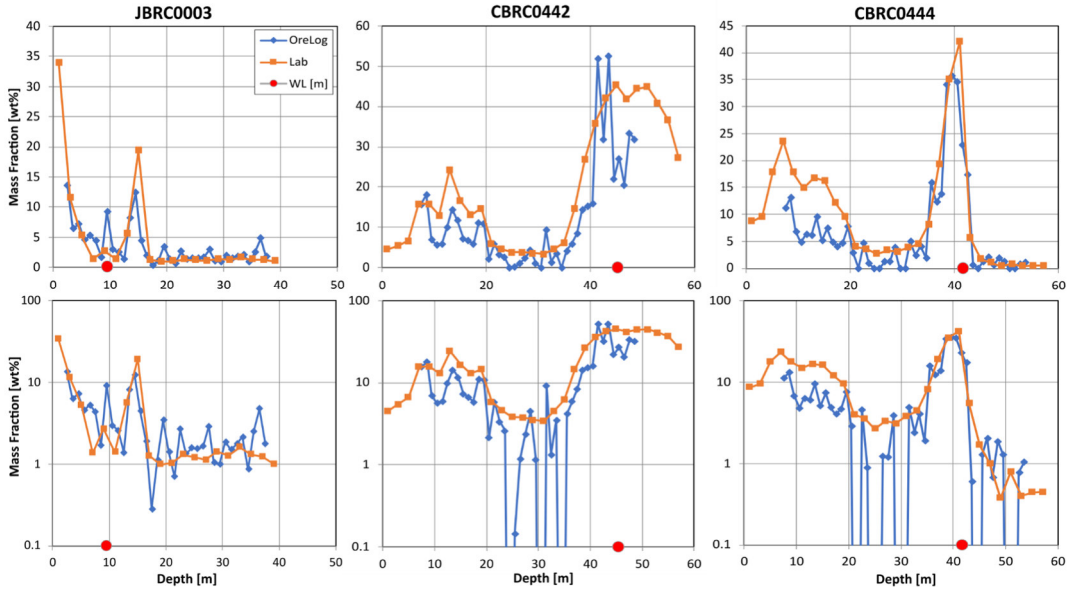

Figure 6.45: Mass fraction of silicon (Si) for three different Pilbara boreholes with linear (top) and logarithmic (bottom) scale for mass fraction.

6.5.5 Calcium

The thermal neutron capture cross-section of calcium (0.431 barn) is higher than the one of aluminum (0.232 barn). Also, more than 50 % of all Ca capture γ-rays contribute to the significant γ-ray at about 2.0 MeV. This is directly on the Compton edge of the hydrogen spectrum. In general, the pattern of the Ca γ-ray energy spectrum is a very characteristic one resulting in good discriminability against other elements. However, a disadvantage is the relatively smooth and indistinguishable shape of the energy-spectrum (cf. Figure 6.29), i.e. most γ-rays are created at 2 MeV or lower energies without any peaks in the high-energy part.

A selection of good examples is shown in Figure 6.46. Ca mass fractions greater than 10 wt% can be detected well. Ca mass fractions below 5 wt% are difficult to detect since they are close to the detection limit.

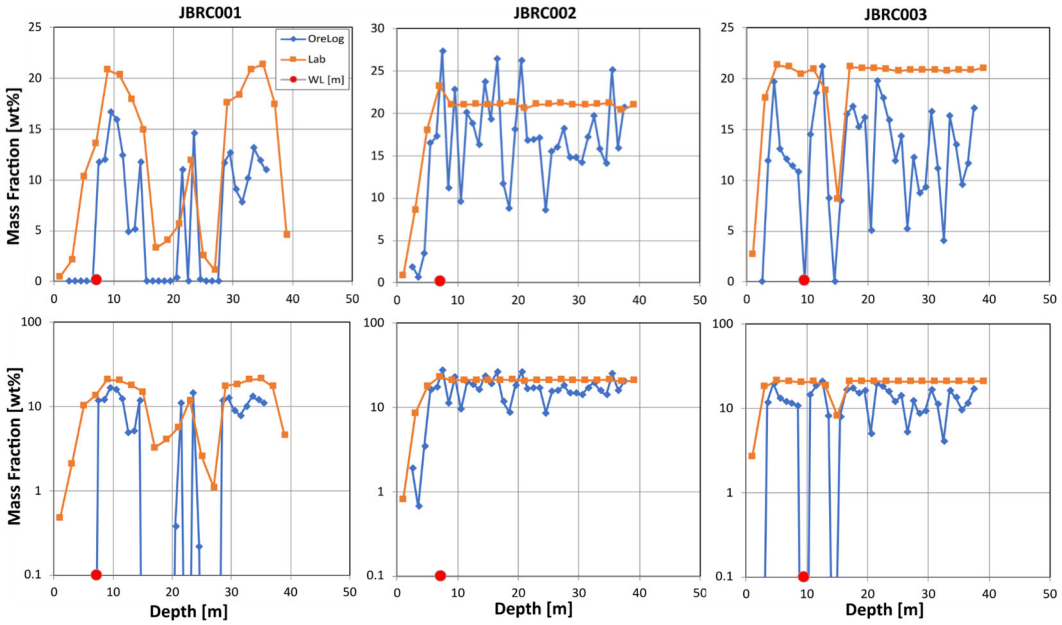

Figure 6.46: Mass fraction of calcium (Ca) for three different Pilbara boreholes with linear (top) and logarithmic (bottom) scale for mass fraction.

6.5.6 Chlorine

Chlorine has an extremely high thermal-neutron absorption cross-section as well as a very significant capture γ-ray energy spectrum. This allows for detection down into the 100 ppm range, i.e. down to mass fractions of 0.005 wt%. The great performance concerning determination of chlorine mass fraction is illustrated in Figure 6.47.

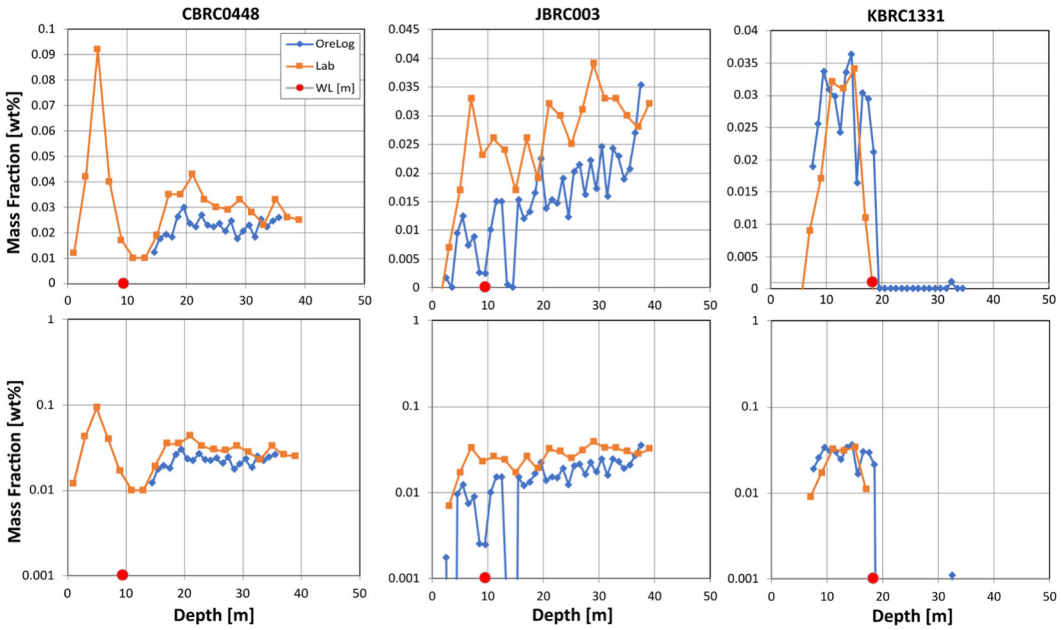

Figure 6.47: Mass fraction of chlorine (Cl) for three different Pilbara boreholes with linear (top) and logarithmic (bottom) scale for mass fraction.

At borehole FMC005 the PVC casing schematically illustrated in Figure 5.10 served as an ideal training environment by surrounding the tool with known material at an exactly known depth. The chlorine contained in PVC causes a strong signal in the γ capture spectrum with the chlorine specific pattern shown in Figure 6.48, which was already confirmed by laboratory experiments in chapter 6.2.8 and illustrated in Figure 6.17. The pattern abruptly disappears at 139 m down to the final depth, where PE casing (free of chlorine) is installed.

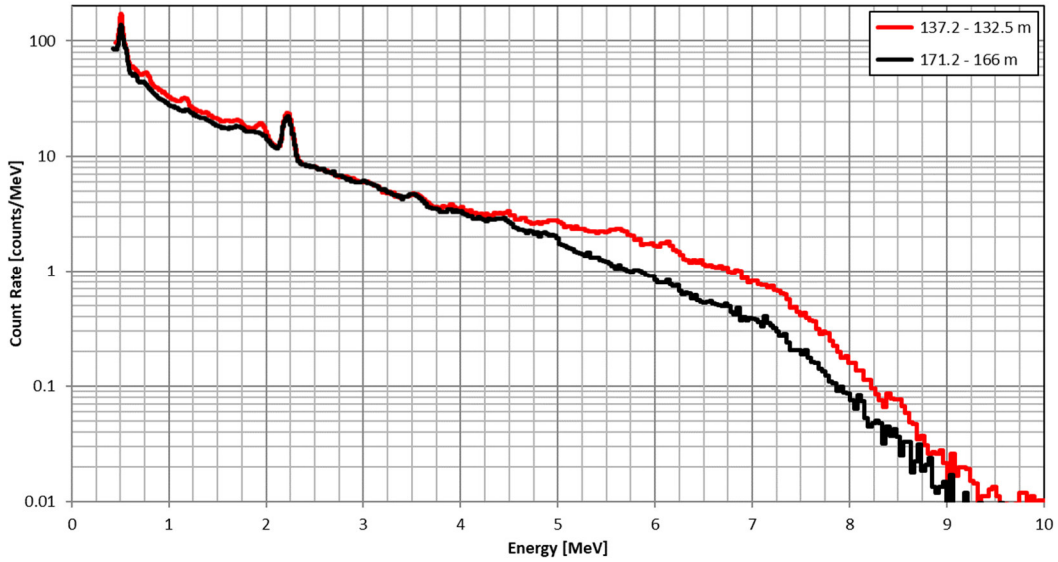

Figure 6.48: OreLog capture γ-ray spectra recorded in FMC005 during an active generator uphole run at depth range 137.2 - 132.5 m (red) with PVC casing and 171.2 – 166 m (black) without PVC casing.

6.5.7 Titanium

Titanium concentrations in core data are usually around 1 wt% or lower and only in some rare cases above 2 wt%. The cross-section is quite large (6.09 barn) but the wide and indistinct peak around 6 MeV (cf. Figure 6.29) does not provide unambiguous discernibility at low grades. Nevertheless, in boreholes with elevated Ti concentrations like RHRC0518 OreLog corresponds well to laboratory data and even in some average grade boreholes the Ti trend could be reflected (RHRC0519 and JBRC0007) as shown in Figure 6.49. Generally, the Ti concentrations of the investigated deposits are relatively low and do not allow conclusive results based on the existing database.

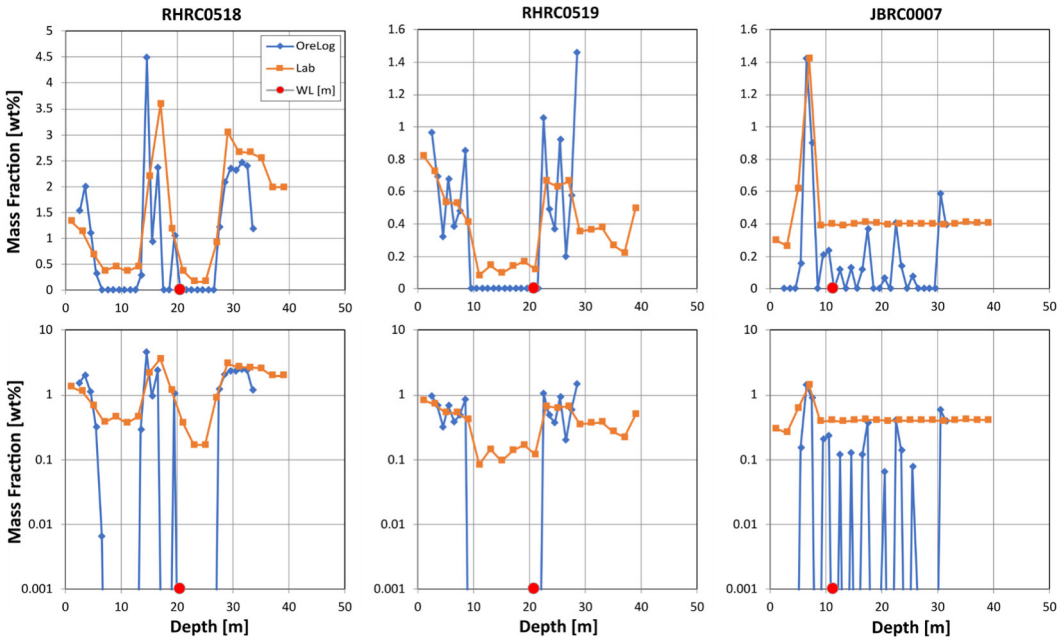

Figure 6.49: Mass fraction of titanium (Ti) for three different Pilbara boreholes with linear (top) and logarithmic (bottom) scale for mass fraction.

6.5.8 Potassium

The cross-section of potassium is with 2.1 barn rather small and the fact that the characteristic peaks are in the high-energy region of the γ spectrum around 5 and 7 MeV are relatively wide. Combined with the low K grades generally around 2 wt% the discernibility of K from background in the investigated deposits was challenging. Partially, there is an acceptable agreement between potassium mass fractions obtained by OreLog and potassium mass fractions obtained by laboratory analyses as shown in Figure 6.50. Both Four Mile and Pilbara results indicate a detection limit of potassium of about 1 to 3 wt%.

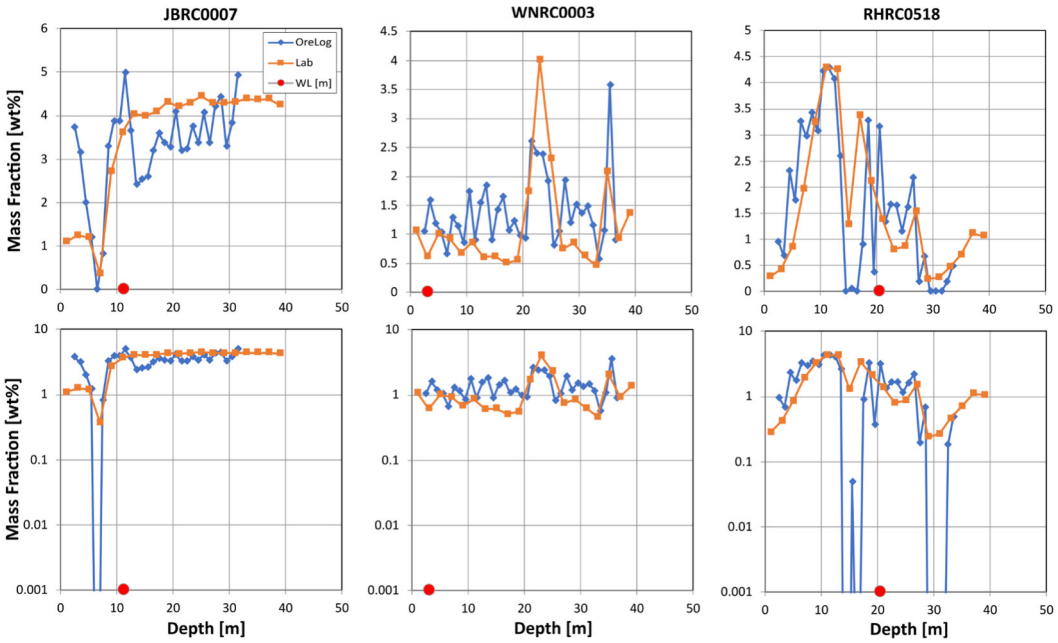

Figure 6.50: Mass fraction of potassium (K) for three different Pilbara boreholes with linear (top) and logarithmic (bottom) scale for mass fraction.

6.5.9 Manganese

Manganese has a rather elevated cross-section of 13.3 barn but no significant peaks in the capture spectrum apart of one small peak just below 3 MeV. The Mn concentrations of the investigated boreholes are generally below 0.1 wt% and only exceptionally reach the single-digit range as exemplarily shown by borehole JBRC0001 in Figure 6.51. For lower Mn grades OreLog showed the potential to reflect the trend and provide semi-quantitative results. Generally, the Mn concentrations of the investigated deposits are very low or below detection limit of the laboratory analytical method and therefore do not allow conclusive results regarding OreLog Mn detection limits and quality.

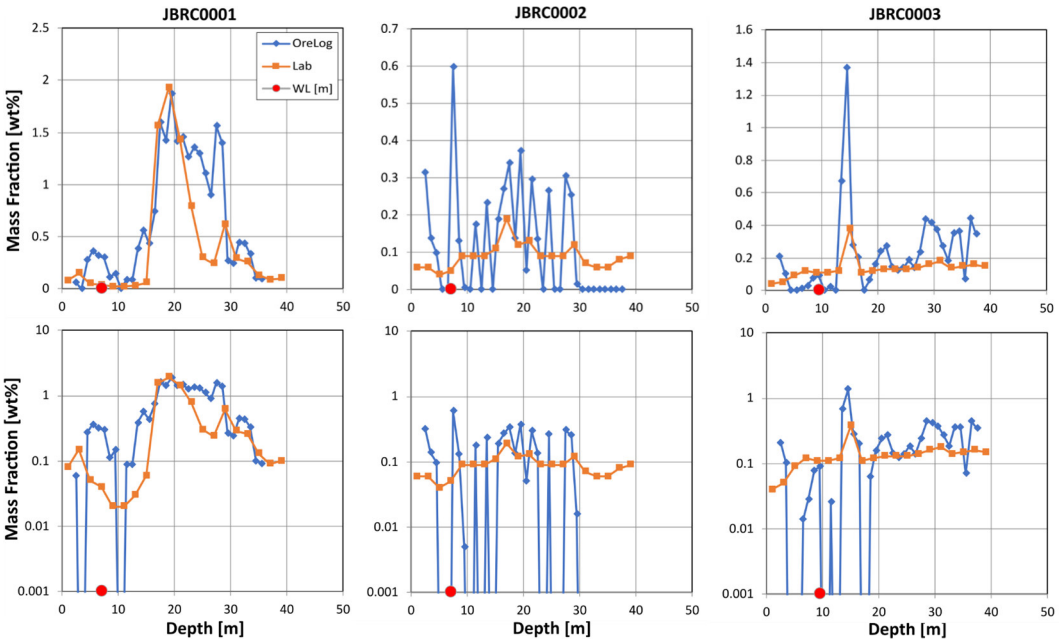

Figure 6.51: Mass fraction of manganese (Mn) for three different Pilbara boreholes with linear (top) and logarithmic (bottom) scale for mass fraction.

6.5.10 Other Elements

The OreLog data analysis algorithm does not only quantify the previously mentioned elements, but it also processes logged data for elemental mass fractions of C, H, Mg, and REE. Since neither the investigated deposits did contain detectable concentrations nor the OreLog tool does yet provide correlated results, only some qualitative observations are compiled here.

Carbon

A carbon pattern as measured in the laboratory tests in chapter 6.2.8 (cf. Figure 6.17) was detected in the burst spectrum of FMC011. Therefore, a carbon-related count-rate was defined relying on the C signal region from 4.23 to 4.63 MeV and the side-band region from 4.68 to 4.93 MeV of the burst spectrum. The actual carbon-related count rate is defined as the difference between the count rates in these two energy-ranges. There are no laboratory assays of carbon available this carbon related OreLog count rate could be compared against, but the visual core logging shows a correlation with carbonaceous layers (Figure 6.52).

Figure 6.52: Carbonaceous interval at 159.1 m in FMC011 alternating with claystone layers.

Hydrogen

The most significant feature present in the capture γ-ray spectrum of a typical log in both investigated deposits is the full-energy peak (PP) of hydrogen capture γ-ray at 2.223 MeV, which is dominant in any energy-spectrum shown in this work (cf. e.g. Figure 6.29 and Figure 6.42). However, there is hydrogen in the following volume-elements around OreLog's neutron source:

1. H in OreLog tool, mainly chassis parts (POM) present around all detectors,
2. H in water in the borehole,
3. H in formation,
   a. H in 'mobile' parts of pores (→ mobile water, effective porosity),
   b. H in 'immobile' parts of pores (→ immobile water, ineffective porosity),
   c. H as part of minerals of formation (→bound water, bound OH), mostly as H_2O or OH in clays and in minerals.

The H-peak at 2.223 MeV is a summation of γ-rays from H of all the sources in the list above. The volume-elements dominantly contributing to the measured H-peak are the ones from the water in the borehole. Therefore, the H-peak area is measured in the spectrum and translated into a borehole diameter as schematically indicated in Figure 4.5. The good correlation of the borehole diameter derived from the H-peak area with the physically measured borehole diameter by a caliper tool is impressively shown in Figure 6.53.

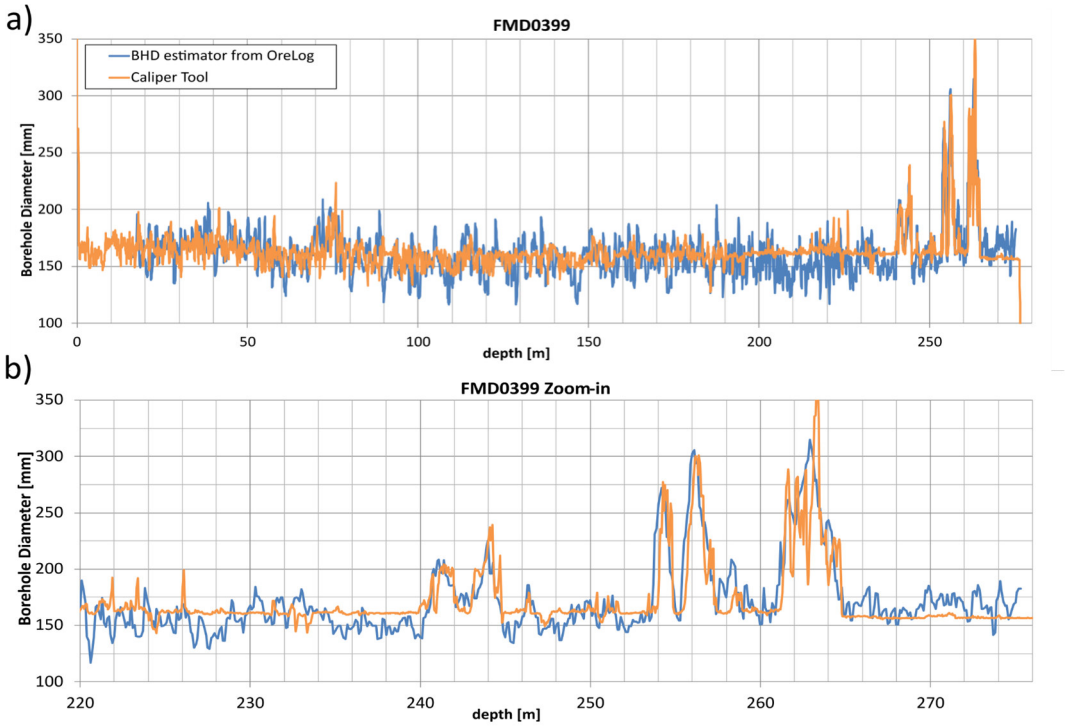

Figure 6.53: Borehole diameter from OreLog (BHD in blue) compared to borehole diameter measured by caliper tool (in orange) over the entire borehole depth of FMD0399 (a). Bottom plot (b) shows a zoom-in of the interesting section from 220 to 276 m.

Magnesium

Except for borehole FSC0009 Mg concentrations are below 1 wt% in Four Mile and due to the low cross-section (0.063 barn) not detectable by OreLog in most boreholes. At Pilbara some intervals contain up to 10 wt% Mg and occasionally OreLog captured those but no statistically significant correlation of laboratory data with OreLog data was found for Mg neither in the laboratory experiment in Dresden nor in the two field tests in Australia. Nevertheless, for the detection of a lithology change from felsic to mafic minerals the OreLog output indicates the correct trends as visible in Figure 5.9.

7 Discussion

7.1 Detectors

Generally, the performance of the source strength detector (CVD detector) at the tested parameters and installed position is as expected and provides the required fast neutron data with sufficient accuracy and in time. The periodic fluctuations and short-term variations of the neutron source strength are recorded with sufficient detail and the absolute source strength became an important parameter to normalize the detector response, especially the count rate of the γ-detector. Several Schlumberger borehole logging tools also use a diamond detector for fast neutron detection and achieve similar results as stated in Rose et al. (2015). The importance of the depth and source strength correction based on the SSD output for the OreLog tool is illustrated in Figure 4.5. Owing the quantum leap in performance of recently available detectors, that for instance Smith et al. (2013) and others were not able to use in their work, caused a significant improvement in data quality and accuracy.

The five ^{3}He neutron detectors at their installed positions (four radial units form the near-detector and one far-detector) and tested parameters (^{3}He gas pressure and bias voltage) performed as expected and provided the required data for time dependent n-distributions for elemental logging. Although the count rate dependent dead time was investigated, which enables the necessary count rate correction, it was recommendable to reduce the count rate to dead time values of 5-10 %, which is the case at 50 - 150 kcps. One option could be the decrease of detection sensitivity of the ^{3}He tubes by reduction of the ^{3}He content. This influence and variation of the ^{3}He partial gas pressure was not investigated in this work since the adaptation of ^{3}He gas filling can only be realized by the manufacturer. The macroscopic neutron-absorption cross-section Σ_B measured by the far thermal detector is a key parameter to account for the matrix-dependency of elemental logging. As shown by the MCNP simulations (cf. chapter 6.3.1) both the far- and near-detectors can measure the thermal neutrons far from and respectively nearby the source. During the field campaigns and data interpretation it became obvious that the near detectors measure the thermal neutrons from the surrounding formation as expected but the exact characterization of the neutron cloud in terms of intensity and shape requires a second neutron detector unit nearby or at the source. This might be achieved by a set of central-detectors directly surrounding the NG and should allow the exact description of the neutron cloud based on the near-and central-detector count rates.

The γ-detector provides many adjustable parameters as extensively documented in chapter 6.2. Compromises between technical feasibility and quality of the γ-spectra had to be made. The initially envisaged but unavailable $LaBr_3$ detector which is implemented in various other tools (Rose et al., 2015) provides similar resolutions as the installed $CeBr_3$ scintillator crystal, which shows significantly better performance (cf. Table 3.2) than industry standard detectors like $LaCl_3$, NaI or BGO as outlined in chapter 3.4.1 or discussed in Celata et al. (1997), Borsaru et al. (2001) and Borsaru et al. (2006). The $LaBr_3$ scintillator crystal displays a higher energy resolution and higher photo yield, which would be advantageous to improve peak discernability, but its intrinsic radioactivity (Shi et al., 2017) poses other challenges. Unfortunately, during the time of tool development and testing as part of this thesis no such scintillator crystal was procurable.

While field-testing the detectors and spectral analysis the idea of implementing a second γ-spectrometer arose. Only with two γ-spectrometers placed at a certain distance or an adapted NG pulsing regime (cf. Figure 7.1), the analysis of inelastic neutron scattering (burst spectrum) is achievable with sufficient accuracy. In this case the second spectrometer needs to be located behind the NG in active mode to be moved through the activated zone during an uphole run. This is required to accurately quantify the oxygen concentration in the surrounding formation and the only appropriate and reliable measuring mode (cf. Table 2.2). However, the variation of oxygen in the investigated deposits is rather small and most minerals contain similar oxygen fractions. Therefore for the purpose of deposit characterization as part of this thesis, oxygen was not considered but could be implemented as outlined in the work of Radtke et al. (2012) and Rose et al. (2015).

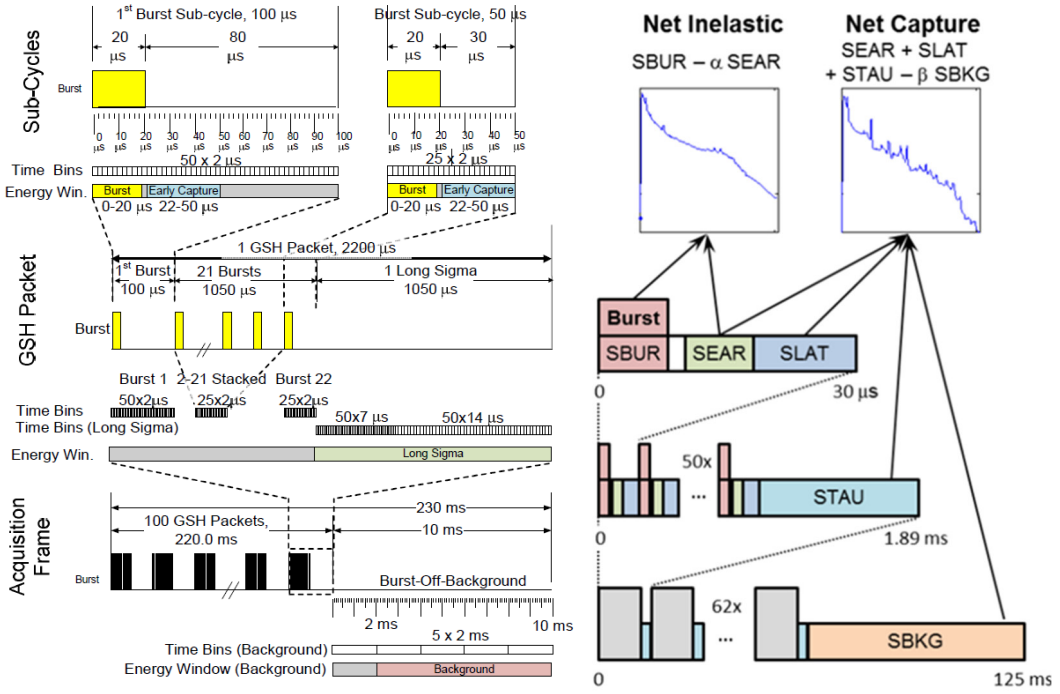

Figure 7.1: PNG pulsing scheme and time windows of γ-detector for data acquisition as used by various Schlumberger tools (Radtke et al., 2012; Rose et al., 2015). OreLog omits the SEAR- and SLAT spectrum and records spectra rather corresponding to SBUR- STAU- , and SBKG-spectra. Abbreviations: SEAR – Early capture spectrum, SLAT – Late capture spectrum, SBUR – Burst spectrum, STAU – Tau spectrum for determination of Σ, SBKG – Background spectrum.

The γ-spectrometer and neutron detectors are currently measuring time-resolved in 3 and 8 time windows (Table 3.1), respectively. In case of the γ-spectrometer the burst window is set according to the NG pulse regime, but its width and the start and width of the subsequent capture and activation windows (currently both set to identical width of 442.5 µs) can be adjusted. Small changes either in the starting point or window width have a significant influence on the resulting count rates and spectra. This also accounts for the 8 time windows of the near- and far-neutron detector units. The fast neutron or source strength detector (cf. chapter 6.1.1) is excluded since it measures continuously the neutron flux at the neutron generator and not the formation response. Adaptations in the gamma time windows and neutron time windows would result in changing elemental concentrations and changing petrophysical formation properties respectively. Therefore, the time windows were chosen carefully based on literature or manufacturer recommendations, expected physical interaction and required count rate ratios (statistics), laboratory testing results and experience of field campaigns as reported in chapters 3, 4, 6.1, and 6.2. Nevertheless, the results in chapter 6.4 and 6.5 showed that there is room for optimization in both the amount of time windows and

their timing as exemplarily illustrated in Figure 7.1. An increase of the amount of time windows provides better resolution and allows the enhanced deduction of physical observations as improved nuclear interaction interpretation (such as inelastic scattering and activation), monitoring of gain instabilities like peak shifts, and element-specific decline times. Figure 7.2 exemplarily shows the resulting spectra of a water tank measurement with 8 time windows (see legend for time window intervals) corresponding to 8 individual spectra instead of 3 providing significantly more information and interpretation potential.

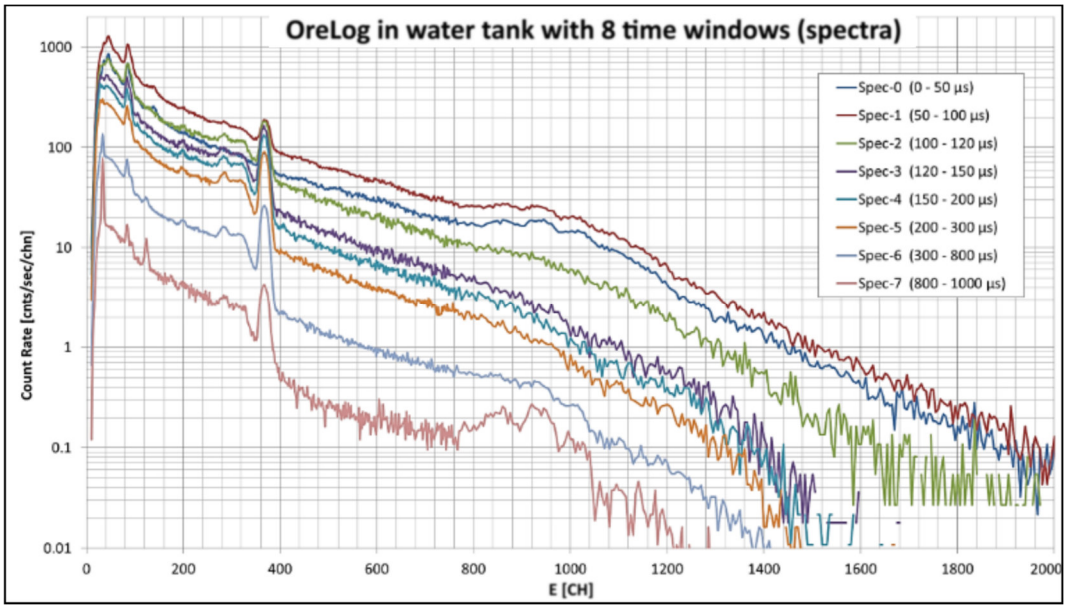

Figure 7.2: Example spectra of γ-detector for 8 instead of 3 time windows.

7.2 Petrophysics

The quantification of petrophysical parameters like density and porosity by OreLog was successful after a site-specific tool calibration. A realistic estimation of permeability was only achievable in well-known lithologies and is not applicable in general. Other petrophysical parameters (e.g. magnetic susceptibility, acoustic/mechanical properties) are not detectable by pulsed neutron logging. The plots in chapter 6.4 confirm the ability of OreLog to reliably depict the density, porosity and permeability trends relative to core analysis and pump tests. Repeatability is confirmed in several boreholes by repeated runs (Figure 6.31 and Figure 6.33). For both the density (Equation 4.29) and the porosity (Equation 4.26) estimator two different calculation approaches relying either on HI or ϕ have been tested. In both cases the HI approach results in estimations closer to the results of core analysis, which suggests a revision of the initial estimator

approach. In case of permeability (Equation 4.36) two datasets (core assays and pump tests) were available for comparison posing a unique situation. As substantiated in chapter 6.3.1, the volume analyzed by OreLog is a cylinder along the borehole of up to 1 m in diameter. Hence the mesoscopic (few cm^3) core plug analysis can be compared to the macroscopic (several m^3) pump test providing permeability data in two completely different scales. In both comparisons the OreLog permeability estimator lies within the measured data (cf. Figure 6.34 and Figure 6.35), also in different zones of the Four Mile deposit. The repeatability is good (Figure 6.35) and proves the applicability of the chosen algorithm.

The deviations of OreLog porosity compared to core assays could also be confirmed in two boreholes (FMC011 and FMC012) where borehole NMR logs were available providing statistical significance compared to the few data points presented in Figure 6.32. Borehole FMC011 was logged by OreLog and NMR and the results of seven core plugs laboratory porosity assays were provided by the mining company. It was logged with a state of the art borehole NMR tool as described in Trofimczyk et al. (2018). Besides the lithological log (cf. appendix A.1), Figure 7.3 compares all available datasets within the interval of interest. The comparison clearly emphasizes the porosity underestimation by OreLog independent of the prevalent lithology and the more realistic porosity estimation by a conventional NMR borehole tool. Müller-Petke et al. (2011) compare the application of surface and borehole NMR and come to a similar conclusion. Therefore, porosity estimations by OreLog do not present a viable alternative to NMR tools based on the current performance. A logging string with both tools (NMR, OreLog) is recommended for a comprehensive petrophysical characterization. There is potential to improve the provisional approach presented here by considering other parameters like Σ or introducing new deposit-specific parameters for the deduction of porosity by OreLog.

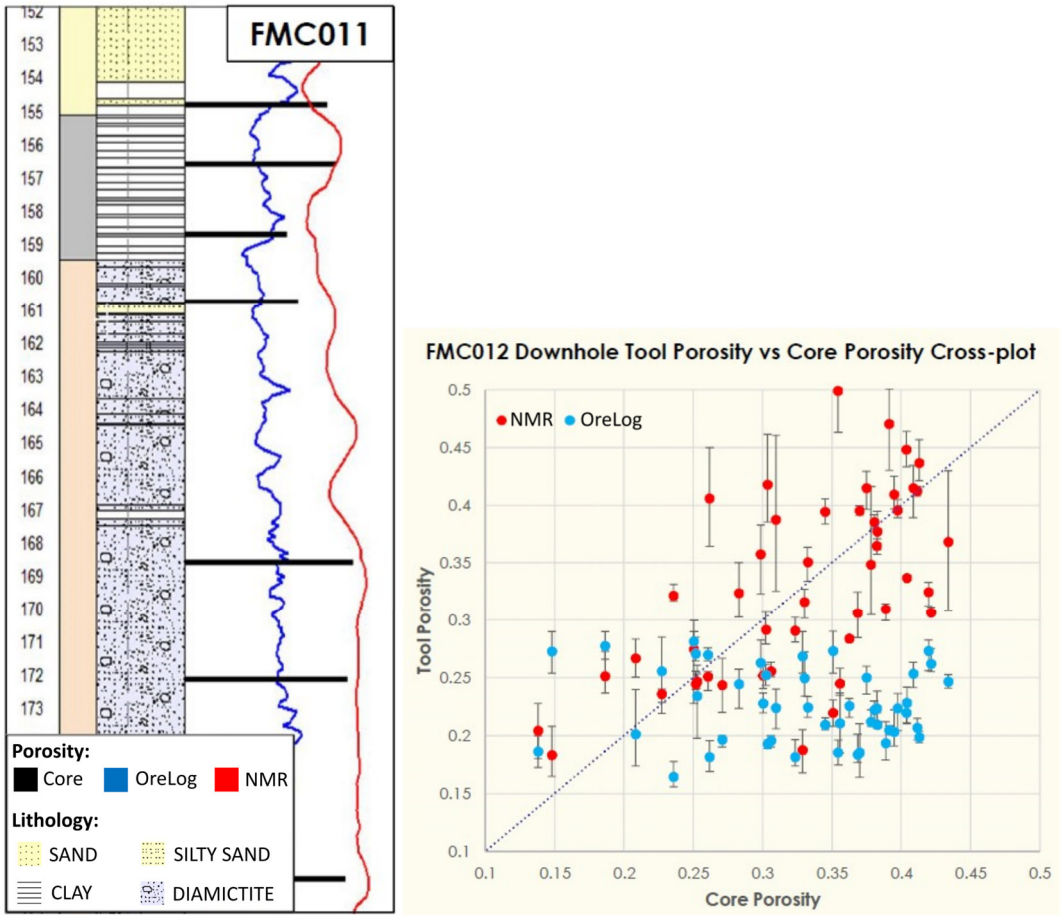

Figure 7.3: Porosity comparison of both OreLog and NMR with core assays in borehole FMC011 and FMC012 illustrated as well-log (WellCAD) and cross-plot (right). NMR data provided as courtesy of HGR and Trofimczyk et al. (2018).

7.3 Elemental Logging

The functionality of elemental logging and the related deposit characterization in terms of ore grade and elemental distribution is the main purpose of this work. The reliability and quality of elemental logging varies significantly between the individual target elements. Most of the initially envisaged elements were detectable in both characterized deposits. The matrix dependency of the γ-ray signals produced by neutron-capture plays a major role in elemental logging. The translation from any element-X-specific γ-ray count rate to its element-abundance in formation (atom-number density, or mass-density of X) is not performed by some constant sensitivity-factor but by some matrix-dependent term proportional to Σ_B as elaborated in Equations 4.55 to 4.57 in chapter 4.5.1. The equations in comparable state of the art tools as presented in Radtke et al. (2012), Gonzalez et al. (2013) and Rose et al. (2015) do not contain such a term. The only matrix-dependency is for normalization to get the sum of all mass fractions by

definition equal to one. This normalization differs from the weighting approach presented in this work. Especially the consideration of the neutron signal measured in the respective neutron detectors in the elemental logging algorithms presents a unique method of deposit characterization. In combination with ever evolving quantity and quality of OreLog-specific elemental templates (cf. chapter 6.3.2) and reference boreholes the accuracy and reliability for the investigated elements as presented in chapter 6.5 will further improve. Based on the results achieved during field testing, most of the target elements outlined in chapter 1 were quantified but are still limited to two depositional environments and their corresponding major lithologies – namely CID (sedimentary rocks) and paleochannels (sedimentary and metamorphic rocks) with limited tests in basement formations (igneous rocks).

One of these target elements in the mentioned environments is iron, also because of its economic potential. Therefore, the evaluation and validation of iron grades is emphasized here with the unique situation that concentrations from less than 1 wt% up to 60 wt% (cf. Figure 6.38 and Figure 6.39) are encountered in various deposit environments as stated in chapter 5.2.1 and 5.3.1. The chosen algorithm and the underlying templates provide very good results for iron grade control in iron ore mines as confirmed during the Pilbara logging campaign in many boreholes. Published data of other pulsed NG borehole tools relying on γ-spectroscopy (Borsaru and Charbucinski, 1997; Smith et al., 2013) in similar iron environments achieved comparable results whereas the tool dimensions were significantly larger as compiled in Table 2.3. Both the detection of iron bearing layers like pyritic sands in sedimentary deposits (Figure 6.36) or grade control of a producing open pit mine with nearly real-time data is achievable. The field campaigns allow the definition of a reliable LOD of about 1 wt% for Fe.

In terms of neutron interaction, iron has many similarities to aluminum as evident in the element-specific templates in Figure 6.29. Besides that, Al also has an elemental capture cross-section larger than silicon (0.23 barn > 0.17 barn), but the partial elemental cross-section responsible for the significant capture γ-ray ($E_\gamma = 7.72$ MeV) is only 0.049 barn and, hence, it is smaller than the one for the significant capture γ-ray of silicon (0.12 barn at $E_\gamma = 3.54$ MeV and 0.11 barn at $E_\gamma = 4.93$ MeV). In addition, γ-ray detection efficiency of nearly 8 MeV γ-ray of aluminum is lower than the one of a sub 5 MeV γ-ray of silicon. In summary, the Al-related γ-ray signal is weaker (smaller count rate) than the Si-related one; it is weaker by more than a factor of 0.4. In addition, iron leaves a nearly identical pattern of γ-rays in the capture spectrum (cf.

Figure 6.41 and Figure 6.42). Gonzalez et al. (2013) state that due to the iron capture cross-section being more than ten times larger than the one of aluminum, the Al-/Fe-pattern is commonly assigned to iron rather than aluminum. The Fe signal γ-ray even has a 25 times larger production cross-section than the Al signal γ-ray. A stationary measurement (with enhanced statistics in the γ-ray capture spectrum) may allow for reliable assignment of Fe-/Al-pattern signals to either aluminum or iron. In addition, consistency with the bulk capture cross-section measured by n-detectors can be checked. For instance, Schlumberger works with a fixed iron-to-aluminum correlation by assigning count rate patterns as the ones for Fe and Al shown in Figure 6.29 to both Fe and Al (Gonzalez et al., 2013). This is realized by the so-called ELAN code (ELemental ANalysis), proprietary to Schlumberger, assuming a certain correlation between Al and Fe derived from laboratory XRF measurements of thousands of core samples typical for hydrocarbon reservoirs. Radtke et al. (2012) and Rose et al. (2015) confirm this, but in the case of OreLog a different approach is pursued, since the application field is focused on mineral deposits. In iron dominated deposits (such as Pilbara) the tested algorithm is able to discern between Al and Fe resulting in a LOD of about 5 to 10 wt% for Al. In other deposits the correlation to core assays is less consistent and only allows for the reproduction of trends (cf. Figure 6.43).

A state of the art PNG tool with comparable characteristics to the OreLog tool and most recent publications is the PES or GSI tool presented in detail in Pemper et al. (2018) and with the most relevant characteristics compiled in Table 2.3. Besides some similarities in the technical design and especially tool diameter (76 vs 82.6 mm) it has to be pointed out that OreLog was explicitly built and optimized for the characterization of mineral deposits whereas the comparison tool was developed for the characterization of hydrocarbon reservoirs. Nevertheless, it serves as a benchmark to assess the quality of elemental logging based on the results achieved under ideal test conditions in two facilities as explained in Pemper et al. (2018) and compiled in Table 7.1.

Silicon shows comparable results to aluminum with the same estimated LOD. The Si-specific γ-ray count rate is measured in both the burst and capture spectrum, i.e. via two independent reactions (inelastic neutron scattering and neutron capture).

Calcium in detectable quantities is mainly present in carbonate layers in the Pilbara. Borehole JBRC0001 shows an alternation of calcrete and goethite layers, which are picked up well by OreLog proving Ca detectability. Constant Ca grades (e.g. JBRC0002 in Figure 6.46) on the other hand are not reproduced accurately and show significant

fluctuations of OreLog grades around the measured concentration. Therefore, the LOD is around 5-10 wt%.

Table 7.1: Comparison of GSI tool measurements with core data from calibration pits at the Weatherford Rock Formation Laboratory (USA) and the Callisto Facility (UK) (Pemper, 2020).

Formation	Borehole Diameter (in.)	Porosity (p.u.)	Grain Density (g/cm³)	Meas.	Sigma (c.u.)	Al	C	Ca	Fe	Gd	K	Mg	S	Si	Ti
Derbyshire Limestone	8.5	8.3	2.70	Core	8.8	0.0	10.4	39.3	0.0	0.5	0.1	0.2	0.0	0.1	0.01
				Tool	8.4	0.0	10.2	40.0	0.0	0.7	-	0.0	0.1	0.0	0.00
Mill Creek Dolomite	7.875	4.2	2.85	Core	5.6	0.1	12.2	21.7	0.1	0.2	0.1	12.5	0.0	0.5	0.01
				Tool	5.8	0.0	12.7	21.7	0.1	0.0	-	12.2	0.1	1.5	0.11
Plumpton Sandstone	8.5	12.2	2.63	Core	9.3	1.2	0.0	0.0	0.2	0.4	1.0	0.0	0.0	44.5	0.04
				Tool	8.8	1.3	0.0	0.0	0.1	1.1	-	0.0	0.0	44.9	0.00
Lac du Bonnet Pink Granite	7.875	0.7	2.64	Core	10.6	7.3	0.0	1.3	1.1	3.4	3.8	0.3	0.0	33.2	0.13
				Tool	11.2	7.0	0.1	2.5	0.2	0.0	-	0.5	0.3	34.4	0.03

The circumstance that Cl is contained in PVC at a known concentration and its nuclear physical properties as described in chapter 6.5.6 make it an ideal element for detection of low concentrations in both laboratory-scale (Figure 6.17) and field-scale (Figure 6.46). This is confirmed by the lowest Root Mean Square Error (RMSE) of all elements and boreholes. However, Cl does not play an important role neither as ore element nor as indicator in the investigated deposits. Its occurrence is minor, and it is mainly incorporated up to several tenths of a percent in hydroxyl minerals such as biotite and hornblende or in anhydrous minerals as feldspars. Economic important and major occurrences of Cl are present in form of halite (NaCl), which were not investigated, but based on the Cl-sensitivity of OreLog are considered a target deposit type (evaporite deposits) for halite detection and characterization. The LOD of Cl is estimated to 0.005 wt%.

Titanium generates γ-ray signals in both the inelastic (burst) and capture spectrum. OreLog detects only Ti concentrations larger than 0.5 - 1 wt% in the investigated deposits which is an unsatisfying LOD compared to other PNG tools reaching LODs around 0.1 wt% for Ti (Pemper, 2020). On the other hand, the RMSE is relatively low (0.061) indicating that the measurement is reliable and hardly biased if within the

OreLog detection range. To lower the LOD the peak resolution at 6 MeV and the Ti specific templates and algorithms require improvement.

Potassium is one of the few elements that can be measured in passive mode, i.e. without NG activation in the natural γ-spectrum. Besides Th and U, K is always measured in the down run of OreLog providing first elemental logging. Deduced observations of these concentrations can be used to indicate zones of interest in terms of clay mineralization or radionuclides (radioactive deposits). The interpretation of the natural γ-spectrum is not part of this work as the focus is on induced γ-spectroscopy and not natural γ-spectroscopy. However, K is also detectable in the capture spectrum, but is hard to be differentiated from the background as the K-specific γ-ray peaks are rather indistinct. The LOD is estimated between 1 - 3 wt% whereas K is not detected by other tools even at elevated concentrations of 3.8 wt% (Table 7.1).

Manganese is one of the elements where the obtained dataset barely justified the inclusion of the results. The correlation is only obvious in one borehole (JBRC0001) and the remaining ones are far below the achievable LOD with the chosen setup. As notable in publications of other tools Mn performance (Radtke et al., 2012), the OreLog elemental logging algorithm for Mn needs to be improved as well as its specific template shape. Since the Mn γ-ray signal can only be identified in the capture spectrum, an adaptation of the capture time window (cf. Table 3.1) for increased count rates and higher Mn sensitivity is another option.

Generally, the variation of burst and capture spectrum time windows and their influence on element-specific resolution was neglected here, but certainly bears large potential to further improve elemental logging.

Based on the large and mostly waterfilled typical borehole diameters (150 mm) of the investigated deposits, hydrogen from the surrounding formation contributes only very little to the H-specific γ-ray count rate. With the tested OreLog system and processing algorithm this minor difference (non-borehole part) cannot be translated to some H-information abundance. As illustrated in Figure 6.53 the H-specific γ-ray count rate measured in capture spectrum is mainly used to determine the borehole diameter in waterfilled boreholes.

Basically, all minerals contain similar fractions of oxygen. Therefore, the variation of true oxygen-abundance in formation is very small and, hence, there is no very-meaningful use of measured oxygen-abundance in the current OreLog application. The fact that oxygen-related triple-peaks (PP, SEP, DEP) at pulse heights of 1100, 1000 and 900 channels are present in the burst spectrum and in the activation spectrum but

are not present in the capture spectrum confirms that these peaks are produced by two different nuclear reactions. The ones in burst spectrum are produced via inelastic scattering of fast neutrons at oxygen. The ones in the activation spectrum are produced via ^{16}N production and subsequently following β-decay of ^{16}N ($T_{1/2} = 7.13$ s). Nevertheless, there are very significant oxygen-related patterns in burst spectra and in activation spectra as visible in Figure 6.17 and Figure 6.23. It would be possible to quantify these oxygen-related count rates, either by the technique used for iron and silicon, or by some alternative technique. This oxygen-related count rate could then be translated into an oxygen abundance. However, a hardware change to upgrade to two γ-detectors as explained under chapter 7.1 would be the most reliable solution for oxygen quantification as already observed and established by Eyvazzadeh et al. (2004). Carbon is only detectable in the burst spectrum of OreLog and according to the vast experience in carbon detection of the hydrocarbon industry plentiful publications are available showing excellent carbon detection reliability (Pemper, 2020). Further investigations of carbon detection for instance in coal deposits can also improve the general interpretation of the burst spectra. Since the focus of this work was on mineral deposits and carbon is an unusual element in the characterized deposit environments, it was not further followed up.

Rare Earth Elements (REE) were not present (below LOD or not analyzed in laboratory assays) in the investigated deposits and therefore no statement about their detectability is possible. Nevertheless, based on the experience of other elements the cross-sections of gadolinium (48770 barn), samarium (5621 barn) and europium (4560 barn) are highly promising as indicator elements for the REE group usually occurring in paragenesis. Pemper (2020) demonstrated a Gd LOD smaller than 1 wt%. Therefore, it is expected that REE grades larger than 1 wt% are detectable by OreLog. The technique of using different fit-ranges for extraction of different elements is an indicator for the validity limits of the current version of the chosen data processing algorithm (cf. chapter 4.5). The following identified issues are the most-likely limitation for the accuracy and validity of the data processing algorithm: Imperfect translation of scalers s_X to mass fractions k_X due to imperfect and difficult parametrization of general neutron flux description or the imperfect shape of element-specific templates generated by MCNP (Figure 6.29). These two items are the most important subjects to improve the data processing algorithm. In addition, an influence of the borehole diameter to the quality and reliability of elemental logging was revealed during the field campaigns. Unfortunately, only little variety of borehole diameters could be tested (114 mm,

152 mm, 191 mm approximately representing only the black, red, and green line of Figure 6.26) and therefore no systematic investigation was possible to prove the entire simulated borehole diameter range from 100 to 300 mm. As shown in Figure 6.53, HI can be used to deduce a borehole diameter estimation in waterfilled boreholes. Either this information or the physical borehole diameter (based on drill head or caliper log) is required to develop a correction term for the dependence of the elemental logging algorithm on the borehole diameter. Besides that, improved accuracy for element-specific γ-ray count rate is essential to ensure and improve the quality and reliability of overall elemental logging.

As already extensively elaborated in chapter 6.3.1 and calculated by Equation 6.4 the discrepancy between the analyzed volume by the laboratory and the in-situ analysis by OreLog is significant. Therefore, when evaluating OreLog data in comparison to core data this must always be considered. The dilemma is that only the punctual laboratory sample is deemed to be the absolute truth to compare the analyzed OreLog volume to, even though that the elemental composition can vary significantly in distance of this punctual sample. Especially in deposits where nugget effects play a role in the mineralization pattern, extreme care is required when interpreting and comparing core data. The spatial variance is obviously element and mineralization style (deposit type) dependent. Carbon and silicon mainly occurring in coal seams alternating with sand layers are considered a rather homogeneous sample in terms of lateral variance, whereas tectonically controlled or hydrothermal deposits rich in elements like Ti or Cl with mineralization spatially bound to the vein are highly variable. The iron investigated in the CID behaves similar to coal seams and therefore is an ideal target for OreLog validation when comparing to punctual laboratory data since this is considered being representative in this depositional environment as the good correlation as previously shown confirms.

The OreLog tool relies on various deposit-specific parameters as introduced in chapters 4.4 and 4.5, which have to be adjusted during site-specific tool calibration. Since no element-specific calibration pits are available, OreLog is usually calibrated based on several well characterized boreholes which are logged at least twice. Depending on the deposit variability and borehole depth 5 to 10 calibration runs are necessary to make sure that the template matching is adjusted to the local conditions. This could be reduced by the usage of calibration pits containing representative ‘standard’ rock formations to cover most common mineral deposits as already common practice for tool calibration in the hydrocarbon industry, exemplarily illustrated for the Callisto

Calibration Facility in the UK (Samworth and Lovell, 2001) in Figure 7.4. Together with the template matching algorithm more confidence of the elemental logging quality in unknown deposits (greenfield exploration) can be achieved by the development of such calibration pits. Besides that, the differentiation between the inelastic and capture depth of investigation (Figure 7.4) as suggested by Pemper et al. (2006) is opposed to the general neutron induced investigation depth assumed in this work in chapter 6.3.1. Especially the comparison of Figure 6.20 with Figure 7.4 shows that interpretations based on the burst (inelastic) spectra are representative for a smaller volume than data derived from the capture spectra. This is currently not considered and might allow further refinement if elemental logging forms the basis of resource estimation.

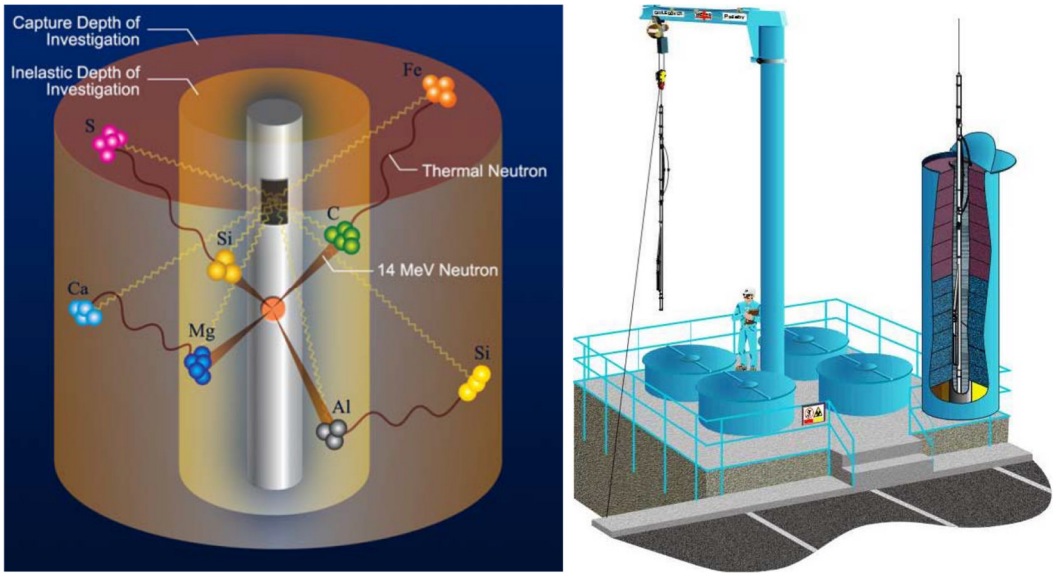

Figure 7.4: Left: Schematic diagram of the inelastic and thermal neutron interactions along with their volumes of investigation (penetration depth) in the formation (Pemper et al., 2006). Right: General arrangement of the Callisto Calibration facility with a cutaway view of a tank containing defined rock blocks 30 cm thick and 2 m in diameter (Samworth and Lovell, 2001).

8 Conclusions

A novel and slim PNG borehole logging tool called OreLog was developed and optimized for the characterization of mineral deposits based on neutron induced time dependent neutron-distributions and γ-spectroscopy. Two deposit types (CID and paleochannel) were characterized for the first time with the OreLog tool regarding petrophysics and elemental composition. Both deposits were characterized by the same methodology whereas the focus at the Four Mile deposits was on petrophysics and at the CID in the Pilbara elemental logging (grade control) was emphasized. Laboratory core and RC chip sample data (geochemistry and petrophysics) besides pump tests and individual core logs were compared to OreLog data. This work is the first successful approach of a comprehensive deposit characterization by only one compact (76 mm diameter and 3 m length, 33 kg weight) and single operator tool, relying exclusively on neutron- and γ-spectroscopy.

This research aimed to establish elemental logging for certain elements in mineral deposits. Based on extensive literature review of common elements logged in the hydrocarbon industry and demands from the mineral resource industry, a list of 16 elements (cf. chapter 1) was defined to ideally be characterized in various deposit types. To acquire the relevant data from the rock formation, state of the art components were installed in the OreLog tool. Both conventional ^{3}He detectors in multi-scaling mode (time windows between the neutron bursts) and a highly innovative neutron source strength detector (CVD detector) were implemented for accurate and fast neutron detection over the entire energy range. Multi-scaling is a specific feature implemented in OreLog enabling the possibility to set time windows or – even better – to collect full-scale time distributions. Neutron distributions (time dependent with reference to primary neutron bursts) from various detectors are processed to quantify specific integral parameters that are related to formation characteristics. It enables the discrimination of γ-spectra of different origin. Together with the large $CeBr_3$ γ-scintillator, the geometrical position and calibration of components were optimized for elemental logging. For the first time in elemental logging both data from the γ-detector as well as from the neutron channels (time-dependent) is combined in support of MCNP simulations and resulting templates for petrophysical and geochemical deposit characterization. This procedure is integrated in a model that combines both nuclear physics and geochemistry to describe the relationship between measured elemental concentrations and all major unmeasurable elements of the investigated formation. It

is required for the proper normalization of elemental measurements that cannot be calibrated in elemental concentrations. The technique is implemented with the installed γ-ray module, that can perform all the elemental measurements in a single logging run, thus overcoming the problems associated with changing hole conditions when data are accumulated in separate logging runs.

The fieldwork showed that petrophysical deposit characterization is achievable to a certain extent based on calibrated OreLog data in saturated sedimentary deposits. Both density and porosity were determined according to two different approaches, whereas only one resulted in correlated results. OreLog permeability data showed good agreement with permeability determined by core assays (small scale) and pump tests (large scale). In terms of resolution and accuracy OreLog relies on neutron induced γ-rays interpreting the hydrogen content (mainly HI), which is an inferior method compared to borehole NMR being the method of choice and providing better results as demonstrated in this work. This is also due to many decades of NMR experience in petrophysical applications. Nevertheless, the initiated work with OreLog for broader petrophysical deposit characterization relying on a PNG shows potential and is recommended to be continued.

Both laboratory and fieldwork for elemental logging were successful. The results presented in the previous chapters allow for the following conclusions regarding elemental logging: OreLog determines elemental mass fractions down to a LOD of 1 wt% for iron, about 5 to 10 wt% for silicon, about 5 to 10 wt% for aluminum, about 5 to 10 wt% for calcium, and about 50 to 400 ppm for chlorine. OreLog also enables elemental logging of further elements such as Ti, K, Mn, and others. However, accuracy and detection limits are subject to further investigations. The LOD and accuracy strongly depends on the matrix composition and the abundance of the element of interest. The best results and highest level of confidence was definitely obtained for iron, which is the element of most economic interest at the same time. In-situ real-time grade control for iron production from open-pit mines can be realized with the required accuracy and reliability based on the presented results and will be pursued.

To further improve accuracy, LOD and increase the suite of detectable elements the implementation of customized and well-defined calibration pits in addition to template matching is recommended. At first, tests in calibration pits conventionally used in the hydrocarbon industry with exactly defined conditions like the Weatherford Rock Formation Laboratory (USA), Baker Atlas Instrument Characterization Center in Houston (USA) or the Callisto Fracility (UK) are recommended. Based on the outcome

customized OreLog calibration pits for elemental logging and potentially petrophysical characterization should be engineered and implemented in the logging routine.

So far, OreLog has not been operated in a carbon-rich formation (coal, graphite, oil) or test pit. Consequently, OreLog should be tested in a well-defined carbon-rich environment to be able to record and interpret the carbon-feature already detected in laboratory tests. A suitable candidate would be the German lignite deposits operated by MIBRAG. Both the Schleenhain or Profen open-pit mines in East Germany entail ideal test conditions.

Potassium is one of the elements with large potential being beneficial in other deposit types such as saline environments. Incorporated in sylvite or carnallite, OreLog measurements of potassium can detect those pay minerals and characterize them. Therefore, salt deposits of K+S for instance are considered as a further test target.

Besides that, another unexpected conclusion is the possibility of applying OreLog in the field of environmental analysis such as detection of contaminants in soils, instead of the mere application in the field of mineral resources and mining. Especially Cl as constituent of many unwanted contaminants (chloro-organic compounds) being already hazardous at low concentrations can be monitored ($>$ 50 ppm) by OreLog. Similarly, the monitoring of Dense Non-Aqueous Phase Liquid (DNAPL) or Light Non-Aqueous Phase Liquid (LNAPL) and differentiation between other water-soluble components at contaminated sites is technically feasible.

In terms of technical improvements, the adaptation of the NG pulse regime according or similar to Figure 7.1 is recommended. This comes along with an improved multi-scaling where an upgrade of the neutron-induced γ-spectra from currently three (burst, capture, activation) to eight is suggested to allow the full observation of physics and further refinement of elemental logging. In this respect, the neutron time channels of the neutron detectors should be upgraded from 8 to 32 improving the determination of Σ_B, important for description of the neutron cloud (shape and time dependence). For oxygen detection and further improvement of elemental logging a second γ-detector is recommended. A different scintillator crystal and a location opposite to the NG is intended for this purpose. Laboratory tests on the scintillator crystal combinability, resolution and exact location are required. To improve peak detection in case of closely neighbored peaks and temperature fluctuations, a LED with exactly known temperature dependency should be placed directly at the scintillator crystal as reference line for spectral energy calibration (channel-to-energy conversion). Currently the neutron burst cycles are divided into eight time windows of variable length. It is

suggested to subdivide this cycle in seven time windows for elemental logging and keep one time window (maybe 20 µs long) for energy calibration (peak height and position) of the γ-detector. Once sufficient field-data is available and a certain amount of deposit types have been logged, a combination of simulated and measured templates (hybrid templates) further improve the elemental logging.

9 References

Aboud, M., Badry, R., Grau, J., Herron, S., Hamichi, F., Horkowitz, J., Hemingway, J., MacDonald, R., Saldungaray, P., Stachiw, D., 2014. High-definition spectroscopy—determining mineralogic complexity. Oilfield Review 26, 34-50.

Abzalov, M.Z., 2012. Sandstone-hosted uranium deposits amenable for exploitation byin situleaching technologies. Applied Earth Science 121, 55-64.

API, 2016. West Pilbara Iron Ore Project (WPIOP). Cardo. API, Perth.

Barson, D., Christensen, R., Decoster, E., Grau, J., Herron, M., Herron, S., Guru, U.K., Jordán, M., Maher, T.M., Rylander, E., 2005. Spectroscopy: the key to rapid, reliable petrophysical answers. Oilfield Review 17, 14-33.

Barzilov, A.P., Novikov, I.S., Womble, P.C., 2012. Material analysis using characteristic gamma rays induced by neutrons. Gamma Radiation, 17-40.

Borsaru, M., 1993. Nuclear techniques for in situ evaluation of coal and mineral deposits. Nuclear Geophysics 7, 555-574.

Borsaru, M., Berry, M., Biggs, M., Rojc, A., 2004. In situ determination of sulphur in coal seams and overburden rock by PGNAA. Nuclear Instruments and Methods in Physics Research Section B: Beam Interactions with Materials and Atoms 213, 530-534.

Borsaru, M., Biggs, M., Nichols, W., Bos, F., 2001. The application of prompt-gamma neutron activation analysis to borehole logging for coal. Applied Radiation and Isotopes 54, 335-343.

Borsaru, M., Charbucinski, J., 1997. Nuclear borehole logging techniques developed by CSIRO - Exploration and Mining for in situ evaluation of coal and mineral deposits. Proceedings of the Second international conference on isotopes.

Borsaru, M., Zhou, B., Aizawa, T., Karashima, H., Hashimoto, T., 2006. Automated lithology prediction from PGNAA and other geophysical logs. Applied radiation and isotopes: including data, instrumentation and methods for use in agriculture, industry and medicine 64, 272-282.

Briesmeister, J.F., 2000. MCNPTM-A general Monte Carlo N-particle transport code. Version 4C, LA-13709-M, Los Alamos National Laboratory 2.

Callen, R.A., 1977. Late Cainozoic environments of part of northeastern South Australia. Journal of the Geological Society of Australia 24, 151-169.

Celata, C.M., Amman, M., Donahue, R., Leung, K., Luke, P.N., Perkins, L.T., Zawislanski, P.T., Greenspan, E., Hua, D., Karni, Y., 1997. A new intense neutron generator and high-resolution detector for well logging applications. In:

Del Guerra, A. (Ed.), 1996 IEEE Nuclear Science Symposium. Conference record: November 2-9, 1996, Anaheim, California. Institute of Electrical and Electronics Engineers, New York, N.Y.

Charbucinski, J., Duran, O., Freraut, R., Heresi, N., Pineyro, I., 2004. The application of PGNAA borehole logging for copper grade estimation at Chuquicamata mine. Applied radiation and isotopes: including data, instrumentation and methods for use in agriculture, industry and medicine 60, 771-777.

Charbucinski, J., Malos, J., Rojc, A., Smith, C., 2003. Prompt gamma neutron activation analysis method and instrumentation for copper grade estimation in large diameter blast holes. Applied Radiation and Isotopes 59, 197-203.

Crangle, R.D., Jr., 2007. Log ASCII Standard (LAS) files for geophysical wire line well logs and their application to geologic cross sections through the central Appalachian basin. United States Geological Survey Open File Report 2007-1142, 14 p.

Cumming, J.D., 1951. Diamond drill handbook. JK Smit.

Curtis, J.L., Brunt, D.A., Binks, P.J., 1990. Tertiary palaeochannel uranium deposits of South Australia. Geology of the mineral deposits of Australia and Papua New Guinea, 1631-1636.

Dahlkamp, F.J., 2010. Uranium deposits of the world: USA and Latin America. Springer Science & Business Media.

Day-Lewis, F.D., Slater, L.D., Robinson, J., Johnson, C.D., Terry, N., Werkema, D., 2017. An overview of geophysical technologies appropriate for characterization and monitoring at fractured-rock sites. Journal of environmental management 204, 709-720.

Dentith, M., Mudge, S.T., 2014. Geophysics for the mineral exploration geoscientist. Cambridge University Press, Cambridge.

Doveton, J.H., Prensky, S.E., 1992. Geological applications of wireline logs: a synopsis of developments and trends. The Log Analyst 33, 286-303.

Dubrovkin, J., 2014. Critical analysis of spectral deconvolution methods. International Journal of Emerging Technologies in Computational and Applied Sciences 1, 10.

Eisler, P.L., 1982. Exploration and grade control neutron logging. IAEA regional training course: use of nuclear techniques in the mineral industry. Australian Atomic Energy Commission Research Establishment, 359-381.

Ellis, D.V., 1987. Nuclear Logging Techniques. Petroleum Production Handbook, Society of Petroleum Engineers, Dallas, TX.

Ellis, D.V., Singer, J.M. (Eds.), 2007. Well Logging for Earth Scientists. Springer Netherlands, Dordrecht.

Evans, L.G., Trombka, J.I., Lapides, J.R., Jensen, D.H., 1981. Determination of elemental composition in geochemical exploration using a 14-MeV neutron generator. IEEE Trans. Nucl. Sci. 28, 1626-1628.

Eyvazzadeh, R., Oscar, K., Hajari, A., Ma, S., Behair, A., 2004. Modern Carbon/Oxygen Logging Methodologies: Comparing Hydrocarbon Saturation Determination Techniques. SPE Annual Technical Conference and Exhibition held in Houston, Texas, U.S.A., 26–29 September 2004.

Fricke, S., Schön, J., 1999. Praktische Bohrlochgeophysik. 31 Tabellen. Enke im Thieme-Verl., Stuttgart.

Gold, R., 1964. An iterative unfolding method for response matrices. Argonne National Laboratory, Chicago, Report no. ANL-6984.

Golder Associates Pty Ltd, 2016. Mt Stuart Iron Ore Joint Venture - Updated Mineral Resource Estimate, Perth.

Gonzalez, J., Lewis, R., Hemingway, J., Grau, J., Rylander, E., Pirie, I., 2013. Determination of formation organic carbon content using a new neutron-induced gamma ray spectroscopy service that directly measures carbon. Unconventional Resources Technology Conference held in Denver, Colorado, USA, 12-14 August 2013, 1100-1109.

Grau, J.A., Schweitzer, J.S., 1989. Elemental concentrations from thermal neutron capture gamma-ray spectra in geological formations. Nuclear Geophysics 3, 1-9.

Grau, J.A., Schweitzer, J.S., Ellis, D.V., Hertzog, R.C., 1989. A geological model for gamma-ray spectroscopy logging measurements. Nuclear Geophysics 3, 351-359.

Heathgate Resources Pty Ltd, 2013. Four Mile West Aquifer Testing. Internal Report, Adelaide.

Herbach, C.-M., Kong, Y., Lentering, R., Neuer, M., Pausch, G., Plettner, C., Ruhnau, K., Stein, J., 2009. A technique for estimating detection limits of radionuclide identifying detectors by means of computer simulations. In: IEEE Nuclear Science Symposium conference record, 2008. 19 - 25 Oct. 2008, Dresden, Germany; contains manuscripts presented at the 2008 IEEE Nuclear Science Symposium, Medical Imaging Conference and Room Temperature Semiconductor Detector Workshop (NSS/MIC/RTSD). IEEE, Piscataway, NJ.

Hertzog, R., 1988. Elemental concentrations from neutron induced gamma ray spectroscopy. IEEE Trans. Nucl. Sci. 35, 827-832.

Hertzog, R., Colson, L., Seeman, B., O'Brien, M., Scott, H., McKeon, D., Wraight, P., Grau, J., Ellis D., Schweitzer, J., Herron, M., 1989. Geochemical logging with spectrometry tools. SPE Formation Evaluation.

Humphreys, D.R., Barnard, R.W., Bivens, H.M., Jensen, D.H., Stephenson, W.A., Weinlein, J.H., 1983. Uranium logging with prompt fission neutrons. The International Journal of Applied Radiation and Isotopes 34, 261-268.

International Atomic Energy Agency, 2007. Database of prompt gamma rays from slow neutron capture for elemental analysis.

James, F., Roos, M., 1975. Minuit: A system for function minimization and analysis of the parameter errors and correlations. Computer Physics Communications 10, 343-367.

Jaynes, E.T., 1957. Information theory and statistical mechanics. Physical review 106, 620-630.

Jaynes, E.T., 1988. How does the brain do plausible reasoning? In: Maximum-Entropy and Bayesian Methods in Science and Engineering. Springer, Dordrecht, pp. 1-24.

Jeuken, B., Märten, H., Phillips, R., 2007. Uranium ISL operation and water management under the arid climate conditions at Beverley, Australia. Proceedings 10th IMWA Congress Karlsbad, Czech Republic, 487-490.

Kausch, P., Bertau, M., Gutzmer, J., Matschullat, J., 2013. Strategische Rohstoffe-Risikovorsorge. Springer-Verlag.

Kavrigin, P., Griesmayer, E., Belloni, F., Plompen, A.J.M., Schillebeeckx, P., Weiss, C., 2016. 13C(n, alpha)10Be cross section measurement with sCVD diamond detector. Eur. Phys. J. A 52, 3833.

Kenyon, W.E., 1997. Petrophysical Principles of Applications of NMR Logging. The Log Analyst 38, 21-43.

Keys, W.S., 1996. A Practical Guide to Borehole Geophysics in Environmental Investigations. CRC Press.

Koelzer, W., 2001. Lexikon zur Kernenergie. Forschungszentrum, Karlsruhe.

Lehmann, B., 2008. Uranium ore deposits. Reviews in Economic Geology AMS Online, 16-26.

Liu, H., Yan, L., Huang, T., Liu, S., Zhang, Z., 2017. Blind spectral signal deconvolution with sparsity regularization: An iteratively reweighted least-squares solution. Circuits Systems and Signal Processing 36, 435-446.

Lone, M.A., Leavitt, R.A., Harrison, D.A., 1981. Prompt gamma rays from thermal-neutron capture. Atomic Data and Nuclear Data Tables 26, 511-559.

Lucy, L.B., 1974. An iterative technique for the rectification of observed distributions. The astronomical journal 79, 745.

Märten, H., Kalka, H., Krause, J., Nicolai, J., Schubert, J., Zauner, M.J., 2015. Advanced in-situ leaching technology for uranium-From innovative exploration to optimized recovery. FOG-Freiberg Online Geoscience.

McDowell, G.M., King, A., Lewis, R.E., Clayton, E.A., Grau, J.A., 1998. In-site nickel assay by prompt gamma neutron activation wireline logging. In: SEG Technical Program Expanded Abstracts 1998. Society of Exploration Geophysicists.

McMonnies, B., Gerrie, V., Milkereit, B. (Eds.), 2007. Ground geophysics and borehole logging—A decade of improvements. Exploration in the New Millennium: Proceedings of the Fifth Decennial International Conference on Mineral Exploration.

Meng, L.J., Ramsden, D., 2000. An inter-comparison of three spectral-deconvolution algorithms for gamma-ray spectroscopy. IEEE Trans. Nucl. Sci. 47, 1329-1336.

Morháč, M., 2006. Deconvolution methods and their applications in the analysis of γ-ray spectra. Nuclear Instruments and Methods in Physics Research Section A: Accelerators, Spectrometers, Detectors and Associated Equipment 559, 119-123.

Morháč, M., Kliman, J., Matoušek, V., Veselský, M., Turzo, I., 1997. Efficient one- and two-dimensional gold deconvolution and its application to γ-ray spectra decomposition. Nuclear Instruments and Methods in Physics Research Section A: Accelerators, Spectrometers, Detectors and Associated Equipment 401, 385-408.

Morháč, M., Kliman, J., Matoušek, V., Veselský, M., Turzo, I., 2000. Identification of peaks in multidimensional coincidence γ-ray spectra. Nuclear Instruments and Methods in Physics Research Section A: Accelerators, Spectrometers, Detectors and Associated Equipment 443, 108-125.

Morris, R.C., Ramanaidou, E.R., 2007. Genesis of the channel iron deposits (CID) of the Pilbara region, Western Australia. Australian Journal of Earth Sciences 54, 733-756.

Müller-Petke, M., Hiller, T., Herrmann, R., Yaramanci, U., 2011. Reliability and limitations of surface NMR assessed by comparison to borehole NMR. Near Surface Geophysics 9, 123-134.

Navarro, J., Ring, T.A., Nigg, D.W., 2015. Gamma-ray simulated spectrum deconvolution of a LaBr 3 1-×1-in. scintillator for nondestructive ATR fuel burnup on-site predictions. Nuclear Technology 190, 183-192.

Pemper, R., 2020. A history of nuclear spectroscopy in well logging. Petrophysics – The SPWLA Journal of Formation Evaluation and Reservoir Description 61, 523-548.

Pemper, R., Pereira, A., Hou, G., Dolliver, D., Tudge, J., Kharrazi, J., Chok, H., Schmid, G., Mekic, N., Blankinship, T., Epstein, R., Cave, T., MacPherson, A., 2018. A new geochemical logging tool for determination of formation chemistry and mineralogy in both conventional and unconventional reservoirs. SPE Annual Technical Conference and Exhibition held in Dallas, Texas, U.S.A., 24–26 September 2018.

Pemper, R.R., Sommer, A., Guo, P., Jacobi, D., Longo, J., Bliven, S., Rodriguez, E., Mendez, F., Han, X. (Eds.), 2006. A new pulsed neutron sonde for derivation of formation lithology and mineralogy, SPE-102770-MS.

Penney, R., 2012. Australian sandstone-hosted uranium deposits. Applied Earth Science 121, 65-75.

Pfennig, G., Klewe-Nebenius, H., Seelmann-Eggebert, W., 1995. Chart of the nuclides. 6. ed. printed by Druckhaus, Haberbeck GmbH, D-32791 Lage/Lippe.

Philip, O., Shestakova, I., Stephenson, K., Pavelkova, T.J., Kynych, P., Marek, T., Novak, E., Mravec, F., Matej, Z., 2019. Neutron Energy Mapping for Two Different D-T Generator Technologies with a Diamond Detector. In: 2018 IEEE Nuclear Science Symposium and Medical Imaging Conference (NSS/MIC). Conference proceedings. IEEE, [Piscataway, NJ].

Prensky, S., 2002. Recent developments in logging technology. Petrophysics 43, 197-216.

Quirein, J., Kimminau, S., La Vigne, J., Singer, J., Wendel, F. (Eds.), 1986. A coherent framework for developing and applying multiple formation evaluation models. Society of Petrophysicists and Well-Log Analysts.

Radtke, R.J., Lorente, M., Adolph, R., Berheide, M., Fricke, S., Grau, J., Herron, S., Horokowitz, J., Jorion, B. (Eds.), 2012. A new capture and inelastic spectroscopy tool takes geochemical logging to the next level. Society of Petrophysicists and Well-Log Analysts.

Rahman, M.S., Cho, G., Kang, B.-S., 2009. Deconvolution of gamma-ray spectra obtained with NAI(Tl) detector in a water tank. Radiation protection dosimetry 135, 203-210.

Ramanaidou, E.R., Morris, R.C., 2010. A synopsis of the channel iron deposits of the Hamersley Province, Western Australia. Applied Earth Science 119, 56-59.

Richardson, W.H., 1972. Bayesian-based iterative method of image restoration. Journal of the Optical Society of America 62, 55-59.

Rinard, P., 1991. Neutron interactions with matter. Passive Nondestructive Assay of Nuclear Materials, Los Alamos Technical Report.

Robb, L., 2020. Introduction to Ore-Forming Processes. John Wiley & Sons.

Rose, D., Zhou, T., Beekman, S., Quinlan, T., Delgadillo, M., Gonzalez, G., Fricke, S., Thornton, J., Clinton, D., Gicquel, F. (Eds.), 2015. An innovative slim pulsed neutron logging tool. Society of Petrophysicists and Well-Log Analysts.

Rust, W.M., 1938. A historical review of electrical prospecting methods. Geophysics 3, 1-6.

Saint-Gobain, 2018. Saint-Gobain Lanthanum Bromide and Enhanced Lanthanum Bromide Material Data Sheet. https://www.crystals.saint-gobain.com/sites/imdf.crystals.com/files/documents/lanthanum-material-data-sheet.pdf (30 December 2020).

Samworth, J., Lovell, M., 2001. CALLISTO- A new world-standard facility for the calibration of nuclear well logs. Canadian Society of Petroleum Geologists.

Schlumberger, 2017. Litho Scanner brochure.

Schweitzer, J.S., Hertzog, R.C., Soran, P.D., 1987. Nuclear data for geophysical spectroscopic logging. Nuclear Geophysics 1, 213-225.

Senftle, F.E., Moxham, R.M., Tanner, A.B., 1972. A comparison of radiative capture with decay gamma-ray method in bore hole logging for economic minerals. Nuclear Instruments and Methods 104, 485-492.

Shepp, L.A., Vardi, Y., 1982. Maximum Likelihood Reconstruction for Emission Tomography. IEEE Trans. Med. Imaging 1, 113-122.

Shi, R., Tuo, X.-G., Li, H.-L., Xu, Y.-Y., Shi, F.-R., Yang, J.-B., Luo, Y., 2017. Unfolding analysis of LaBr3:Ce gamma spectrum with a detector response matrix constructing algorithm based on energy resolution calibration. Nuclear Science and Techniques 29, 1.

Skirrow, R.G., 2009. Uranium ore-forming systems of the Lake Frome region, South Australia. Geoscience Australia, 151.

Smirnova, M., Shmanin, E., Galavanov, A., Shustov, A., Ulin, S., Vlasik, K., Dmitrenko, V., Novikov, A., Orlov, A., Petrenko, D., Shmurak, S., Uteshev, Z., 2016. LaBr 3 (Ce) gamma-ray detector for neutron capture therapy. Journal of Physics: Conference Series 675, 42050.

Smith, C.P., Jeaneau, P., Maddever, R.A.M., Fraser, S.J., Rojc, A., Lofgren, M.K., Flahaut, V., 2013. PFTNA logging tools and their contributions to in-situ elemental analysis of mineral boreholes. TOS Forum 2013, 157.

Smith, R.C., Bush, C.H., Reichardt, J.W., 1988. Small accelerators as neutron generators for the borehole environment. IEEE Trans. Nucl. Sci. 35, 859-862.

Soppera, N., Bossant, M., Dupont, E., 2014. JANIS 4: An improved version of the NEA java-based nuclear data information system. Nuclear Data Sheets 120, 294-296.

Spies, B.R., 1996. Electrical and electromagnetic borehole measurements: A review. Surveys in Geophysics 17, 517-556.

Stoian, L.M., 2010. Palynology of Mesozoic and Cenozoic sediments of the Eromanga and Lake Eyre basins: results from recent drilling in the northwest Frome Embayment. MESA Journal 57, 27-35.

Tian, L., Zhang, F., Liu, J., Zhang, Q., Wang, X., Chen, Q. (Eds.), 2017. A new PGNAA borehole logging method for determining copper and nickel grade. Society of Exploration Geophysicists.

Trofimczyk, K., Downey, M., Hopper, T., Neville, T., Birt, B., 2018. Continuous hydrogeological characterisation in iron ore deposits using borehole magnetic resonance. ASEG Extended Abstracts 2018, 1-6.

van Cittert, P.H., 1931. Zum Einfluß der Spaltbreite auf die Intensitätsverteilung in Spektrallinien. II. Zeitschrift für Physik 69, 298-308.

Vourvopoulos, G., Womble, P.C., 2001. Pulsed fast/thermal neutron analysis: a technique for explosives detection. Talanta 54, 459-468.

Weiss, C., Frais-Kölbl, H., Griesmayer, E., Kavrigin, P., 2016. Ionization signals from diamond detectors in fast-neutron fields. Eur. Phys. J. A 52, 337.

Werner, C.J., 2017. MCNP Users Manual-Code Version 6.2. Los Alamos National Laboratory, Los Alamos.

Wonik, T., Olea, R.A., 2007. Borehole Logging. Environmental Geology: Handbook of Field Methods and Case Studies, 431-474.

Wülser, P.-A., Brugger, J., Foden, J., Pfeifer, H.-R., 2011. The sandstone-hosted Beverley uranium deposit, Lake Frome Basin, South Australia: mineralogy, geochemistry, and a time-constrained model for its genesis. Economic Geology 106, 835-867.

Zauner, M., Weller, A., Halisch, M., 2020. Laboratory core investigations of sandstone-hosted uranium for in situ recovery. Applied Earth Science 129, 27-40.

Zhang, F., Tian, L., Liu, J., Wang, X., 2017. Numerical simulation on scintillator detector response for determining element content in PGNAA system. Journal of Radioanalytical and Nuclear Chemistry 311, 1309-1314.

A Appendices

A.1 Core and Mud Logs

The geological log may be based on visual inspection of either drill cores or chip samples (cuttings) brought to the surface. Core and mud logging are the systematic recording and measuring of as much information as possible or required to determine the lithology, mineralogy, potential geological history, structure and alteration zones. The logs presented here are based on the perception and personal experience of the logger.

A.1.1 Pilbara

Compilation of all relevant core and mud logs acquired during Pilbara field work. The logs contain excerpts of the geochemical core analysis for the most relevant elements in the column 'Assay Results'. The complete geochemical data can be requested from the author. The following acronyms and abbreviations are used in the logs:

Hole ID	Borehole Identification
MZ	Micha Zauner
RL	Relative Level
EOH	End of Hole
LOI371	Loss on Ignition at 371 °C
LOI1000	Loss on Ignition at 1000 °C
BGL	Below Ground Level

In the Australian iron ore industry (mainly Pilbara), typically 2 or 3 weight loss measurements are realized. The LOI371 is a good proxy for the amount of goethite, FeOOH, present assuming a stoichiometric loss in weight for goethite of 10.1 wt%. However, the presence of gibbsite, which dehydrates over approximately the same temp. range as goethite can overestimate the amount of goethite using this method. For example, gibbsite has a weight loss of about 34 %. So, the presence of only 5 - 10 % gibbsite can significantly add to the weight loss measured and, thus, overestimate the goethite content. The LOI1000 weight loss includes any residual water remaining in hydrohematite, which is not fully dehydrated until about 900 - 1000 °C, and weight loss associated with the decomposition of any carbonates, that may also be present. Carbonates, such as calcite, dolomite, ankerite show a weight loss of about 44-46 wt% (evolution of CO_2). So, the presence of 10 wt% carbonate will contribute nearly 5 % to the loss in weight recorded.

The geological codes used for the Pilbara field work are shown on the following two pages.

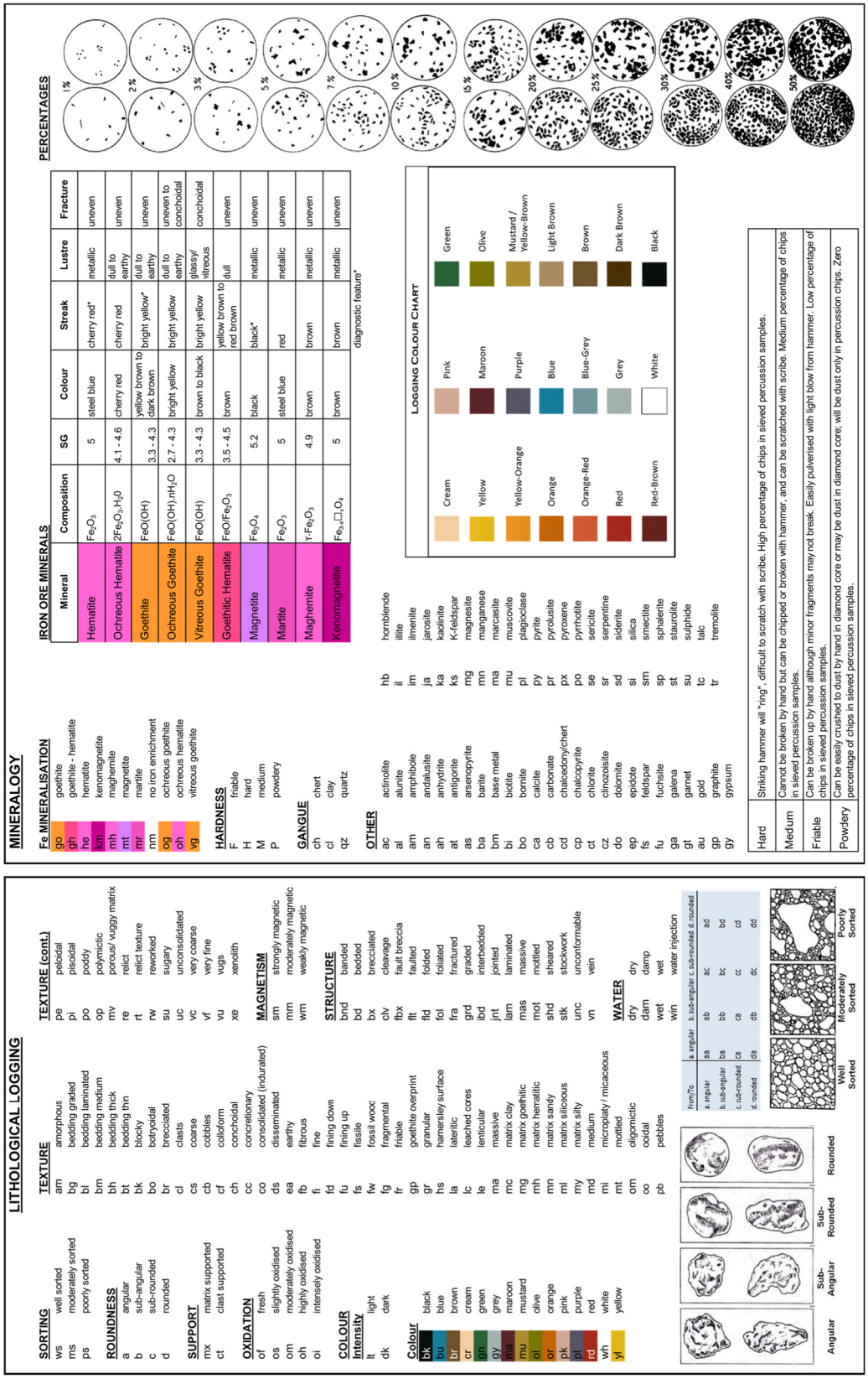

Figure A.1: Geological codes (part 1 of 2) as used during the Pilbara tests.

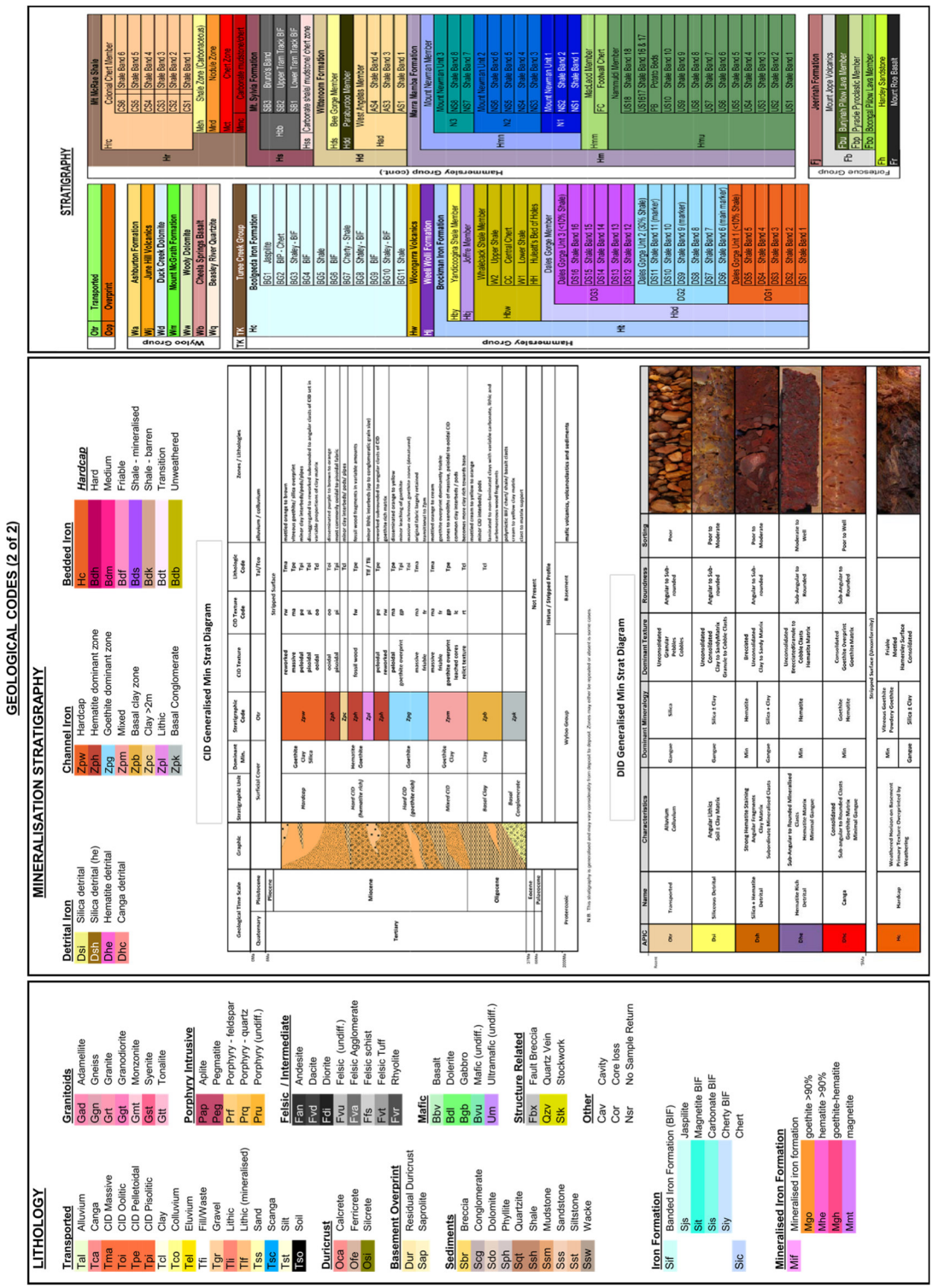

Figure A.2: Geological codes (part 2 of 2) as used during the Pilbara tests.

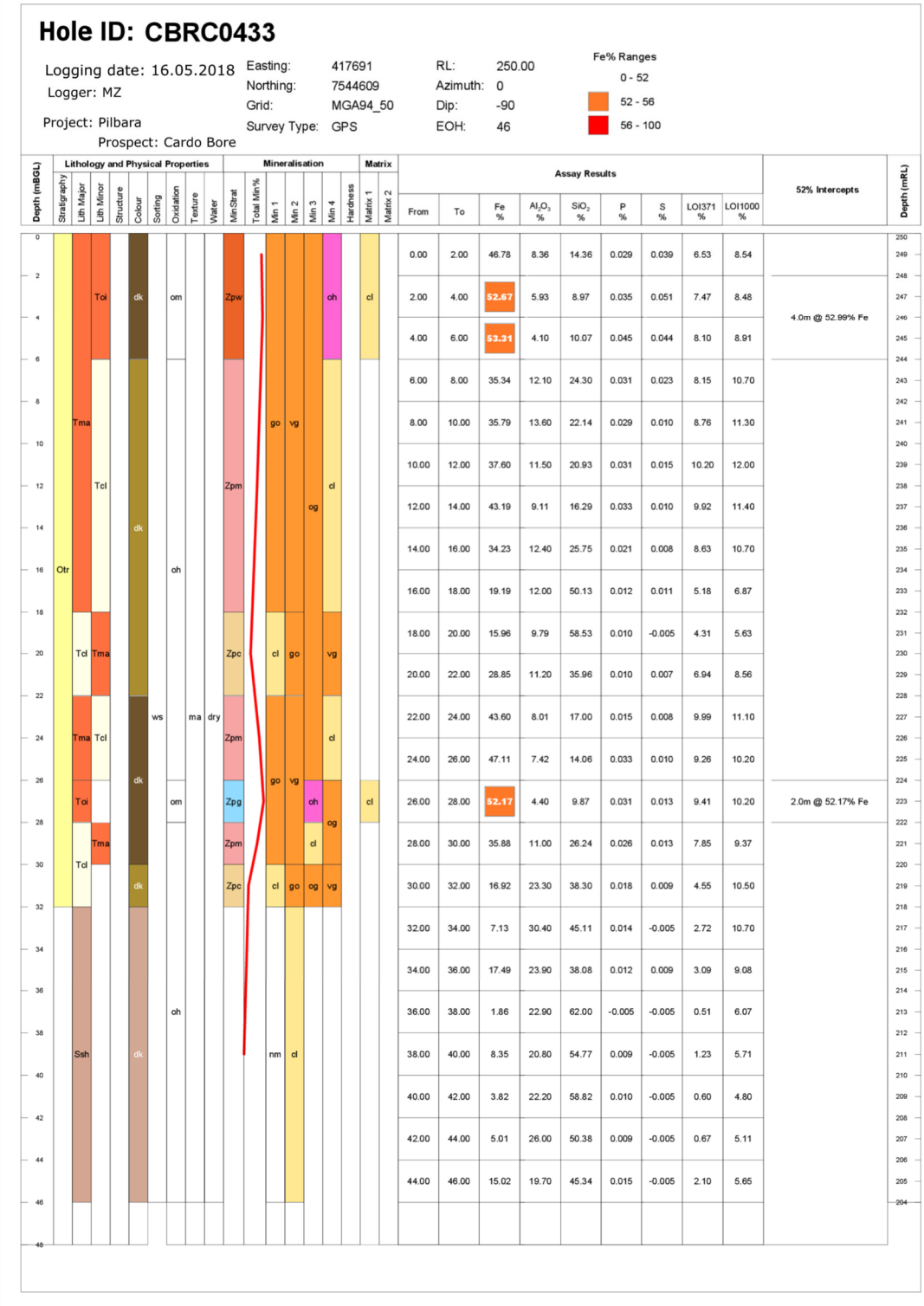

Figure A.3: Log of borehole CBRC0433.

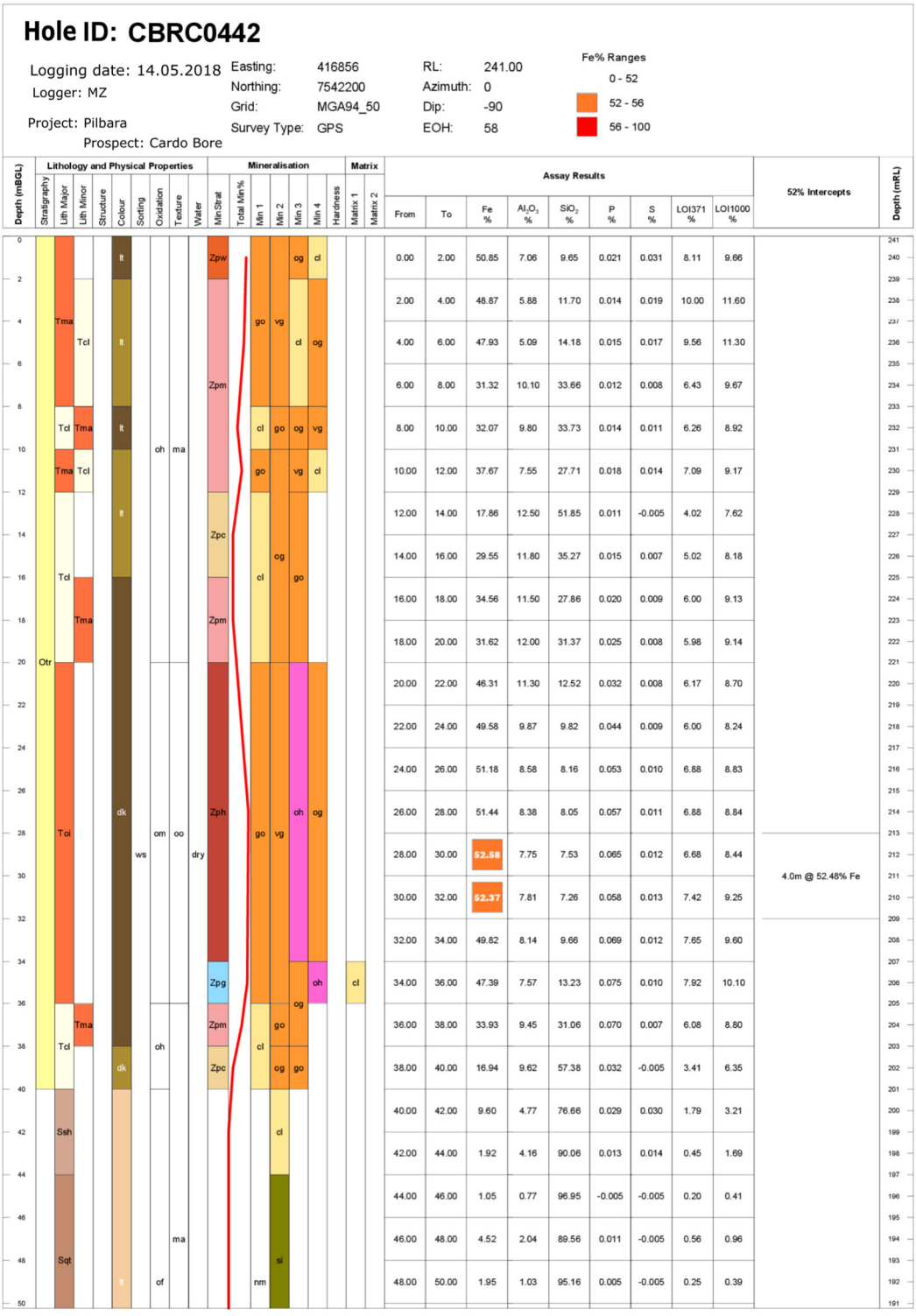

Figure A.4: Log of borehole CBRC0442.

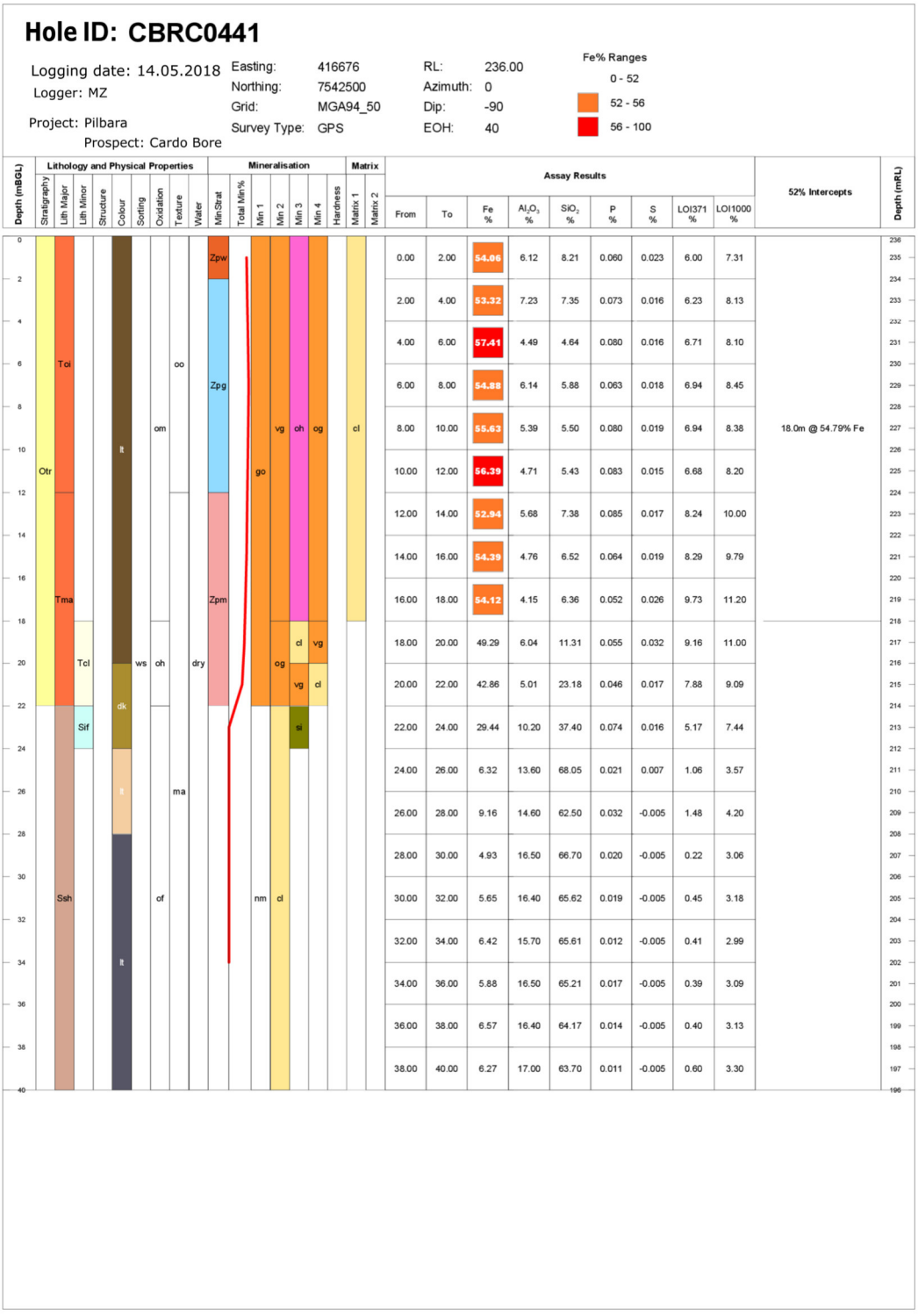

Figure A.5: Log of borehole CBRC0441.

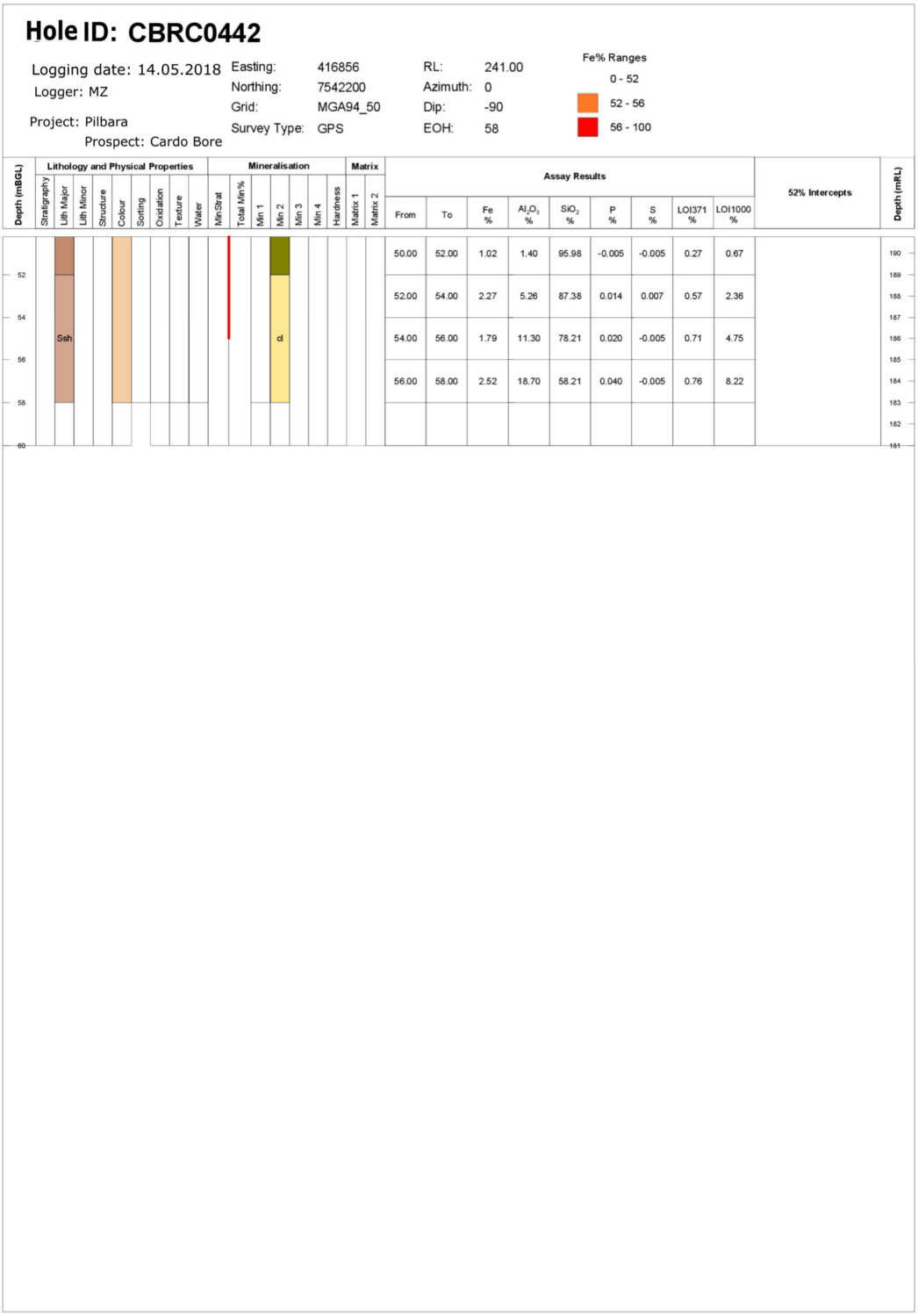

Figure A.6: Log of borehole CBRC0442.

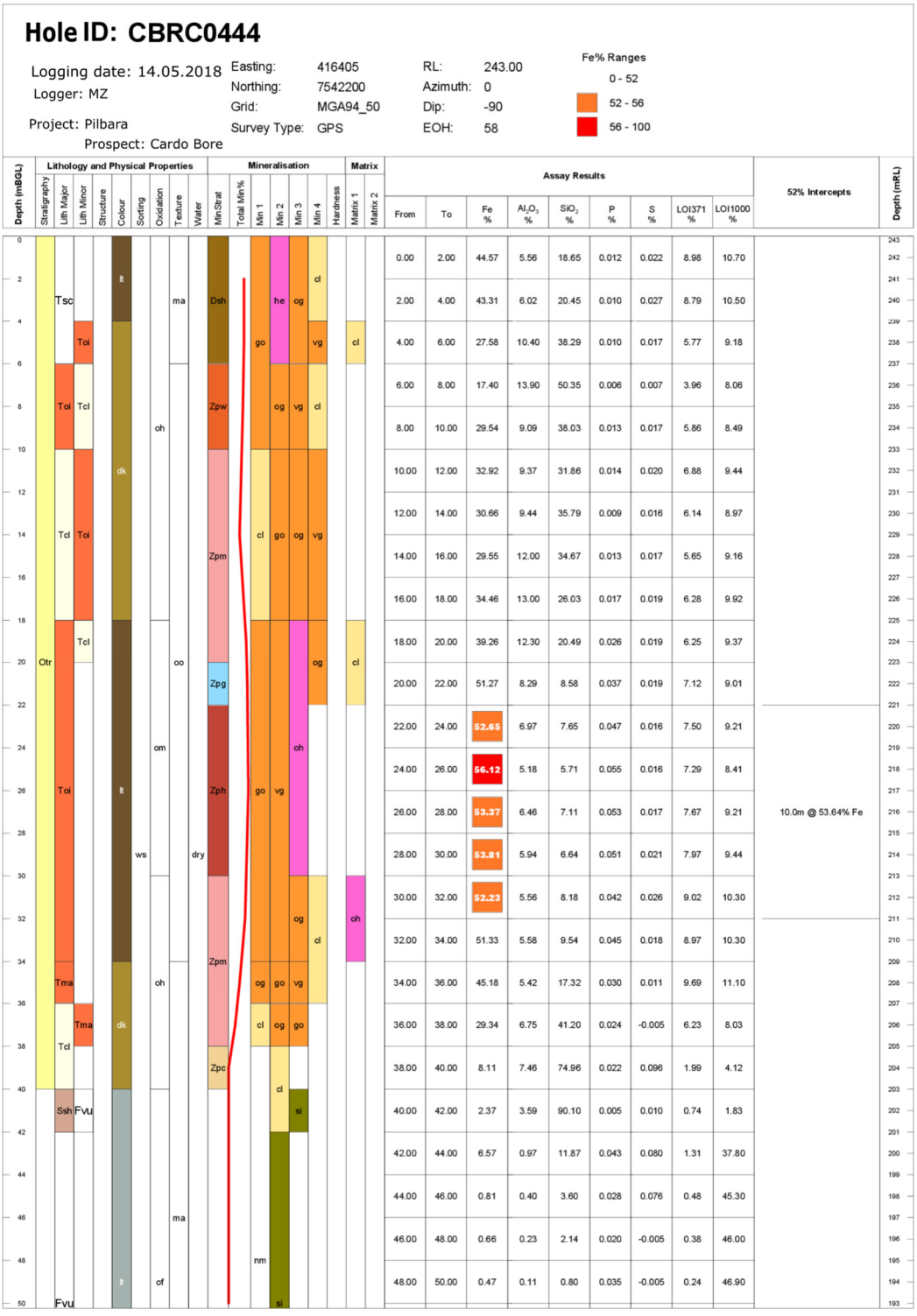

Figure A.7: Log 1 of 2 of borehole CBRC0444.

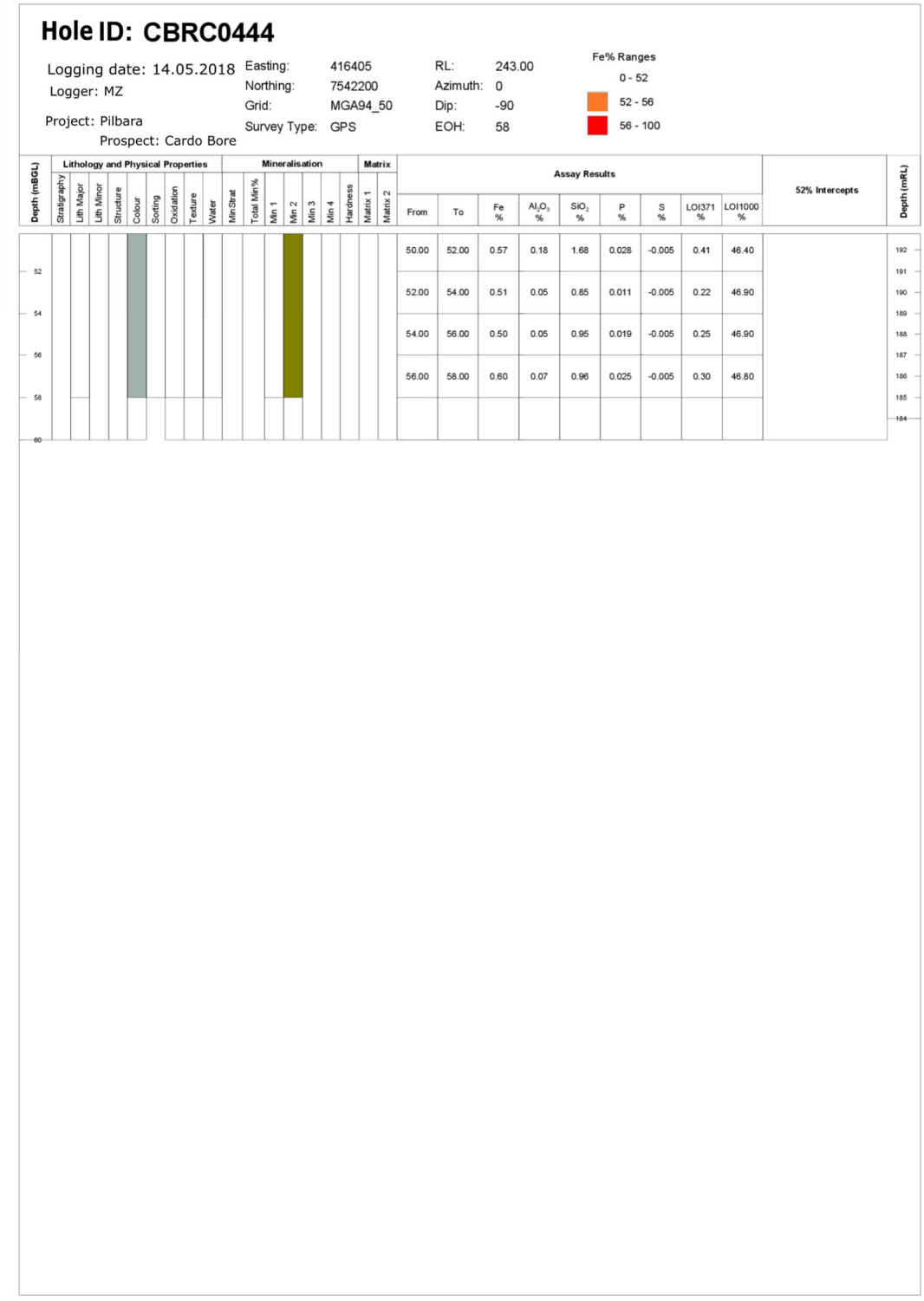

Figure A.8: Log 1 of 2 of borehole CBRC0444.

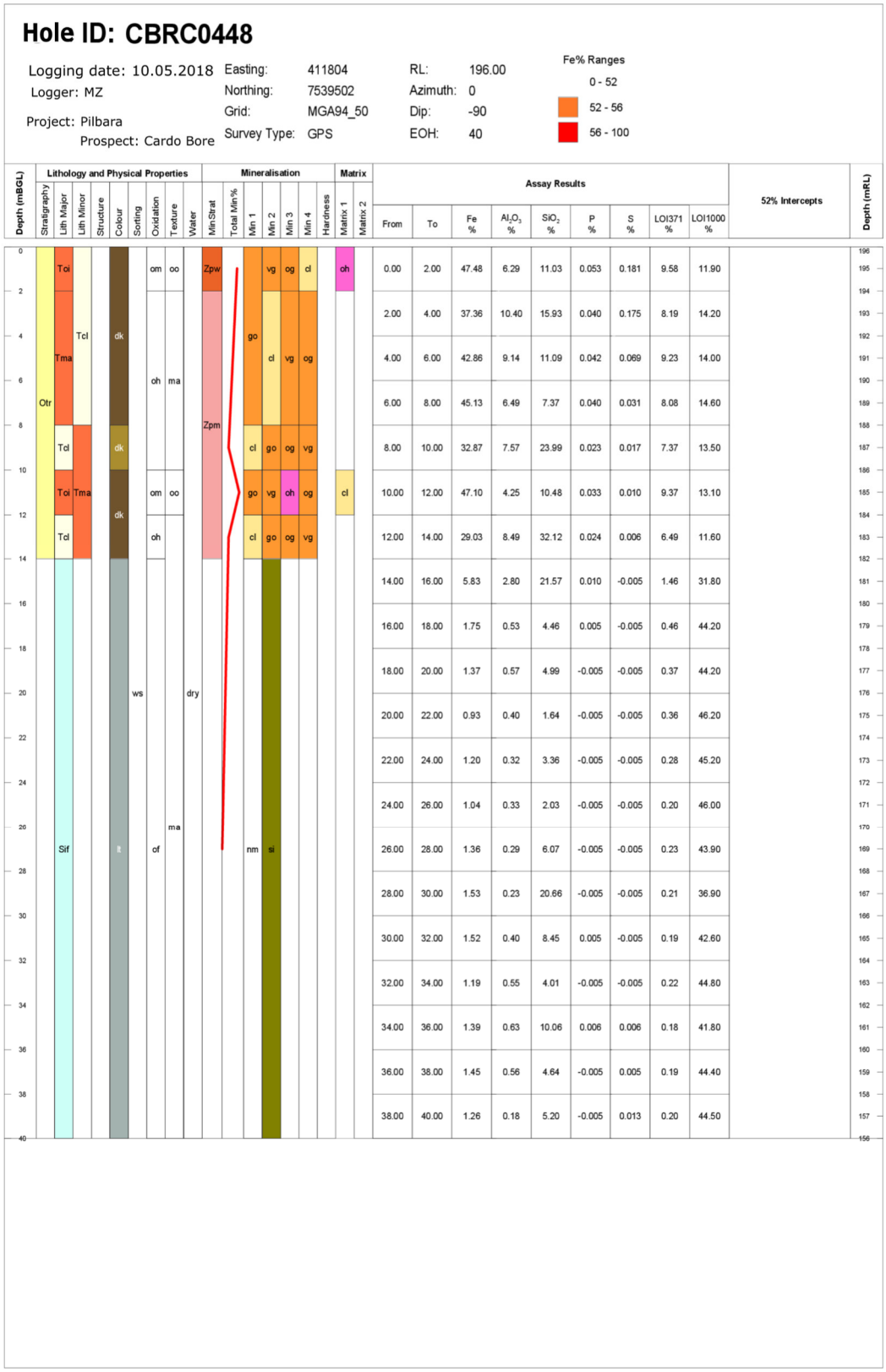

Figure A.9: Log of borehole CBRC0448.

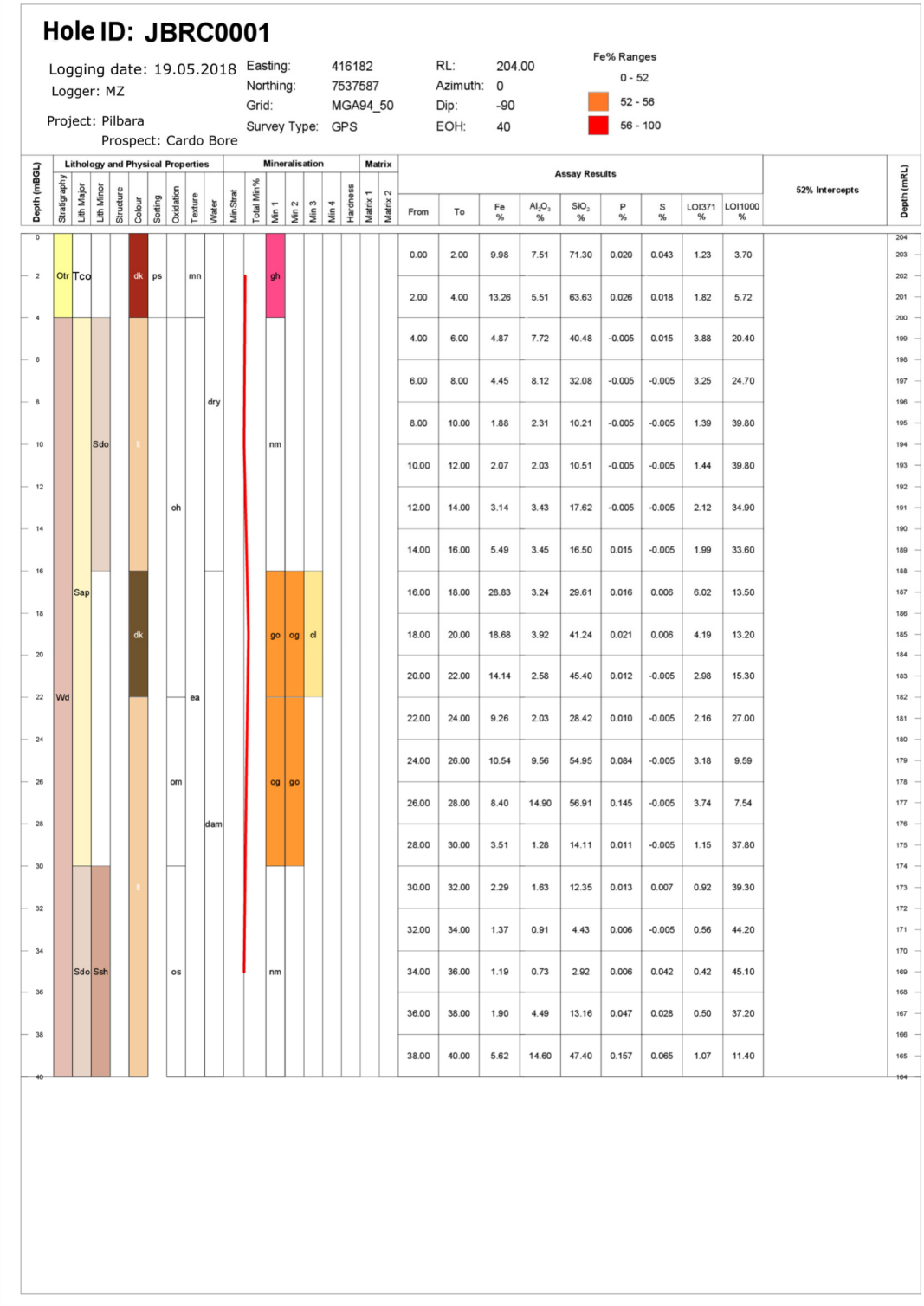

Figure A.10: Log of borehole JBRC0001.

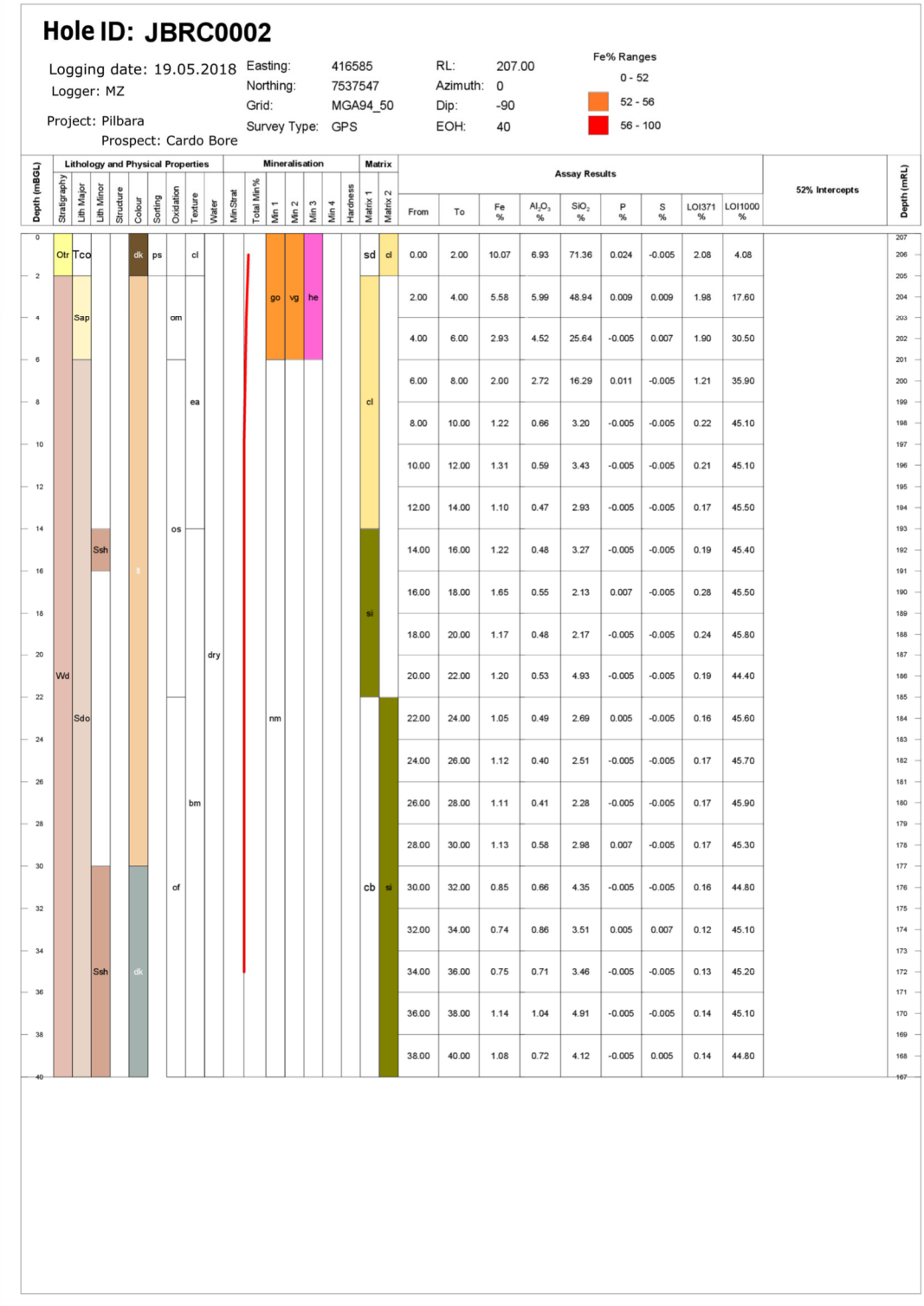

Figure A.11: Log of borehole JBRC0002.

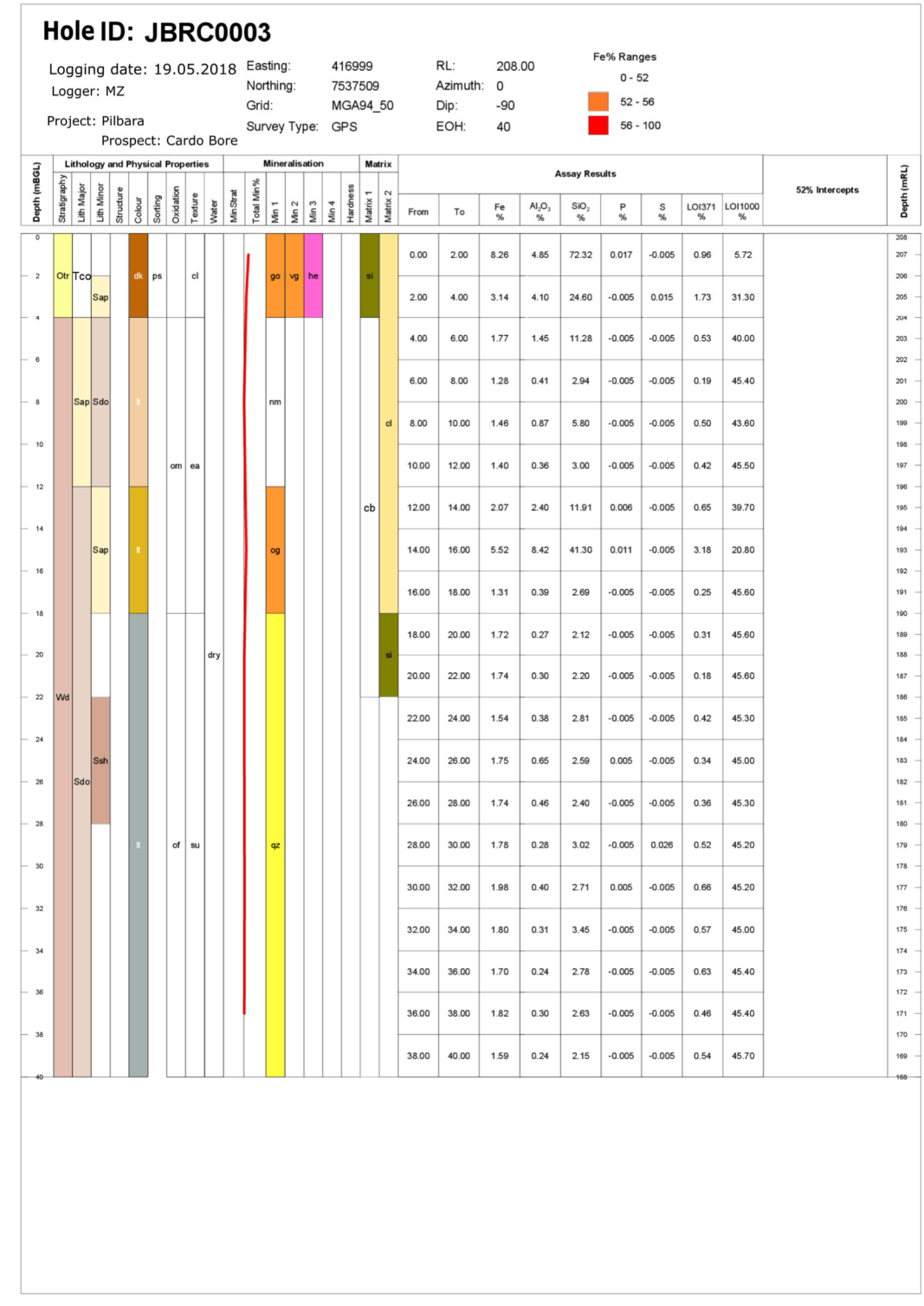

Figure A.12: Log of borehole JBRC0003.

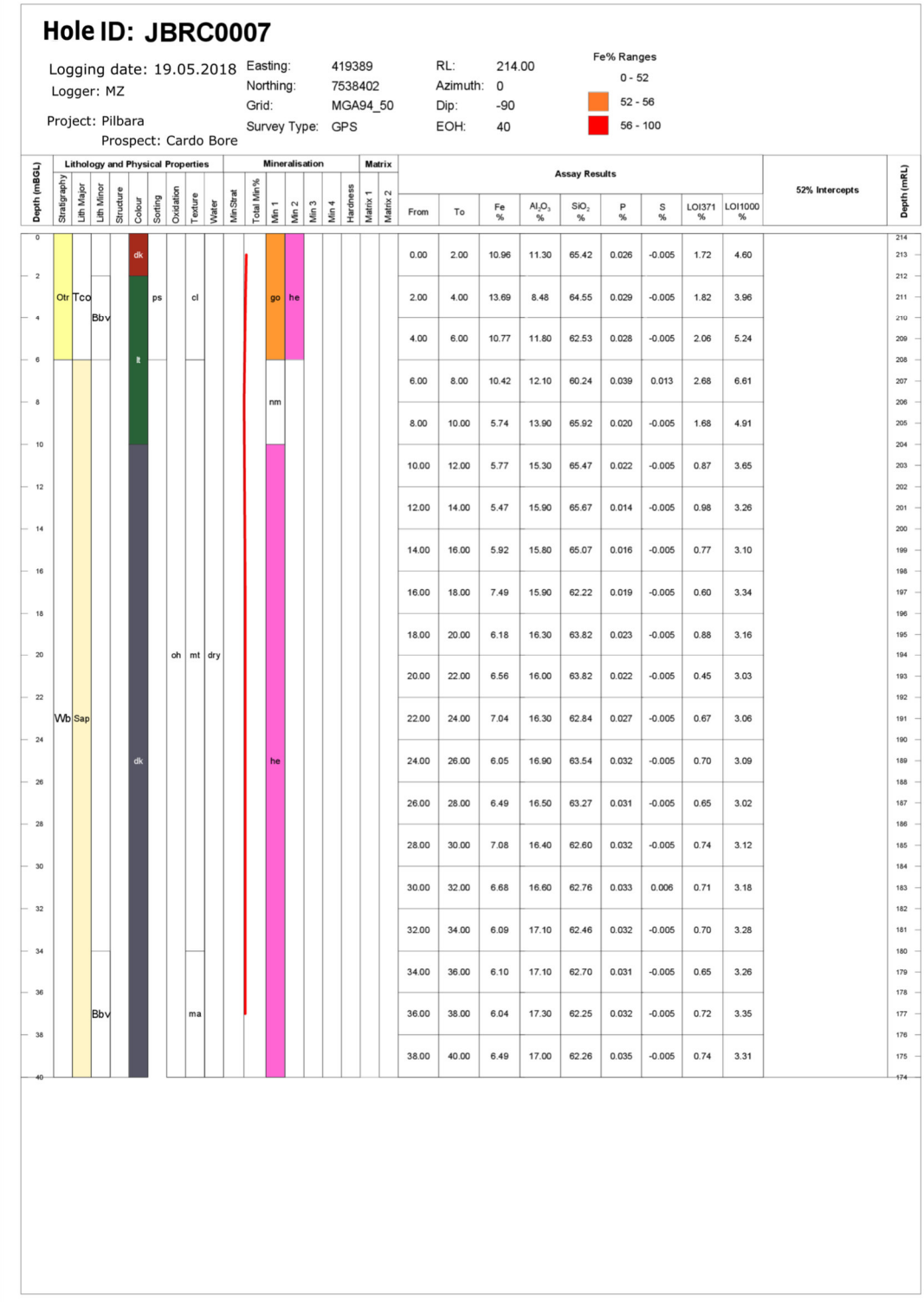

Figure A.13: Log of borehole JBRC0007.

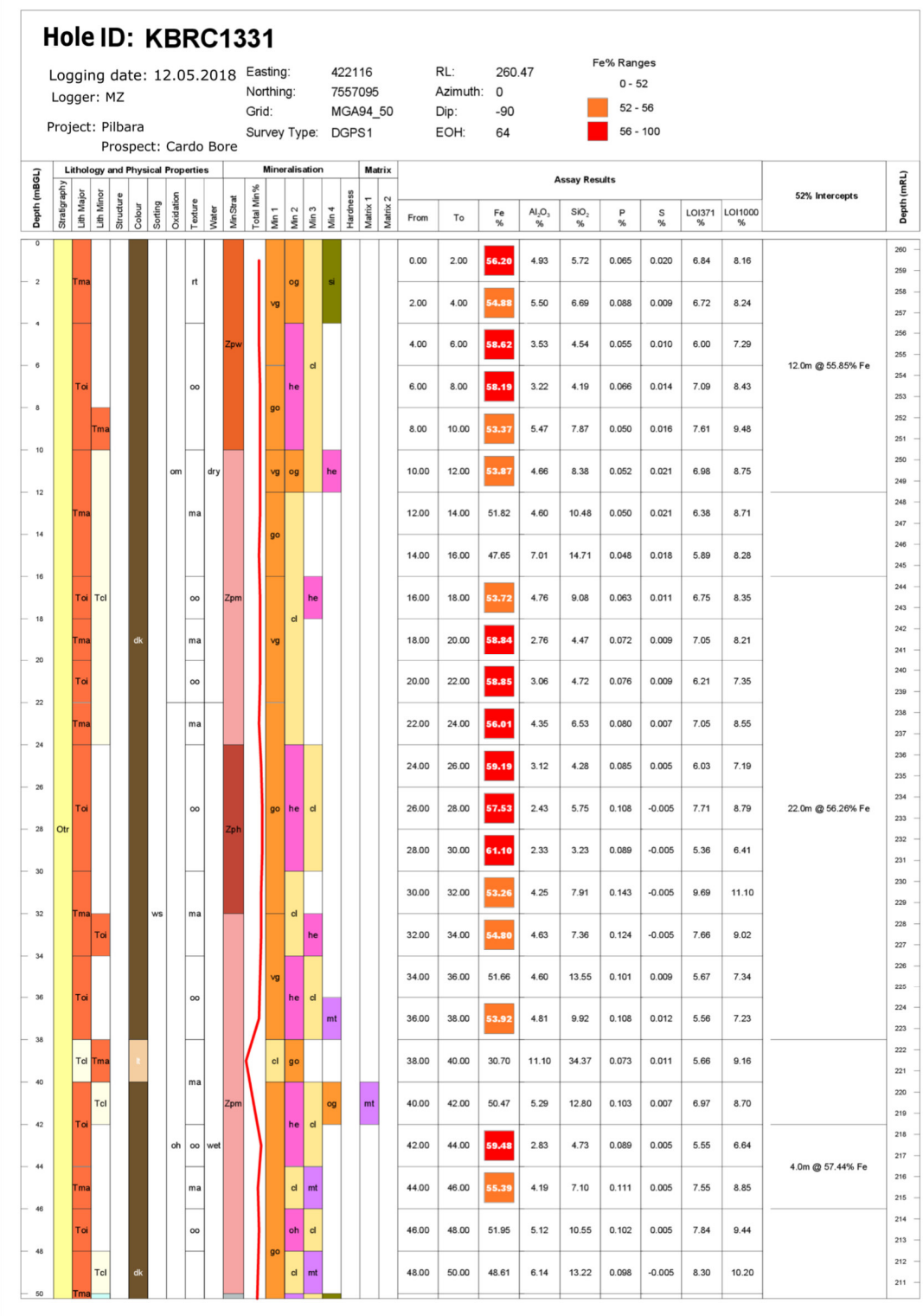

Figure A.14: Log of borehole KBRC1331.

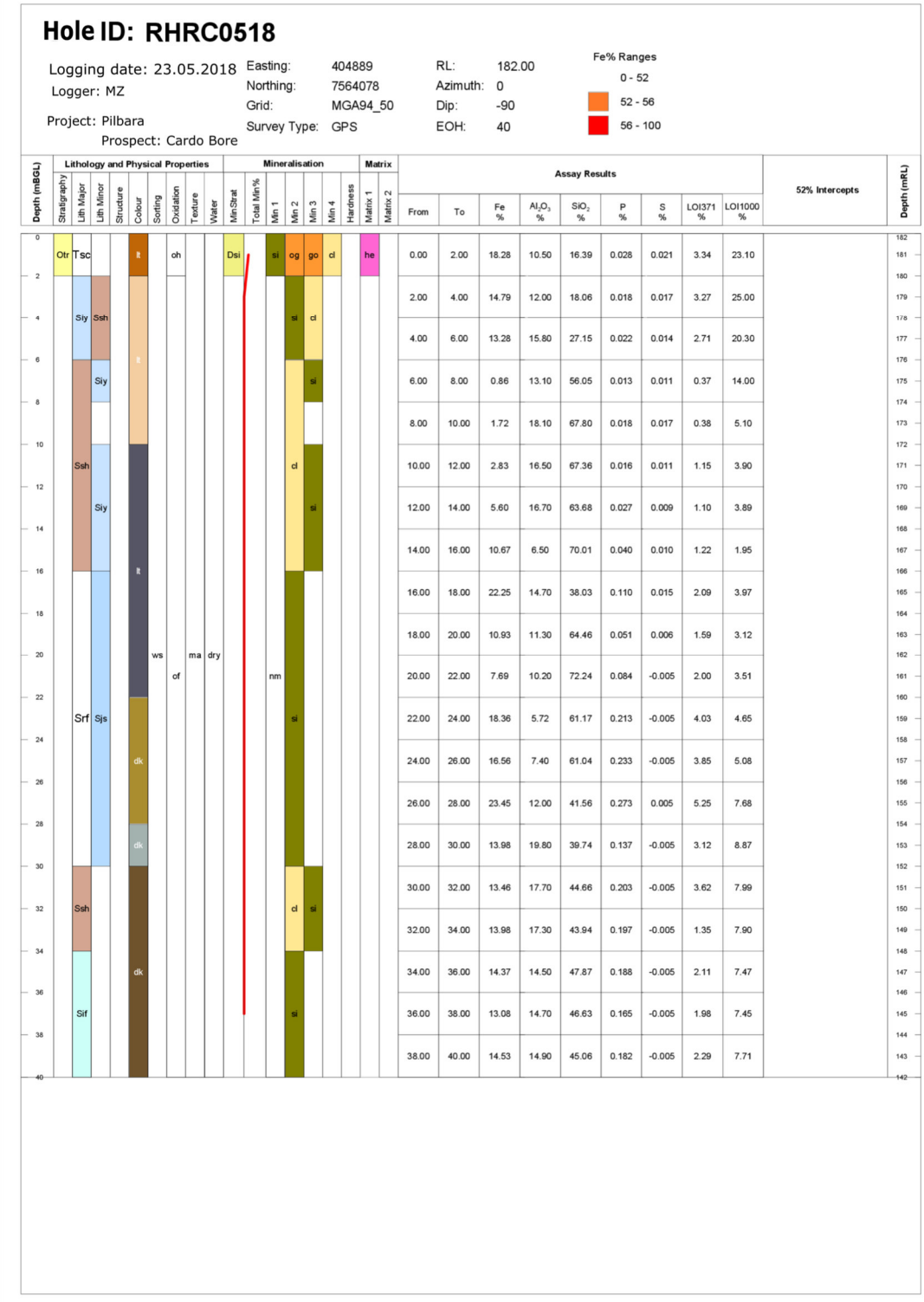

Figure A.15: Log of borehole RHRC0518.

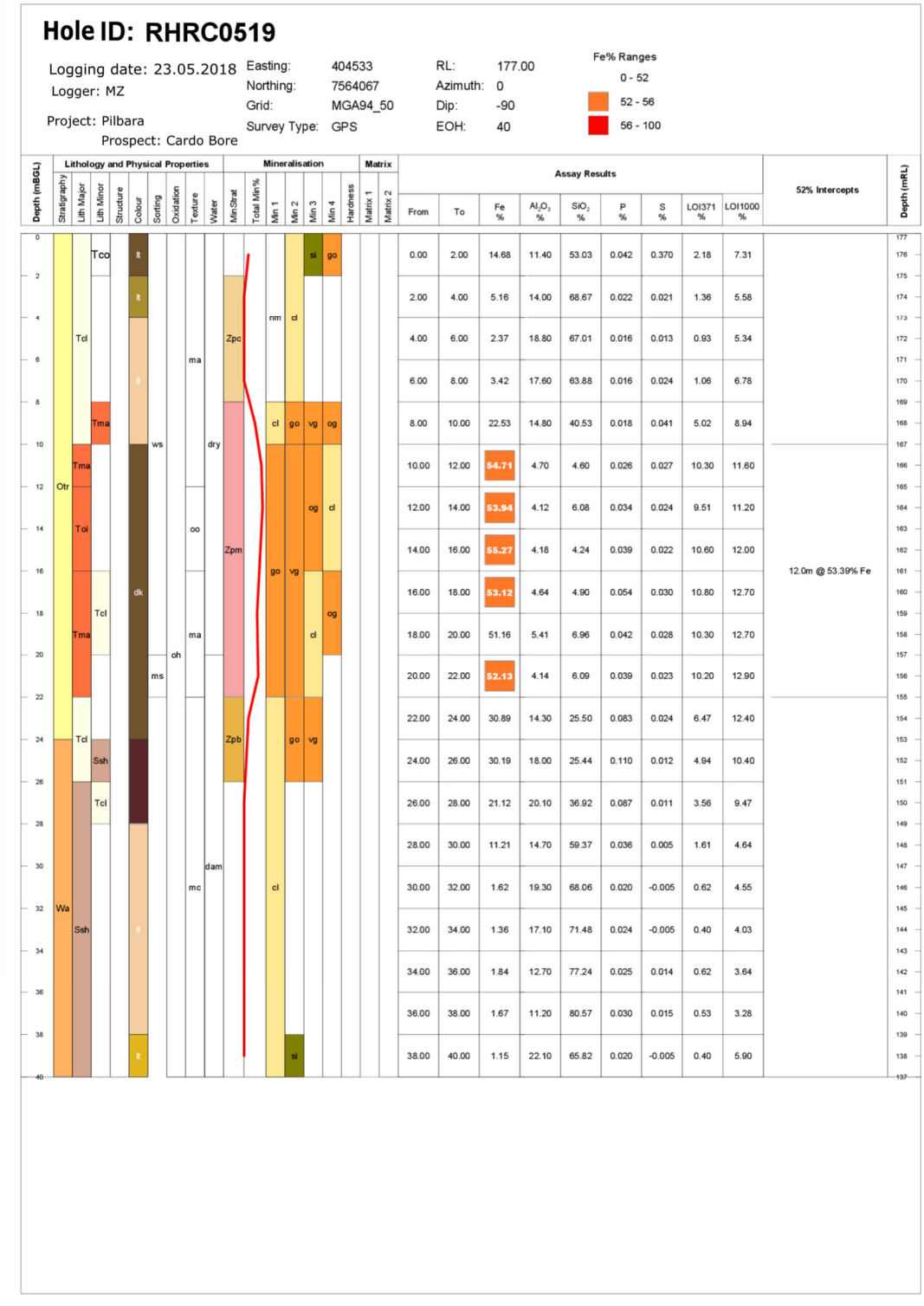

Figure A.16: Log of borehole RHRC0519.

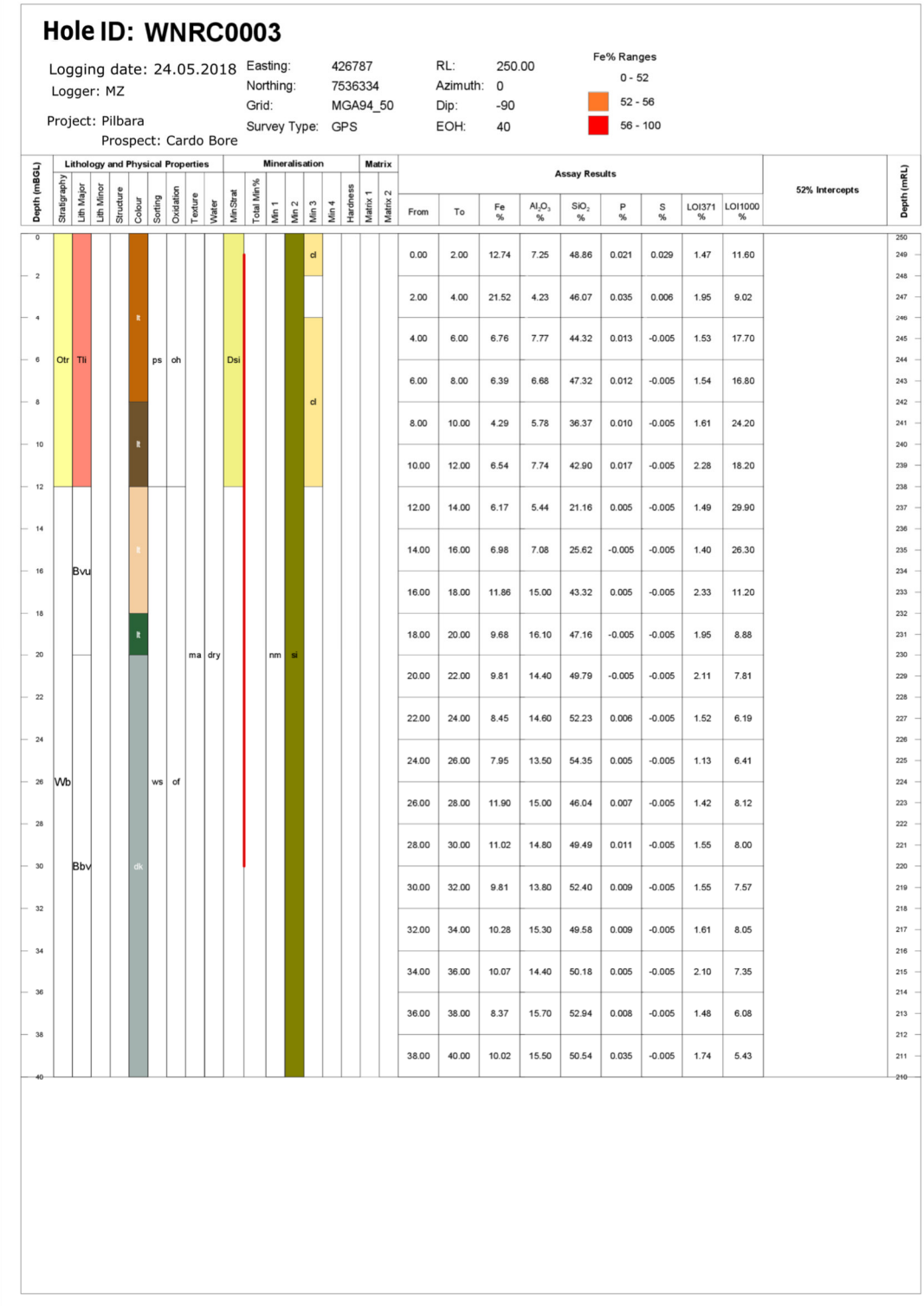

Figure A.17: Log of borehole WNRC0003.

A.1.2 Four Mile

Compilation of some relevant core and mud logs acquired during Four Mile field work. The complete logging and geochemical data can be requested from the author. As shown in Table A.3, the following acronyms and abbreviations are used in the logs.

Table A.1: Geological codes as used during the Four Mile tests.

Lith List	Description
AND	ANDESITE
BAS	BASALT
BASM	BASEMENT (Inferred)
BSMf	basement, felsic
BSMm	basement, mafic
BSWf	Weathered Felsic Basement
BSWm	Weathered Mafic Basement
BX	BRECCIA
CACT	CALCRETE
CCLY	CARBONACEOUS CLAY
CDLS	Clayey Dolomitic Limestone
CGLM	CONGLOMERATE
CGRV	CLAYEY GRAVEL
CLAY	CLAY
CLCO	CLAY WITH COAL
CLSL	CLAYEY SILT
CLST	CLAYSTONE
COAL	COAL
CRSD	Coarse Sand
CS	CALCSILICATE
CSAN	CARBONACEOUS SAND
CSLT	CARBONACEOUS SILT
CSND	CLAYEY SAND
CYSD	Clay and Sand
DIAM	DIAMICTITE
DIO	DIORITE
DLST	Dolomitic Limestone
DOL	DOLERITE
FECR	FERRICRETE
FGLM	Willawortina Fm (Fanglomerate)
FINT	Felsic Basement
GAB	GABRRO
GCLY	GRAVELLY CLAY
GPSM	GYPSUM
GRA	GRANITE
GRVL	GRAVEL/CONGLOMERATE
GSND	GRAVELLY SAND

Porosity List	Description
H	High - Sand
L	Low - Clay
MH	Mod-High - Clayey Sand
ML	Mod-Low - Sandy Clay

Grain Size List	Description
CLY	Clay
COB	Cobble
CS	Coarse sand
FS	Fine sand
GRV	Granule
MS	Medium sand
PEB	Pebble
SLT	Silt
VCS	Very coarse sand
VFS	Very fine sand

Grain Sorting List	Description
G	Graded
M	Moderately Sorted
P	Poorly Sorted
PM	Poor-Moderate
W	Well Sorted
WM	Well-Moderate

Grain Shape List	Description
A	Angular
HR	Highly Rounded
R	Rounded
SA	Sub-Angular
SR	Sub-Rounded

Sedn Fining	Description
CU	Coarsening Upwards
FU	Fining Upwards

Color/Munsel Code	Description

KCLY	KAOLINITIC CLAY
LCLY	LIGNITIC CLAY
LIGN	LIGNITE
LMST	LIMESTONE
LOSS	Loss (core)
LSND	LIGNITIC SAND
LSTC	Limestone and Clay
MD	MAFIC DYKE
MDST	MUDSTONE
META	METASEDIMENT
MINT	Mafic Intrusive
NL	Not Logged
PORP	PORPHYRY
PYSD	Pyritic Sand
QV	QUARTZ VEIN
QZT	QUARTZITE
REGO	REGOLITH/ SOIL
RHY	RHYOLITE
RHYD	RHYODACITE
SAND	SAND
SASL	SANDY SILT
SCLY	SANDY CLAY
SCOL	SANDY COAL
SDST	SANDSTONE
SGRV	SANDY GRAVEL
SILC	SILCRETE
SILT	SILT
SLCL	SILTY CLAY
SLSA	SILTY SAND
SLST	Sandy Limestone
SNCO	SAND WITH COAL
VFSD	VF Sand
VOLC	Volcanisclastic
XXXX	BLANK
SCH	Schist

Strat List	**Description**
A	Alpha
AM	Alpha Mudstone
Amch	Alpha Mudstone Channel Sands (AMch)
Ams	Alpha Mudstone Sands (AMs)
AS	Alpha Sand
B	Beta
BC	Beverley Clay
BM	Beta Mudstone
BS	Beverley Sand
BSl	Lower Beverley Sands (BSl)
BSM	Undifferentiated Basement
BSWf	Weathered Felsic Basement
BSWm	Weathered Mafic Basement
BSMf	Felsic Basement

0	No color
N9	White
N8	Very light grey
N7	Light grey
N6	Medium light grey
N5	Medium grey
N4	Medium dark grey
N3	Dark grey
N2	Grayish black
N1	Black
5YR8/1	Pinkish grey
5YR6/1	Light brownish grey
5YR4/1	Brownish grey
5YR2/1	Brownish black
5Y8/1	Yellowish grey
5Y7/2	Yellowish grey
5Y6/1	Light olive grey
5Y5/2	Light olive grey
5Y4/1	Olive grey
5Y2/1	Olive black
5YR8/4	Moderate orange pink
5YR7/2	Greyish orange pink
5YR6/4	Light brown
5YR5/2	Pale brown
5YR5/6	Light brown
5YR4/4	Moderate brown
5YR3/4	Moderate brown
10YR7/4	Greyish orange
10YR6/6	Dark yellowish orange
10YR5/4	Moderate yellowish brown
5R7/4	Moderate pink
5R6/2	Pale red
5R5/4	Moderate red
5R4/6	Moderate red
5R4/2	Greyish red
5R3/4	Dusky red
10R5/4	Pale reddish brown
10R4/6	Moderate reddish brown
10R3/4	Dark reddish brown
5R2/2	Blackish red
5GY8/1	Light greenish grey
5GY7/2	Greyish yellow green
5GY5/2	Dusky yellow green
5G7/4	Light green
5G5/6	Moderate green
5G8/1	Light greenish grey
5B7/1	Light bluish grey
5B5/1	Medium bluish grey
5B6/2	Pale blue
5PB5/2	Greyish blue
10G4/2	Greyish green

BSMm	Mafic Basement	10G6/2	Pale green
Bsu	Upper Beverley Sand (BSu)	10G8/2	Very pale green
BULL	Bulldog Shale	10GY3/2	Dusky yellowish green
BvC	Beverley Clay	10GY4/4	Dark yellowish green
BvS	Beverley Sand	10GY5/2	Greyish green
CP	Cadna-Owie Formation	10GY6/4	Moderate yellowish green
E	Eyre	10GY7/2	Pale yellowish green
EYRE	Eyre Formation	10R2/2	Very dusky red
FMD	FM Diamictite	10R4/2	Greyish red
FMG	FM Basal Conglomerate	10R6/2	Pale red
G	Gamma	10R6/6	Moderate reddish orange
GM	Gamma Mudstone	10R7/4	Moderate orange pink
GS	Gamma Sand	10R8/2	Greyish orange pink
KC	Cretaceous clay	10Y4/2	Greyish olive
KS	Cretaceous sand	10Y5/4	Light olive
LNc	Lower Namba carbonate	10Y6/2	Pale olive
NAM	Namba Formation	10Y6/6	Dark greenish yellow
U	Upper	10Y7/4	Moderate greenish yellow
W	Willawortina	10Y8/2	Pale greenish yellow
		10YR2/2	Dusky yellowish brown
Oxidised Mineral List	**Description**	10YR4/2	Dark yellowish brown
goet	Goethite - mustard-orange	10YR6/2	Pale yellowish brown
hem	Haemetite - pink-red	10YR8/2	Very pale orange
lim	Limonite - yellow	10YR8/6	Pale yellowish orange
		5B5/6	Moderate blue
Oxidised Style	**Description**	5B7/6	Light blue
MO	mottled	5B8/2	Very pale blue
PE	pervasive	5B9/1	Bluish white
SP	speckled	5BG3/2	Dusky blue green
ST	stripy / banded	5BG4/6	Moderate blue green
VN	vein / fracture	5BG5/2	Greyish blue green
		5BG6/6	Light blue green
Reductant	**Description**	5BG7/2	Pale blue green
CAB	carbonaceous	5G2/1	Greenish black
LIG	lignite / humic	5G3/2	Dusky green
SUL	sulphides	5G4/1	Dark greenish grey
		5G5/2	Greyish green
Oxidised List	**Description**	5G6/1	Greenish grey
N	Neutral	5G6/6	Brilliant green
O	Oxidised	5G7/2	Pale green
R	Reduced	5GY2/1	Greenish black
		5GY3/2	Greyish olive green
Oxidised Abundance List	**Description**	5GY4/1	Dark greenish grey
C	complete : sulp + maf all replace by limonite	5GY6/1	Greenish grey

M	moderate : sulp + maf to signif limonite	5GY7/4	Moderate yellow green
S	strong : sulp + maf to near all by limonite	5P2/2	Very dusky purple
T	trace-ox : mostly fresh sulphides, minor limonite	5P4/2	Greyish purple
U	un-oxid : fresh sulphides + mafics	5P6/2	Pale purple
W	weak ox : sulp + maf to minor limonite, signif lim fracs	5PB3/2	Dusky blue
		5PB7/2	Pale blue
		5R2/6	Very dark red
		5R6/6	Light red
		5R8/2	Greyish pink
		5RP2/2	Very dusky red purple
		5RP4/2	Greyish red purple
		5RP6/2	Pale red purple
		5RP8/2	Pale pink
		5Y3/2	Olive grey
		5Y4/4	Moderate olive brown
		5Y5/6	Light olive brown
		5Y6/4	Dusky yellow
		5Y7/6	Moderate yellow
		5Y8/4	Greyish yellow
		5YR2/2	Dusky brown
		5YR3/2	Greyish brown
		Not Specified	Not Specified

Table A.2: Logs of boreholes FSC0008, FSC0009, FMC024.

HoleID	from	to	Lith	Lith2	Porosity	SedGrainSize_1	SedGrainSize_2	SedGrainSort	SedGrainRound	Color_1	Color_2	OxidIndex	OxidAbundance	OxidMineral	StratLocalUnit
FSC0008	0.00	6.00	SCLY		ML	CS	CLY	WM	SA	10YR5/4	0	O	M	hem	W
	6.00	8.00	CSND		MH	CS	CLY	WM	SR	5R6/2	0	O	M	hem	W
	8.00	12.00	CSND		MH	CS	CLY	WM	SA	N7	5YR8/1	O	M	hem	W
	12.00	28.00	SCLY		ML	MS	CLY	WM	SA	5R6/2	5R7/4	O	S	hem	W
	28.00	36.00	CSND		MH	CS	CLY	WM	SR	5R5/4	5R4/6	O	M	hem	W
	36.00	44.00	CSND		ML	CS	CLY	WM	SR	5R7/4	5YR8/1	O	M	hem	NAM
	44.00	50.00	SCLY		ML	MS	CLY	WM	SR	5R5/4	5R6/2	O	S	hem	NAM
	50.00	58.00	SCLY		ML	CS	CLY	WM	SA	N9	5R7/4	O	M	hem	NAM
	58.00	60.00	SCLY		ML	CS	CLY	WM	SR	5R7/4	5R6/2	O	M	hem	NAM
	60.00	62.00	SCLY		ML	MS	CLY	WM	SR	10YR5/4	5R7/4	O	M	hem	NAM
	62.00	76.00	SCLY		ML	MS	CLY	M	SR	5R7/4	5YR8/4	O	M	hem	NAM

	76.00	92.00	CLAY	SCLY	ML	MS	CLY	WM	SR	5R6/2	5R7/4	O	M	hem	NAM
	92.00	94.00	SAND	CSND	H	VCS	CLY	WM	SA	5YR5/6	10YR7/4	O	S	goet	NAM
	94.00	98.00	SAND	CSND	H	CS	CLY	WM	SA	5YR8/1	5YR7/2	O	M	hem	NAM
	98.00	104.00	SAND	CSND	H	CS	CLY	WM	SA	5R6/2	5YR8/1	O	M	hem	EYRE
	104.00	106.00	CLAY		L	SLT	CLY	W		10YR7/4	N8	O	S	lim	EYRE
	106.00	108.00	CLAY		L	CLY		W		N9	0	R			EYRE
	108.00	124.00	CLAY			CLY				N8	N9	R			EYRE
	124.00	144.00	BSWf							5R6/2	0	O			BSWf
	144.00	156.00	BSWf							5R5/4	5R6/2	O	S	hem	BSWf
	156.00	159.52	BSWf							5R6/2	0	O	S	hem	BSWf
	159.52	160.00	BSWf							10YR6/6	5R7/4	O	S	hem	BSWf
	160.00	160.80	BSWf							10YR6/6	5R7/4	O	M	hem	BSWf
	160.80	161.30	BSWf							5R7/4	5GY8/1	O	M	hem	BSWf
	161.30	162.00	BSWf	QV						5R7/4	5GY8/1	O	M	hem	BSWf
	162.00	163.00	BSWf	QV						5R5/4	5R7/4	O	S	hem	BSWf
	163.00	164.32	BSWf							5R5/4	5R7/4	O	S	hem	BSWf
	164.32	164.82	BSWf	QV						5R5/4	5R7/4	O	S	hem	BSWf
	164.82	165.26	BSWf							5R5/4	5R7/4	O	S	hem	BSWf
	165.26	165.70	BSWf	QV						5R5/4	5R7/4	O	S	hem	BSWf
	165.70	166.75	BSWf							5R5/4	5R7/4	O	S	hem	BSWf
	166.75	167.00	BSWf	QV						5R6/2	5YR7/4	O	M	hem	BSWf
	167.00	167.35	BSWf	QV						5R6/2	5YR7/4	O	S	hem	BSWf
	167.35	168.50	BSWf							10R4/6	10R5/4	O	S	hem	BSWf
	168.50	169.30	BSWf	QV						10R4/6	10R5/4	O	S	hem	BSWf
	169.30	169.67	BSWf	QV						5R6/2	N6	O	W	hem	BSWf
	169.67	170.15	BSWf							5R6/2	N6	O	W	hem	BSWf
	170.15	170.40	BSWf							5R5/4	N6	O	W	hem	BSWf
	170.40	171.33	BSWf							5R5/4	N6	O	T	hem	BSWf
	171.33	171.90	BSWf	QV						5R5/4		O	W	hem	BSWf
	171.90	172.80	BSWf							5R6/2	5R5/4	O	M	hem	BSWf
	172.80	173.32	BSWf	QV						10R4/6	N9	O	S	hem	BSWf
	173.32	173.60	BSWf	QV						10R4/6	N9	O	S	hem	BSWf
	173.60	174.00	BSWf							10R4/6	N9	O	S	hem	BSWf
	174.00	174.77	BSWf							10R4/6	N9	O	M	hem	BSWf
	174.77	175.70	BSWf	QV						10R4/6	N9	O	M	hem	BSWf
	175.70	175.95	BSWf							10R4/6	N9	O	M	hem	BSWf
	175.95	176.20	BSWf	QV						10R4/6	N9	O	M	hem	BSWf
	176.20	177.05	BSWf							10YR6/6		O	M	geot	BSWf
	177.05	177.40	BSWf	QV						10YR6/6		O	M	geot	BSWf
	177.40	177.72	BSWf	QV						10YR6/6	N9	O	M	geot	BSWf
	177.72	178.95	BSWf							10YR6/6	N9	O	M	geot	BSWf
	178.95	179.50	BSWf							5R7/4	10YR7/4	O	M	hem	BSWf
	179.50	180.00	BSWf	QV						5R7/4	10YR7/4	O	M	hem	BSWf

	180.00	180.85	BSWf	QV						10R5/4	5YR8/1	O	M	hem	BSWf
	180.85	181.75	BSWf							10R5/4	5YR8/1	O	M	hem	BSWf
	181.75	182.45	BSWf							10R5/4	10R4/6	O	S	hem	BSWf
	182.45	182.95	BSWf	QV						10R5/4	5YR8/1	O	S	hem	BSWf
	182.95	183.55	BSWf	QV						10R5/4	5R7/4	O	S	hem	BSWf
	183.55	184.27	BSWf							5R6/2	5R7/4	O	M	hem	BSWf
	184.27	184.80	BSWf	QV						5R7/4	10YR6/6	O	M	goet	BSWf
	184.80	186.12	BSWf							10YR6/6	10YR6/4	O	M	goet	BSWf
	186.12	187.00	BSWf	QV						10R5/4	5R7/4	O	S	hem	BSWf
	187.00	188.30	BSWf	QV						10R5/4	5R7/4	O	S	hem	BSWf
	188.30	188.72	BSWf							10R5/4	5R7/4	O	S	hem	BSWf
	188.72	189.05	BSWf	QV						10R5/4	5R7/4	O	S	hem	BSWf
	189.05	190.55	BSWf	QV						10R5/4	5YR8/1	O	S	hem	BSWf
	190.55	191.20	BSWf	QV						10R5/4	5YR8/1	O	S	hem	BSWf
	191.20	191.53	BSWf							10YR7/4	5YR8/4	O	M	goet	BSWf
	191.53	192.15	BSWf							5R7/4		O	M	hem	BSWf
	192.15	193.05	BSWf							10R5/4	5R6/2	O	M	hem	BSWf
	193.05	193.47	BSWf	QV						10R5/4	5R6/2	O	M	hem	BSWf
	193.47	194.25	BSWf							10R5/4	5R6/2	O	M	hem	BSWf
	194.25	194.60	BSWf	QV						10R5/4	5R6/2	O	M	hem	BSWf
	194.60	194.80	BSWf							10R5/4	5R6/2	O	M	hem	BSWf
	194.80	196.10	BSWf							5GY7/2	10YR7/4	O	T	goet	BSWf
	196.10	196.52	BSWf	QV						10R5/4	5R6/2	O	M	hem	BSWf
	196.52	196.87	BSWf							5R6/2	10YR7/4	O	T	goet	BSWf
	196.87	197.27	BSWf	QV						5GY7/2	5YR6/6	O	M	goet	BSWf
	197.27	197.71	BSWf							5GY7/2	5YR6/6	O	M	goet	BSWf
	197.71	198.00	BSWf							5R6/2	10R4/6	O	M	hem	BSWf
	198.00	198.40	BSWf	QV						10R4/6	5R6/2	O	M	hem	BSWf
	198.40	198.65	BSWf	QV						N9	10R4/6	O	M	hem	BSWf
	198.65	199.67	BSWf	QV						10R5/4	5YR8/1	O	W	hem	BSWf
	199.67	200.00	BSWf	QV						5GY7/2	5R4/6	O	T	hem	BSWf
	200.00	202.11	BSWf	QV						10R5/4	10R4/6	O	S	hem	BSWf
	202.11	202.87	BSWf							5GY5/2	5YR6/6	O	T	goet	BSWf
	202.87	203.50	BSWf	QV						10R4/6	10R5/4	O	S	hem	BSWf
	203.50	204.25	BSWf							5GY5/2	5YR6/6	O	T	goet	BSWf
	204.25	204.50	BSWf							5GY5/2	5YR6/6	O	M	goet	BSWf
	204.50	205.10	BSWf							5GY5/2	10YR7/4	O	S	hem	BSWf
	205.10	205.47	BSWf	QV						10R5/4	10R4/6	O	S	hem	BSWf
	205.47	206.00	BSWf	QV						10R4/6	5YR8/1	O	S	hem	BSWf
	206.00	206.48	BSWf							10R4/6	5YR8/1	O	S	hem	BSWf
	206.48	207.00	BSWf	QV						10R4/6	5YR8/1	O	S	hem	BSWf
	207.00	207.65	BSWf	QV						10R4/6	5YR8/1	O	S	hem	BSWf
	207.65	207.42	BSWf	QV						10R4/6	5YR8/4	O	S	hem	BSWf

	207.42	208.70	BSWf							10R4/6	5YR5/6	O	S	hem	BSWf
	208.70	209.10	BSWf	QV						5GY7/2	10YR7/4	O	T	goet	BSWf
	209.10	210.10	BSWf	QV						10R4/6		O	S	hem	BSWf
	210.10	210.36	BSWf	QV						5GY7/2	10YR7/4	O	T	goet	BSWf
	210.36	212.35	BSWf	QV						10R4/6		O	S	hem	BSWf
	212.35	212.90	BSWf	QV						5YR5/6	5YR4/4	O	S	goet	BSWf
	212.90	213.83	BSWf	QV						5YR5/6	5YR4/4	O	S	goet	BSWf
	213.83	214.33	BSWf	QV						10R4/6	10R5/4	O	S	hem	BSWf
	214.33	215.35	BSWf	QV						10YR6/6	10YR7/4	O	M	goet	BSWf
	215.35	216.45	QV	BSWf						N8	5YR5/6	O	M	goet	QV
	216.45	218.30	BSWf	QV						5YR5/6	N8	O	M	goet	BSWf
	218.30	218.70	BSWf	QV						10R4/6	5R3/4	O	S	hem	BSWf
	218.70	219.77	BSWf	QV						10R5/4	5GY5/2	O	M	hem	BSWf
	219.77	220.82	BSWf	QV						5GY5/2	10R5/4	O	W	hem	BSWf
	220.82	221.83	BSWf	QV						5GY5/2	10YR7/4	O	T	goet	BSWf
	221.83	222.50	BSWf	QV						5GY5/2		O	T	goet	BSWf
	222.50	223.32	BSWf	QV						5GY5/2	10YR6/6	O	W	goet	BSWf
	223.32	224.20	BSWf	QV						10R6/6	10R4/6	O	S	goet	BSWf
	224.20	224.70	BSWf	QV						10R6/6	N8	O	W	goet	BSWf
	224.70	224.95	QV	BSWf						N8	10R6/6	O	W	goet	BSWf
	224.95	225.62	BSWf	QV						10R4/6	10R5/4	O	S	hem	BSWf
	225.62	226.00	BSWf	QV						10YR7/4	10YR6/6	O	M	goet	BSWf
	226.00	226.24	BSWf	QV						10YR7/4	10YR6/6	O	M	hem	BSWf
	226.24	226.50	BSWf	QV						N6	10R4/6	O	T	hem	BSWf
	226.50	226.80	BSWf							10R4/6	10YR6/6	O	M	hem	BSWf
	226.80	227.80	BSWf							5GY5/2	N6	O	T	goet	BSWf
	227.80	227.43	BSWf							10R4/6	5R4/2	O	M	hem	BSWf
	227.43	228.20	BSWf	QV						10R4/6	5R4/2	O	M	hem	BSWf
	228.20	228.95	BSWf							10R4/6	5R4/2	O	M	hem	BSWf
	228.95	229.22	BSWf	QV						10YR6/6	10YR7/4	O	S	goet	BSWf
	229.22	229.50	BSWf	QV						10YR7/4	10YR6/6	O	M	goet	BSWf
	229.50	230.45	BSWf							10YR7/4	10YR6/6	O	S	goet	BSWf
	230.45	231.60	BSWf	QV						10YR7/4	10YR6/6	O	S	goet	BSWf
	231.60	232.00	BSWf							5Y5/2	N6	O	T	goet	BSWf
	232.00	232.65	BSWf	QV						5GY5/2	10YR7/4	O	T	goet	BSWf
	232.65	233.00	BSWf							5GY5/2	10YR7/4	O	T	goet	BSWf
	233.00	234.25	BSWf	QV						5GY5/2	N6	O	T	goet	BSWf
	234.25	234.50	BSWf							5GY5/2	N6	O	T	goet	BSWf
	234.50	234.75	BSWf							5YR5/6	N5	O	W	goet	BSWf
	234.75	235.00	BSWf							5YR5/6	N5	O	T	goet	BSWf
	235.00	235.70	BSWf							10YR7/4	10YR6/6	O	M	goet	BSWf
	235.70	238.60	BSWf	QV						10YR7/4	N6	O	M	goet	BSWf
	238.60	239.30	BSWf							10YR7/4	N6	O	M	goet	BSWf

	239.30	239.70	BSWf	QV						10YR7/4	N6	O	M	goet	BSWf
FSC0009	0.00	4.00	GCLY		MH	SLT	GRV	P	SA	5YR5/6	5Y7/2	O	S	hem	W
	4.00	10.00	GRVL		H	PEB		PM	A	5YR5/6	5R5/4	O	S	hem	W
	10.00	16.00	SLSA	GRVL	MH	SLT	CS	P	SA	0	0	O	S	hem	W
	16.00	20.00	SASL		ML	SLT	MS	PM	SR	5R4/6	5Y7/2	O	S	hem	W
	20.00	22.00	GRVL	SASL	H	PEB	SLT	PM	A	5R4/6	5Y7/2	O	S	hem	W
	22.00	32.00	SLSA		ML	CS	SLT	PM	SR	5R4/6	5YR5/6	O	S	hem	W
	32.00	36.00	SGRV		H	PEB	CS	PM	SA	5R4/6	10YR7/4	O	S	hem	W
	36.00	40.00	SASL		ML	SLT	MS	WM	SR	10YR7/4	5Y7/2	O	S	hem	W
	40.00	46.00	SLSA		ML	CS	SLT	WM	SR	5Y8/1	5R4/6	O	S	hem	W
	46.00	52.00	SASL		MH	SLT	CS	WM	SR	5R4/6	5Y8/1	O	S	hem	W
	52.00	58.00	SASL		ML	SLT	MS	WM	SR	10YR7/4	5Y7/2	O	S	hem	NAM
	58.00	62.00	SASL		MH	SLT	CS	WM	SR	5R4/6	5Y7/2	O	S	hem	NAM
	62.00	66.00	SLSA		MH	CS	SLT	WM	R	5Y8/1	5R5/4	O	M	hem	NAM
	66.00	68.00	SLSA		H	CS	SLT	WM	R	5R3/4	0	O	S	hem	NAM
	68.00	72.00	SAND		H	CS		W	R	5R5/4	0	O	S	hem	NAM
	72.00	76.00	SASL		MH	SLT	CS	PM	SR	10YR7/4	5Y8/1	O	M	goet	NAM
	76.00	80.00	SASL		ML	SLT	MS	PM	SR	5Y8/1	5R5/4	O	M	goet	NAM
	80.00	86.00	SASL		MH	SLT	CS	WM	SR	5R4/6	5Y8/1	O	S	hem	NAM
	86.00	88.00	SASL		ML	SLT	CS	WM	SR	5YR5/6	0	O	M	goet	NAM
	88.00	90.50	GSND		H	COB	MS	P	SA	5YR4/4	5YR6/4	O	C	hem	NAM
	90.50	91.50	CSND		MH	CS	CLY	WM	SA	5YR4/4	5YR6/4	O	S	goet	NAM
	91.50	93.00	SAND	CSND	MH	CS	CLY	WM	SA	10YR7/4	5YR6/4	O	S	goet	NAM
	93.00	94.15	CSND		MH	CS	CLY	WM	SA	5YR8/4	5YR6/4	O	M	goet	NAM
	94.15	95.70	GCLY		MH	VCS	CLY	WM	SA	5YR8/4	5YR6/4	O	M	goet	NAM
	95.70	96.60	GCLY		MH	COB	CLY	WM	SA	5YR8/4	5YR6/4	O	M	goet	NAM
	96.60	98.00	GCLY		MH	PEB	CLY	WM	SA	5YR8/4	5YR6/4	O	M	goet	NAM
	98.00	98.50	CSND		MH	VCS	CLY	WM	SA	5YR8/4	5YR6/4	O	M	goet	NAM
	98.50	98.90	CSND		MH	PEB	CLY	WM	SR	10YR7/4	5YR4/4	O	W	goet	NAM
	98.90	99.30	GSND		H	PEB	MS	P	SR	5YR3/4	10YR7/4	O	M	goet	NAM
	99.30	99.85	CSND		MH	CS	CLY	WM	SR	5YR4/4	10R3/4	O	S	hem	EYRE
	99.85	100.81	CLAY	SCLY	ML	FS	CLY	W	SR	5R6/2	0	O	S	hem	EYRE
	100.81	101.33	SCLY		ML	MS	CLY	WM	SR	5YR8/4	5R7/4	O	W	hem	EYRE
	101.33	101.60	CSND		MH	CS	CLY	WM	SR	5YR8/4	5R7/4	O	W	hem	EYRE
	101.60	101.95	CSND		MH	VCS	CLY	WM	SR	5YR4/4	5YR8/4	O	S	goet	EYRE
	101.95	103.20	SCLY		ML	MS	CLY	WM	SR	5YR4/4	5R7/4	O	M	hem	EYRE
	103.20	103.29	CSND		MH	VCS	CLY	WM	SR	5YR5/6	10R5/4	O	M	goet	EYRE
	103.29	105.24	CSND	SAND	MH	CS	CLY	WM	SR	5Y7/2	5YR8/1	O	W	hem	EYRE
	105.24	105.83	CLAY	SCLY	ML	FS	CLY	W	SR	5Y7/2	5YR8/1	O	T	hem	EYRE
	105.83	106.60	SCLY		ML	FS	CLY	W	SA	5Y7/2	0	O	T	hem	EYRE
	106.60	106.82	SCLY		ML	FS	CLY	W	SR	10YR7/4	0	O	S	goet	EYRE
	106.82	107.25	GSND		MH	PEB	MS	P	SA	5YR3/4	5YR4/4	O	S	goet	EYRE
	107.25	107.90	GSND		MH	COB	MS	P	SA	5YR3/4	5YR4/4	O	S	goet	EYRE

	107.90	109.80	SCLY	KCLY	ML	CS	CLY	WM	SR	5Y7/2	5R7/4	O	W	hem	EYRE
	109.80	112.00	CSND		MH	CS	CLY	WM	SR	5Y7/2	5R7/4	O	W	hem	EYRE
	112.00	112.50	CSND		MH	MS	CLY	WM	SR	5Y7/2	5R7/4	O	W	goet	EYRE
	112.50	113.50	CSND		MH	VCS	CLY	WM	SR	5Y7/2	5YR8/4	O	M	goet	EYRE
	113.50	114.28	SCLY		ML	CS	CLY	WM	SR	5Y7/2	5YR8/4	O	M	goet	EYRE
	114.28	114.76	SCLY		ML	MS	CLY	WM	SR	5Y7/2	5YR8/4	O	M	goet	EYRE
	114.76	114.95	SAND	CSND	MH	VCS	CLY	M	SR	5Y7/2	5YR8/4	O	W	goet	EYRE
	114.95	115.83	SILT		ML	VCS	CLY	P	SR	5Y7/2	N8	R			EYRE
	115.83	115.90	SILT		ML	VCS	CLY	P	SR	5Y7/2	5R6/2	O	M	hem	EYRE
	115.90	116.70	SILT	CLAY	ML	FS	CLY	WM	SR	5YR8/4	5Y7/2	O	W	goet	EYRE
	116.70	116.95	CSND		MH	PEB	MS	WM	SR	5YR8/4	5Y7/2	O	T	goet	EYRE
	116.95	117.62	KCLY	SCLY	L	FS	CLY	W	SR	5Y8/1	5Y7/2	R			EYRE
	117.62	119.00	KCLY		L	SLT	CLY	W		5Y8/1	0	R			
	119.00	120.55	KCLY	SCLY	L	CS	CLY	W	SR	5Y8/1	5YR8/1	O	T	hem	EYRE
	120.55	121.00	KCLY		L	CS	CLY	W	SR	5Y8/1	5YR8/1	O	T	hem	EYRE
	121.00	121.70	KCLY		L	SLT	CLY	W	SR	5Y8/1	5YR8/1	O	T	hem	EYRE
	121.70	123.00	KCLY	GCLY	ML	PEB	CLY	W	SA	5Y8/1	0	R			EYRE
	123.00	123.95	KCLY		L	FS	CLY	W	SR	5Y8/1	5YR8/1	O	W	hem	EYRE
	123.95	124.30	KCLY	SCLY	ML	MS	CLY	W	SR	5Y8/1	0				EYRE
	124.30	124.60	GCLY		ML	PEB	CLY	WM	SR	5Y8/1	5Y6/1				EYRE
	124.60	126.60	CSND		MH	CS	CLY	WM	SR	5Y6/1	10YR7/4	O	W	goet	EYRE
	126.60	127.30	CSND		MH	VCS	CLY	WM	SR	5Y6/1	10YR7/4	O	W	goet	EYRE
	127.30	130.50	SCLY		ML	MS	CLY	WM	SR	5Y6/1	0				EYRE
	130.50	130.65	CSND		MH	CS	CLY	WM	SR	5Y6/1	5YR8/1	O	T	hem	EYRE
	130.65	131.15	SCLY		ML	FS	CLY	WM	SR	5Y6/1	0				EYRE
	131.15	131.35	SCLY		ML	VCS	CLY	WM	SR	5Y6/1	5YR8/1	O	T	hem	EYRE
	131.35	132.30	SCLY		ML	MS	CLY	WM	SR	5Y6/1	5Y8/1	O	T	goet	EYRE
	132.30	132.50	SCHw		ML	VCS	CLY	WM	SR	5Y8/1	5YR8/4	O	T	goet	BSWf
	132.50	133.50	SCHw		ML	CS	CLY	WM	SR	5Y8/1	0	R			BSWf
	133.50	134.22	SCHw		ML	VCS	CLY	PM	SR	5Y8/1	0	R			BSWf
	134.22	134.85	SCHw		ML	PEB	CLY	PM	SR	5Y8/1	0	R			BSWf
	134.85	135.00	SCHw		ML	VCS	CLY	PM	SR	5Y8/1	0	R			BSWf
	135.00	136.42	SCHw		ML	FS	CLY	WM	SR	5Y8/1	0	R			BSWf
	136.42	136.55	SCHw		ML	CS	CLY	WM	SR	5Y8/1	5YR8/4	R			BSWf
	136.55	136.76	SCHw		ML	MS	CLY	WM	SR	5Y8/1	0	R			BSWf
	136.76	137.20	SCHw		ML	PEB	CLY	WM	SR	5Y8/1	0	R			BSWf
	137.20	138.62	SCHw		ML	MS	CLY	WM	SR	5Y8/1	0	R			BSWf
	138.62	139.63	SCHw		ML	VCS	CLY	WM	SR	5Y8/1	0	R			BSWf
	139.63	139.85	SCHw		ML	CS	CLY	WM	SR	5Y8/1	0	R			BSWf
	139.85	140.05	SCHw		ML	PEB	CLY	WM	SR	5Y8/1	0	R			BSWf
	140.05	140.65	SCHw		ML	VCS	CLY	WM	SR	5Y8/1	N8	R			BSWf
	140.65	140.85	SCHw		ML	PEB	CLY	WM	SR	5Y8/1	N8	R			BSWf
	140.85	141.63	SCHw		ML	MS	CLY	W	SR	5Y8/1	0	R			BSWf

	141.63	142.64	SCHw		ML	FS	CLY	W	SR	5Y8/1	5Y6/1	R			BSWf
	142.64	143.65	SCHw		ML	FS	CLY	W	SR	5Y6/1	5Y8/1	R			BSWf
	143.65	143.83	SCHw		MH	PEB	CLY	PM	SR	5Y6/1	0	R			BSWf
	143.83	144.15	SCHw		ML	CS	CLY	WM	SR	5Y6/1	5Y8/1	R			BSWf
	144.15	145.30	SCHw		ML	FS	CLY	WM	SR	5Y8/1	0	R			BSWf
	145.30	145.60	SCHw		ML	FS	CLY	WM	SR	5Y6/1	5YR8/4	R			BSWf
	145.60	145.80	SCHw		ML	COB	CLY	WM	SR	5Y6/1	5YR8/4	R			BSWf
	145.80	146.00	SCHw		ML	VCS	CLY	WM	SR	5Y6/1	5YR8/4	R			BSWf
	146.00	147.80	SCHw		ML	MS	CLY	WM	SR	5Y6/1	0	R			BSWf
	147.80	148.20	SCHw		ML	CS	CLY	WM	SR	5Y6/1	5YR6/4	R			BSWf
	148.20	148.85	SCHw		ML	VCS	CLY	WM	SR	5Y6/1	5YR6/4	R			BSWf
	148.85	150.00	SCHw		ML	FS	CLY	WM	SR	5Y6/1	5YR8/1	R			BSWf
	150.00	150.42	SCHw		ML	VCS	CLY	WM	SR	5Y6/1	5YR8/4	R			BSWf
	150.42	151.40	SCHw		ML	VCS	CLY	WM	SR	5Y6/1	0	R			BSWf
	151.40	152.37	SCHw		ML	FS	CLY	W	SR	5Y6/1	N8	R			BSWf
	152.37	152.70	SCHw		ML	FS	CLY	W	SR	N8	5Y6/1	R			BSWf
	152.70	153.10	SCHw		ML	VCS	CLY	WM	SR	N8	N7	R			BSWf
	153.10	153.30	SCHw		ML	MS	CLY	W	SR	N8	N7	R			BSWf
	153.30	153.52	SCHw		ML	VFS	CLY	W	SR	N8	N7	R			BSWf
	153.52	154.00	SCHw		ML	FS	CLY	WM	SR	N7	N8	R			BSWf
	154.00	155.70	SCHt		ML	FS		WM	SR	N7	N8	R			BSWf
	155.70	156.30	SCHt		ML	FS		WM	SR	N6	N7	R			BSWf
	156.30	156.74	SCHt		ML	CS		WM	SR	N6	N7	R			BSWf
	156.74	157.00	SCHt		ML	PEB		WM	SR	N7	5GY7/2				BSWf
	157.00	157.60	SCHt		L	CS		WM	SR	N7	5GY7/2				BSWf
	157.60	158.47	SCHt		L	FS		WM	SR	5GY7/2	N7				BSWf
	158.47	158.70	SCHt		L	FS		WM		5GY7/2	N7				BSWf
	158.70	159.20	SCHt		L			WM		5GY5/2	5GY7/2				BSWf
	159.20	160.70	SCHt		L	COB		WM	SR	5GY5/2	5GY7/2				BSWf
	160.70	160.90	SCHt		L	VCS			SA	5GY5/2	5GY7/2				BSWf
	160.90	161.30	SCHt		L	COB		WM	SA	5GY5/2	5GY7/2				BSWf
	161.30	162.70	SCHt		L	VCS		M	SA	5GY5/2	5GY7/2				BSWf
	162.70	162.90	SCHt		L	PEB		P	SA	5GY5/2	5GY7/2				BSWf
	162.90	163.10	SCHw		ML	CS		P	SR	5GY5/2	N1				BSWf
	163.10	163.30	SILT		ML	MS		P	SR	5Y4/1	5Y5/2				BSWf
	163.30	163.80	COAL		ML	MS		P	SR	N1	5Y4/1				BSWf
	163.80	164.05	SCHw		L	FS		WM		5Y6/1	5Y5/2				BSWm
	164.05	165.58	SCHf		L					5Y5/2	5Y4/1				BSWm
	165.58	168.20	SCHf							5GY5/2	5Y5/2				BSWm
	168.20	171.90	SCHt							5GY7/2	0				BSWm
	171.90	173.60	SCHt							5GY7/2	5GY8/1				BSWf
	173.60	174.20	SCHt							0	0				BSWf
	174.20	175.70	SCHt							5GY8/1	0				BSWf

	175.70	178.20	SCHt							5GY7/2	5GY8/1	O	T	hem	BSWf
	178.20	178.95	SCHt							5GY7/2	5R6/2	O	W	hem	BSWf
	178.95	179.25	SCHf							5GY7/2	0				BSWf
	179.25	181.28	SCHf							5GY7/2	5R6/2	O	T	hem	BSWf
	181.28	182.10	SCHf							5GY7/2	5R7/4	O	T	hem	BSWf
	182.10	182.25	SCHt							5GY8/1	N8				BSWf
	182.25	183.40	SCHf							5GY7/2	5GY8/1				BSWf
	183.40	185.78	SCHf							5GY7/2	5GY8/1	O	W	hem	BSWf
	185.78	186.10	SCHf							5GY7/2	5GY8/1	O	T	hem	BSWf
	186.10	187.30	SCHf							5GY7/2	5R7/4	O	W	hem	BSWf
	187.30	188.90	SCHf							N8	5GY8/1	O	T	hem	BSWf
	188.90	189.70	SCHw							N8	0	O	T	hem	BSWf
	189.70	189.85	SCHw							N6	N3	O	W	goet	BSWf
	189.85	190.05	SCHw							5YR4/4	N7	O	S	goet	BSWf
	190.05	190.40	SCHw							5YR4/4	5YR6/4	O	S	goet	BSWf
	190.40	190.90	SCHw							N6	5YR6/4	O	W	goet	BSWf
	190.90	191.60	SCHw							10YR6/6	5YR3/4	O	S	goet	BSWf
	191.60	192.00	SCHw							5YR6/4	10YR7/4	O	W	goet	BSWf
	192.00	192.35	SCHw							5YR5/2	N7	O	T	goet	BSWf
	192.35	194.90	SCHt							5GY8/1	N8				BSWf
	194.90	195.85	QZT							N7	10R5/4	O	M	hem	BSWf
	195.85	197.40	QZT							N7	10R5/4	O	W	hem	BSWf
	197.40	201.20	SCHf							5GY5/2	5Y8/1				BSWf
	201.20	202.70	SCHf							5GY5/2	5Y8/1				BSWf
	202.70	203.15	SCHf							5GY5/2	N6				BSWf
	203.15	203.75	SCHf							5GY5/2	N6				BSWf
	203.75	204.50	SCHf							5GY5/2	N6				BSWf
	204.50	205.20	SCHf							5GY5/2	N6	O	W	hem	BSWf
	205.20	208.20	SCHf							N5	5GY5/2				BSWf
	208.20	210.10	SCHf							N5	5GY5/2	O	S	hem	BSWf
	210.10	212.53	SCHf							5GY5/2	5GY7/2				BSWf
	212.53	212.86	SCHf							5GY5/2	5GY7/2			hem	BSWf
	212.86	213.73	SCHf							5GY5/2	5GY7/2	O	S	hem	BSWf
	213.73	215.60	SCHf							5GY5/2	5GY7/2				BSWf
	215.60	216.20	QZT							10R5/4	N8	O	S	hem	BSWf
	216.20	216.50	QZT							10R5/4	N8	O	M	hem	BSWf
	216.50	218.70	QZT							10R5/4	N8	O	M	hem	BSWf
	218.70	218.85	QZT							10R5/4	N8	O	M	hem	BSWf
	218.85	220.70	QZT							10R5/4	N8	O	M	hem	BSWf
	220.70	221.90	QZT							10R5/4	N8	O	S	hem	BSWf
	221.90	222.20	QZT							10R5/4	N8	O	W	hem	BSWf
	222.20	222.95	QZT							10R5/4	N8	O	S	hem	BSWf
	222.95	225.88	QZT							N8	5YR8/1	O	W	hem	BSWf

	225.88	226.50	QZT							5GY7/2	N8	O	W	goet	BSWf
	226.50	226.85	QZT							10R5/4	N8	O	S	hem	BSWf
	226.85	227.20	QZT							10R5/4	N8	O	M	hem	BSWf
	227.20	230.20	QZT							10R5/4	N8	O	S	hem	BSWf
	230.20	231.10	QZT							5Y5/2	N7	O	W	hem	BSWf
	231.10	232.42	QZT							5R6/2	N7	O	W	hem	BSWf
	232.42	235.50	QZT							5GY5/2	N7	O	W	hem	BSWf
	235.50	238.20	QZT							5GY5/2	10R5/4	O	S	hem	BSWf
	238.20	239.15	QZT							5GY5/2	10R5/4	O	S	hem	BSWf
	239.15	239.45	QZT							5GY5/2	5Y8/1				BSWf
	239.45	240.20	QZT							5GY5/2	0	O	W	hem	BSWf
FMC024	0.00	2.00	CGRV	GCLY	MH	GRV	CLY	P	SA	5YR4/4	5YR5/2	O	C	hem	W
	2.00	6.00	GRVL	GRVL	H	GRV	GRV	P	SA	5YR5/2	5R6/2	O	T	hem	W
	6.00	8.00	SGRV	GSND	ML	GRV	CS	P	SA	5YR5/2	10YR7/4	O	M	goet	W
	8.00	12.00	SGRV	GSND	MH	CS	GRV	P	SA	10YR7/4	5YR5/2	O	S	goet	W
	12.00	14.00	GSND	SGRV	MH	CS	GRV	P	SA	10YR7/4	5YR4/4	O	S	goet	W
	14.00	16.00	GSND	SGRV	MH	CS	GRV	P	SA	10YR7/4	5YR5/2	O	S	goet	W
	16.00	20.00	GSND	SGRV	ML	CS	gvv	P	SA	10YR7/4	5YR4/4	O	M	hem	W
	20.00	24.00	GSND	SGRV	MH	FS	GRV	P	SA	5YR5/6	10YR7/4	O	M	goet	W
	24.00	26.00	GSND	SGRV	MH	CS	GRV	P	SA	5YR5/2	5G8/1	O	M	goet	W
	26.00	28.00	GSND	SGRV	MH	CS	gvv	P	SA	5YR5/6	10YR7/4	O	M	goet	W
	28.00	30.00	GSND	SGRV	MH	FS	GRV	P	SA	10YR7/4	5YR5/2	O	M	goet	W
	30.00	32.00	CSND	SCLY	ML	FS	CLY	P	SA	10YR7/4	10YR6/6	O	C	goet	W
	32.00	36.00	GSND	SGRV	MH	MS	GRV	P	SA	10YR7/4	5YR5/2	O	S	goet	W
	36.00	38.00	CSND	SCLY	ML	CS	CLY	P	SA	10YR7/4	10YR6/6	O	S	goet	W
	38.00	40.00	CSND	SCLY	MH	MS	CLY	P	SA	10YR7/4	5YR5/2	O	M	goet	W
	40.00	46.00	GSND	SGRV	MH	FS	GRV	P	SA	10YR7/4	5GY7/2	O	W	goet	W
	46.00	54.00	GSND	SGRV	MH	CS	gvv	P	SA	N9	10YR7/4	O	T	goet	NAM
	54.00	56.00	CSND	SCLY	MH	CS	CLY	P	SA	N9	10YR7/4	O	W	goet	NAM
	56.00	60.00	CSND	SCLY	MH	FS	CLY	P	SA	N8	10YR7/4	O	T	goet	NAM
	60.00	62.00	CSND	SCLY	MH	FS	CLY	P	SA	10YR7/4	5GY7/2	O	M	goet	NAM
	62.00	68.00	SASL	SLSA	MH	SLT	FS	P	SA	N9	5GY7/2	O	T	goet	NAM
	68.00	72.00	GRVL	SAND	MH	GRV	CS	P	SA	5YR5/2	5G8/1	O	T	goet	NAM
	72.00	78.00	CSND	SCLY	MH	FS	CLY	P	SA	N8	10YR7/4	O	T	goet	NAM
	78.00	82.50	GRVL	SAND	MH	GRV	CS	P	SA	5YR5/2	N8	O	T	goet	NAM
	82.50	82.69	LOSS												BULL
	82.69	82.97	CLAY		L	SLT	CLY	W	R	10YR7/4	N9	O	S	GOET	BULL
	82.97	83.00	LOSS												BULL
	83.00	84.47	CLAY		L	SLT	CLY	W	R	10YR7/4	5R5/4	O	S	GOET	BULL
	84.47	85.00	CLAY		L	SLT	CLY	W	R	5R5/4	10YR7/4	O	S	HEM	BULL
	85.00	85.40	CLAY		L	SLT	CLY	W	R	N9	5YR7/2	O	W	HEM	BULL
	85.40	86.01	CLAY		L	SLT	CLY	W	R	5R4/6	N9	O	S	HEM	BULL
	86.01	86.12	CLAY		L	SLT	CLY	W	R	5YR8/1	N9	O	W	HEM	BULL

	86.12	87.79	CLAY		L	VFS	CLY	W	R	10YR7/4	5Y7/2	O	M	GOET	BULL
	87.79	88.28	CLAY	SILT	L	SLT	CLY	W	R	N7	N8	R			BULL
	88.28	89.80	DIAM		ML	FS	CLY	WM	SR	N6		R			FMD
	89.80	90.50	DIAM		ML	FS	CLY	WM	SR	N4	N5	R			FMD
	90.50	91.85	DIAM		ML	FS	CLY	WM	SR	N6		R			FMD
	91.85	92.28	DIAM	GRVL	MH	GRV	CLY	P	SA	N7	N9	R			FMD
	92.28	92.66	DIAM	SAND	MH	MS	CLY	M	SR	N7	N6	R			FMD
	92.66	93.94	DIAM		L	VFS	CLY	WM	SR	N6		R			FMD
	93.94	94.80	DIAM	GRVL	ML	GRV	CLY	P	SA	N6	N8	R			FMD
	94.80	95.37	DIAM	GRVL	ML	GRV	CLY	P	SR	N7		R			FMD
	95.37	95.77	DIAM		ML	FS	CLY	WM	SR	10YR7/4	5YR8/1	O	S	GOET	FMD
	95.77	95.86	DIAM		ML	VFS	CLY	WM	SR	5R4/6		O	C	HEM	FMD
	95.86	96.11	DIAM	GRVL	MH	PEB	CLY	P	SR	10YR7/4	5YR8/4	O	S	GOET	FMD
	96.11	96.46	DIAM		MH	CS	SLT	MP	SA	5R4/2		O	S	HEM	FMD
	96.46	96.67	DIAM		MH	CS	CLY	MP	SA	N9	5YR8/1	O	T	HEM	FMD
	96.67	97.53	DIAM		MH	FS	SLT	WM	SR	5R7/4		O	M	HEM	FMD
	97.53	97.59	DIAM		MH	VFS	SLT	WM	SR	10YR7/4	5YR8/4	O	M	GOET	FMD
	97.59	98.68	DIAM		MH	FS	CLY	WM	SR	5YR7/2	5YR8/4	O	M	HEM	FMD
	98.68	99.83	DIAM		MH	FS	CLY	WM	SR	5YR8/4	N9	O	W	HEM	FMD
	99.83	100.90	DIAM		MH	MS	SLT	WM	SR	5YR7/2		O	M	HEM	FMD
	100.90	101.00	LOSS												FMD
	101.00	102.55	DIAM		ML	MS	CLY	M	SA	5YR8/1	5YR8/4	O	W	HEM	FMD
	102.55	103.35	DIAM		ML	FS	CLY	WM	SR	5YR8/4		O	W	GOET	FMD
	103.35	103.43	DIAM	KCLY	ML	VFS	CLY	W	SR	N9	5Y7/2	N			FMD
	103.43	105.50	DIAM		ML	FS	CLY	WM	SR	5YR8/4	5R4/6	O	W	HEM	FMD
	105.50	106.43	DIAM		ML	FS	CLY	WM	SR	N9	5R4/6	O	M	HEM	FMD
	106.43	107.08	DIAM		ML	FS	CLY	WM	SR	5YR7/2		O	M	HEM	FMD
	107.08	108.20	DIAM		ML	FS	CLY	WM	SR	5Y7/2	5YR8/4	O	W	GOET	FMD
	108.20	108.32	DIAM	GRVL	MH	GRV	CLY	P	SR	5Y7/2	5YR8/4	O	T	GOET	FMD
	108.32	109.46	DIAM		ML	MS	CLY	M	SR	10YR7/4		O	S	GOET	FMD
	109.46	109.51	KCLY	DIAM	L	SLT	CLY	W	R	N9		N			FMD
	109.51	112.36	DIAM		ML	MS	CLY	M	SR	5YR7/2	5YR8/4	O	M	HEM	FMD
	112.36	113.47	DIAM		ML	VFS	CLY	WM	SR	10YR7/4		O	M	GOET	FMD
	113.47	114.40	DIAM		ML	VFS	CLY	WM	SR	5YR8/1	5YR8/4	O	T	HEM	FMD
	114.40	115.21	DIAM		ML	VFS	CLY	WM	SR	10YR7/4	5YR8/1	O	W	GOET	FMD
	115.21	116.00	DIAM		ML	FS	CLY	WM	SR	10YR7/4		O	M	GOET	FMD
	116.00	117.44	DIAM		ML	FS	CLY	WM	SR	N4		R			FMD
	117.44	118.60	DIAM		ML	MS	CLY	M	SR	N5		R			FMD
	118.60	119.10	DIAM		ML	FS	CLY	WM	SR	N5		R			FMD
	119.10	119.11	COAL		ML	VFS		W	R	N1		R			FMD
	119.11	119.90	DIAM		ML	FS	CLY	WM	SR	N5		R			FMD
	119.90	122.27	DIAM		ML	MS	CLY	M	SR	N5		R			FMD
	122.27	122.69	DIAM		MH	GRV	CLY	P	SR	N5	N6	R			FMD

	122.69	123.87	DIAM		ML	MS	CLY	M	SR	N6		R			FMD
	123.87	123.97	DIAM	GRVL	ML	PEB	CLY	P	SR	N7	5Y7/2	R			FMD
	123.97	124.59	DIAM		ML	FS	CLY	WM	SR	N7	5Y7/2	R			FMD
	124.59	125.25	DIAM	GRVL	MH	GRV	CLY	P	SA	N6		R			FMD
	125.25	126.48	DIAM		ML	VFS	CLY	WM	SR	N5	N4	R			FMD
	126.48	126.93	DIAM	GRVL	MH	GRV	CLY	P	SA	5Y7/2	N7	R			FMD
	126.93	127.10	GRVL	DIAM	MH	GRV	CLY	P	SR	N8	N6	R			FMD
	127.10	127.82	DIAM		L	CLY		W	R	N5		R			FMD
	127.82	128.17	DIAM	GRVL	MH	GRV	CLY	P	SA	N6	N5	R			FMD
	128.17	129.33	DIAM	CLAY	ML	VCS	CLY	MP	SA	N5		R			FMD
	129.33	131.35	DIAM	GRVL	MH	GRV	CLY	P	SA	N6		R			FMD
	131.35	131.45	DIAM	CLAY	L	VFS	CLY	WM	SR	N6	N5	R			FMD
	131.45	171.75	DIAM		ML	MS	CLY	M	SR	N6		R			FMD
	171.75	131.96	BASM	DIAM	ML	CS	CLY	MP	SA	N6	N9	R			FMD
	131.96	134.20	DIAM		ML	MS	CLY	M	SA	N7	N6	R			FMD
	134.20	135.05	DIAM	GRVL	MH	GRV	CLY	P	SR	N7		R			FMD
	135.05	136.67	PORP		MH					5R7/4	5G7/4	N			BSMf
	136.67	136.68	XXXX							N1		R			BSMf
	136.68	137.08	PORP		MH					N9	5YR8/1	O	W	HEM	BSMf
	137.08	141.50	PORP		MH					5R7/4	5G7/4	N			BSMf
	141.50	144.33	PORP		ML					5G7/4		N			BSMf
	144.33	150.00	PORP		ML					5YR8/1	5G7/4	N			BSMf
	150.00	152.75	PORP		ML					5G7/4	5YR8/1	N			BSMf
	152.75	155.06	PORP		ML					5R7/4	5G7/4	N			BSMf
	155.06	157.27	PORP		ML					5G7/4	5YR8/1	N			BSMf
	157.27	157.61	PORP		ML					5G7/4	N9	N			BSMm
	157.61	160.10	BSMM		L					5G5/6	N9	N			BSMm